UNIVERSITY OF SOUTHAMPTON

Faculty of Engineering, Science and Mathematics

School of Engineering Sciences

Photon Transport in Fluorescent Solar Collectors

by

Thomas J. J. Meyer

Thesis for the degree of Doctor of Philosophy

July 2009

UNIVERSITY OF SOUTHAMPTON

ABSTRACT

FACULTY OF ENGINEERING, SCIENCE AND MATHEMATICS

SCHOOL OF ENGINEERING SCIENCES

MATERIALS RESEARCH GROUP

Doctor of Philosophy

PHOTON TRANSPORT IN FLUORESCENT SOLAR COLLECTORS

by Thomas J. J. Meyer

The high cost of crystalline silicon (c-Si) is the principal barrier to wider use of traditional solar arrays. Fluorescent solar collectors (FSCs) represent a promising alternative since the use of silicon in such devices is minimized. The theoretical efficiency of a FSC has been shown to be practically equal to that of the Shockley-Queisser detailed-balance model. In practice, however, FSC efficiencies do not exceed few percents.

This thesis presents theoretical modelling exploring the physics of photon transport in fluorescent collectors and experimental work assessing the potential of such devices coupled to c-Si solar cells. To accomplish this aim the research has pursued the following objectives:

- fabrication and characterization of an experimental batch of high-efficiency $n^+/p/p^+$, c-Si solar cells (this effort, in the Microelectronic Fabrication Unit at Southampton University, was in its final stage when a major fire destroyed the facilities)
- development of a simple semi-analytical detailed-balance model for multiple-junction solar cells
- fabrication and detailed characterization of liquid fluorescent solar collectors.
- characterization and modelling of photon transport losses within the collector plate by ray-tracing and theoretical techniques based on the "two-flux model" developed in the Solar Energy Lab.

Principal results include the fabrication of a two-dye collector with optical efficiency of 7% which compares well with the best devices fabricated elsewhere. Numerical simulations by ray tracing indicate that collector efficiency is practically independent of shape and that thin-film collectors do not perform any better than standard flat-plate devices. Fundamental characterization of the fluorescent light chemical

potential shows that FSCs operate close to thermodynamic limitations. Non-radiative losses do not affect the chemical potential of the light escaping from the collector - a major advantage over simple semiconductor-based solar cells, where non-radiative losses significantly affect the open-circuit voltage.

A semi-analytical model for P-N junction cells has been developed which is sufficiently accurate for practical applications. The model, in various forms of its implementation, makes it possible to examine in detail the operation of crystalline silicon solar cell as well as estimate the efficiency and fundamental losses in multijunction cells, including the modelling of what is probably the highest efficiency achievable by a photovoltaic device – that is 85 % for an infinite stack of cells under 45000 suns.

Contents

List of figures

List of tables

Declaration of Authorship

I, Thomas John Julien Meyer declare that the thesis entitled:

PHOTON TRANSPORT IN FLUORESCENT SOLAR COLLECTORS

and the work presented in the thesis are both my own, and have been generated by me as the result of my own original research. I confirm that:

this work was done wholly or mainly while in candidature for a research degree at this University;

- where any part of this thesis has previously been submitted for a degree or any other qualification at this University or any other institution, this has been clearly stated;
- where I have consulted the published work of others, this is always clearly attributed;
- where I have quoted from the work of others, the source is always given. With the exception of such quotations, this thesis is entirely my own work;
- I have acknowledged all main sources of help;
- where the thesis is based on work done by myself jointly with others, I have made clear exactly what was done by others and what I have contributed myself;
- parts of this work have been published as:

1. *The chemical potential of light in fluorescent solar collectors.* **T.J.J. Meyer, T. Markvart.** 6, 2009, Journal of applied physics, Vol. 105, pp. 063110-8.

2. *Raytracing techniques applied to the modeling of fluorescent solar collectors.* **T.J.J Meyer, J. Hlavaty, L. Smith, E.R. Ferniere, T. Markvart.** 2009, in *Physics and Simulation of Optoelectronic Devices XVII*, edited by Marek Osinski, Bernd Witzigmann, Fritz Henneberger, Yasuhiko Arakawa, Proceedings of SPIE Vol. 7211 (SPIE, Bellingham, WA, 2009) 72110N.

3. *The chemical potential of fluorescent light.* **T.J.J. Meyer, T. Markvart.** 2008, Proceedings of the 23rd European photovoltaic solar energy conference, Valencia, Spain, pp. 399-403. 1CV.1.53.

4. *The role of fluorescent collector edge on the fluorescent solar collector performance.* **P. Kittidachachan, T.J.J. Meyer, N. Soleimani, L. Danos and T. Markvart.** 2008, Proceedings of the 4th photovoltaic science application and technology, Bath, UK. PVSAT4_0.17.

5. *The chemical potential of light.* **T.J.J Meyer, T. Markvart.** 2008, Proceedings of the 4th photovoltaic science application and technology, Bath, UK. PVSAT4_0.14.

6. *Photon collection efficiency of fluorescent solar collectors.* **P. Kittidachachan, L.Danos, T.J.J. Meyer, N. Alderman, and Tom Markvart.** 12, 2007, Chimia international journal for chemistry, Vol. 61, pp. 780-786.

7. *Fluorescent solar collectors, the solar cell of tomorrow*. **T.J.J. Meyer, T. Markvart, L. Danos, R. Greef and P. Kittidachachan.** 2007, Research showcase NOCS, Southampton, UK.

8. *Spectroscopic characterisation of liquid fluorescent solar collectors.* **T.J.J. Meyer, T. Markvart, L. Danos, R. Greef, P. Kittidachachan.** 2007, Proceedings of the 3rd photovoltaic science application and technology, Durham, UK.

9. *Characterisation of fluorescent collectors in terms of fluorescence collection efficiency.* **P. Kittidachachan, T.J.J. Meyer, L. Danos, R. Greef, T. Markvart.** 2007, Proceedings of the 22nd European photovoltaic solar energy conference, Milan, Italy, pp. 301-305. 1CV.1.23.

10. *Characterisations and modelling of liquid fluorescent solar collectors.* **T.J.J. Meyer, L. Danos, R. Greef, P. Kittidachachan, T. Markvart.** 2006, London institute of physics conference IOP, London, UK.

11. *An analysis of fluorescent solar collectors by fluorescent collection efficiency.* **P. Kittidachachan, T.J.J. Meyer, L. Danos, R. Greef, T. Markvart.** 2006, London institue of physics conference IOP, London, UK.

12. *Characterisation of fluorescent collectors based on solid, liquid and Langmuir-Blodgett films.* **L. Danos, P. Kittidachachan,T.J.J. Meyer, R. Greef, T. Markvart.** 2006, Proocedings of the 21st European photovoltaic solar energy conference, Dresden, Germany, pp. 443-446. 1CV.1.25.

13. *Modelling the efficiency of multi-junction solar cells.* **T.J.J. Meyer, T. Markvart.** 2005, Proceedings of the 2nd photovoltaic science application and technology conference, Loughborough, UK.

Signed: Date:

Acknowledgements

First of all I would like to acknowledge my sponsors; this work was funded through the SUPERGEN (Sustainable Power Generation and Supply) project. SUPERGEN is an EPSRC funded programme with the aim of improving renewable energy technologies in the UK. The solar energy branch of this project consists on the collaboration between six universities: Loughborough, Bangor, Bath, Durham, Southampton and Northumberland.

It is my pleasure to acknowledge many stimulating discussions with my colleagues and friends: Prof. T. Markvart for giving me the opportunity and freedom to carry out my doctoral research, Dr R. Greef for the optic related technical discussions, Prof. D. Bagnall and Dr S. Boden for the c-Si fabrication related discussions, Dr. R. Knox for the help with the thermodynamics of fluorescence, Dr L. Danos and P. Kittidachachan for the help with experimental measurements, P. Wright for his help with the computer aided design of the liquid collectors, B.C. Rowan for the help with data on Lumogen dyes, F. Pace, Dr J. King for editorial advices and C. Hickey for proofreading.

I would also like to thank the individuals from the industry cooperating with us, especially B. Calt, Ed Freniere, J. Hlavaty (TracePro®) for a free licence, P. Bailey (Hellma) helping with the collector design, L. Lyons (Bentham) for his help with the system calibration and D. Turner (BASF) for kindly donating the Lumogen dyes.

At least but not last I would like to acknowledge Rob, Chris and Gwyneth for their technical and administrative support.

List of symbols

Symbol	Description	Preferred unit
$A_{0\rightarrow1}$	Einstein A coefficient	s^{-1}
$B_{1\rightarrow0}$	Einstein B coefficient	"
A_x	Area of x	cm^2 or m^2
A_{cell}	· area of the solar cell	"
A_{front}	· area of the front collector surface	"
A_{edge}	· collector edge area	"
Abs	Absorbance	-
α	· absorption coefficient	cm^{-1}
α_{eff}	· effective absorption coefficient	cm^{-1}
$\sigma(\lambda)$	· cross-section	cm^2
$\xi(\nu)$	· molar decadic absorption coefficient	$L\ mol^{-1}\ cm^{-1}$
C	Concentration	$mol\ L^{-1}$
c	Speed of light	$m\ s^{-1}$
ς	Conductivity	$(\Omega\ cm)^{-1}$
D	Diffusion coefficient	$cm^{-2}s^{-1}$
D_n	· diffusion coefficient of electrons	"
D_p	· diffusion coefficient of holes	"
$D_{Earth-sun}$	Distance between the sun and Earth	km
$\vec{E}$	Electric field	$V\ cm^{-1}$
E	Energy	eV
E_{trap}	· trapping level energy	"
E_{gap}	· semiconductor band gap energy	"
E_{S_1}	· energy of the excited state	"
E_{S_0}	· energy of the ground state	"
$\dot{f}$	Photon flux	$ph\ cm^{-2}nm^{-1}$
$\dot{f}_{sun}$	· Sun photon flux	"
$\dot{f}_{front}$	· Photon flux emitted through the collector front face	"
$\dot{f}_e$	· Edge fluorescence photon flux	"
$\dot{f}_{ind}$	· absorbed photon flux	"
$\dot{f}_{abs}$	· induced photon flux	"
$\dot{f}_1$	· first-generation fluorescence photon flux	"
f	Irradiance	$W\ m^{-2}eV^{-1}$
f_{sun}	· sun spectral irradiance	"
$\mathcal{F}_e$	· Quasi-blackbody irradiance	"
f_1	First fluorescence emissive power	$W\ Hz^{-1}$
ν	Frequency	s^{-1}

FF		Fill factor	-
I		Current	A
	I_0	· dark current	"
	I^{ll}	· current generated under illumination	"
	I_{sc}	· short-circuit current	"
	I_{cell}	· cell generated current	"
$\boldsymbol{G}$		Optical Gain	-
$\boldsymbol{g}$		statistical weight	-
	$\boldsymbol{g}^*$	· statistical weight of the excited level	-
G		Excitation rate	$cm^{-3}s^{-1}$
	G_n	· electron generation rate	"
	G_p	· hole generation rate	"
h		Planck's constant	J s or eV s
$h\nu$		Energy	eV
	$h\nu_{gap}$	· semiconductor band gap energy	"
	$\mathrm{h}\nu_0$	· $S_0 \rightarrow S_1$ energy separation	"
H		Solar cell thickness	mm
J		Current density	$A\ cm^{-2}$
	J_{drift}	· drift current	
	J_{dif}	· diffusion current	
	J_{total}	· total current	
k		Boltzmann's constant	$J\ K^{-1}$ or $eV\ K^{-1}$
k_{x}		Rate of x	s^{-1}
	k_{rad}	· emissive radiative rate	"
	k_{nr}	· non-emissive de-excitation rate	"
	k_{abs}	· absorption rate	"
L		Length	cm or mm
	L	· collector length	"
	l	· light path length	"
	L_n	· electron diffusion length	"
	L_h	· hole diffusion length	"
λ		Wavelength	nm
	λ_{g}	Semiconductor band gap wavelength	"
$\boldsymbol{\mu}$		Carrier mobility	$cm^2\ Vs$
	$\boldsymbol{\mu_n}$	· electron mobility	-
	$\boldsymbol{\mu_p}$	· hole mobility	-
μ		Chemical potential	eV
	μ_{flux}	· edge fluorescence chemical potential	-
	μ_{dye}	· dye chemical potential	-
	μ_{theo}	· theoretical chemical potential	-
n		Refractive index	-
	n_{col}	· collector refractive index	-
	n_a	· active layer refractive index	-

	n_s	· substrate refractive index	-
η		Efficiency	-
	η_{ult}	· ultimate cell efficiency	-
	η_{cell}	· efficiency of the PV cell (theoretical)	-
	η_{PV}	· efficiency of the PV cell (practical)	-
	η_{col}	· optical efficiency of the collector	-
	η_{FSC}	· efficiency of the fluorescent solar collector	-
N_a		Avogadro number	mol^{-1}
P		Probability of emission inside the escape cone	-
	P_{eff}	· effective probability of emission inside the escape cone	-
$\boldsymbol{P}$		Probability of occupation	-
q		Electron charge	C
Q_a		Absorption efficiency	-
Q_c		Collection efficiency	-
	Q_c^1	· first-generation collection fluorescence	-
	$\chi(\lambda)$	· spectral photon collection probability	-
R		Re-absorption probability outside the escape cone	-
	$\bar{R}$	· re-absorption probability inside the escape cone	-
R		Resistance	Ω
	$R_{//}$	· shunt resistance	"
	R_s	· series resistance	"
$\mathfrak{R}$		Recombination rate	$cm^{-3}s^{-1}$
	$\mathfrak{R}_n$	· electron recombination rate	"
	$\mathfrak{R}_p$	· hole recombination rate	"
$\mathfrak{R}_0$		van Roosbroeck and Shockley recombination rate	$cm^{-3}s^{-1}$
$\mathbb{R}$		Reflection coefficient	-
	$\mathbb{R}_{cell}$	· solar cell reflection coefficient (air/solar cell)	-
	$\mathbb{R}_{front}$	· collector reflection coefficient (air/collector)	-
	$\mathbb{R}_{edge}$	· edge solar cell reflection (collector/solar cell)	-
SR		Spectral response	AW^{-1}
	SR_{dh}	· silicon photodiode spectral response	-
	SR_{hv}	· c-Si cell spectral response	-
σ_{SB}		Stephan-Boltzmann constant	$Wm^{-2}K^{-4}$
S_x		Electronic state x	-
	S_0	· Ground state	-
	S_1	· First excited electronic state	-
S_p		Hole surface recombination velocity	$cm\ s^{-1}$
S_n		Electron surface recombination velocity	-

T		Temperature	K
	T_s	· source temperature	"
	T_{sun}	· sun temperature	"
	T_{cell}	· cell temperature	"
	T^*	· effective temperature of fluorescence radiation	"
τ		Lifetime	ns
	τ_{tot}	· total lifetime	"
	τ_{rad}	· radiative lifetime	"
	τ_{nr}	· non-radiative lifetime	"
	τ_n	· electron lifetimes	"
	τ_p	· holes lifetimes	"
t		Time	s
	$t = 0$	· time at 0 second	"
V		Voltage	V
	V_{oc}	· open-circuit voltage	"
W		Junction thickness	μm
$[x]$		Densities of x	cm^{-3}
	$[n]$	· electron density	"
	$[p]$	· holes density	"
	$[N^*]$	· concentration of excited molecules	"
	$[N]$	· concentration of molecules in the ground state	"
	$[N_D^+]$	· density of ionized donors	"
	$[N_A^-]$	· density of ionized acceptors	"
$\tilde{x}$		Quantity x normalized	-
Ω_{sun}		Sun solid angle	sr
	C	· sun concentration	-
	f_w	· geometrical factor	-
Ω_{cone}		Escape cone solid angle	sr
Ω_s		Source solid angle	-
φ		Quantum yield	-
ρ		Space-charge density	$C\ cm^{-3}$
$Ø_{sun}$		Sun diameter	km

List of abbreviations

$III-V$	Semiconductors compound composed with at least one group III (IUPAC group 13) element and at least one group V element (IUPAC group 15).
AM	Air mass
As	Arsenic
ARC	Anti-reflection coating
a-Si	Amorphous silicon
B&E	Bose and Einstein
B-Z	Batchelder–Zewail
c-Si	Crystalline silicon
CL2	Calibrated irradiance source
C540-A	Coumarin 540A
DCM	Dichloromethane
DCM-dye	4-dicyanomethylene-2-methyl-6-p-dimethylaminostyryl-4 H-pyran
DMSO	Dimethyl sulfoxide
DH-Si	Silicon photodiode (Bentham)
F305	Lumogen Frot 305
FTIR	Fourier transform infrared spectroscopy
FWHM	Full width half maximum
FSC	Fluorescent solar collectors
Cd	Cadmium
Ga	Gallium
Ge	Germanium
IUPAC	International union of pure and applied chemistry
IV	Current–Voltage characteristics
In	Indium
K-S	Kennard-Stepanov
NREL	USA national energy laboratory
NPL	National physical laboratory
P-N	Junction formed by combining P-type and N-type semiconductors

PV	Photovoltaic
PVC	Polyvinyl chloride
PC1D®	Computer program written for IBM-compatible personal computers which solves the fully coupled nonlinear equations for the quasi-one-dimensional transport of electrons and holes in crystalline semiconductor devices.
PMMA	Poly(methyl methacrylate)
QNN	Quasi Neutral N region
QNP	Quasi Neutral P region
QD	Quantum dots
R6G	Rhodamine 6G
RB	Rhodamine B
SMA	Subminiature version A
S&B	Strickler and Berg
S&Q	Shockley and Queisser
Si	Silicon
TIR	Total internal reflection
TMc300	Bentham monochromator
Te	Tellurium
TCO	Transparent conducting oxide
TPF	Two-photon-fluxes model
U.S	United States of America
UV	Ultra violet
VIS	Visible
W&L	Weber and Lambe
A2048	Avantes AvaSpec spectrometer

Introduction

In recent times the world demand for energy has risen exponentially with time. Until the beginning of the 20^{th} century, the consumption of fossil fuel reserves (gas, coal, oil) was practically negligible [1]; since then, energy consumption has risen to $4.1 \times 10^{20}\ J$ per year, and this is projected to more than double by 2050 and to triple by the end of the 21^{st} century [2].

Fuel sources, which currently provide 80 % of the world's energy, are a finite resource [1] and, when burned, they produce carbon dioxide, the gas most commonly associated with the "greenhouse effect". In view of these facts, there is an urgent need to shift our energy supply from fossil fuels to renewable sources, which at this point appears to be the more sustainable long-term option.

Among renewable sources, solar energy is one of the most promising candidates. Sunlight is by far the largest of all carbon-neutral energy sources: more solar energy strikes the Earth in an hour ($4.3 \times 10^{20}\ J$) than is consumed on the entire planet in a year [2]. Sunlight can be directly transformed into electricity using photovoltaic (PV) solar cells. Covering 0.16 % of the Earth's land surface with 10 % efficient solar cells would provide nearly twice as much energy as the world now consumes in fossil energy [1], and yet in 2007 solar electricity provided less than 0.05 % of the world's energy [3].

Because of their high cost, the use of photovoltaic cells is not yet widespread. Solar energy will become truly mainstream only when its economic viability – its cost per unit of power – becomes comparable to that of other energy sources [2].

Terrestrial solar cells are generally fabricated using silicon – more precisely, crystalline silicon (c-Si). Silicon dominates other III – V semiconductors, such as gallium arsenide (GaAs), because: (i) silicon technology had already been extensively developed for the electronics industry before the advent of photovoltaics; and (ii) processing costs for c-Si wafers for photovoltaic applications are cheaper than for III – V semiconductors [4].

Despite the existing advantages of silicon technology, silicon solar cells are still expensive because of the high price of the base material – half of a solar module's cost is due simply to the extensive use of silicon, with more than 95 % of it being used for light absorption rather than for the production of electricity [5; 6].

For this reason, there is considerable interest in technologies which minimize the use of silicon, and in those where sunlight absorption takes place in a medium other than a thick layer of silicon. Among the various approaches to reducing the price of PV energy, thin films and concentrators are of particular interest.

Thin-film c-Si solar cells have the potential to reduce the cost of the active material to the point where the substrate is the limiting cost. Concentrators can increase the photon flux onto solar cells so that high performance can be achieved without covering large surfaces with c-Si cells.

This thesis presents an original type of device, the fluorescent solar collector (FSC), in which both concentrator and thin-film technologies can be applied together, resulting in a greatly reduced use of bulk semiconductor [7]. FSCs combine the high optical absorption of an organic dye with the energy conversion efficiency of a c-Si cell, as shown in Fig. 1.

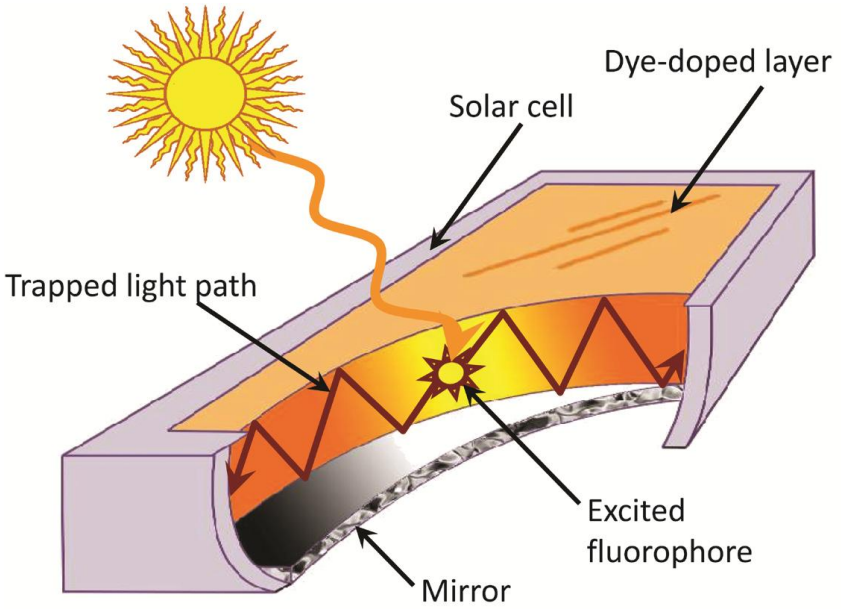

Fig. 102: Perspective view of a fluorescent solar collector. Sunlight is absorbed by a collector (orange fluorescent layer) of area A_{front} ; fluorescence, trapped by total internal reflection, is re-directed towards the edge of the collector where a solar cell of area A_{edge} is placed. The concentration factor or gain in such a device is given by the ratio $A_{front}\,/A_{edge}$.

In conventional FSCs, the collector (absorber) is generally composed of a mixture of fluorescent dyes embedded in a transparent medium such as PMMA, glass or even a liquid solution (Fig. 1). When exposed to sunlight, the dye absorbs the incoming light and re-emits photons at a longer wavelength within the fluorescent layer. Because most of the fluorescence is re-emitted at angles more oblique to the surface than the critical angle for total internal reflection, photon collection by the edge solar cell is in theory quite efficient.

Fluorescent solar collectors are active concentrators, whose operation rests on a light frequency shift mechanism. This is a great advantage in comparison to concentrators based on geometrical optics (mirrors or lenses), which are limited by their acceptance angle. Because they absorb both direct and diffuse light, fluorophores require no sun-tracking mechanism.

The solar cell at the rim of the collector can be a thin film. Indeed, there is no need for a thick layer of semiconductor material because light absorption has already taken place in the collector, over a wide range of frequencies. In addition, the choice of dyes allows the fluorescence frequency to be tuned to match the optimum absorption of the edge solar cell.

Theoretical limitations to FSC efficiency have been studied [8-9]. The results indicate that efficiencies of up to 27 % are achievable – a remarkable level when compared with the theoretical limits of bare c-Si cells (30 %) [10].

Clearly FSCs have enormous potential to be the next generation of affordable solar cells. The practical efficiencies achieved so far, however, do not exceed a few percent. The reasons for this are a lack of suitable dyes which absorb across the solar spectrum, and losses due to photon transport in the fluorescent layer.

New collector designs (e.g. thin-film collectors [11], photonic band-stop collectors [12] and quantum dot doped collectors [13]), aimed at enhancing FSC efficiencies, have been suggested recently in the literature. This thesis reviews these designs and explores the feasibility of the FSC concept for solar energy conversion.

Thesis aims and objectives

This thesis presents theoretical and experimental work exploring the viability of fluorescent collectors to reduce the cost of c-Si solar cells. To accomplish this aim the research has pursued the following objectives:

- fabrication and characterization of an experimental batch of high-efficiency $n^+/p/p^+$ c-Si solar cells (this effort, in the Microelectronic Fabrication Unit at Southampton University, was in its final stage when a major fire destroyed the facilities).
- development of a simple semi-analytical detailed-balance model for multiple-junction solar cells which is sufficiently accurate for practical applications.
- fabrication and characterization of liquid fluorescent solar collectors, based on one or several dyes.

- characterization and modelling of photon transport losses within the collector plate, using :
  - numerical simulation, based on ray-tracing techniques, which indicate that collector efficiency is practically independent of shape and that thin-film collectors do not perform any better than standard flat-plate devices.
  - fundamental characterization of the fluorescent light chemical potential, which shows that the FSC operates close to its thermodynamic limitations.
  - analysis of the photon transport losses using an analytical "two-photon-fluxes" model.

Thesis outline

This thesis is articulated around two main research streams. The first stream, constituting Chapters 2 and 3, deals with classical P-N junction solar cells, with a focus on crystalline silicon (c-Si) solar cells. The second stream, in Chapters 4 through 8, presents studies and experiments focused on fluorescent solar collectors.

The detailed structure of this thesis is as follows:

Chapter 1, Photons – presents the characteristics and main physical laws applicable to the two photon sources of interest for fluorescent solar collectors: incandescent sources (e.g. the Sun) and cold sources (e.g. fluorophores).

Chapter 2, Ideal P-N junction solar cells – describes the operation of an ideal P-N junction solar cell, i.e. one subject only to unavoidable losses such as electron thermalization, radiative recombination, and absorption losses due to the semiconductor band gap. Accounting for these losses leads to the detailed-balance efficiency model of Shockley and Queisser, reviewed in this chapter. A simple "semi-analytical" version of this model is also derived, and is shown to be a versatile tool, applicable to tandem cells and to an infinite stack of junctions.

Chapter 3, Solar cell modelling and design – deals with cells in practice. Common solar cells show weaknesses in carrier collection, associated with material defects, dead layers or bad passivation of the cell surface. Such "practical" losses are discussed in this chapter and accounted for in the design of a highly efficient solar cell (2^{nd} cell batch 2005, S. Boden, D. Bagnal, T.J.J. Meyer). This batch of cells was in the final stage of fabrication at the INNOS clean room when a fire destroyed the facilities. Replacements for these lost cells were purchased commercially (from Solartec) rather than being developed at the university.

Chapter 4, Fluorescent solar collectors – presents an up-to-date literature review on the subject of FSCs, including their history, operational principles, losses, performance and improved designs. Attention is given to inhomogeneous structures, also known as "waveguide designs" (e.g. thin-film and liquid collectors), since such designs have been suggested to improve the collector's photon transport capabilities.

Chapter 5, Techniques and models for analysis of FSC performance – reviews the models used for quantitative analysis of FSC performance, and introduces the "two-photon-fluxes" model. This model, based on a detailed-balance argument, allows a deeper insight into FSC operation and shows that re-absorption dramatically limits FSC operation. Using ray-tracing simulations carried out with TracePro®, the re-absorption probabilities of collectors of various shapes (e.g. triangle, half disk) as well as of inhomogeneous structures (e.g. liquid collectors) are modelled.

Chapter 6, Experimental procedures – describes the methodology for measurements on inhomogeneous structures (e.g. liquid collectors). The liquid collector structure, properties of the materials used in its fabrication, and equipment for measuring photon fluxes escaping the collector are reviewed.

Chapter 7, FSC performance characterization – presents the experimental records and data analysis. The validity of the two-photon-fluxes model is confirmed by comparing the efficiency of an actual FSC with the value predicted by the model. Re-absorption profiles for thin-film and liquid collectors are compared to ray-tracing simulations; no improvement is found over the corresponding homogeneous collectors. A map, based on the experimental results, of losses occurring during photon transport suggests that conventional FSCs based on total internal reflection are unlikely to reach high efficiencies because of re-absorption phenomenon and a lack of suitable fluorescent dyes.

Chapter 8, Photon chemical potential – deals with energy aspects of the fluoresced photons. The photon chemical potential, i.e. the photon's free energy, is experimentally quantified. The key argument in this characterization is the assumption of thermal equilibrium for the emitted photons upon multiple re-absorption and re-emission events. It is demonstrated that fluorescent collectors operate like blackbody convertors in a restricted frequency range, transforming a hot incident photon flux at a temperature with zero chemical potential into a cold fluorescent flux with a chemical potential close to the thermodynamic limit.

Chapter 1

Photons

Photons are the key elements in solar energy conversion, the medium by which the sun transfers its energy to Earth and to photovoltaics. Travelling at a speed of $c \approx 3 \times 10^8\, m\, s^{-1}$ in a vacuum, each photon carries an energy proportional to its frequency. The photon energy range of interest in the present research lies between $1.12\, eV$ $(1107\, nm)$ and $\approx 4\, eV$ $(309\, nm)$, corresponding respectively to the minimum energy required to excite silicon (Si) – the photovoltaic material – and the uppermost energy carried by photons on Earth (Fig. 104). Photons are bosons, particles that only interact with matter; at thermal equilibrium their distribution is described by Bose-Einstein (*B&E*) statistics [14].

The first and second sections of this chapter introduce two photon sources of interest for fluorescent solar collectors – incandescent sources (e.g. the sun) and cold sources (e.g. fluorophores) – and the physical laws applicable to them. The third section discusses photon interactions with matter, the absorption properties of crystalline silicon (c-Si), and laser dyes.

1.1 Incandescent sources

Incandescent sources (e.g. the sun or a tungsten lamp) are spectrally broad and are characterized by their temperature. The radiative energy output from the sun comes from nuclear fusion: the sun emits $\approx 4 \times 10^{20}$ W. As a result of atmospheric effects, the amount of radiation reaching the Earth's surface is variable. The properties of radiation at the surface depend on the so-called air mass, defined as atmospheric path length relative to the minimum path length (i.e. when the sun is at the zenith) [5;15].

1.1.1 Air mass spectra

The intensity of solar radiation just outside the atmosphere defines the solar constant, $1367\, W\, m^{-2}$. The solar spectrum at this point is referred to as the "air mass zero" spectrum or $AM\ 0$ (Fig. 103). The solar spectrum at the Earth's surface when the sun is at the zenith is called the "air mass one" spectrum or $AM\ 1$.

The further the sun is from the zenith, the longer the path length of solar radiation through the atmosphere to the Earth's surface (Fig. 103). $AM\ 1.5$ designates the solar spectral distribution corresponding to an air mass of 1.5. The air mass at an angle θ from the zenith is proportional to $1/\cos(\theta)$, so $AM\ 1.5$ corresponds to an angle of 48.2° [16] between the zenith and the incident light beam (Fig. 103).

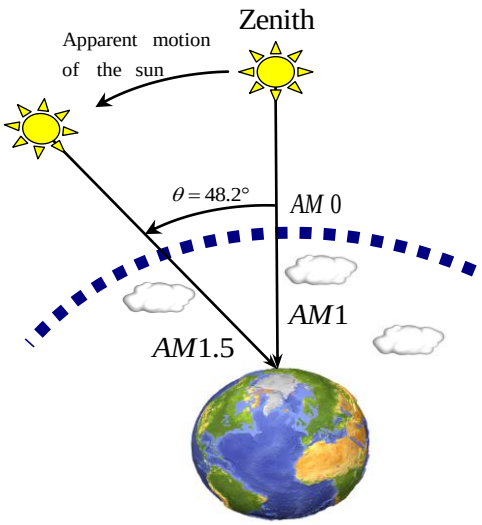

Fig. 103: Reference air mass conditions. Air mass is proportional to $1/\cos(\theta)$, where θ is the angle between the zenith and the incident light beam. (Graph adapted from [17])

Since photovoltaic systems are spectrally selective, air mass spectra are a useful reference for assessing solar converter performance and charting performance improvements. The photovoltaic industry, in association with research laboratories, predominantly uses the AM 1.5 as reference standard. This distribution of power as a function of wavelength (e.g. in $W\ m^{-2}\ nm^{-1}$) provides a common reference for the evaluation of spectrally selective photovoltaic materials with various natural and artificial light sources. The conditions defining this spectrum are considered to be a reasonable average for the 48 contiguous states of the U.S.A over a period of one year. The AM 1.5 spectrum is defined for a cloudless sky ($25\ km$ visibility) with a $1.42\ cm$ water vapour rural aerosol model; the data are available in the document, ASTM G-173-03.

AM 1.5 spectrum serve as reference for comparing efficiencies, but is not necessarily adequate for all solar converter designs. For active concentrators such as fluorescent solar collectors, capable of capturing diffuse light, corrections may be needed if they are used in regions (such as England) with cloudier skies [16]. Consequently, the norm ASTM G-173-03 defines two AM 1.5 spectra: global AM 1.5 which includes direct and diffuse light and the direct normal AM 1.5 which only considers direct light.

The integration of the global AM 1.5 spectrum over all wavelengths gives an irradiance of about $967\ W\ m^{-2}$, which has been normalized to $1000\ W\ m^{-2}$ because of system design considerations (ISO 9845-2: 1992 and ASTM E892-87: 1992).

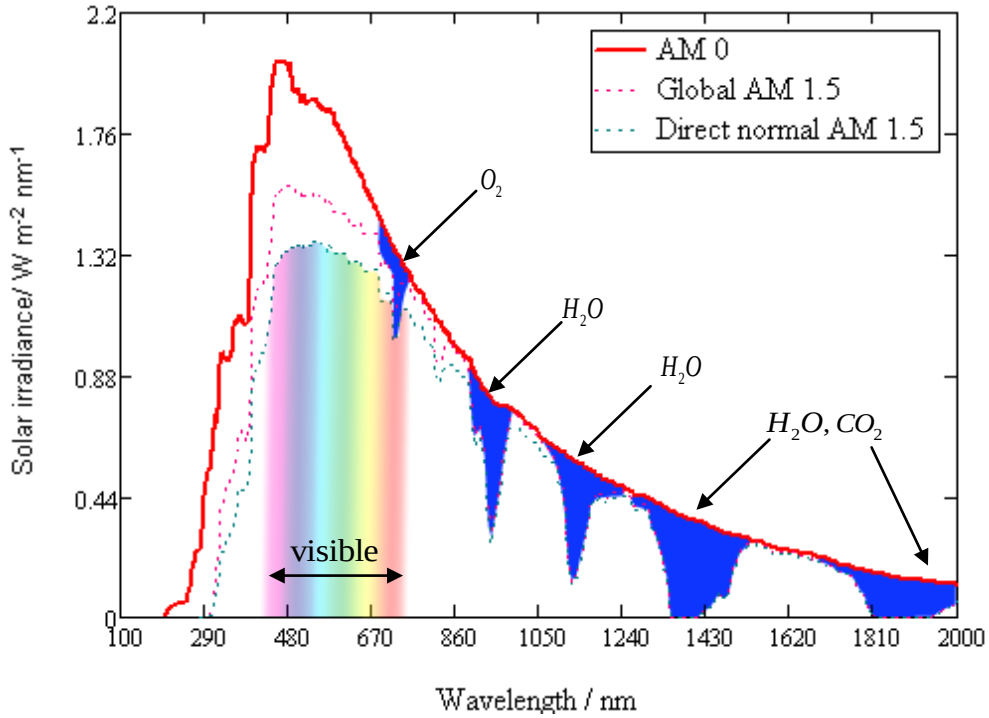

Fig. 104: Comparison of *AM* 0 spectrum with global *AM* 1.5 and direct normal *AM* 1.5 spectra. Differences are due to the inclusion of diffuse light in global *AM* 1.5. The regions in blue are the absorption bands of the main chemical compounds present in the atmosphere. The solar constant outside the atmosphere is $1367\ W\ m^{-2}$ while at the Earth's surface the global solar constant is about $1000\ W\ m^{-2}$ and the direct solar constant is $770\ W\ m^{-2}$ [18]. (Data taken from the ASTM G-173-03 norm)

1.1.2 Blackbody

A "blackbody" is a hypothetical body which completely absorbs any radiation falling on it and re-emits all the absorbed radiation. The usual description of a blackbody is a pinhole in an empty container maintained at constant temperature: any radiation leaking out of the hole has been absorbed and re-emitted so many times inside that it has reached thermal equilibrium with the walls.

The sun behaves much like a blackbody: photons emitted in the core of the sun have suffered many absorption/re-emission events, gradually bringing them into thermal equilibrium before their emission into space.

1.1.2.1 Photon statistics

Photons are bosons. Their distribution function $P_{stat}\,(\nu, T_s, \mu)$, describing the probability of occupation of the state with energy $h\nu$, is given by:

$$P_{stat}\,(\nu, T_s, \mu) = \frac{1}{\exp\left(\frac{h\nu-\mu}{kT_s}\right)-1}, \tag{1}$$

where h is Planck's constant, ν is the frequency, k the Boltzmann constant, T_s the temperature of the source and μ the photon chemical potential.

For solar radiation the photon chemical potential is zero, the main argument being the non-conservation of photons [19]. With quantized radiation processes such as fluorescence, the number of photons is conserved, and it will be shown that for fluorescence the photon chemical potential is positive [20] and experimentally quantifiable [9] (Chapter 8).

Under an irradiation of one sun, which corresponds to AM 1.5, stimulated emission can be neglected. This simplification, referred to as the "classical limit", leads to the suppression of the -1 term in the denominator of Eqn. (1). The difference between the two distributions is shown in Fig. 105.

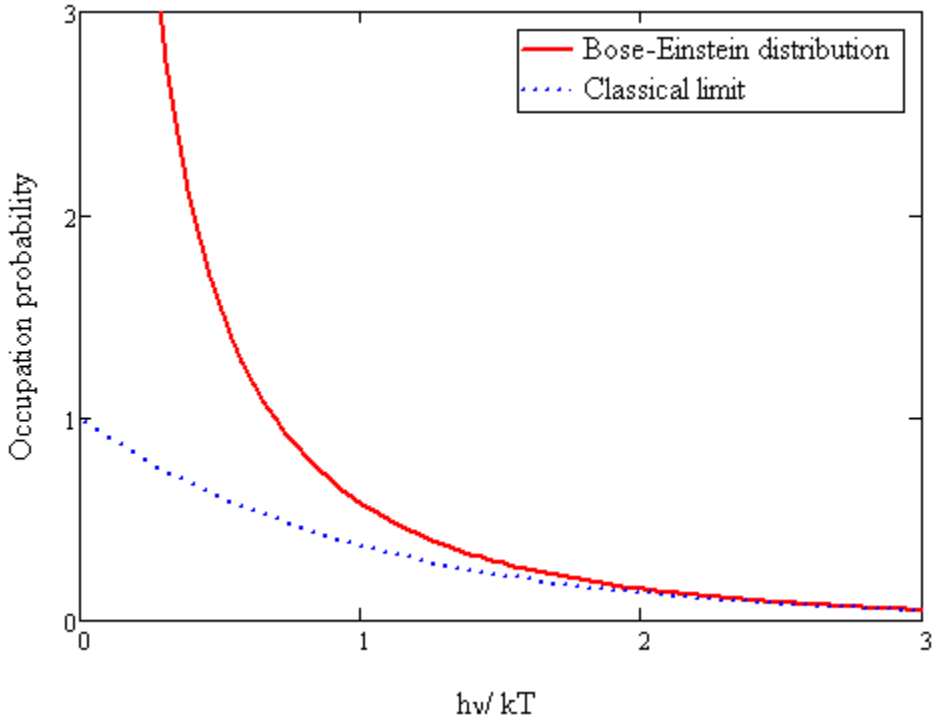

Fig. 105: Bose-Einstein distribution (red line) given by Eqn. (1) with a chemical potential equal to zero, compared with the simplified classical distribution $\exp(-h\nu/kT)$ (dotted blue line) [1].

Fig. 105 shows that neglecting stimulated emission is a fine approximation for $h\nu > 2kT$. For a source at $T_s = 6000\,K$ this corresponds to energies above $1.03\,eV$ ($1127\,nm$). In the present research, stimulated emission is often neglected.

1.1.2.2 Planck's law

Planck's law of blackbody radiation, giving the spectral energy density of a blackbody (in units of energy per unit frequency per unit volume, e.g. $J\,m^{-3}\,Hz^{-1}$), can be written as the product of the occupation probability (Eqn. (1)) and the density of state:

$$\mathbf{Pl}(\nu, T_s) = \frac{8\pi h\nu^3}{c^3}\frac{1}{\exp\left(\frac{h\nu}{kT_s}\right)-1}. \quad (2)$$

Considering the small solid angle of the sun as seen on Earth, and neglecting stimulated emission, the energy intensity per unit area per second unit per unit frequency striking Earth can be described to a good approximation by:

$$f_{sun}(\nu, T_{sun}, \Omega_{sun}) \cong \frac{2h\nu^3}{c^2}\exp\left(\frac{-h\nu}{kT_{sun}}\right)\Omega_{sun}. \quad (3)$$

It is often more convenient to deal with a flux of photons per unit bandwidth. Dividing Eqn. (3) by the energy per photon gives photon flux, while $h\nu = hc/\lambda$ can be used to express this in terms of wavelength. Because wavelength is not proportional to frequency, the frequency dependence of f_{sun} may be converted to a wavelength dependence using $(f_{sun}(\lambda) = f_{sun}(\nu)d\nu/d\lambda = \mathrm{c}/\lambda^2 f_{sun}(\nu))$. The photon flux striking Earth per second per unit area per unit wavelength is then given by:

$$\dot{f}_{sun}(\lambda, T_{sun}, \Omega_{sun}) \cong \frac{2hc^2}{\lambda^5}\exp\left(\frac{-hc}{\lambda k T_{sun}}\right)\Omega_{sun}. \quad (4)$$

In this thesis, energy is expressed in eV rather than joules, and wavelength by nm. A dot on top of the variable, $\dot{f}$, always indicates a photon flux.

1.1.2.3 Solar solid angle

The sun, as viewed from the Earth, fills a solid angle:

$$\Omega_{sun} = \pi \mathrm{f_w} = \pi\frac{(\emptyset_{\mathrm{sun}})^2}{(\mathrm{D_{Earth\ -sun}})^2} = \pi\left(\frac{6.95\times10^{11}}{150\times10^{12}}\right)^2 = 6.85\times10^{-5}\ sr, \quad (5)$$

where $\mathrm{D_{Earth\ -sun}}$ is the sun-Earth distance and $\emptyset_{\mathrm{sun}}$ the diameter of the sun. The constant $\mathrm{f_w}$, called the geometrical factor, is often used with the Stefan-Boltzmann law, $\mathrm{f_w}\sigma_{SB}{T_{sun}}^4 = 1367\ Wm^{-2}$ (where σ_{SB} is the Stephan-Boltzmann constant), to describe solar radiation incident on the Earth (see Eqn. (35)). As viewed from the Earth, the sun subtends a solid angle of $6.85\times10^{-5}\ sr$, which defines a concentration factor of one sun. Concentrating systems, such as those using parabolic mirrors, can theoretically concentrate the sun up to a full hemisphere, i.e. ≈ 45 000 suns.

A blackbody radiation spectrum using the sun's surface temperature $T_{sun} = 5900\ K$ is compared to the AM 0 spectrum in Fig. 106.

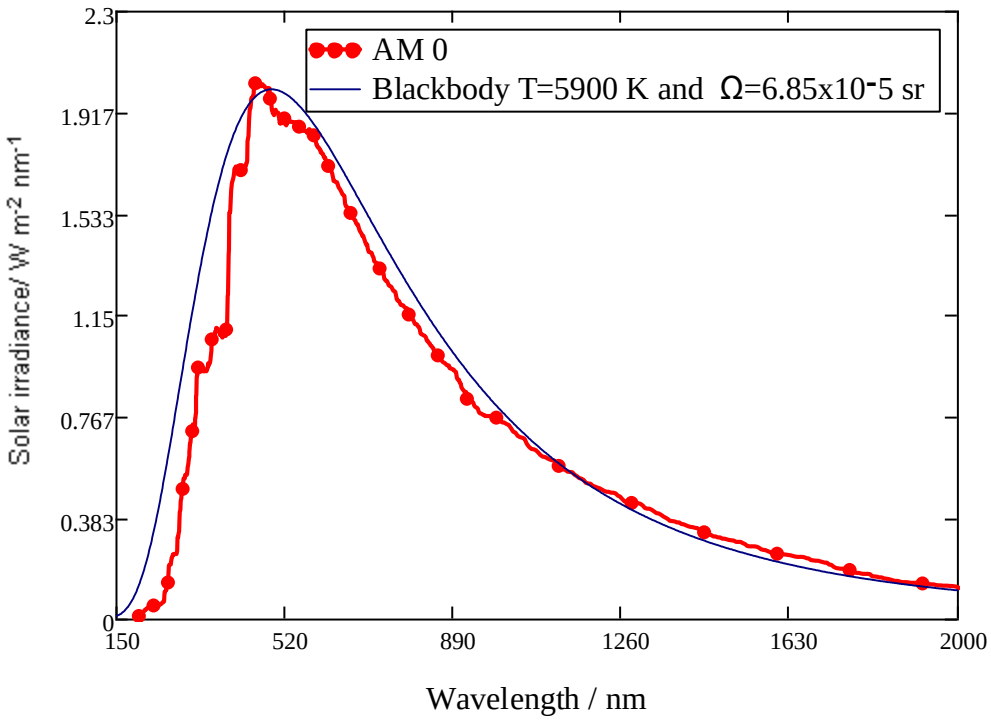

Fig. 106: Blackbody radiation compared to the $AM\ 0$ spectra. The temperature of the blackbody is $5900\ K$ with a solar solid angle of $6.85 \times 10^{-5}\ sr$. In the present research the solar spectrum is usually approximated by a blackbody radiator at $6000\ K$.

1.2 Cold sources

Fluorescence – first observed in tonic water containing quinine by Sir John Frederick William Herschel in 1845 – is today a well known phenomenon used by scientists in biology, medicine, geography, solar energy studies and other disciplines. Named after the mineral fluorite (composed of calcium fluoride), fluorescence is red-shifted radiative emission triggered by the molecular absorption of photons. It differs from incandescence (emission of light due to high temperatures), and is commonly referred to as "cold light" because most fluorescing substances produce very little heat. Two types of fluorophore are currently available: organic dyes (e.g. laser dyes) and inorganic dyes (e.g. rare-earth dyes, quantum dots). A survey of the optical properties of dyes is given in Chapter 4; here the focus is on the physics of the fluorescence phenomenon.

1.2.1 Fluorescence

Fluorescence occurs when an electron in an atom or molecule returns from an excited state to its ground state, giving up its energy in the form of a photon.

The Jablonski [21] diagram in Fig. 107 illustrates various molecular processes that can occur in the molecular excited states of a fluorophore.

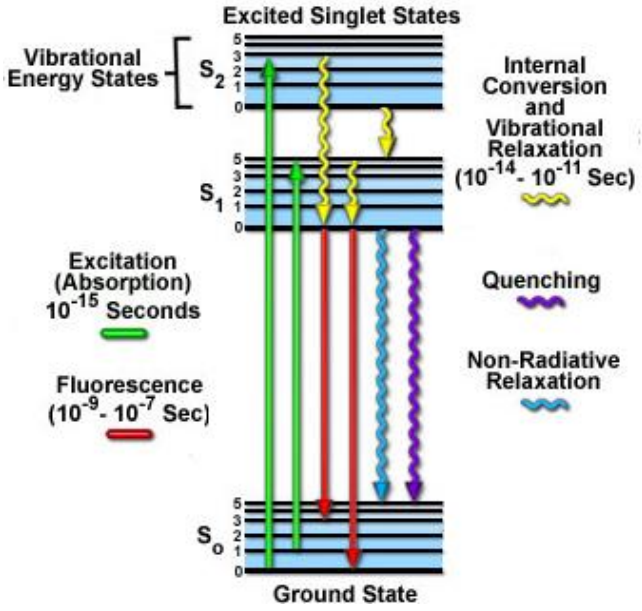

Fig. 107: Simplified Jablonski diagram showing excitation into a higher-energy state S_1 or S_2 by absorption of a photon (green), internal conversion between excited states (yellow) and fluorescence emission (red). Quenching and non-radiative relaxation can also occur, reducing the probability of photon emission (quantum yield). Energy transfer, phosphorescence and solvent interactions are not shown here. (Graph adapted from [21] and [22])

Fluorescence emission is a complex process. The molecule first absorbs the energy of the incident light. This energy is transferred to an electron which is excited from a vibrational level in the electronic ground state to one of many vibrational levels in an electronic excited state. In organic compounds, the first excited state is usually the first singlet state, where all the electrons in the molecule are spin-paired. Following excitation, the excited electron quickly falls into the lowest vibrational level of the excited singlet state S_1 by losing energy to other molecules through collision. This process, occurring within $10^{-12}s$ or less, is called internal conversion and is responsible for the red shift of the fluorescence spectrum, the so-called Stokes shift [22]. Internal conversion generally takes place prior to emission since fluorescence lifetimes are typically around $10^{-8}s$. Thus fluorescence generally occurs from a thermally equilibrated excited state S_1 [23-24].

De-excitation typically occurs to the ground state S_0. Because photon absorption does not alter the molecular geometry [25], the differences between vibrational energy levels in the excited state tend to be similar to those in the ground state [26]. The fluorescence spectrum, therefore, is generally the mirror image of the absorbance spectrum, as shown in Fig. 108. Electrons may be absorbed into higher states, as shown in Fig. 107, leading to asymmetry between absorbance and fluorescence spectra in some cases, but transitions from S_2 to S_0 are rare. Most emission occurs from S_1, so fluorescence is generally a mirror image of the $S_0 \rightarrow S_1$ transition.

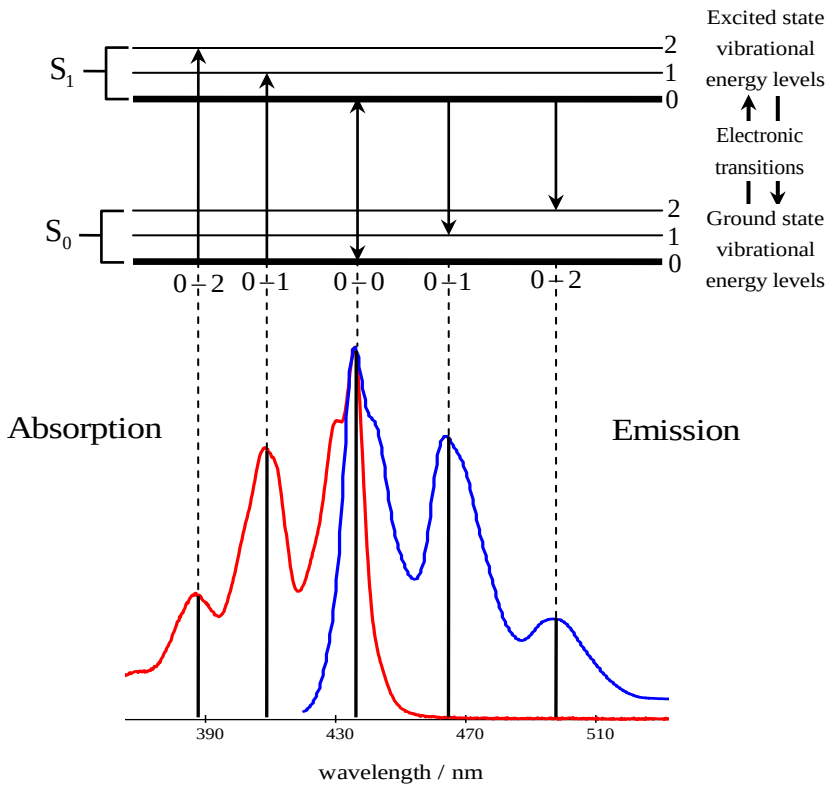

Fig. 108: Illustration of the mirror-image rule, showing the spectrum of perylene in benzene. The absorption band is shown in red and fluorescence in blue. (Graph adapted from [27], absorption and emission spectrum measured at 315 *K* using an A2048 spectrometer)

Each electronic state consists of an almost continuous manifold of vibrational levels, so the absorbance and fluorescence spectra of dyes show bands rather than discrete electronic transitions. This effect is often accentuated as a result of interactions between the energy levels of the dye and those of the solvent. In most cases absorbance and fluorescence spectra can be fit using Gaussian curves [28].

Fluorescence spectra are generally independent of the excitation source, provided the source has enough energy to excite the fluorophore. This is known as Kasha's rule [22], and it implies that the quantum yield is also independent of excitation wavelength. Although the quantum yield of fluorescence is independent of the source, fluorescence can be quenched by several processes, e.g. energy transfer and solvent interactions.

In addition to fluorescence and non-radiative relaxation processes, phosphorescence can also take place. An excited electron may change its spin during excitation and end up in an overlapping excited triplet state. It then loses energy by vibrational relaxation and ends up in the lowest excited triplet state. The electron returns to a stable electronic ground state by emitting a photon (phosphorescence). This differs from fluorescence on two counts: first, photons of phosphorescence have lower energy than those of fluorescence; second, the lifetime of the excited triplet state can be up to 10 seconds, compared with an

average lifetime of $10^{-9}\ s$ to $10^{-5}\ s$ for an excited singlet state. Phosphorescence is a long-lived process because the transition of electrons of the same spin is forbidden; hence relaxation to the ground state occurs slowly and emission from triplet/singlet transitions may continue after initial irradiation. On the other hand, triplet/singlet transitions (phosphorescence) are much less probable than singlet/singlet transitions, which explains why it is so much easier to observe fluorescence, and why phosphorescence is not prominent in fluorescent collectors.

1.2.1.1 Stokes shift

"Stokes shift" refers to the red shift that occurs during a fluorescence reaction. It is generally measured between the peaks of the absorbance and fluorescence bands, and may be expressed in terms of either wavelength or frequency. Internal conversion is the phenomenon behind the Stokes shift, the energy difference being dissipated as heat in the surrounding medium.

Organic dyes can re-absorb their own fluorescence. The extent to which they do so is related to the sample geometry and to the Stokes shift describing the overlap between fluorescence and absorption spectra.

The re-absorption phenomenon is central to this thesis, bringing photons into thermal equilibrium and linking fluorescence with thermodynamics. It was first investigated by Kennard [23;29]. Later this link was rediscovered and independently simplified by Stepanov [30-31]. Today the thermodynamic relationship between absorption and fluorescence spectra is known as the Kennard-Stepanov (*K*-*S*) theory. This theory is reviewed in Section 1.3.3 of this chapter and will be used to characterize the effective temperature of fluorescence radiation.

1.2.1.2 Quantum yield (φ)

Fluorescence quantum yield φ is the ratio of the number of photons emitted to the number of photons absorbed. Despite this simple definition, quantifying the number of photons re-emitted is challenging in practice. Quantum yield can be measured experimentally by the method of Williams [32]. The fluorescence spectra of a standard dye of known quantum yield and of the unknown dye are recorded at a particular absorbance and integrated over frequency or wavelength to give the values OD_a and OD_b, respectively. This is repeated for a range of absorbance values, and a plot of the ratio OD_a/OD_b as a function of absorbance gives a straight line with a slope related to the dye's quantum yield.

This method is limited by the requirement for accurate calibration of the detection system. The reported accuracy of such quantum yield measurements [33] is typically 10 % even when integrating spheres are

used in the experiments [34]. To bypass this difficulty, quantum yield may be expressed in terms of the lifetime of the dye:

$$\varphi = \frac{k_{rad}}{k_{nr} + k_{rad}} = k_{rad}\,\tau_{tot}\,, \tag{6}$$

where k_{rad} is the emissive radiative rate and k_{nr} the non-emissive de-excitation rate (in s^{-1}). These rates are linked to the total lifetime τ_{tot} of the dye by:

$$k_{tot} = (k_{rad} + k_{nr}),\ \text{and}\ {\tau_{tot}}^{-1} = 1/\tau_{rad} + 1/\tau_{nr}\ . \tag{7}$$

1.2.1.3 Lifetime

The lifetime τ_{tot} of a fluorophore can be characterized by the decay of fluorescence intensity following a short pulse. Indeed, the fluorescence intensity f_{fluo} at any time t after excitation by a Dirac function of light at $t = 0$ is proportional to the instantaneous concentration $[N^*]$ of excited molecules in the solution. In classical kinetics, the rate of disappearance of excited molecules can be expressed by the following differential equation:

$$\frac{-d[N^*]}{dt} = (k_{rad} + k_{nr})[N^*]. \tag{8}$$

The solution of this equation is well known, leading to:

$$[N^*] = [N^*]_{t=0}\,\exp\left(\frac{-t}{k_{rad} + k_{nr}}\right) = [N^*]_{t=0}\,\exp\left(-\frac{t}{\tau_{tot}}\right), \tag{9}$$

where $[N^*]_{t=0}$ is the concentration of excited molecules at $t = 0$.

Fluorescence decay is usually a mono-exponential function. Most common fluorophores (e.g. xanthenes and Lumogen® dyes) employed in the fabrication of FSCs have fluorescence lifetimes on the order of nanoseconds (Chapter 8).

The radiative lifetime of a compound can be calculated theoretically from absorption and fluorescence spectra using the Strickler-Berg (*S&B*) relation [35]. The *S&B* relation uses the generalization of Einstein's A and B coefficients [36] for broad molecular bands [23]. Einstein showed that for sharp atomic lines the radiative lifetime was inversely proportional to the corresponding emission probability $B_{1\to0}$ and to the third power of the transition frequency $\nu_{1\to0}$.

$$\frac{1}{\tau_{rad}} = 8\pi h \nu_{1\to0}^3 c^{-3} B_{1\to0}\ . \tag{10}$$

Using the normalized fluorescence spectrum to describe the photon distribution, Strickler and Berg related the coefficient $B_{1\to0}$ to the absorption intensity of fluorescent molecules in liquid solutions emitting in broad molecular bands rather than sharp lines:

$$\frac{1}{\tau_{rad}} = \frac{8\pi n^2 \times 2303}{c^2 N_a} \frac{\int \tilde{f}_1(\nu) d\nu}{\int \tilde{f}_1(\nu) \nu^{-3} d\nu} \int \frac{\xi(\nu)}{\nu} d(\nu), \tag{11}$$

where N_a is the Avogadro number, n is the refractive index of the solution, $\xi(\nu)$ is the molar (decadic) absorption coefficient (commonly expressed in $L\,mol^{-1}cm^{-1}$), and $\tilde{f}_1(\nu)$ is the normalized intensity spectrum of fluorescence. For clarity throughout this thesis, any function topped with a tilde (~) indicates that it is normalized. The normalization rule for $\tilde{f}_1(\nu)$ is:

$$\int \tilde{f}_1(\nu)\, d\nu = \varphi. \tag{12}$$

The *S&B* values for the radiative lifetimes of dyes are often in good agreement with experimental data (Chapter 8). In the case of strong interaction with the solvent, however, where change occurs in the excited-state geometry, the relation of Strickler and Berg fails to agree with experiments.

1.2.1.4 Quenchers

"Quencher" is a generic term for any process that reduces fluorescence intensity. Collisional quenching occurs when excited dye molecules are deactivated upon contact with other molecules in the solution (the molecules are not otherwise altered in this process). Fluorophores can also form non-fluorescent complexes, a process referred to as static quenching since it does not rely on the movement of particles.

Fluorescence can also be quenched by the fluorophore itself: if it is in too high a concentration the molecules can aggregate, creating dimmers and non-fluorescent particles. Temperature can dramatically alter the quantum yields of some dyes: with Rhodamine B, for example, a decrease in fluorescence of 20 % to 70 % was observed when the solvent/dye solution was warmed above room temperature [37]. Temperature does not affect all dyes; Rhodamine 101, for example, shows no significant loss of fluorescence when warmed, and as a result is often used as a standard in the Williams method. Quenching depends on numerous parameters (e.g. the solvent, the presence of oxygen) and is not yet fully understood [27].

1.3 Photon interactions with matter

Photons only interact with matter, and the degree to which they are absorbed by a material depends on its properties. For a semiconductor material like silicon (Si) photon absorption is determined by the threshold photon energy $h\nu_{gap}$, which depends on the energy gap of the semiconductor. If a photon has enough

energy to excite the illuminated material (dye or semiconductor) the probability of absorption is given by the Beer-Lambert law.

The absorbance (Abs) increases with increasing attenuation of the incident beam intensity I_0 crossing the sample. Absorbance is directly proportional to the path length l of the light within the material, and to the concentration C of the absorbing species:

$$Abs(\lambda) = \log\left(\frac{I_0(\lambda)}{I(\lambda)}\right) = \xi(\lambda) l C \ . \tag{13}$$

Equation (13) is expressed as a wavelength dependency because most spectrometers are wavelength dependent rather than frequency dependent. In the present research, absorbance or optical density is always expressed as the decimal log of $I_0(\lambda)/I(\lambda)$; this parameter is related to the Naperian absorption coefficient $\alpha(\lambda)$ by :

$$\alpha(\lambda) = \frac{Abs\,(\lambda)}{l}\ln(10)\ , \tag{14}$$

where α has units of reciprocal length (e.g. cm^{-1}). The absorption cross-section $\sigma(\lambda)$of the absorbing material is related to the molar decadic extinction coefficient by:

$$\sigma(\lambda) = \frac{\alpha(\lambda)}{[N]} = \frac{1000}{N_a}\ln(10)\xi(\lambda)\ , \tag{15}$$

where $[N]$ is the number of molecules per unit volume. The right hand side of Eqn. (15) gives cross-sections in cm^2 with $\xi(\lambda)$ in $L\ mol^{-1}\ cm^{-1}$.

1.3.1 Photon absorption in semiconductors

Crystalline silicon, a semiconductor of choice (Chapter 2) for the fabrication of solar cells, is an indirect band gap material. Photon absorption is a two-step process: absorption of an energetic photon and phonon emission. This lowers the absorption coefficient of silicon when compared to direct band gap semiconductors (Fig. 109).

The complicated band structure of silicon is illustrated in Fig. 109: photons of energy $1.1 - 3.2\ eV$ are absorbed within the lowest indirect band gaps, and only those of energy $> 3.2\ eV$ within the direct band gap. Direct band gap materials do not show this behaviour, which is why a GaAs semiconductor, for example, is a much better absorber than silicon.

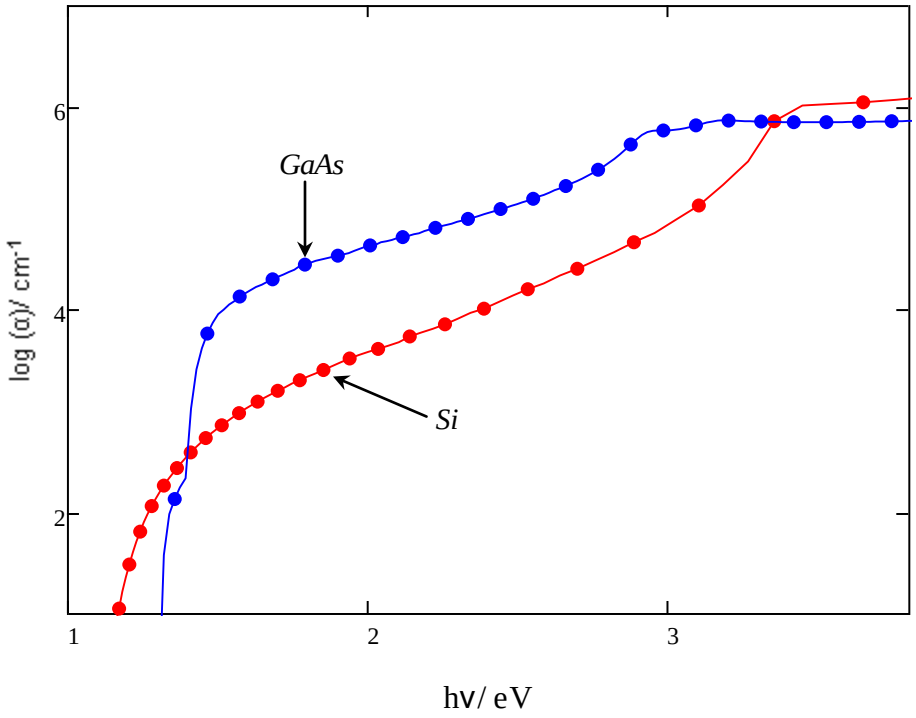

Fig. 109: Absorption coefficient of silicon (red line) showing the effect of indirect band gaps, compared with the absorption coefficient of a GaAs direct band gap semiconductor (blue line). (Experimental data taken from [38])

1.3.2 Photon absorption in fluorescent dyes

Absorption coefficients for the organic laser dyes used in the present research are remarkably high. It is not uncommon to find compounds with extinction coefficients $\xi(\lambda) > 100\,000\, L\, mol^{-1}\, cm^{-1}$ (e.g. Rhodamine B, Rhodamine 6G, Frot 305). This makes laser dyes ideal candidates for fluorescent collectors in which sunlight is absorbed by the dye rather than the solar cell (Chapter 4).

1.3.3 Photon re-absorption

Re-absorption, also known as photon recycling [39], refers to a mechanism in which the absorbing material emits a photon and then re-absorbs it. Re-absorption occurs in semiconductors and in most fluorescent materials (Section 1.2.1.1). Several theories which assume that re-absorption allows photons to enter into thermodynamic equilibrium with matter – Kennard-Stepanov [24] for fluorescent dyes and van Roosbroeck-Shockley [39] for semiconductors – have been developed to characterize various properties of the absorber material.

1.3.3.1 Radiative recombination (van Roosbroeck and Shockley)

The van Roosbroeck and Shockley [40] model quantifies the spontaneous radiative recombination rate in semiconductors.

A photon generated by an electron-hole recombination (Chapters 2-3) can subsequently be absorbed (Fig. 9). For a semiconductor with absorption coefficient $\alpha(\nu)$, the inverse photon lifetime (or photon absorption probability per unit time) can be written:

$$\frac{1}{\tau} = \alpha(\nu)\, c\ \ \frac{d\nu}{d(n\nu)}, \tag{16}$$

where the refractive index n takes account of the photon's speed in the semiconductor.

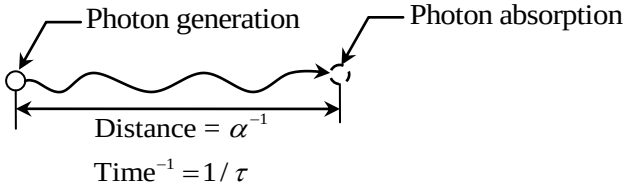

Fig. 110: Distance and elapsed time between photon generation and absorption events.

The absorption rate per unit volume in the frequency interval $\nu \to \nu + d\nu$ is given by the photon density divided by the mean photon lifetime. Since the photons are in thermal equilibrium with the semiconductor, the photon density in [39] is given by Planck's law:

$$\mathfrak{R}_0(\nu) = \frac{\mathbf{Pl}(\nu)}{\tau(\nu)} \approx \frac{8\pi\nu^2 n^2}{c^3} \frac{1}{\exp\left(\frac{h\nu}{kT}\right)-1}\, c\, \alpha(\nu). \tag{17}$$

Integration over all frequencies yields the famous van Roosbroeck and Shockley relation:

$$\mathfrak{R}_0 = \int_0^\infty \mathfrak{R}_0(\nu) d\nu \approx \int_0^\infty \frac{8\pi\nu^2 n^2}{c^2} \frac{1}{\exp\left(\frac{h\nu}{kT}\right)-1}\ \ \alpha(\nu)\, d\nu. \tag{18}$$

Values of $\mathfrak{R}_0$ for various semiconductors are presented in Section 2.1.2.

1.3.3.2 Effective temperature of fluorescent radiation (Kennard-Stepanov)

Photon re-absorption is not unique to semiconductors. Dyes with small Stokes shifts, for example, have overlapping absorbance and fluorescence bands (Fig. 108). This leads to an artificial red-shifting of fluorescence [22] and, as already mentioned, gradually brings photons into thermodynamic equilibrium.

The Kennard-Stepanov relation, which is essentially similar to the van Roosbroeck and Shockley relation, is written in its most common form as:

$$\ln\left(\frac{c^2 \mathrm{f}_1(\nu)}{8\pi h\nu^3 \sigma(\nu)}\right) = -\frac{h\nu}{kT} + D(T), \tag{19}$$

where $\mathrm{f}_1(\nu)$ is the spectral emissive power (in WHz^{-1}) and $D(T)$ is a function independent of the frequency [41-42].

The Kennard-Stepanov law is generally used to characterize the effective temperature of fluorescence; indeed, as shown in Chapter 8, the logarithmic ratio on the left hand side of Eqn. (19) is proportional to frequency and inversely related to the temperature T of the dye.

It is important to stress that the *K&S* relation holds for absorption to and emission from the same energy level. Therefore only a limited range of energies can be explored. In practice the optimal region is the Stokes region, where there is an overlap between the absorption and fluorescence bands. It has been observed experimentally that Eqn. (19) often holds even when the temperature T is not equal to the temperature of the emitting substance (Table 1). For this reason, we adopt the notation T^* for the effective temperature, to characterize the relationship between absorption and emission processes [43]:

$$T^*(\nu) = -\frac{k}{h}\frac{d}{d\nu}\ln\left(\frac{c^2}{8\pi h}\frac{\mathrm{f}_1(\nu)}{\nu^3\sigma(\nu)}\right)^{-1}. \tag{20}$$

In Stepanov's version of the theory the relation holds if two conditions are satisfied: (i) thermodynamic equilibrium in an excited state is possible and is achieved prior to photon emission, (ii) non-exciting absorption (transitions between two vibrational levels of the ground state) is negligible [30-31].

The first steps of the *K&S* theory resemble those of the Strickler-Berg relation, since common spectroscopic parameters like spectral absorption cross-section $\sigma(\nu)$ and fluorescence $\mathrm{f}_1(\nu)$ are described in terms of Einstein's A and B coefficients. The theory of Kennard and Stepanov can be divided into four parts:

- expression of the spectral absorption $\sigma(\nu)$ in terms of the $B_{0\to1}$ Einstein coefficient
- expression of the spectral emissive power $\mathrm{f}_1(\nu)$ in terms of the $\mathrm{A}_{0\to1}$ Einstein coefficient
- calculation of the ratio $\mathrm{f}_1(\nu)/\sigma(\nu)$ and transformation of the $A_{0\to1}$ coefficient into a $B_{0\to1}$ coefficient using Einstein's early work
- assumption of thermal equilibrium, so that electron occupation of the excited state has a Boltzmann distribution at the temperature T^*, the effective temperature of fluorescence radiation.

For a complex molecule with an energy-level diagram which includes vibrational levels and two electronic states S_0 and S_1, the spectral absorption cross-section $\sigma(\nu)$, proportional to the absorbance spectrum [44], can be described by counting the number of transitions from S_0 to S_1 within the energy range dw. In the same manner the fluorescence emissive power can be described by counting the number of transitions from S_1 to S_0 within the energy range dw^* (Fig. 111).

It can be shown [45] that:

$$\mathrm{f}_1(\nu) = Z\int A_{1\to0}\boldsymbol{g}^*(w^*)\boldsymbol{P}(w^*)dw^* \tag{21}$$

and

$$\sigma(\nu) = Z' \int B_{0\to1}\boldsymbol{g}(w)\exp^{\left(\frac{-w}{kT}\right)}dw\,, \tag{22}$$

where $\boldsymbol{g}(w)$ and $\boldsymbol{g}^*(w^*)$ are the statistical weights of the ground and excited levels, respectively, $B_{0\to1}$ is the $S_0 \to S_1$ transition probability, $A_{1\to0}$ is the $S_1 \to S_0$ probability, and $\boldsymbol{P}(w^*)$ is the probability of state occupation at energy w^*. The $\boldsymbol{P}(w^*)$ function is central to subsequent discussions.

The ratio $\mathrm{f}_1(\nu)/\sigma(\nu)$ becomes:

$$\frac{\mathrm{f}_1(\nu)}{\sigma(\nu)} = \frac{\int A_{1\to0}\boldsymbol{g}^*(w^*)\boldsymbol{P}(w^*)dw^*}{\int B_{0\to1}\boldsymbol{g}(w)\exp\left(\frac{-w}{kT}\right)dw} D(T)\,, \tag{23}$$

where T is the temperature of the solution, assumed to be at ambient temperature, and $D(T)$ is a constant linked to the ratio (Z/Z') of partition functions. The constant $D(T)$, identified in [28], does not prevent characterization of the temperature of fluorescence radiation in the following development.

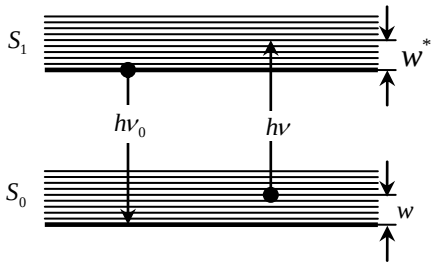

Fig. 111: Electronic diagram of a complex molecule considered in the *K&S* theory. The molecule absorbs a photon of energy $h\nu$ and promotes one electron to a vibrational energy state of the S_1 singlet state. Vibrational relaxation occurs through the energy range $w^*$and a photon of energy $h\nu_0$ is emitted. The energies of the excitation and emission are linked by the simple relation $h\nu_0 + w^* = h\nu + w$.

Introducing the Einstein coefficients and replacing $B_{0\to1}$ in Eqn. (23), we obtain:

$$A_{1\to0}\boldsymbol{g}^*(w^*)dw^* = \frac{8\pi h\nu^3}{c^2}B_{0\to1}\boldsymbol{g}(w)dw, \tag{24}$$

hence

$$\frac{\mathrm{f}_1(\nu)}{\sigma(\nu)}\frac{c^2}{8\pi h\nu^3} = \frac{\int \boldsymbol{P}(w^*)dw}{\int \exp\left(\frac{-w}{kT}\right)dw} D(T). \tag{25}$$

Using the energy relation shown in Fig. 111, and assuming thermal equilibrium in the excited state of the molecule prior to photon emission, the probability of state occupation $\boldsymbol{P}(w^*)$ can be expressed as a Boltzmann distribution:

$$\boldsymbol{P}(w^*) = \exp(-w^*/kT) = \exp[(-w + h\nu - h\nu_0)/kT]. \tag{26}$$

Introduction of this distribution into Eqn. (25) leads directly to Eqn. (19). An interesting fact about the Kennard-Stepanov theory is that, because the slope is proportional to frequency and inversely related to the temperature $T^*$of the dye, Eqn. (19) can be simplified to:

$$\ln\left(\frac{\sigma(\nu)}{\tilde{f}_1(\nu)}\nu^2\right) = \frac{h\nu}{kT^*} + D(T)\ . \tag{27}$$

There has been much speculation about the reasons for deviations from Eqn. (19). Inhomogeneous broadening [46] and frequency-dependent fluorescence yield [47] have been identified as possible causes [48].

Table 1: *K&S* parametric temperatures for various dye/solvent combinations, the temperatures highlighted in red show the disagreement between the *K&S* temperature and the ambient temperature.

Solute	Solvent	*solvent* T(K)	T^*(K)	Ref
Rhodamine 6G	Water	293	295	[49]
Fluorescin	Glycerine	298	299	[45]
Perylene	(vapour)	513	556	[45]
Chlorophyll A	Carbon disulfide	296	298	[45]
Eosin extra VA	Water	293	310	[50]
Eosin extra	Water	293	340	[50]
Rose Bengal	Ethanol	262	351	[45]
Trypaflavin	Glycerine	262	342	[45]
Trypaflavin	1-butanol	293	391	[45]
2,5 di(4-biphenylyl) oxazole	PMMA	298	430	[45]
Erythrosine	Ethanol	338	456	[45]
Flavophosphin	Ethanol	262	344	[45]

1.4 Discussion

This chapter has presented the physics of photon sources – essential background to the operation of fluorescent collectors. The sun delivers $1000\,Wm^{-2}$ to Earth. The standard solar irradiance spectra $AM1.5$, used for charting the performance of photovoltaic devices, were introduced.

The physics of fluorescent dyes was reviewed, and it was shown that four parameters – Stokes shift, quantum yield, lifetime and specific temperature – are required for the characterization of fluorescent sources. The interaction of photons with matter was briefly reviewed, and it was demonstrated that c-Si is a weak absorber compared to direct band gap semiconductor or organic fluorescent dyes.

The phenomenon of photon re-absorption was discussed, and the related theories of van Roosbroeck-Shockley and Kennard-Stepanov were reviewed.

Chapter 2

Ideal P-N junction solar cells

A semiconductor solar cell is a device consisting of a large-area P-N junction, capable of generating electricity in the presence of sunlight. As noted in Chapter 1, a photon must have an energy greater than the band gap of the cell material in order to excite an electron from the valence band into a conduction band. The solar spectrum is approximated by a blackbody spectrum at $6000\ K$ (Fig. 106), and most solar radiation reaching the Earth consists of photons with energies greater than the band gap of silicon ($1.12\ eV$), the standard semiconductor material for solar cells. Photons of energy below the band gap pass straight through the cell whilst high-energy photons create electron-hole pairs, which are collected by metal contacts. The excited carriers quickly "thermalize" to the edge of the band gap, losing energy as heat. These unavoidable losses in a semiconductor solar cell define its ultimate efficiency.

A detailed-balance efficiency model formulated by Shockley and Queisser (*S&Q*) [10], which takes account of the unavoidable losses associated with the band gap, radiative recombination and the solid angle subtended by the sun, sets an upper theoretical limit on the efficiency of standard single-junction semiconductor solar cells (also referred to as "first-generation" cells). More efficient alternatives exist, grouped under the term "third-generation solar cells". Third-generation cells have been developed that exceed the *S&Q* efficiency limit ($\approx 30\%$ for c-Si) through reduction or elimination of unavoidable losses. Particular attention will be paid here to a particular type of third-generation configuration, namely tandem cells – in which the solar spectrum is split by combining materials with different band gaps – because:

- the concept can be adapted at low cost to fluorescent solar collectors (Chapter 4)
- this is the only type of third-generation cell which exceeds the *S&Q* efficiency limit.

The detailed-balance efficiency limit will be derived for such a structure, and it will be shown that tandem cells under one sun can reach theoretical efficiencies as high as $\approx 42\%$. Before the detailed-balance model is introduced, however, a brief overview of solar cell operation is in order.

2.1 Operation of an ideal P-N junction solar cell

A diagram of a typical P-N junction solar cell is presented in Fig. 112. The device is composed of a P side (excess of holes) and an N side (excess of electrons). At the P-N junction the excess of holes recombines with electrons, creating a depletion region and an electric field $\vec{E}$ between the P and N sides. When this is illuminated, photons excite electrons in the conduction band on either side of the junction (Fig. 113). The electrons, once in the conduction band, are free to diffuse within the crystal towards the junction. When they reach the junction, the generated carriers are swept away by the electric field and collected at contacts on the top and bottom of the cell.

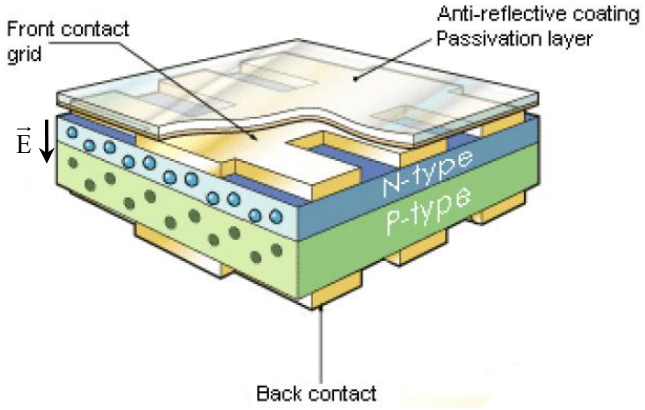

Fig. 112: Schematic diagram of a P-N junction solar cell showing the P side (P-type) with an excess of holes (dark green) and the N side (N-type) with an excess of electrons (dark blue). This junction of P and N materials creates an electric field. (Figure adapted from Discovery Communications, LLC)

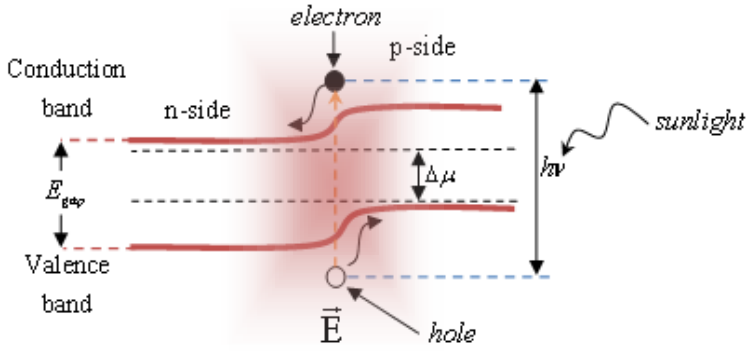

Fig. 113: Energy-band diagram of a P-N junction solar cell. Photons with energy higher than the band gap ($h\nu > E_{gap}$) excite electrons from the valence band to the conduction band. The generated carriers diffuse to the depletion region (red shaded region) where they are swept across the junction by the electric field. The two dashed black lines represent the quasi-Fermi levels for the electron and hole populations. The difference between them is equal to the difference in chemical potential – a concept used in this thesis to characterize the theoretical limit to cell output voltage.

2.1.1 Electrical characteristics

A conventional solar cell like the one illustrated in Fig. 112 is just a large P-N junction diode exposed to the sun. In the dark, the cell behaves like a diode, with electrical characteristics given by the relation:

$$I(V,T) = I_0\left(\exp^{\left(\frac{qV}{kT}\right)} - 1\right), \tag{28}$$

where I is the current, I_0 is the dark current, V is the voltage and q is the electronic charge.

2.1.1.1 One-diode model

Under illumination a cell behaves like a current generator in parallel with a diode. The resulting equivalent circuit models the characteristics of an ideal solar cell, and is referred to as the one-diode model (Fig. 114). This simple electrical model will be revisited in the next chapter (Section 3.3.1) to suit more realistic devices.

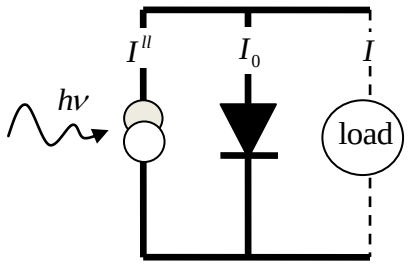

Fig. 114: Equivalent electrical circuit for an ideal solar cell under illumination [4].

The current reaching the load in Fig. 114 is given by:

$$I(V,T) = I^{ll} - I_0\left(\exp^{\left(\frac{qV}{kT}\right)} - 1\right), \tag{29}$$

where I^{ll} represents the current generated by the cell under illumination. From this relation it is clear that the current–voltage (IV) characteristics of an illuminated cell resemble those of a diode, but shifted as a result of the current generated by illumination (Fig. 115) [18].

2.1.1.2 IV characteristics

Four output parameters are usually used to describe solar cell performance: the short-circuit current I_{sc}, the open-circuit voltage V_{oc}, the fill factor FF and of course the efficiency η_{cell} of the cell.

The short-circuit current is the maximum current that the cell can produce when the voltage is set to 0. When $V = 0$ in Eqn. (29), $I_{sc} = I^{ll}$.

The open-circuit voltage is the maximum voltage extractable from the cell when the current is set to 0. When $I = 0$ in relation (29):

$$V_{oc} = \frac{kT}{q} \ln\left(\frac{I^{ll}}{I_0} + 1\right). \tag{30}$$

Fill factor measures the "squareness" of the cell output as compared with the ideal, indicated by the black dotted line in Fig. 115:

$$FF = \frac{I_{mp}\, V_{mp}}{I_{sc} V_{oc}}. \tag{31}$$

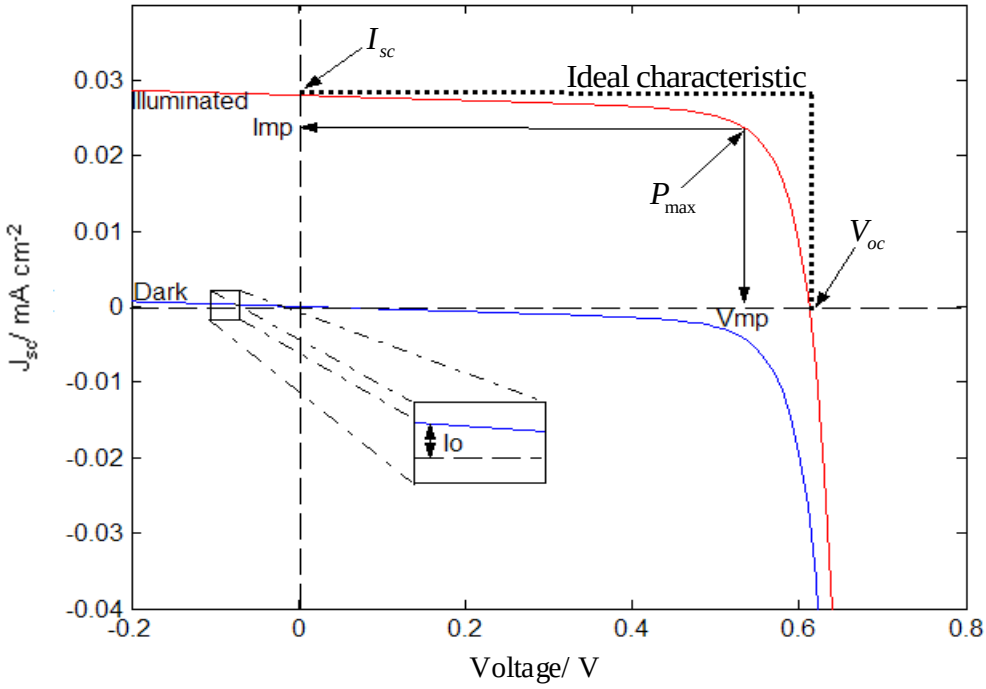

Fig. 115: *IV* characteristics of a solar cell: in the dark (blue line) and illuminated (red line). The light-generated current is superimposed on the normal rectifying current-voltage characteristics of a diode. Typical *IV* characteristics fall within the fourth quadrant, but in practice solar *IV* characteristics are often displayed in the first quadrant, as in this figure. The maximum power can be extracted at the point P_{max}, where the product of voltage V_{mp} and current I_{mp} is greatest.

The efficiency of the cell is the ratio of maximum power output to power input under standard conditions ($AM1.5$ spectrum and temperature 25°C) [5]:

$$\eta_{cell} = \frac{P_{\max}}{incident\ \ solar\ \ power} = \frac{V_{mp}\, I_{mp}}{\int_0^\infty f_{sun}(\nu, T_{sun}, \Omega_{sun})\, d\nu} = \frac{V_{oc}\, I_{sc}\, FF}{\int_0^\infty f_{sun}(\nu, T_{sun}, \Omega_{sun})\, d\nu}. \tag{32}$$

The definition of the function f_{sun} can be found in Chapter 1, Eqn. (3).

Losses of various kinds – optical (e.g. reflection), electrical (e.g. resistivity of the semiconductor) and other non-radiative effects (e.g. Auger recombination) – related to the quality of the materials

will decrease the efficiency of the cell. Even with ideal materials, the solar cells pictured in Fig. 112 and Fig. 113 cannot reach 100 % efficiency because of "unavoidable" losses associated with the band gap of the semiconductor.

2.1.2 Unavoidable losses

The band gap or cut-off frequency of a semiconductor introduces a major loss because photons of energy $h\nu < E_{gap}$ cannot be absorbed. Looking back at the solar spectrum $AM1.5$ (Fig. 104) and assuming a silicon solar cell with a band gap near $1100\ nm$ (Si), one can see that almost a quarter of the solar spectrum is lost. In addition, photons of high energy $h\nu >> E_{gap}$ which are absorbed by the semiconductor create high-energy electron-hole pairs which quickly thermalize back to the edge of the band gap, losing their energy as heat [15;17]. This loss is known as electron thermalization.

As a consequence of Kirchhoff's law [1;51], an irradiated solar cell will unavoidably re-emit photons, an effect known as radiative recombination. U_{rad} is proportional to the product of the concentration $[n]$ of electrons in the conduction band and the concentration $[p]$ of holes in the valence band:

$$U_{rad} = B([n][p] - n_i^2), \tag{33}$$

where n_i is the intrinsic carrier concentration and B is a constant for a given semiconductor.

The constant B (often expressed in terms of $\Re_0 = Bn_i^2$) has been derived for solar cells (Section 1.3.3.1); for silicon it is $1.8 \times 10^{-15}\ cm^{-3}s^{-1}$, for gallium arsenide $7.2 \times 10^{-10}\ cm^{-3}s^{-1}$, for indium phosphide $6.25 \times 10^{-10}\ cm^{-3}s^{-1}$. Silicon shows fewer radiative recombination losses than the other semiconductors because of its optical properties, as discussed in Chapter 1.

2.2 Ultimate efficiency

As noted in the introduction to this chapter, the ultimate efficiency of a semiconductor solar cell takes into account the thermalization of charge carriers and the loss of electrons with energy below the band gap. The ultimate efficiency model of Shockley and Queisser [10] is based on two main assumptions:

- The solar cell, at a temperature $T_c = 0\ K$, is surrounded by a blackbody radiation emitter (the sun) at a temperature of $T_s = 6000\ K$. This statement assumes that some means exist for keeping the temperature of a solar cell at $0\ K$.

- Each photon with an energy greater than the semiconductor band gap produces one electron-hole pair of energy $q \times V_g$, where $V_g = h\nu_{gap}\, q^{-1} = E_{gap}\, q^{-1}$.

As stated in Eqn. (32), the efficiency of a solar cell is the ratio of output power to input power. Considering the first assumption above, the input power of the sun is given by integrating the solar intensity given by Planck's law (Chapter 1):

$$\text{Solar input power} = A_{cell} \int f_{sun}\,(\nu, T_{sun})\,d\nu = \frac{2\pi h}{c^2} \int_0^{\infty} \left[\frac{\nu^3}{\exp\left(\frac{h\nu}{kT_s}\right)-1}\right] d\nu. \tag{34}$$

Setting $x = h\nu/kT_s$,

$$\int f_{sun}\,(\nu, T_{sun})\,d\nu = \frac{2\pi (kT_s)^4}{h^3 c^2} \int_0^{\infty} \left[\frac{x^3}{\exp\,(x)-1}\right] dx = \frac{2\pi^5 (kT_s)^4}{15 \cdot h^3 c^2} = \sigma_{SB} {T_s}^4. \tag{35}$$

Integration of the solar intensity thus leads to the Stefan-Boltzmann law, with $\sigma_{SB} = 5.67 \times 10^{-8}\ W\, m^{-2} k^{-4}$. The input power to the cell is the area A_{cell} of the cell times $\sigma_{SB} {T_s}^4$.

The output power of the cell is determined using the same argument since each photon creates an electron-hole pair; the integration of solar intensity from $h\nu_{gap}$ to infinity gives the number of generated charge carriers. Output power is calculated from the flux of photons with energy higher than the band gap times the energy $h\nu_{gap}$.

$$\text{Cell output power} \;=\; A_{cell}\, h\nu_{gap} \int_{h\nu_{gap}}^{\infty} \dot{f}_{sun}\,(\nu, T_{sun})\; d\nu, \tag{36}$$

where

$$\int_{h\nu_{gap}}^{\infty} \dot{f}_{sun}\,(\nu, T_{sun})\;\; d\nu = \frac{2\pi}{c^2} \int_{h\nu_{gap}}^{\infty} \frac{\nu^2}{\exp\left(\frac{h\nu}{kT_s}\right)-1}\;\; d\nu. \tag{37}$$

Setting $x = h\nu/kT_s$ and $x_g = h\nu_{gap}/kT_s$,

$$\int_{h\nu_{gap}}^{\infty} \dot{f}_{sun}\,(\nu, T_{sun})\;\; d\nu = \frac{2\pi (kT_s)^3}{h^3 c^2} \int_{x_g}^{\infty} \left[\frac{x^2}{(\exp\,(x)-1)}\right]\;\; dx\;. \tag{38}$$

Combining Eqns. (38), (36) and (35), the ultimate efficiency η_{ult} is given by:

$$\eta_{ult}\,(x_g) = \frac{\text{Cell output power}}{\text{Solar input power}} = \frac{x_g \int_{x_g}^{\infty} \left[\frac{x^2}{(\exp\,(x)-1)}\right] \cdot dx}{\int_0^{\infty} \left[\frac{x^3}{\exp\,(x)-1}\right] \cdot dx} = \frac{x_g \int_{x_g}^{\infty} \left[\frac{x^2}{(\exp\,(x)-1)}\right] \cdot dx}{\frac{\pi^4}{15}}\,. \tag{39}$$

Fig. 116 shows a plot of ultimate efficiency against semiconductor band gap. The maximum efficiency is about 44 %, for crystalline silicon (c-Si). Values for other commonly used semiconductors are also shown.

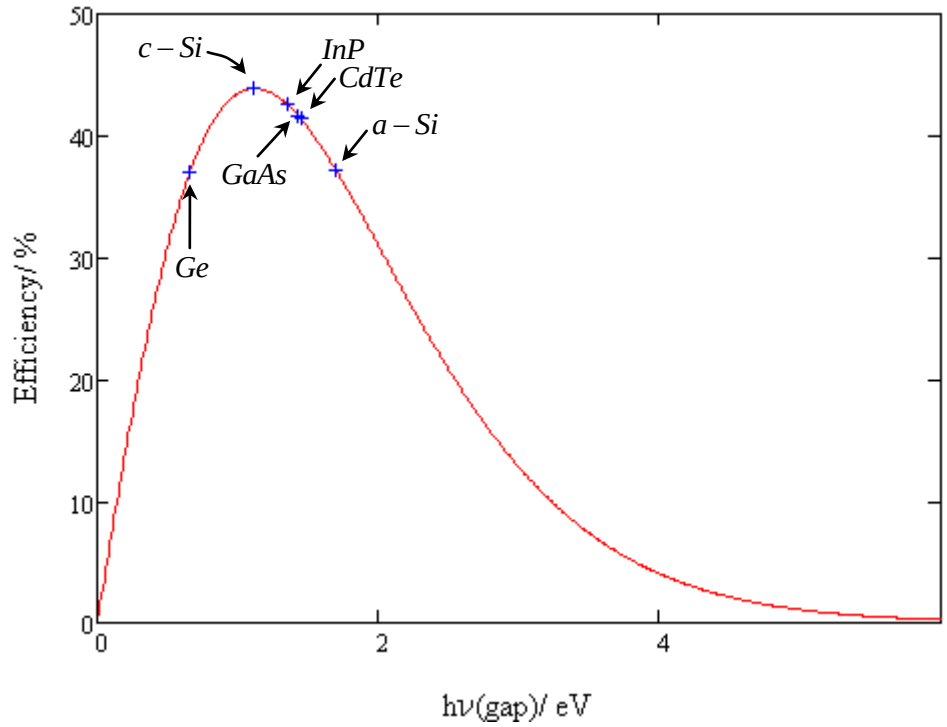

Fig. 116: Ultimate efficiency of a semiconductor solar cell as a function of the semiconductor band gap. Crystalline silicon has the highest efficiency, at 44%. Band gaps for the materials shown are: germanium Ge, 0.66 *eV*, indium phosphide InP, 1.35 *eV*, gallium arsenide GaAs, 1.43 *eV*, cadmium telluride CdTe, 1.45 *eV* and amorphous silicon a-Si, 1.7 *eV*.

2.3 Detailed-balance efficiency (single-junction)

The detailed-balance model of Shockley and Queisser [10] is certainly the most widely cited in the literature, because it can be applied not just to a specific type of solar cell but to any single junction devices. The model is derived twice in the discussion that follows: the first derivation is identical to that set out by *S&Q*, using numerical integration, while the second derivation uses only analytical expressions. In the second derivation the open-circuit voltage is expressed through a Carnot engine efficiency factor, stressing the thermodynamic origins of V_{oc} [52-53]. A comparison between the numerical and analytical derivations is given at the end of this section.

The detailed-balance model estimates the efficiency a solar cell could reach if it were free of avoidable losses.

The model assumes that:

- there is no photon reflection, hence no optical losses
- each photon with energy greater than the semiconductor band gap produces one electron-hole pair
- the generated carriers are collected with 100 % efficiency
- the recombination of one electron-hole pair produces exactly one photon
- only interband radiative recombination is considered
- quasi-Fermi levels remain constant along the P-N junction, as shown in Fig. 113.

The detailed-balance model has been revisited and improved by many authors, each reducing the number of assumptions. For example, Araujo [54] and Bremner [55] considered non-constant quasi-Fermi levels across the cell, while Honsberg [56] generalized the detailed balance to three-level systems. The detailed-balance concept is still used for assessing the efficiency of new concepts such as fluorescent solar collectors [8;57].

2.3.1 Shockley and Queisser derivation

The essence of the *S&Q* theory lies in the assumption that the cell-generated current I_{cell} is the difference between the photon flux absorbed,

$$\int_{h\nu_{gap}}^{\infty} \dot{f}_{sun}(\nu, T_{sun}, \Omega_{sun})\ d\nu = \dot{\mathbf{F}}_{abs}(\nu, T_{sun}, \Omega_{sun}) \tag{40}$$

and the photon flux re-emitted by the cell,

$$\int_{h\nu_{gap}}^{\infty} \dot{f}_{cell}(\nu, T_{cell}, \Omega_{cell}, \mu)\ d\nu = \dot{\mathbf{F}}_{cell}(\nu, T_{cell}, \Omega_{cell}, \mu), \tag{41}$$

where photons re-emitted by the cell escape from both side of the cell, with a non-zero chemical potential [56]:

$$I_{cell} = \underbrace{q(\dot{\mathbf{F}}_{abs}(\nu, T_{sun}, \Omega_{sun})A_{cell}}_{I^{ll}} - \underbrace{2A_{cell}\dot{\mathbf{F}}_{cell}(\nu, T_{cell}, \Omega_{cell}, \mu)}_{I_0\left(\exp\frac{qV}{kT}-1\right)} \tag{42}$$

The open-circuit voltage is calculated as a function of the illuminated current and the dark current using Eqn. (30), re-written here as $V_{oc} = kT_{cell}/q\ln(1 + I^{ll}/I_0)$. The short-circuit current I_{sc} is the product of the integrated solar photon flux density, the area of the cell and the elementary charge:

$$I_{sc} = q\dot{\mathbf{F}}_{abs}(\nu, T_{sun}, \Omega_{sun})A_{cell} \tag{43}$$

The detailed-balance efficiency is obtained from the product $V_{oc}I_{sc}FF$ over the incident solar power from a blackbody at $6000\,K$.

2.3.2 Semi-analytical approach

In the semi-analytical approach the output power of a solar cell is still computed from the product $V_{oc}I_{sc}FF$, but V_{oc} is calculated thermodynamically, following a derivation proposed in [52] while the fill factor *FF* is derived from an empirical law extracted from [17].

2.3.2.1 Open-circuit voltage

In this section the approach of Ruppel and Würfel [52] is followed to obtain an analytical expression for V_{oc} depending on T_{cell}, T_{sun}, Ω_{sun} and the semiconductor band gap.

Considering a solar cell absorbing all the incoming photons with energy $> E_{gap}$. The photon balance for the open circuit state in flow equilibrium requires that the rate of photons absorbed from the sun at T_{sun} with no chemical potential equals the rate of photon emitted by the cell at T_{cell} with a non zero chemical potential:

$$\dot{\mathbf{F}}_{abs}(\nu, T_{sun}, \Omega_{sun}) = \dot{\mathbf{F}}_{cell}(\nu, T_{cell}, \Omega_{cell}, \Delta\mu), \tag{44}$$

$$\Omega_{sun}\int_{h\nu_{gap}}^{\infty}\frac{\nu^2}{\exp\left(\frac{h\nu}{kT_{sun}}\right)-1}\,d\nu = \Omega_{cell}\int_{h\nu_{gap}}^{\infty}\frac{\nu^2}{\exp\left(\frac{h\nu-\Delta\mu}{kT_{cell}}\right)-1}\,d\nu. \tag{45}$$

The chemical potential ($\Delta\mu$) of the re-emitted photons correspond to the free energy per electron-hole pairs recombined. Therefore, $\Delta\mu$ is directly related to the open-circuit voltage by $\Delta\mu = V_{oc}q$ [58].

Neglecting stimulated emission, and replacing Ω_{cell} by π - the etendue – in Eqn. (45), the chemical potential of the re-emitted photons is equal to:

$$\Delta\mu = V_{oc}q = h\nu_{gap}\left(1 - \frac{T_{cell}}{T_{sun}}\right) + kT_{cell}\ln\left(\frac{T_{sun}}{T_{cell}}\right) - kT_{cell}\ln\left(\frac{\pi}{\Omega_{sun}}\right) + \cdots \tag{46}$$

The first term of Eqn. (46) gives the maximum energy generated by a two-level converter, equal to the energy band gap times the Carnot efficiency $(1 - T_c/T_s)$. The middle term is a contribution due to the kinetic energy of the charge carriers, and is therefore present in a system consisting of bands rather than energy levels. The last term takes in account the sun dilution. The three dots represent a correction factor which can be added for an accuracy $\approx 0.01\ eV$:

$$kT_{cell} \ln\left(\frac{1+\wp(\nu_{gap}, T_{sun})}{1+\wp(\nu_{gap}, T_{cell})}\right), \tag{47}$$

where

$$\wp(\nu, T) = 2\frac{kT}{h\nu} + 2\left(\frac{kT}{h\nu}\right)^2. \tag{48}$$

The result of the full Eqn. (46) is plotted as a function of the material band gap in Fig. 16.

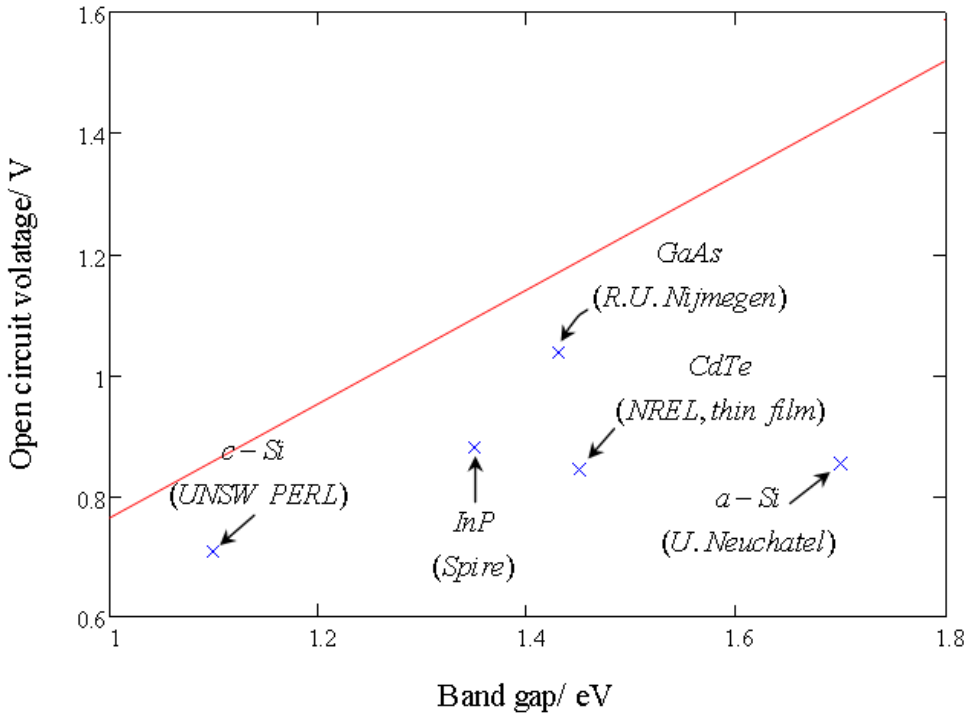

Fig. 117: Theoretical limit of the open-circuit voltage (red) for one sun at 6000K and cell at 300K. The points correspond to the devices with the best open-circuit voltages under *AM* 1.5 (Figure adapted from [59] and updated using the latest efficiency table [60])

2.3.2.2 Short-circuit current

Under ideal conditions, I_{sc} depends only on the flux of photons with energies higher than the semiconductor band gap. The argument is similar to that used by *S&Q* (Eqn. (43)). The optimum short-circuit current under one sun as a function of semiconductor band gap is plotted in Fig. 118.

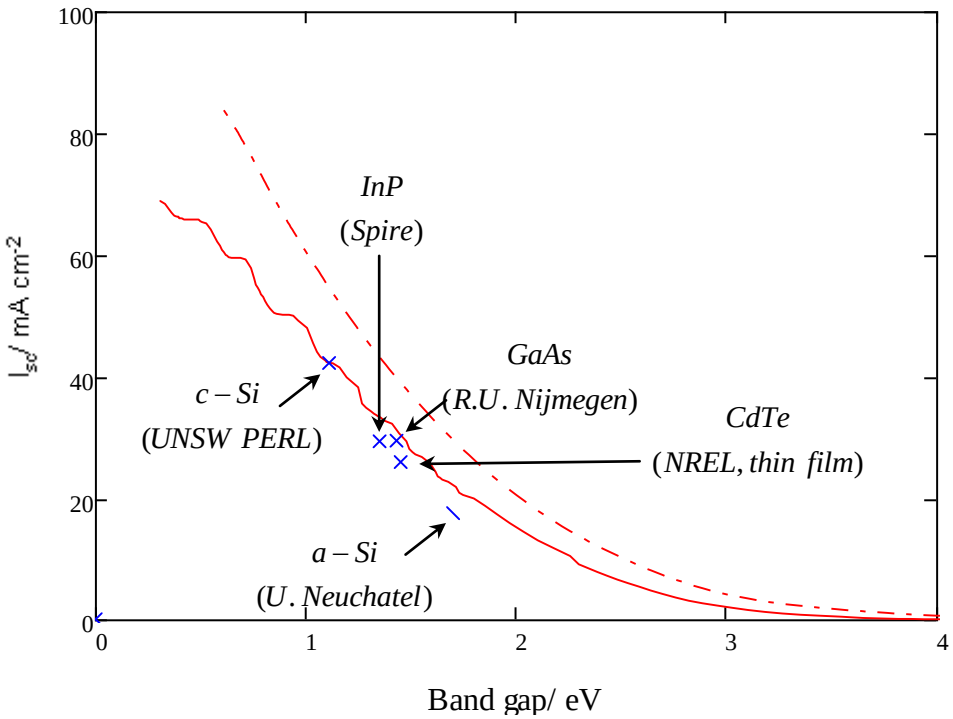

Fig. 118: Optimal photo-generated current (solid red line, $AM1.5$; dashed red line, $AM\ 0$), compared to the best measured devices. (Figure adapted from [59] and updated using the latest efficiency table [60])

It is not surprising to see an increase in the short-circuit current when the band gap is reduced since with a smaller band gap, photons of low energy can be absorbed. However, the smaller the band gap, the lower the energy carried by the electron-hole pairs, and the lower the open-circuit voltage. To have an efficient solar cell, a compromise is required. For silicon solar cells the optimum short-circuit current corresponds to 44 $mA\ cm^{-2}$.

Fig. 118 shows that solar cells are very efficient devices in terms of photon-electron conversion: the actual short-circuit currents of the PERL c-Si and GaAs cells, for example, match the theoretical limit.

2.3.2.3 Fill factor

The expression for the fill factor derives from an empirical equation suggested in [17]:

$$FF = \frac{\frac{V_{oc}}{(kT_{cell})q^{-1}} - \ln\left(\frac{V_{oc}}{(kT_{cell})q^{-1}} + 0.72\right)}{\frac{V_{oc}}{(kT_{cell})q^{-1}} + 1}. \qquad (49)$$

Fill factor is plotted as a function of open-circuit voltage in Fig. 18.

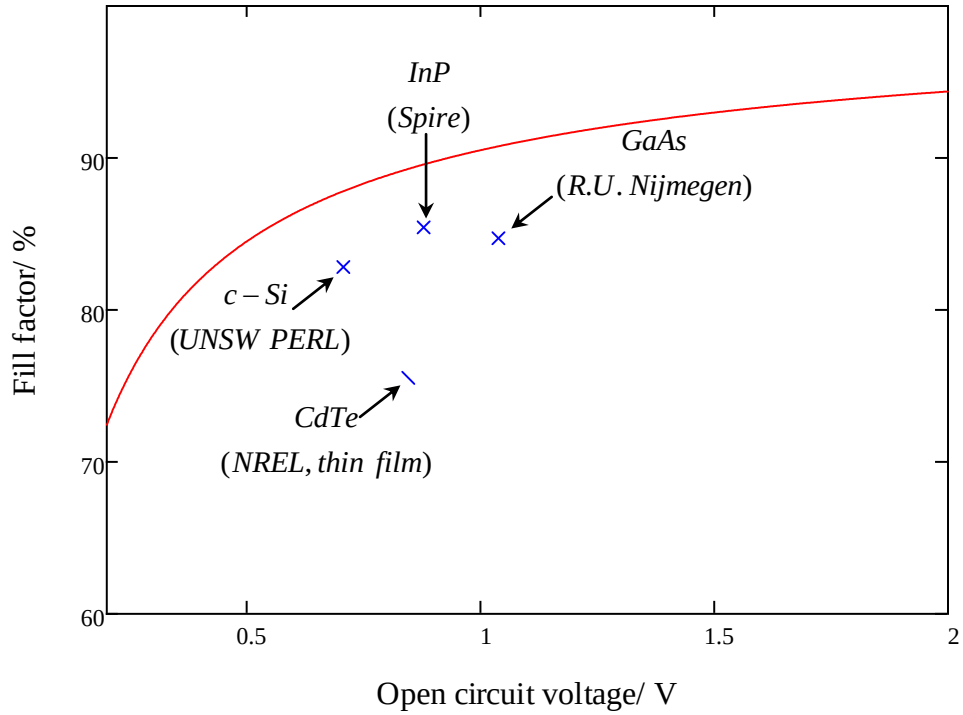

Fig. 119: Fill factor as a function of the open-circuit voltage for a cell at 300 K compared to the best measured device [60] under $AM1.5$. For c-Si the FF is about *85%* when estimated with Eqn. (49). (Figure adapted from [59] and updated using the latest efficiency table [60])

2.3.3 Detailed-balance results

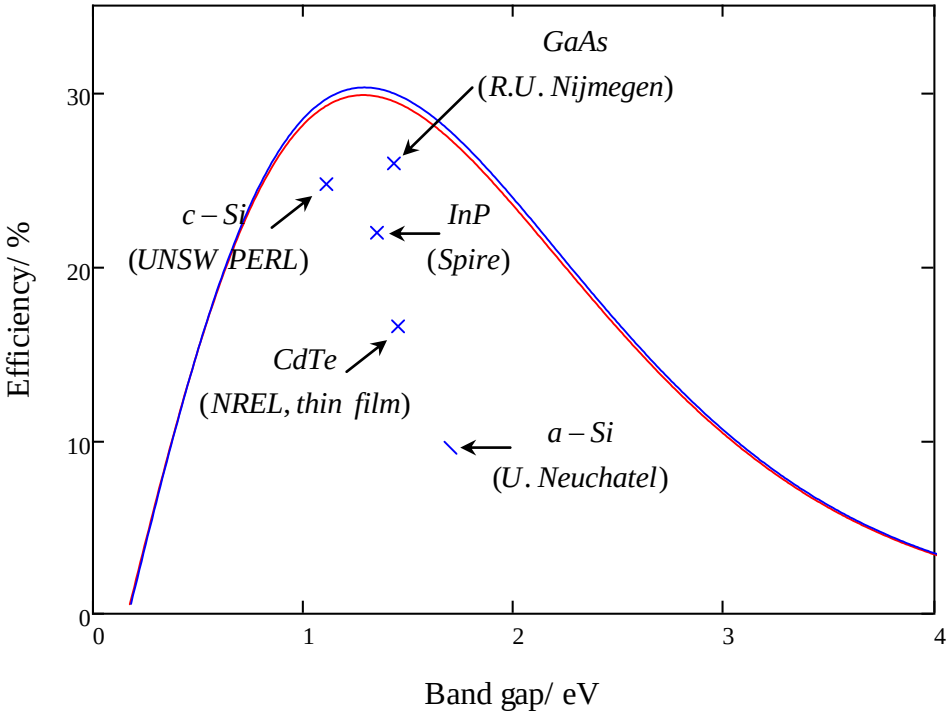

Fig. 120: *S&Q* detailed-balance efficiency (red line) compared with the semi-analytical model (blue line). The two models fit together with an overall deviation of less than 1%. The crosses indicate the efficiencies of the best available solar cells under $AM1.5$ [60].

Fig. 19 compares the results from the numerical integration of *S&Q* with the semi-analytical model derived in the previous section (for one sun at $6000\,K$). These are compared with the efficiencies of the best available solar cells under $AM1.5$.

2.4 Detailed-balance efficiency (two-junction)

The *S&Q* detailed-balance efficiency gives the upper limit for a single-junction semiconductor solar cell. Using more than one junction can help to overcome this limitation by reducing the loss of photons from non-absorption and from electron thermalization. This technique is known as spectral splitting, and a two-junction cell is called a tandem cell. The aim here is to adapt the semi-analytical model reviewed in the Section (2.3.2) to derive the detailed-balance efficiency of a tandem cell.

In a typical multi-junction cell, individual cells with different band gaps are stacked on top of one another in such a way that sunlight falls first on the material having the largest band gap. Photons not absorbed in the first cell are transmitted to the second cell, which then absorbs the lower-energy portion of the remaining solar radiation (Fig. 121). This selective absorption processes is enhanced with an increasing number of judiciously chosen cells with different band gaps.

The detailed-balance efficiency of a tandem cell is computed using the analytical relation for V_{oc}, FF and I_{sc}. The assumptions are similar to those made by *S&Q*, with the following additions:

- The photon flux re-emitted by cell 1 is not re-absorbed by cell 2, and vice versa [61].
- The two junctions are represented by two independent cells, i.e. they are not electrically connected to one another (four-point electrical contact).

The tandem cell considered here consists of two stacked flat cells with different cut-off frequencies $h\nu_{gap}^{1}$ and $h\nu_{gap}^{2}$, where $h\nu_{gap}^{1} > h\nu_{gap}^{2}$.

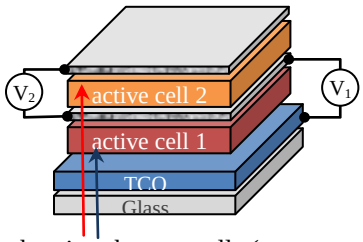

Fig. 121: Geometry of a tandem cell, showing the two cells (orange and red) stacked on top of one another. Photons of energy $h\nu > h\nu_{gap}^{1}$ (blue arrow) are absorbed in the first cell, while photons of energy $h\nu < h\nu_{gap}^{1}$ (red arrow) pass through the first cell and are absorbed in the second cell.

Since the cells are assumed to be independent of one another, the efficiency of the tandem cell is the sum of the individual efficiencies. The open-circuit voltage and fill factor are calculated separately for each cell as a function of their band gaps, using Eqns. (46) and (49). The short-circuit current is the sum of the currents generated by each cell under illumination, minus terms representing the light re-emitted by the cells:

$$I_{sc} = q\begin{pmatrix} \int_{h\nu_{gap}^2}^{h\nu_{gap}^1} (\dot{f}_{sun}(\nu, T_{sun}, \Omega_{sun})\, d\nu \; - \dot{f}_{cell}(\nu, T_{cell}, \Omega_{cell}, \mu)\, d\nu) \\ + \int_{h\nu_{gap}^1}^{\infty} (\dot{f}_{sun}(\nu, T_{sun}, \Omega_{sun})\, d\nu - \dot{f}_{cell}(\nu, T_{cell}, \Omega_{cell}, \mu)\, d\nu) \end{pmatrix}. \quad (50)$$

2.4.1 Results

Fig. 122 and Fig. 123 show the ideal efficiency of the tandem cell configuration as a function of the band gaps $h\nu_{gap}^1$ and $h\nu_{gap}^2$. When the band gap of one cell is set to zero one can recognize the detailed-balance contour for a single cell, with a maximum theoretical efficiency of 30 %, as already noted (Fig. 19).

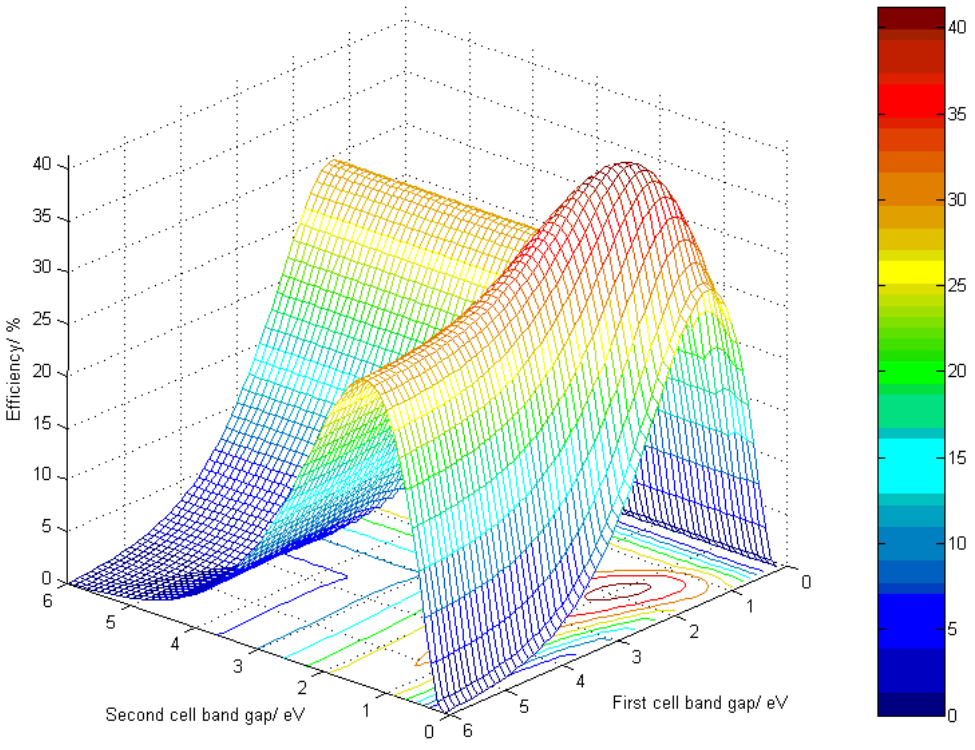

Fig. 122: Tandem cell detailed-balance efficiency as a function the band gaps of cells 1 and 2. The maximum efficiency (under one sun) is around 42 % for 1.5 $eV < h\nu_{gap}^1 < 2.3\ eV$ and 0.8 $eV < h\nu_{gap}^2 < 1.2\ eV$. (Figure published in [62])

With a second non-zero band gap, the computed detailed-balance efficiency, under one sun, is about 40 %, reaching a maximum of 42 % for the band gap ranges 1.5 $eV < h\nu_{gap}^1 < 2.3\ eV$ and

$0.8\,eV < h\nu_{gap}^2 < 1.2\,eV$. These results match those of DeVos [61], obtained using a much simpler calculation avoiding numerical integration.

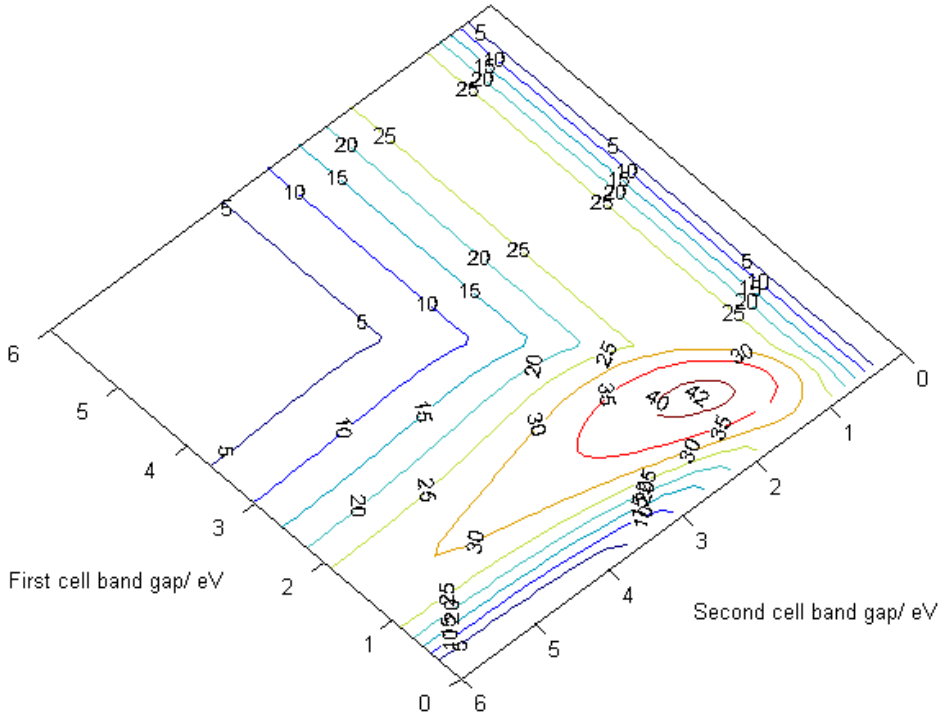

Fig. 123: Contour plot of Fig. 122. (Figure published in [62])

In practice, a multi-junction cell can be made in two different ways: mechanical stacking or monolithic. In the former approach, the individual solar cells are made independently, one with a high band gap and one with a lower band gap, and mechanically stacked on top of one another. In the latter, a complete solar cell is made and then the layers for the second cell are grown or deposited directly onto the first converter (Fig. 124).

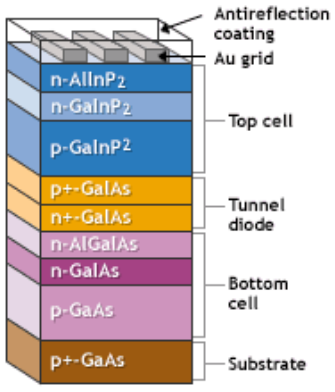

Fig. 124: State-of-the-art tandem device with a gallium indium phosphide top cell, a "tunnel junction" allowing the flow of electrons between the cells, and a bottom cell of gallium arsenide. (Source: UNSV)

Much current research in multi-junction cells focuses on III – V semiconductors. Such cells can reach practical efficiencies of over 30 % under one sun. Table 2 shows current reported efficiencies.

Table 2: Reported efficiencies for current multi-junction solar cells. Data taken from Refs. [59-60]

Multi-junction	V_{oc} (V)	I_{sc} $(mA\ cm^{-2})$	FF (%)	η_{cell} (%)	Description
GaInP/GaAs/Ge	2.622	14.37	85	32	Spectrolab (monolithic)
GaInP/GaAs	2.48	14.22	85.6	30.3	Japan Energy (monolithic)
GaInP/CIS	-	-	-	25.8	Kopin/Boeing (four-terminal thin film)

2.5 Detailed-balance efficiency (infinite stack)

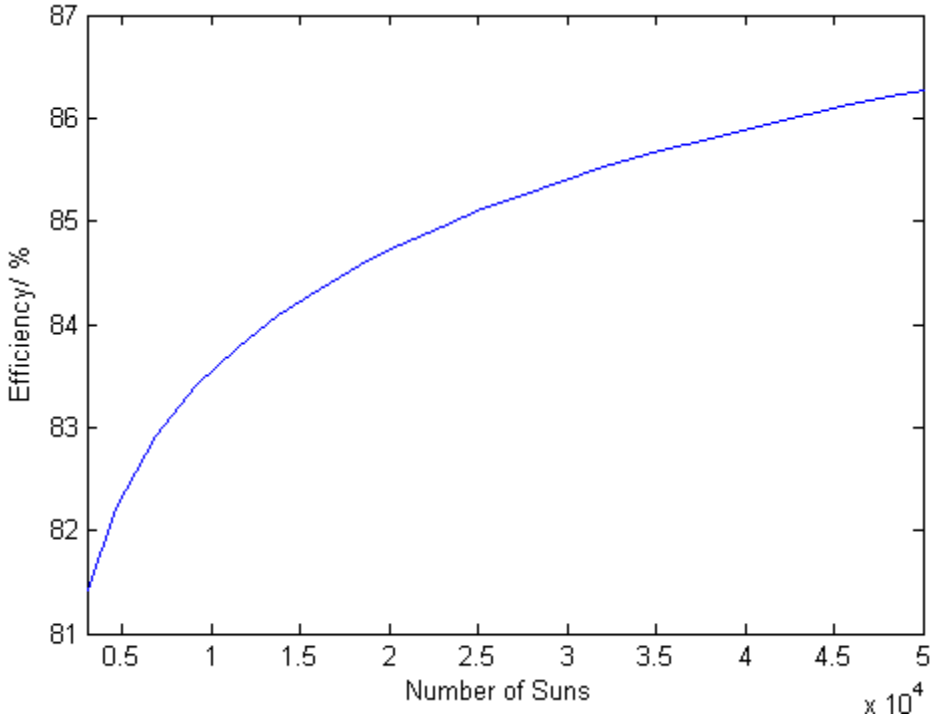

Fig. 125: Detailed-balance efficiency of an infinite stack of cells as a function of the sun's concentration. The results correspond to those in [61] within 1%, using the analytical relations in Eqns. (51), (49) and (46). (Figure published in [62])

The efficiency calculation for a tandem cell can be extended theoretically to an infinite stack of cells. The open-circuit voltage, short-circuit current and fill factor are calculated for band gaps from zero to infinity in infinitesimal increments $d(h\nu)$. The maximum achievable efficiency is then the sum of the efficiencies for the band gaps $h\nu_{gap}$ to $h\nu_{gap} + d(h\nu)$:

$$\eta_{\infty} = \sum_{h\nu=0}^{h\nu=\infty} \left[\frac{V_{oc\,(h\nu\,gap)} \cdot FF_{(h\nu\,gap)} \cdot q \int_{h\nu\,gap}^{h\nu\,gap+dh\nu} \dot{f}_{sun}(\nu, T_{sun}, \Omega_{sun}, C) d\nu}{C f_w \sigma T_{sun}{}^4} \right]. \quad (51)$$

The maximum theoretical efficiency calculated in this way is 68 % under one sun ($\Omega_{sun} = 6.85 \times 10^{-5} sr$), and 85 % under the maximum concentration of about $C = 45\,000$ suns.

2.6 Discussion

In this chapter, ultimate and detailed ideal efficiencies have been reviewed. The detailed-balance model for solar cells has been derived as in the original paper [10] and in a semi-analytical form. Both approaches – allowing for unavoidable losses such as: radiative recombination, electron thermalization, band gap selective absorption and taking into account the solid angle subtended by the sun – showed similar results.

The semi-analytical model, one of the easiest ways to calculate detailed-balance efficiency, has been applied to third-generation devices: tandem cells and infinite stacks of cells. The highest efficiency for a tandem cell under one sun was approximately 42 %. This shows that third-generation cells can be extremely efficient; three-junction solar cells from Boeing Spectrolab show practical efficiencies > 40 %.

The real challenge now, for a massive integration of photovoltaic systems and widespread use, is not making converters more efficient but finding ways to achieve such high efficiencies using cheaper materials.

Chapter 3

Solar cell modelling and design

As demonstrated in the previous chapter, solar cell efficiencies can be modelled using the Shockley-Queisser detailed-balance model or other models derived from it. These models give an understanding of the basic mechanisms of solar cells, but at a research level they are not adequate to describe the detailed behaviour of practical devices. Common solar cells show weaknesses in carrier collection associated with defects in the material, dead layers and poor passivation of the cell surface. New models, based on investigations into the base (P side), emitter (N side) and depletion regions (Fig. 112), are required.

This chapter describes the modelling of a P-N junction solar cell under low dopant injection conditions [63]. Analytical current relations are derived for each part of the cell, and the effects of relevant solar cell parameters such as diffusion length and surface recombination on the device efficiency are discussed. The validity of this model is then verified using PC1D®, a R&D simulation software for solar cells.

The first section of the chapter treats non-ideal solar cell operation and "avoidable" cell losses. The second section introduces an enhanced cell ($n^+/p/p^+$ structure), designed at the Southampton University clean-room facilities, which reduces these avoidable losses. The resulting cell structure, with a shallow emitter, is analytically modelled in the third section.

3.1 Practical losses in solar cell operation

Real solar cells suffer not only from "unavoidable" losses but from "avoidable" losses of three types:

- optical (e.g. top surface reflection, shading by electrical contacts: fingers and bus bar)
- electrical (e.g. resistive losses associated with the fingers, at the contact between metal and silicon)
- non-radiative recombination (e.g. defect-assisted and Auger recombination).

Losses in solar cells have been reviewed in papers on high efficiency crystalline solar cells [64-65] and in specialized text books [4-5;17;59]. Fig. 126 gives an overview of the principal types of losses occurring in the operation of solar cells.

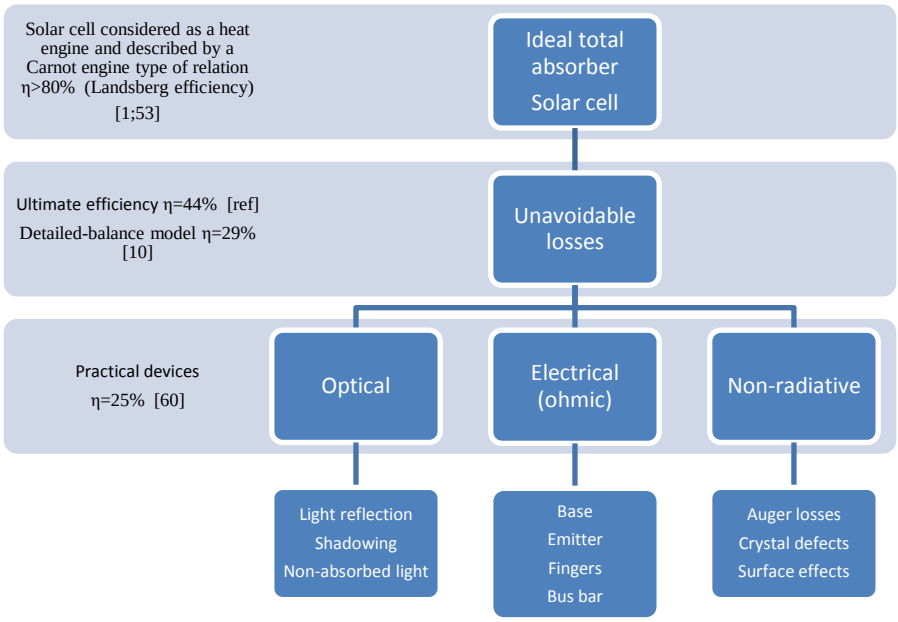

Fig. 126: Overview of the various losses occurring in the operation of crystalline solar cells.

Optical losses mainly affect the short-circuit current, reducing the number of photons that can be absorbed in the cell. These losses are of four types:

- Reflection – For bare silicon under daylight exposure, over 40 % of incident light is reflected. Lower reflection coefficients can be achieved with a single or double anti-reflection coating or by texturing the surface of the solar cell (Fig. 130).
- Shading – Shading by the grid reduces the probability of electron-hole pair generation. Reducing the cross-section of the fingers is not a solution since the resistivity of the metal bar depends on this cross-section.
- Cell thickness – If the cell is too thin, much light passes through without interacting with it. If it is too thick, the carriers have a greater distance to travel and can recombine before reaching the contacts. The optimum absorption thickness for c-Si, $0.8 - 0.9\ mm$ [4], is huge in comparison with other semiconductors (only $0.09\ mm$ is required with GaAs cells [38]).
- Metal contacts – Fingers in front of the solar cell block 5 to 15 % of incoming light depending on grid configuration; to avoid this loss some modern cells have no contacts on the top [66].

Contacts create resistance and influence the electrical output of the solar cell. Two types of electrical losses are usually present in a practical device:

- Shunt resistance ($R_{//}$) arises from point defects in the crystal and from current leakage along the cell edges. This can create disruptions in the P-N junction, principally affecting the open-circuit voltage and the fill factor.
- Series resistance (R_s) occurs in silicon because of its own resistivity, in the contact metals and at every contact point between materials. Series resistance is related to structure and design parameters, e.g. choice of material, size and spacing between fingers.

Radiative recombination (unavoidable losses) and non-radiative recombination (avoidable losses) of electron-hole pairs occur throughout the solar cell, but in certain regions other losses dominate (Fig. 127):

- Surface recombination occurs at the front and back of the cell where the silicon surface contains many defects, e.g. dangling bonds, introducing allowed energy levels where electron-hole pairs can recombine.
- Defect recombination occurs mainly in the space-charge region (junction) and in the N-layer, where defect levels are introduced during the emitter diffusion.
- Auger recombination occurs in the highly doped region (usually the N layer).

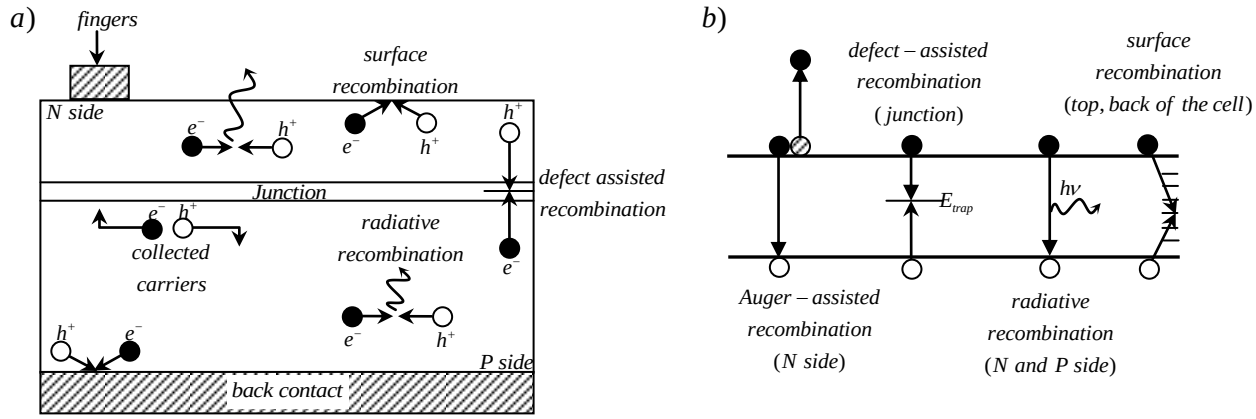

Fig. 127: Recombination losses in a solar cell: a) diagram of an actual cell (arrows indicate charge movements); b) energy diagram of the principal recombination process (arrows indicate electron or hole transitions). (Figures adapted from Refs. [59] and [15])

3.1.1 Two-diodes model

Losses affect the electrical output of solar cells (*IV* curves). The easiest way to understand these losses is to model the cell as an electrical circuit: the two-diodes model.

In contrast to the ideal solar cell considered in Fig. 114, an actual solar cell can be modelled as a current source I^{ll} in parallel with two diodes and a resistor $R_{//}$, and in series with a resistor R_s [17;59]. The first diode models an ideal P-N junction, the second one models the recombination in the depletion region [63] and the resistors model the electric losses within the solar cell (Fig. 128).

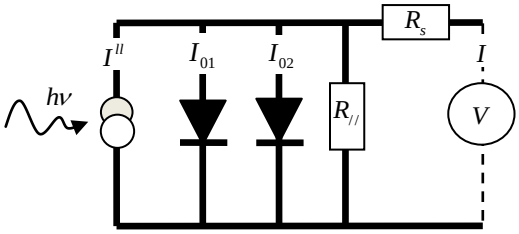

Fig. 128: Equivalent circuit for the two-diodes model of a real solar cell [4].

The current I passing through the load is given by:

$$I(V, R_s, R_{//}) = I^{ll} - I_{01}\left(e^{\left[\frac{V-IR_S}{kT}\right]} - 1\right) - I_{02}\left(e^{\left[\frac{V-IR_S}{2kT}\right]} - 1\right) + \frac{V-IR_s}{R_{//}}, \quad (52)$$

where I^{ll} is the current generated under illumination, I_{01} is the current in the first diode and I_{02} is the current in the second diode. The effect of ohmic losses can be modelled in *IV* curves by varying the series and shunt resistances in the diode model, as illustrated in Fig. 28:

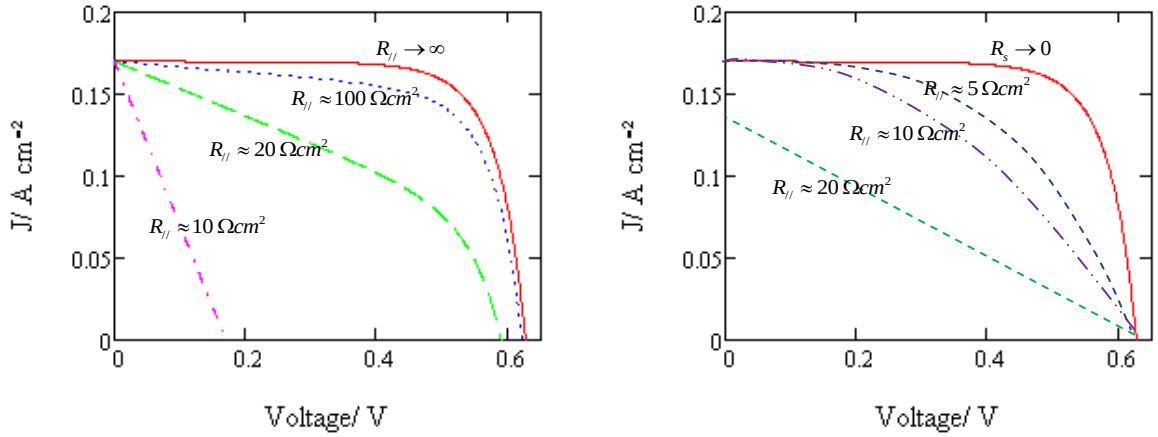

Fig. 129: Effect of series resistance (left) and shunt resistance (right) on the *IV* characteristics of a solar cell. These plots show that high shunt resistance and low series resistance are essential to the conservation of the fill factor.

The two-diodes model is re-used in Chapter 6 to characterize the *IV* curve of the solar cell coupled to the fluorescent collector.

3.2 Design considerations and modern solar cell structure

In real solar cells, minimizing avoidable losses and keeping *IV* parameters as close as possible to their theoretical limits are accomplished through cell design, with materials and dimensions chosen to optimize cell performance.

Modern solar cells are usually N-P rather than P-N structures, because N-type diffused silicon has a higher surface quality than P-type diffused silicon, and because electron mobility is higher in P-doped (e.g. boron-doped) silicon than is hole mobility in N-doped (e.g. phosphorous-doped) silicon [38]. As a consequence of the low mobility of holes, the emitter is designed to be shallow and heavily doped (e.g. $1 \times 10^{19}\ cm^{-3}$ of boron) in order to reduce resistivity losses.

3.2.1 Junction depth and cell thickness

Cell thicknesses between $200\ \mu m$ and $500\ \mu m$ are typical in the fabrication of c-Si cells [38]. The junction in a solar cell is shallow, between $0.5\ \mu m$ and $1\ \mu m$ so that a large fraction of the carriers generated by the high-energy photons are created within a diffusion length of the P-N junction.

Cells are usually made with a thick, lightly doped (e.g. $1 \times 10^{14}\ cm^{-3}$ of phosphorous) P base which absorbs low-energy photons.

3.2.2 Highly doped regions, $n^+/p/p^+$ structures

Solar cells have now evolved towards a $n^+/p/p^+$ structure, where $^+$ indicates a highly doped region. The highly doped emitter has a lower resistivity while the extra p^+ layer acts as an electrical "mirror", repelling the electrons inside the built-in electric field.

Care must be taken in using highly doped materials because localized high dopant concentrations can lead to dead layers, where losses such as Auger recombination dramatically decrease the lifetime of the generated charges [67].

3.2.3 Contacts

The series resistance of the front contact grid is reduced by ensuring clean and passivated surfaces at the metal/silicon interface. Series resistance and shadowing losses are usually difficult to include within such a complex model, which also includes losses due to the grid shadow, losses in grain boundaries due to the metal/semiconductor contact, power dissipated in the resistance of layers between the bars, and losses in the grid metallization. A standard technique consists in evaporating different aluminium grids onto each wafer and characterizing the cell experimentally after fabrication [68].

3.2.4 Light-trapping scheme and anti-reflection coatings

The front surface is usually coated with an anti-reflection layer to decrease the reflectivity of silicon. TiO_2 ($70\ nm$) and MgF_2 ($110\ nm$) are applied on top of the cell as an anti-reflection coating. Conjointly, light-trapping schemes such as pyramidal structures can be formed on silicon to increase absorption efficiency (Fig. 130). Anti-reflection coatings are crucial to the efficient operation of a solar cell since these layers also passivate the surface of the cell.

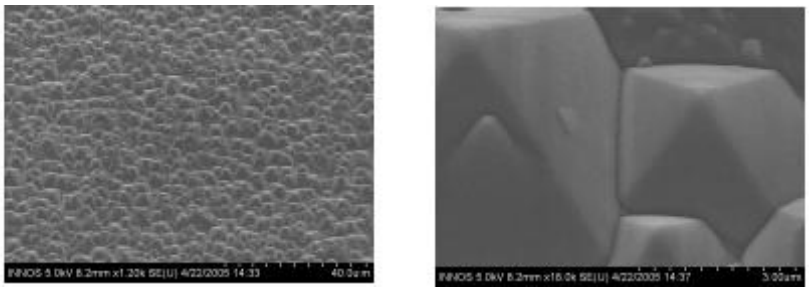

Fig. 130: Light-trapping structures: scanning electron micrograph (1.5% KOH at 70°C for 60 mins) of c-Si surface texture, carried out at Southampton University (2nd cell batch 2005). (Joint work with S. Boden and D. Bagnall)

3.2.5 Enhanced structure

Taking into account all the parameters reviewed in this section, the structure of a modern, high-efficiency c-Si solar cell can be represented as in Fig. 30.

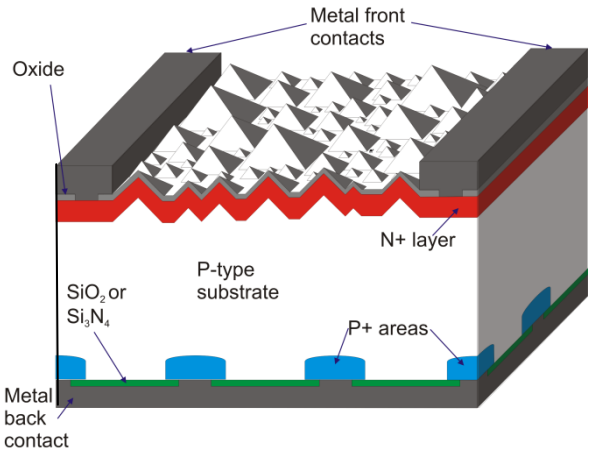

Fig. 131: Structure of an efficient c-Si solar cell, showing an $n^+/p/p^+$ configuration with a light-trapping scheme. Fabrication of such cells was initiated at the University of Southampton. (Figure reproduced from Ref. [69])

The starting material was monocrystalline wafers of P-type silicon of thickness $400\ \mu m$, with (100) surfaces and resistivities of 1 to 3 $\Omega\ cm^{-1}$. Phosphorus diffusion times were varied for the six wafers (60 to 180 mins) with a temperature diffusion of 800˚C. Each wafer contained 42 one-cm^2 solar cell devices, the spacing and width of the top contacts being varied for each cell. Details on this batch can be found in Ref. [69].

This design (2nd cell batch 2005, S. Boden, D. Bagnall and T.J.J. Meyer) of a highly efficient solar cell was in the final stage of fabrication at the INNOS clean room when a fire destroyed the facilities. The cells to be coupled to the fluorescent collector were subsequently purchased from Solartec rather than being developed at the university.

3.3 Modelling

The P-N junction cell shown in Fig. 131 can be modelled using the physics of charge transport in semiconductor materials. In this section a simple quantum efficiency model is developed and the effects of crucial parameters, e.g. surface recombination and diffusion length, are examined. Section 3.3.1 presents the characteristics of the modelled cell, Section 3.3.2 deals with the physics of charge transport and Section 3.3.3 describes its application to the cell structure.

3.3.1 Modelled cell structure

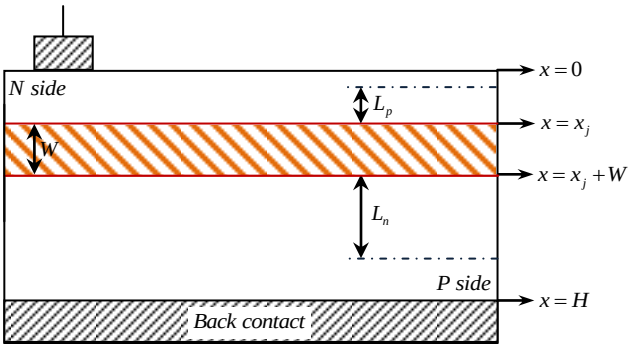

Fig. 132: Schematic of a typical c-Si solar cell showing the shallow N layer, the thick P doped base and the depletion region (orange hatching). W, L_n and L_p are the depletion region thickness and the diffusion lengths of electrons and holes, respectively.

The modelled cell structure resembles the device shown in Fig. 131. For simplicity the p^+ regions and optical effects due to the textured surface are not considered. The cell consists of three regions: a quasi-neutral N region from $x = 0$ to x_j, a depletion region from x_j to $x_j + W$ and a quasi-neutral P region from $x_j + W$ to H.

3.3.2 Charge transport in a semiconductor

The charge transport in a solar cell is often described by the variation in concentration of minority carriers at each side of the junction. For the P side, the change in hole concentration under illumination is relatively small, whereas the change in electron density is quite large. For this reason scientists usually prefer to work with minority carriers.

3.3.2.1 Continuity equation

Under illumination, conduction phenomena (i.e. drift and diffusion current) coexist with the generation and recombination of electron-hole pairs [70]. These effects must be taken into account in describing the conduction process since the recombination or generation of electrons can cause variations in carrier distribution. The continuity equations for holes and electrons can be written in the form [38]:

$$\frac{dJ_{tota\ l_n}(x)}{dx} \cdot \frac{1}{q} + G_n - \Re_n = 0, \tag{53}$$

$$-\frac{dJ_{tota\ l_p}(x)}{dx} \cdot \frac{1}{q} + G_p - \Re_p = 0, \tag{54}$$

where the subscripts p and n refer to holes and electrons: G_n, G_n, $\Re_n$ and $\Re_p$ are, respectively the electron generation rate, hole generation rate, electron recombination rate and hole recombination rate; x measures depth in the solar cell.

The total current density for electrons ($J_{tota\ l_n}(x)$) or holes ($J_{tota\ l_p}(x)$) is the sum of the drift and diffusion currents:

$$J_{tota\ l_p} = \overbrace{-q \cdot D_p \cdot \frac{d[p]}{dx}}^{\text{diffusion}} + \overbrace{q[p(x)] \cdot \boldsymbol{\mu}_{\mathrm{n}} \cdot \vec{E}(x)}^{\text{drift}}, \tag{55}$$

$$J_{tota\ l_n} = +q \cdot D_n \cdot \frac{d[n]}{dx} + q[n(x)] \cdot \boldsymbol{\mu}_{\mathrm{p}} \cdot \vec{E}(x), \tag{56}$$

where $[p]$ and $[n]$ are the concentrations of holes and of electrons, D_n the diffusion coefficient for electrons, D_p the diffusion coefficient for holes, $\boldsymbol{\mu}_{\mathrm{n}}$ the electron mobility and $\boldsymbol{\mu}_{\mathrm{p}}$ the hole mobility. The diffusion coefficient is linked to the diffusion length by the relation $L = (D\tau)^{1/2}$ where τ is the lifetime of charge carriers.

3.3.2.2 Poisson's equation

Poisson's equation, derived from Maxwell's equations, relates the static electric field $\vec{E}$ to the space-charge density ρ:

$$-\frac{d\vec{E}}{dx} = -\frac{\rho}{\varepsilon_0 \varepsilon_s}. \tag{57}$$

In the simplified, one-dimensional form of the Poisson equation presented here, ε_o is the permittivity of the vacuum and ε_s is the permittivity of the semiconductor. Considering the contributors to charge density in a semiconductor, each electron in the conduction band gives a

charge $-q$, and each hole in the valence band returns a charge $+q$. Because a donor impurity has a net positive charge, and taking similar account of the acceptor impurities, which give a negative charge, the space-charge density ρ may be expressed as:

$$\rho = q([p] - [n] + [N_D^+] - [N_A^-]), \tag{58}$$

where $[N_A^-]$ and $[N_D^+]$ are the densities of ionized donors and acceptors, respectively.

3.3.2.3 Charge carrier generation and recombination rates

The generation of charge carriers depends on both the energy of the incident photons and the thickness of the solar cell. The generation rate is the product of: the absorption probability at a certain depth given by Beer-Lambert law, the flux of incident photons per unit bandwidth. Considering the reflectivity of the solar cell:

$$G(\lambda, x) = \alpha(\lambda)\dot{f}_s(\lambda, T_s)[1 - \mathbb{R}_{cell}(\lambda))]e^{(-\alpha(\lambda)\cdot x)}, \tag{59}$$

where $\mathbb{R}_{cell}(\lambda)$ is the solar cell's reflection coefficient.

On the other hand, the recombination rate for minority charge carriers can be obtained from the carrier lifetimes. For holes,

$${}^N\mathfrak{R}_p = \frac{[{}^N p] - [{}^N p_0]}{\tau_p}, \tag{60}$$

and for electrons,

$${}^P\mathfrak{R}_n = \frac{[{}^P n] - [{}^P n_0]}{\tau_n}. \tag{61}$$

The superscript indicates the region of the cell where the equation is applicable, e.g. ^{N}x indicates that the variable x is being considered in the N region. As expressed above, the recombination rate of excess minority carriers is valid for low doping concentrations [63]. The differences $[{}^P n] - [{}^P n_0]$ and $[{}^N p] - [{}^N p_0]$ represent the densities of excess minority carriers.

3.3.3 Internal quantum efficiency

The quantum efficiency of the cell (Fig. 33) can be derived using the continuity equation, Poisson's equation and the generation/recombination relations for electron-hole pairs. The quantum efficiency is the probability of electron-pair generation per incident photon. In order to avoid complex numerical integrations and maintain a simple view of the process, several assumptions are made:

- Dopant concentrations are uniform on both sides of the junction [38].

- The emitter is lightly doped, with recombination rates for charge carriers defined by Eqns. (60) and (61) [63].
- The junction is free of interface states [70].
- The junction is abrupt, i.e. the electric field is negligible on the P and N sides. This approximation divides the solar cell into three blocks: the depletion region, the quasi-neutral N region (QNN) and the quasi-neutral P region (QNP).

Using these approximations and combining relations (53) to (61), the current contributions of minority carriers on either side of the junction can be expressed as a set of differential equations:

$$D_p \frac{d^2[p(x)]}{dx^2} + \alpha(\lambda)\dot{f}_s(\lambda, T_s) \cdot [1 - \Re_{cell}(\lambda)] \cdot \exp^{[-\alpha(\lambda)\cdot x]} - \frac{[^N p] - [^N p_0]}{\tau_p} = 0 \,, \tag{62}$$

$$D_n \frac{d^2[n(x)]}{dx^2} + \alpha(\lambda)\dot{f}_s(\lambda, T_s) \cdot [1 - \Re_{cell}(\lambda)] \cdot \exp^{[-\alpha(\lambda)\cdot x]} - \frac{[^P n] - [^P n_0]}{\tau_n} = 0 \,. \tag{63}$$

To solve these differential equations we apply the superposition principle, resolve the homogeneous equation add the particular solution to finally obtain a set of analytical solutions describing the current densities in a P-N junction.

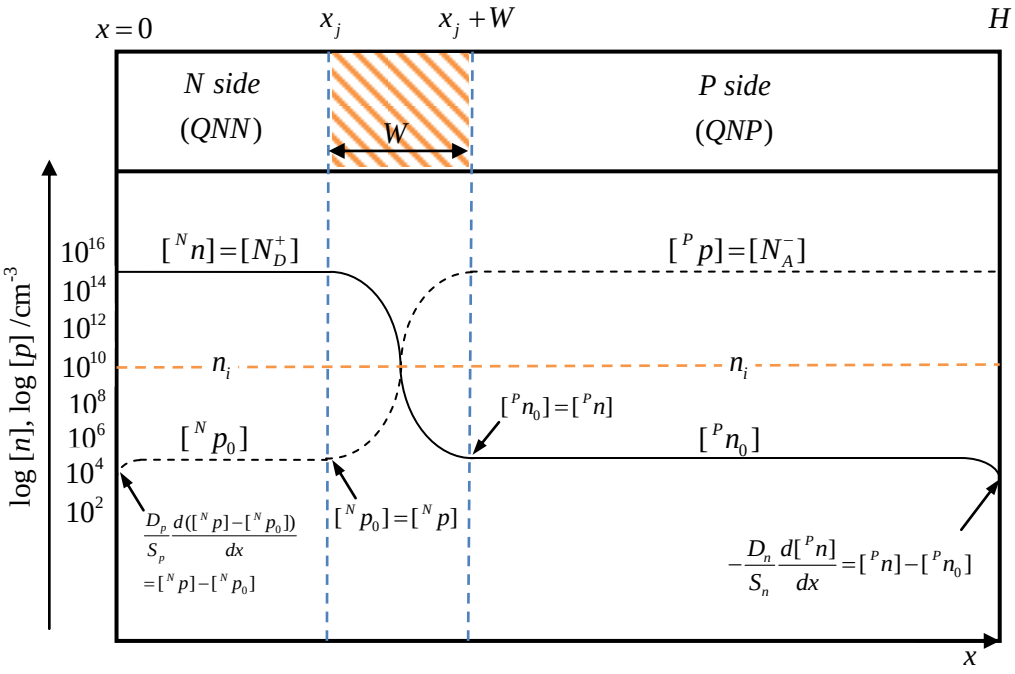

Fig. 133: Structure of the modelled solar cell, superimposed on the charge carrier distribution across the cell (approximate curves). S_p, S_n are the surface recombination velocities. (Figure adapted from Ref. [4])

Fig. 133 shows:

- the structure of the cell superimposed on the charge carrier distribution across the cell (approximate curves)
- the boundary conditions for resolving Eqns. (62) and (63).

Combining the boundary conditions with the differential equations (62) and (63), the analytical solution for current density on the N side of the junction at x_j is:

$$ {}^{N}J_p(x_j) = \frac{qL_p\alpha\dot{f_s}\cdot[1-\mathbb{R}_{cell}]}{{L_p}^2\alpha^2-1}\cdot\left[\frac{\left(\frac{S_pL_p}{D_p}+\alpha L_p\right)-\exp^{(-\alpha x_j)}\left(\frac{S_pL_p}{D_p}\cosh\left(\frac{x_j}{L_p}\right)+\sinh\left(\frac{x_j}{L_p}\right)\right)}{\frac{S_pL_p}{D_p}\sinh\left(\frac{x_j}{L_p}\right)+\cosh\left(\frac{x_j}{L_p}\right)}-\alpha L_p\exp^{(-\alpha x_j)}\right]. \quad (64) $$

The solution for current density on the P side at $x_j + W$ is:

$$ \begin{aligned} {}^{P}J_n(x_j+W) &= \frac{L_nq\alpha\dot{f_s}\cdot[1-\mathbb{R}_{cell}]}{{L_n}^2\alpha^2-1}\cdot\exp^{(-\alpha(x_j+W))}\times \\ &\left[L_n\alpha-\frac{\frac{S_nL_n}{D_n}\left(\cosh\left(\frac{H'}{L_n}\right)-\exp^{(-\alpha H')}\right)+\sinh\left(\frac{H'}{L_n}\right)+\alpha L_e\exp^{(-\alpha H')}}{\frac{S_nL_n}{D_n}\sinh\left(\frac{H'}{L_n}\right)+\cosh\left(\frac{H'}{L_n}\right)}\right], \end{aligned} \quad (65) $$

where H' is the thickness of the base, $H' = H - x_j + W$.

The current density in the space-charge region is easier to derive because the high electric field pushes out the generated carriers before they have time to recombine. The generated photocurrent is then the sum of all photons absorbed between x_j and $x_j + W$:

$$ {}^{DR}J = q\dot{f_s}(\lambda, T_S)\cdot[1-\mathbb{R}_{cell}(\lambda)]\exp(-\alpha x_j)[1-\exp(-\alpha W)]. \quad (66) $$

The junction of a solar cell is typically a few micrometers thick; only a small amount of current is generated in the depletion region.

The total current of a cell is the sum of the photocurrent created in the base and in the space-charge region of the emitter [63]. The internal quantum efficiency $IQE(\lambda)$ of a cell is the total photocurrent, as a function of wavelength, divided by the number of photons entering the cell and by the elementary charge [38]:

$$ IQE(\lambda) = \frac{{}^{P}J(\lambda)+{}^{N}J(\lambda)+{}^{DR}J(\lambda)}{q\dot{f_s}(\lambda,T_s)[1-\mathbb{R}_{cell}(\lambda)]}. \quad (67) $$

Quantum efficiency (Eqn. (67)) can be plotted as a function of wavelength for various parameter values using MatLab 6.5® software, as presented in the following figures. Cell dimensions, doping concentrations, junction thickness and average carrier lifetimes used in the following computations are reported in Table. 3.

Table 3: Input of the model (the cell dimensions correspond to a batch of solar cells fabricated in the Microelectronic Fabrication Unit at Southampton University [6], lifetimes and surface recombination velocities parameters corresponding to a classical c-Si solar cell were taken from Ref. [38], the reflectivity of the cell was not taken into account.

$x_j\ (\mu m)$	$H\ (\mu m)$	$S_p\ (cm\ s^{-1})$	$S_n\ (cm\ s^{-1})$	$\tau_n\ (\mu s)$	$\tau_p\ (\mu s)$	$[N_D^+]\ (cm^{-3})$	$[N_A^-]\ (cm^{-3})$
0.5	450	1×10^4	1×10^5	10	0.4	5×10^{19}	1.5×10^{16}

The results of the computation are shown in Fig. 134.

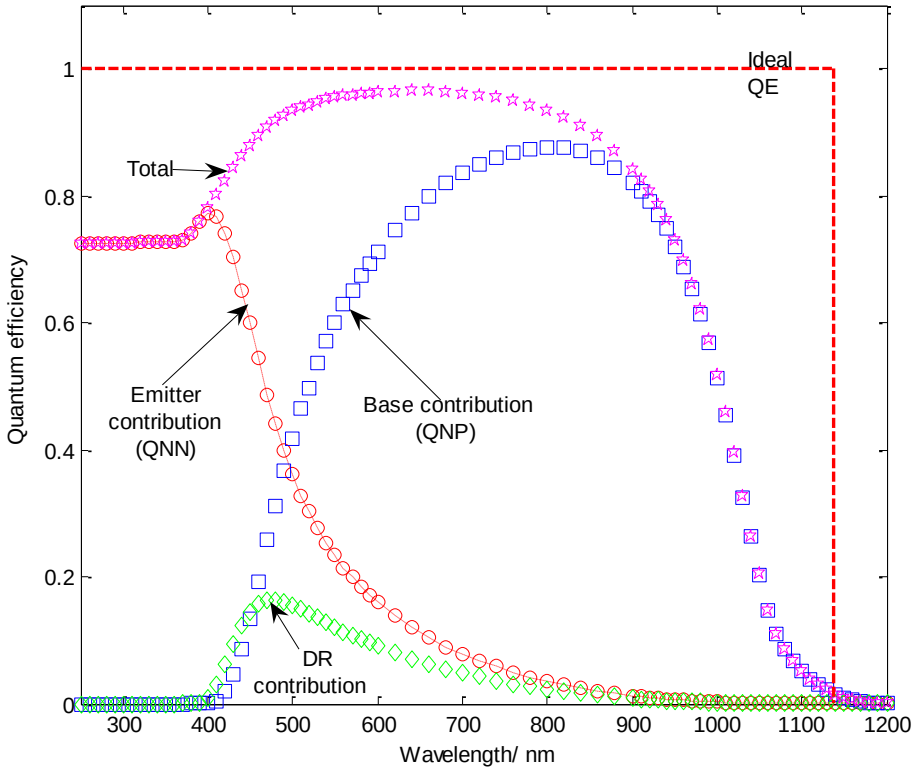

Fig. 134: Internal quantum efficiency, showing the contributions from each cell region (QNN, QNP and depletion regions), compared with the response of an ideal cell.

The figure shows that low-energy photons are absorbed in the base and high-energy photons in the emitter. Indeed, as pointed out previously, photons at low energy need a long travel path in the silicon in order to be absorbed, while high-energy ($< 450\ nm$) photons can directly excite carriers in the emitter.

3.3.3.1 Model validity

The validity of the analytical model derived in this chapter was checked against PC1D®, a commercial software programme which solves fully coupled non-linear equations for one-dimensional transport of carriers in crystalline silicon solar cells. Fig. 135 compares the results of the programme and the analytical model, using a uniform doping profile. Identical parameters were supplied to the model and to the software; the diffusion lengths and diffusion coefficients are listed in Table. 4.

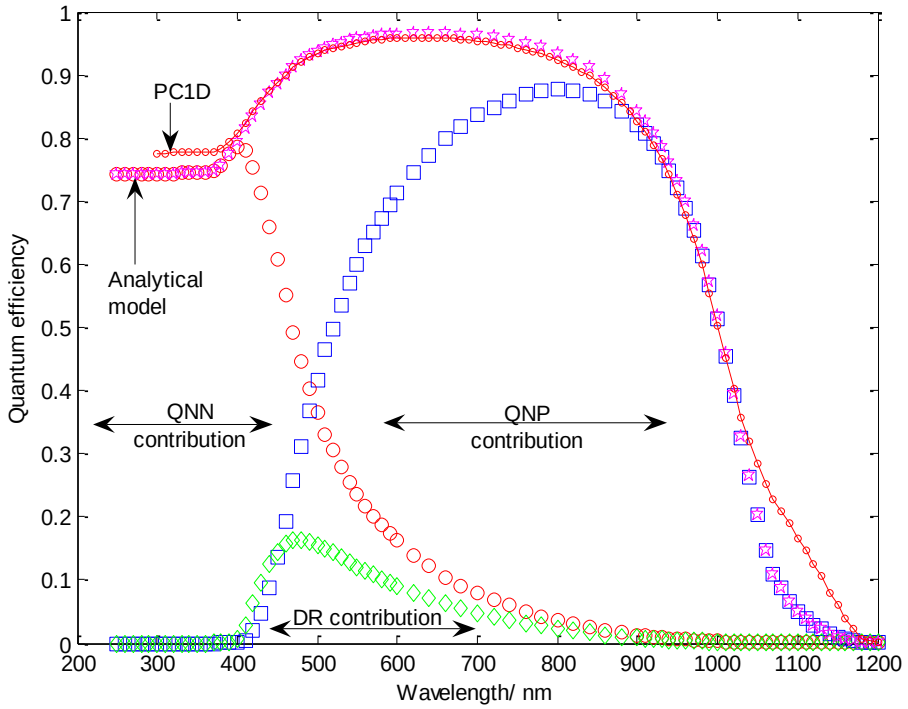

Fig. 135: Analytical IQE model compared with PC1D® results. The analytical model fits well with the PC1D® computation. The discrepancy in the 1000-1200 *nm* region is the result of assumptions made in Section 3.3.3.

Table 4: Diffusion lengths and diffusion coefficients [6;38]

$W\ (cm)$	$L_p\ (cm)$	$L_n\ (cm)$	$D_n\ (cm^2 s^{-1})$	$D_p\ (cm^2 s^{-1})$
2.85×10^{-5}	7.24×10^{-4}	1.76×10^{-2}	34.96	1.43

The analytical model agrees well with PC1D® for a uniform doping profile. The minor discrepancies observed in the 300-400 nm and 1100-1200 nm regions comes from the fact that in both cases carrier generation near the top or bottom surface is important and the finer details of the bands are not well reproduced in the simple model.

In practice the doping profile of a solar cell is more complex (e.g. Gaussian or exponential). Under these conditions the analytical model loses its accuracy because heavy doping effects (e.g.

band-gap narrowing) affect the photocurrent collected in the emitter [67]. Nevertheless, the analytical model can be used to study solar cell parameters such as diffusion length and surface recombination under a uniform doping approximation.

3.3.3.2 Surface recombination and diffusion length effects

Fig. 136 illustrates the effect of poor passivation on the top of the solar cell. For surface recombination velocities $< 100\, cm\, s^{-1}$, internal quantum efficiency shows a nearly ideal response, while for higher values the current response of the emitter decreases dramatically. The effect of electron diffusion length on the efficiency of the base is highlighted in Fig. 137. A shorter electron diffusion length decreases the photocurrent generated by the base. Other parameters are unchanged from those shown in Fig. 33.

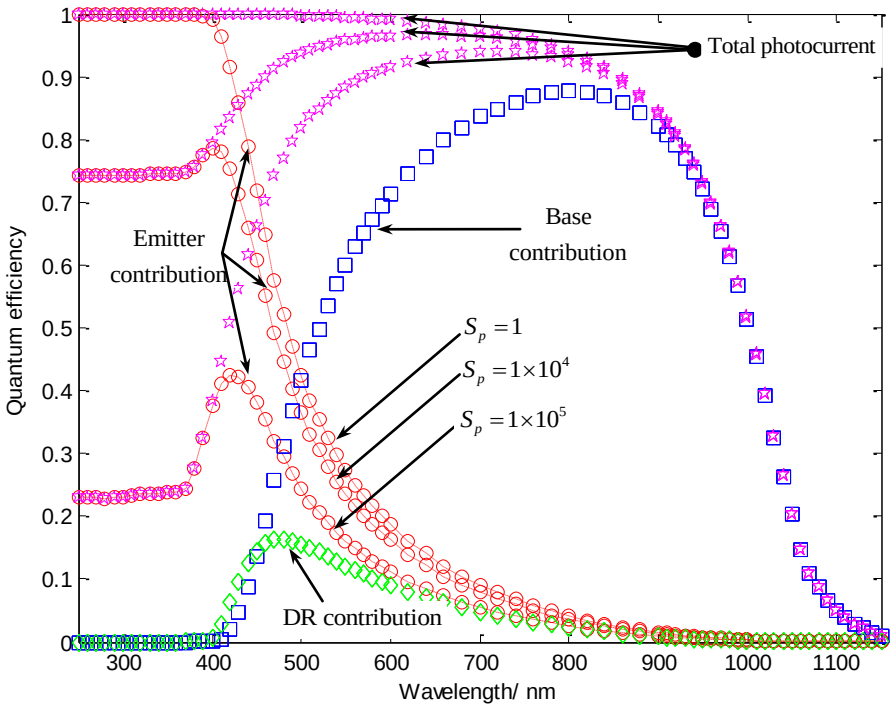

Fig. 136: Effect of a high surface recombination velocity on the internal quantum efficiency. S_p is in units of $cm\, s^{-1}$ in this graph.

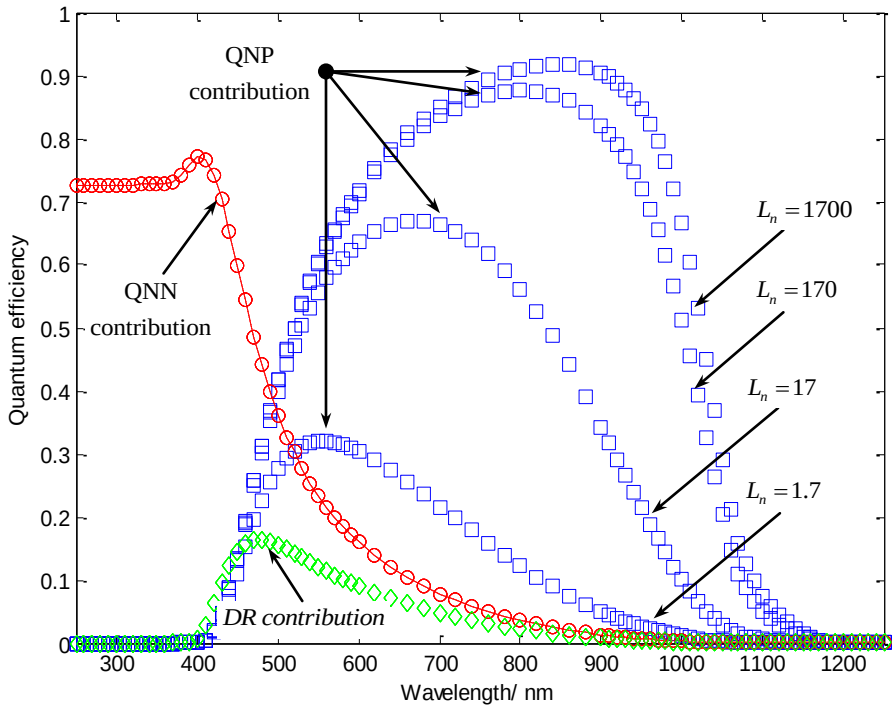

Fig. 137: Effect on internal quantum efficiency of changing the electron diffusion length. L_n is in units of μm in this graph.

3.4 Discussion

The essence of solar cell operation, rather than accurate numerical modelling, has been the subject of this chapter, which has examined losses of a "practical" nature that limit cell operation. Modern cells are being designed to minimize such losses. Light-trapping structures such as anti-reflection coatings and pyramids are commonly used to reduce reflection losses. Electrical losses can be reduced with highly doped emitters and back field regions. Shading losses can be reduced using laser-grooved contacts. Such modifications can lead to actual c-Si cell efficiencies of up to 25 %, only few percent lower than the theoretical limit.

The importance of charge carrier diffusion length and front surface passivation have been highlighted using an analytical model for the current relations in each part of the cell. Clearly, to make a good solar cell, a long carrier diffusion length and a well passivated surface are essential. The validity of the model, resting on uniform doping, has been verified using PC1D® software, and it has been shown that a full numerical treatment gives similar results.

Despite its low absorption coefficient, crystalline silicon is a very good electronic material; it is not uncommon to measure solar cell quantum response cells exceeding 95 % for incoming light within the wavelength region $500 - 600\ nm$.

The next chapter introduces the concept of the fluorescent solar collector, which makes use of the excellent electronic characteristics of c-Si and bypasses the absorption issue by separating photon absorption from electron generation.

Chapter 4

Fluorescent solar collectors

Fluorescent solar collectors (FSCs) represent an attractive photovoltaic technology for solar energy conversion as they have the potential to decrease the size of solar cells substantially, thereby reducing the overall system costs. First introduced by Weber and Lambe [7], fluorescent solar collectors were extensively studied in the 1980s. However, as a result of a lack of suitable materials, especially fluorophores, research on FSCs nearly stopped in the 1990s. This research has restarted only recently, following the discovery of new fluorophores [71], quantum dots [72] and photonic band-stop filters [12]. This chapter reviews the concept of FSCs and developments in their design since their beginnings in 1976.

4.1 FSC, a simple concept

Fluorescent solar collectors concentrate incident sunlight to make optimal use of a fixed area of solar cells. As noted in the introduction, FSC operation relies on four mechanisms: light absorption, light emission, light propagation and the conversion of light into electricity. When a collector (orange slab Fig. 138a) is exposed to sunlight, incident photons are absorbed and subsequently re-emitted at longer wavelengths (Chapter 1). A large fraction of the re-emitted light is trapped within the collector because the refractive index of the collector material (matrix) is higher than that of the surrounding medium. This trapped light is then delivered by total internal reflection to solar cells at the edges of the collector, where it is converted to electricity. The collector (also called the absorber) is generally composed of a mixture of fluorescent dyes embedded in a transparent medium such as PMMA (acrylic), glass or even a liquid solution.

Broad absorption of the incident light is achieved by the use of an appropriate mix of dyes. This mix is crucial in the fabrication of a good FSC device. For optimal absorption of solar radiation the emission region should be spectrally narrow [8] and as close as possible to the semiconductor wavelength band gap λ_g. At the same time, it is important to ensure that this emission region is absorption-free as shown in Fig. 37b.

In practice, FSC efficiency, defined in section 4.3 of this chapter, drops off with increasing dye concentration because the latter gives rise to increasing re-absorption losses (Section 4.5) as a result of the overlap between fluorescence and absorbance bands. We may also note that, according to Kennard-

Stepanov's laws (Chapter 1), the bands of a given fluorophore are thermodynamically linked; and it is impossible to create a window completely free of absorption in a system that absorbs light efficiently [8;73].

Re-absorption of fluorescence is known to be the key factor limiting a collector's efficiency. For example, in a glass collector the photon collection probability at the edge of the collector drops by about half within four re-absorption events [7;73-74].

Various collector shapes [75] and designs (e.g. thin-film and collector-stack) have been suggested to improve photon transport capabilities [6;11;76]. Such designs will be reviewed in this chapter (Section 4.6) and their efficiency compared with tables drawn from the literature.

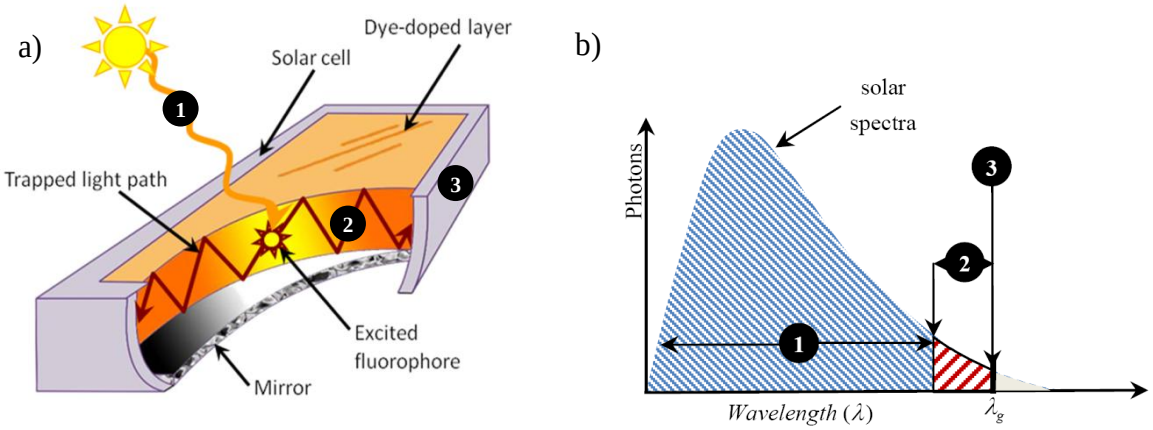

Fig. 138 : a) Cut-away view of a fluorescent solar collector, illustrating its primary mechanisms: ❶ light absorption, ✸ light emission, ❷ light propagation and ❸ conversion of light into electricity. The optical gain of this device is defined as the ratio $A_{front}\,/A_{edge}$, where A_{front} is the area of the fluorescent medium (orange) exposed to sunlight and A_{edge} is the area of the solar cells (grey) at the edge of the collector. b) Idealized spectral operation of a fluorescent solar collector: the absorption region ❶ (blue hatched area) stretches across most of the solar spectrum while the emission region ❷ (red hatched area) is narrow, absorption-free, and close to the band gap λ_g of the edge cells.

FSCs differ from other dye-sensitized solar cells, such as "Gratezel" cells in that the separation of charge carriers occurs within the semiconductor cell. The main difference between FSCs and classical solar cells is that photon absorption is separated from electron-hole pair generation – a major benefit when compared to standard c-Si cells, in which most of the semiconductor material is used for light absorption rather than for electricity generation [6].

4.1.1 Advantages of FSCs

The first advantage of FSCs is that they can exploit the diffuse light scattered in all directions from clouds. Since such diffuse light represents 60 % of surface illumination in northern Europe and in most regions of the USA [77], this does away with the constraints imposed by tracking systems, which are not

only subject to mechanical breakdown but also collect less energy annually than stationary tilted systems capable of collecting diffuse light [78].

Furthermore, FSCs can achieve high concentration gain factors because they are easily tuned. Using a 10 cm by 10 cm by 2.5 cm collector, for example, an optical concentration ratio of 100 is achievable. The concentration factor **G** (for gain) is defined as the ratio of the front-facing area to the edge area:

$$\mathbf{G} = \frac{A_{front}}{A_{edge}} \tag{68}$$

The use of a collector increases heat dissipation, a common source of loss in solar cells. The energy lost in red-shifting incident photons is distributed across the large area of the luminescent plate in contact with air rather than in the silicon solar cells [79].

A further advantage of FSCs is that front metal contacts, which can shadow up to 15 % of the cell's active area in conventional solar cells, are not an absolute requirement. A long solar cell can be designed with a contact bus outside the light-collecting area because light escapes in a narrow line. If fingers are present in the light-collecting area of the cell, any light incident on them will be reflected, with a chance of being re-absorbed by the dye and subsequently re-emitted towards the PV cell.

Finally, the choice of luminescent dye allows optimization of the frequency of the concentrated light for maximum spectral sensitivity of the edge light-converting device and of the front anti-reflection coating.

4.2 Historical development

The first application of the fluorescent collector concept was not to solar energy. The principle of dye-doped plastic films was used by Shurcliff, Jones and Garwin from 1949 to 1960 for radiance amplification in scintillation counters [80-81]. The first operational plastic radiation converter, designed by Keil for scintillation counters, appeared in the literature in the early 1970s [82].

The earliest application of the fluorescent collector concept in the field of solar energy was described in a 1973 grant proposal to the National Science Foundation put forward by Weilmenster, at that time working at MIT. The proposal was rejected and none of the MIT work was published; even Weilmenster's 1975 senior thesis, *Radiation transfer process in Rhodamine 6G/ methanol applied to solar energy conversion*, is not publically available.

The first journal publication describing the concept was written in 1976 by Weber and Lambe (*W&L*) [7]. Working for the Ford Motor Company's Scientific Research Laboratory, *W&L* proposed using inorganic dyes to harvest solar flux and redirect it onto small silicon solar cells. FSCs were at that time known as

"luminescent greenhouse collectors"; today the scientific community prefers "fluorescent solar collector" as it more accurately describes the physical processes occurring within the device. According to the *International Dictionary of Physics*, fluorescence is the "simultaneous radiation emitted as a consequence of the absorption of some other radiation", while the more general term luminescence refers to light emission arising from anything other than thermal excitation (Chapter 1).

The first operational FSC was described by Levitt and Weber in 1977 [83] and subsequently elaborated simultaneously by Zewail, Batchelder and Cole at the California Institute of Technology [74;84-88] and by Goetzberger and Greubel at the Fraunhofer Institute for Solar Energy in Germany [75-89]. Goetzberger was the first to introduce a third-generation FSC [90] based on spectral splitting (Chapter 3), using a stack of different collectors, a design reviewed in Section 4.6.

As noted in the introduction, the lack of suitable materials, especially fluorophores, brought research almost to a standstill in the 1990s, to restart only in the new millennium. The original research – carried out from 1977 to 1985, largely in American universities and research laboratories such as the Ford Research Laboratory – still offers a benchmark for present and future work. Since 2000, however, the primary research on the subject has been carried out in Europe.

The focus in the early years was on analytical models to predict the effect of re-absorption on collector efficiency [7;74;91;92], the study of various collector shapes [93] and matrix (collector material) losses [94]. It is now well established that re-absorption, also referred to as self-absorption (Chapter 1 and 8, and Section 4.5), is what limits the operation of fluorescent collectors, leading to practical efficiencies below 5 % (Section 4.3). Current research has shifted to overcoming the poor FSC efficiencies reported so far (Section 4.6). State-of-the-art collection techniques now include: energy transfer between dyes [95], photonic structures [12], photon management [73] and collectors doped with quantum dots [72;96-97].

4.3 Practical performance of FSCs

Despite the advantages of fluorescent collectors discussed here, over the last 30 years the overall experimental efficiency for a fabricated device has not exceeded 5 % [90]. It is difficult to compare the efficiencies of FSCs (η_{FSC}) -see Section 7.7.1 for analytical definition- because of variations in geometry, gain factor, dye doping, edge solar cell and design (e.g. thin-film, collector-stack). In addition, research groups present their results in various ways; some, for instance, examine collector efficiency (η_{col}) and extrapolate the expected efficiency of the whole device (FSC+PV) without attaching any solar cells, reporting overall efficiencies of up to 14.5 % [98]. However, practical measurements of efficiency with a cell coupled to the collector are well below the 10 % benchmark for potential industrial applications.

Table 5 lists the efficiencies of plate collectors using silicon solar cells as reported in the literature from 1981 to the present. The collectors are classified in terms of their gain.

Table 6 lists the efficiencies of plate collectors using GaAs cells. Because III – V semiconductors, having larger band gaps matching the frequency of the light emitted by standard fluorophores, (Chapters 7, Fig. 95), improved efficiencies are expected in these cases.

Table 5: Efficiencies of FSC plates coupled to a c-Si cell, as reported in the literature; the highest efficiency for a single plate collector is about 3 %. The colours in the table define a gain range, blue correspond to a gain >30, green gain 20-30, light red gain 10-20.

Year	Edge solar cell	Gain	Number of dyes	Efficiency (%)	Reference	
1981	c-Si	133	1	1.1	[75]	Gain >30
1982	c-Si	101	1	0.39	[92]	
1983	c-Si	68	1	1.3	[88]	
1983	c-Si	92	1	0.9	[86]	
1985	c-Si	62	1	2.3	[99]	
1985	c-Si	100	1	1.9	[99]	
1981	c-Si	28	1	1	[100]	Gain 20-30
1982	c-Si	28	1	1.5	[101]	
1983	c-Si	23	2	1.9	[88]	
1984	c-Si	20	1	1.4	[93]	
1985	c-Si	16	1	2.3	[99]	Gain 10-20
2008	m-Si	10	2	2.4	[102]	
2009	c-Si	12.5	1	2.4	[103]	
2009	c-Si	12.5	2	2.7	[103]	

The highest efficiency reported in Table 5 is 2.7 %, for a collector with a gain factor of 12.5. Collector efficiency tends to decrease as gain increases: with a high-gain collector, dye doping must be strong in order for sunlight to be absorbed within the thickness of the fluorescent plate, and strong doping in turn leads to re-absorption effects (Section 4.5, Chapters 5 and 7) and a drop in efficiency. Such limitations can be eased by using low-gain collectors since, for a given photon absorption, doping can be reduced by exploiting the collector thickness.

Table 6: Efficiencies of FSC plates coupled to $GaAs$ cells, as reported in the literature. The colours in the table define a gain range, blue correspond to a gain >30, light red gain 10-20, red gain < 10.

Year	Edge solar cell	Gain	Number of dyes	Efficiency (%)	Reference	
1984	GaAs	35	1	2.5	[93]	Gain >30
1985	GaAs	33	1	2.6	[99]	
1985	GaAs	33	1	4	[99]	
1984	GaAs	17	1	4	[93]	Gain 10-20
2008	GaAs	10	2	4.6	[104]	
2008	GaAs	2.5	2	7.1	[104]	Gain <10

Table 6 shows that efficiencies increase (by up to 7.1 %) when collectors are coupled to $GaAs$ cells. But while gain reduction and the use of $III - V$ semiconductors may increase efficiency, they also increase

overall costs, whereas the main argument for the use of fluorescent solar collectors is that they reduce costs through light concentration. It is alleged that for commercial applications the benchmark is an overall efficiency of ≈ 10 % with a light concentration factor of ≈ 20.

4.3.1 Origins of poor FSC performance

The practical efficiency of an operational FSC is less than the theoretical value calculated by Rau [105] and Markvart [8] because not all the incident daylight is absorbed, not all the absorbed light is re-emitted and not all the fluorescence reaches the edge mounted PV cell. The loss mechanisms in a collector can be classified into two groups: dye losses and photon transport losses.

i. Dye losses: organic and inorganic dyes have physical limitations including absorption bandwidth, quantum yield and photostability (Chapter 1). Because these losses are intrinsic to the dyes, their properties can only be modified through a new synthesis. The absorption band of an organic fluorescent dye typically covers 10 % to 15 % of the visible spectrum. One must therefore mix several dyes in order to harvest the maximum light, leading to self-absorption and, in many cases, to quenching of the fluorescence.
ii. Photon transport losses: these losses are associated with the transport of photons to the edge solar cell. Re-absorption, resulting from the overlap of fluorescence and absorption bands, dramatically reduces a FSC's performance (Chapter 5). Photon transport can also be affected by losses of a more practical nature, such as the roughness of the collector surface.

Loss mechanisms are surveyed in Section 4.5 of this chapter, but it is essential first to examine the optical requirements for an optimal fluorescent collector and compare these requirements with the properties of materials currently available.

4.4 Material requirements

A good FSC requires materials which absorb solar radiation efficiently and are also intensely luminescent in the region where the quantum efficiency of the PV cell is optimal. The dye and the matrix medium (the material forming the collector) are the two main components of a fluorescent collector. The following review presents the specifications of components needed for efficient collector design.

4.4.1 Dyes and pigments

The ideal dye has:

- long photostability, ideally 20 to 40 years
- strong absorption, preferably with a molar extinction coefficient $\xi(\nu) > 30\,000\ cm^{-1}M^{-1}$over the absorption band, so that the collector can be very thin

- a large absorption band across the UV/visible spectrum, ideally absorbing like a blackbody from $\approx 200\ nm$ up to $\approx 950\ nm$ (for a c-Si coupled solar cell [106])
- a narrow emission band near the infrared, ideally emitting from $\approx 950\ nm$ up to $\approx 1100\ nm$ (for a c-Si coupled solar cell [106])
- high quantum yield, ideally unity and temperature-independent
- no spectral overlap between absorption and fluorescent bands (no self-absorption of fluorescence, Chapter 5)
- high thermal resistivity, preferably up to $\approx 400\ K$
- Low cost and no toxicity.

No single inorganic or organic dye possesses all of these qualities. One must therefore trade off the advantages and disadvantages of the various dyes available on the market. The following sections examine inorganic and organic dyes for specific application to FSCs.

4.4.1.1 Inorganic dyes

The first fluorescent collector ever fabricated was doped with an inorganic dye (Nd^{3+}) [83]. Inorganic dyes have high thermal resistivity, and several rare-earth dyes are free of self-absorption. In addition, the photostability of many inorganic compounds is excellent, especially coloured minerals which do not fade for thousands of years.

Many inorganic dyes have been investigated, e.g. Pr^{3+}, Nd^{3+}, Sm^{3+}, Eu^{3+}, Tb^{3+}, Dy^{3+}, Ho^{3+}, Er^{3+}, Tm^{3+}, UO_2^{2+}, Yb^{3+} and Cr^{3+} [11;77;83]. The Cr^{3+} ion is certainly the most attractive because it shows two broad absorption bands, one at $450\ nm$ and the other at $650\ nm$, covering a major part of the solar spectrum with a fluorescence band free of re-absorption at $850\ nm$. The major drawback of this rare-earth ion is its low quantum efficiency, i.e. 17 % in silicate glass and 22 % in lithium lanthanum phosphate substrate.

Low quantum efficiency and weak absorption are the major disadvantages of inorganic compounds. They must therefore be used in high concentrations, which often leads to self-quenching of luminescence. A promising approach to this problem by B.C. Rowan and B.S. Richards [107] consists in coupling lanthanide ions with an absorbing antenna such as an organic dye, although improvements are yet to be demonstrated.

4.4.1.2 Organic dyes

Organic dyes show large variations in absorption and emission spectra, have very high extinction coefficients and frequently show quantum efficiencies close to unity, e.g. K1, 3655, Fluoroirot and R 101 [27;108]. Over their absorption bands organic dyes show strong isotropic absorption [109], making

organic fluorophores the ideal candidates for capturing daylight efficiently. Unfortunately, organic dyes are not photostable, and the few organic dyes with high quantum efficiency emit in the green-yellow spectral region, far from the c-Si band gap.

From a plot of fluorescence quantum efficiency versus emission wavelength for a range of available dyes (Fig. 139), it is clear that the longer the emission wavelength, the lower the quantum efficiency. Highly quantum efficient dyes ($\varphi \approx 1$) emit in the range $500 - 600\ nm$. From 600 to 700 nm the quantum yield of dyes averages around $\varphi \approx 0.6$, from 700 nm to 800 nm it drops to $\varphi \approx 0.4$, and beyond the limit of 800 nm, the band of most interest, the average quantum yield decreases to a low of $\varphi \approx 0.2$.

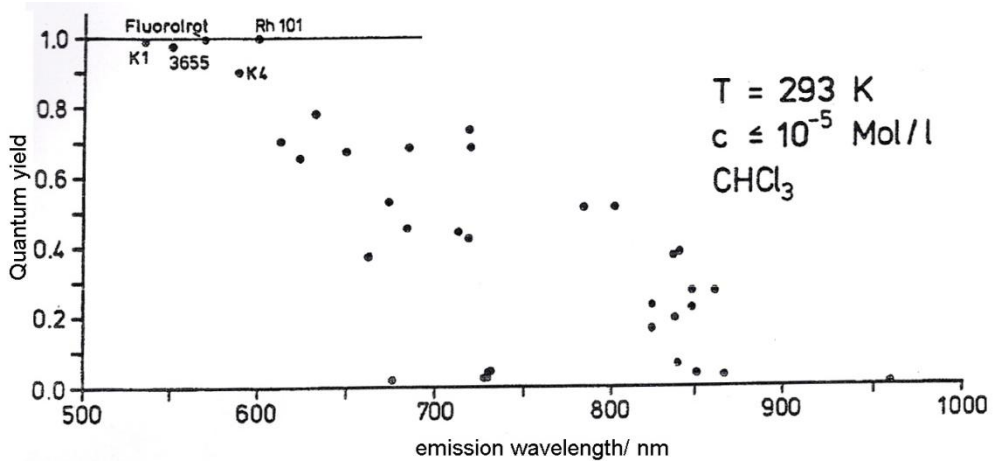

Fig. 139: Dye quantum yield as a function of emission wavelength (data taken from [110] and [90]).

Attempts have been made by BASF to synthesize a "black" dye – a fluorophore which is black in the visible region with a narrow emission band in the near infrared – but the results of this study [111] have not been published. Table 7 presents the main families of dyes with their respective emission colours, and Table 8 reviews the specifications of some selected fluorophores in more detail.

Table 7: Families of dyes available for FSC

Fluorescence	Dye family
Yellow-green	Rhodamine
Blue-green	Coumarin
Green	Perylene
Violet	Cresyl

The dyes in Table 8 are the principal organic chemicals used in the fabrication of FSCs over the last 30 years. The main reason for using these dyes is their high absorption coefficients coupled with high fluorescence quantum yields. The most commonly used ones are those that show the largest Stokes shift, limiting re-absorption losses (e.g. DCM-dye).

Table 8: The principal organic dyes used in fluorescent solar collectors. The usual

Dye name	$\xi(max)$ $(mol\,cm^{-1}L^{-1})$	Absorbance peak (nm)	Fluorescence peak (nm)	Stokes shift (nm)	Quantum yield
Coumarin 480 Coumarin 102	22 000	389	472	83	0.58 [112] Solvent: Ethanol
Coumarin 500	19 900	390	495	105	0.53 [112] Solvent: Ethanol
Coumarin 535 Coumarin 7	52 200	432	490	50	-
Coumarin 540 Coumarin 6	52 200	458	507	49	0.78 [112] Solvent: Ethanol
DCM-dye	28 900	465	636	171	0.71 [113] Solvent: DMSO
Rhodamine 560 Rhodamine 110	82 000	497	525	28	0.85 [114] Solvent: Ethanol
Rhodamine 575	93 800	517	546	29	-
Rhodamine 6G Rhodamine 590	107 000	528	555	27	0.98 [114] Solvent: Methanol
Rhodamine 610 Rhodamine B	114 000	544	571	27	0.5 [114] Solvent: Ethanol
Kiton red 620 Sulforhodamine B	111 000	556	580	24	0.83 [108] Solvent: Ethanol
Rhodamine 640 Rhodamine 101	106 000	566	594	28	[114] Solvent: Ethanol
Cresyl violet 670 Oxazine 9	57 900	592	622	30	0.54 [27] Solvent: Methanol
Oxazine 720	81 800	619	642	23	-
Oxazine 750	90 600	660	692	32	-
DODCI	238 000	583	605	22	-
DOTCI	236 000	677	714	37	-
IR 144	153 000	737	834	97	-

BASF laboratories are currently developing the best fluorophores for application in FSCs. In their reference system, any designation starting with K1 or F indicates a dye meeting specific requirements of fluorescent collectors [110;112]. Some recently synthesized dyes, the famous Lumogen series [71] (e.g. Frot 305, Forange 240), have been used in almost every fabricated collector since 2007 [73;103-104;115]. All Lumogen dyes show quantum yields > 0.95 in plastic plates [115-116] and strong absorption of light, are non-toxic, and have photostability guaranteed over 10 years provided they are shielded by a UV layer [71]. At the present time, the only limitations of organic dyes are their narrow absorption band and their small Stokes shift. Details and spectra of the Lumogen dyes are provided in Chapters 7 and 8.

4.4.1.3 Quantum dots

The technique of quantum dots (QD), developed primarily by L.E. Brus, shows promise for application to FSCs for several reasons. QD allows the emission wavelength to be tuned as a function of the dot diameter [115]. It offers high quantum yield (cadmium selenide/cadmium sulphide quantum dots have

shown a quantum yield of 80 % [117]), long photostability, and re-absorption can be reduced by altering the dots' separation in the matrix [118].

Qualitatively speaking, the band gap energy determining the frequency of light emission is inversely proportional to the quantum dot diameter. The larger the dot, the more red the fluorescence; the smaller the dot, the more blue it is.

Groups at the Dublin Institute of Technology [13;119] and Imperial College London [96;120-121] are pioneering QD doping of the FSC matrix. No breakthrough has yet been reported, as the technique appears to suffer from strong re-absorption issues. The only remarkable result appearing so far is the experimental observation of multiple excitons [122]. Photons of energy two to three times greater than the band gap of the quantum yield can lead to multiple emissions [115]. Under such conditions the quantum yield reported in [122] exceeds 300 %. However, multiple emissions under solar illumination have yet to be demonstrated.

4.4.2 Matrix materials

The principal requirements for a first class matrix medium are:

- crystal clarity, ideally 100 % optical transparency in the visible and near infrared
- chemical stability, ideally inertness
- formability (easily cast)
- high mechanical strength: a large FSC plate must support its own weight
- outstanding weather resistance (temperature fluctuation, wind, oxidation), ideally for 20–30 years
- low density, preferably < 1 $g\ cm^{-3}$, so that a 100 $cm \times 100\ cm \times 1\ cm$ sheet weighs < 10 kg
- low cost
- zero toxicity
- high refractive index (Section 5).

Again, no single inorganic or organic matrix meets all these requirements, although materials such as glass and PMMA come close. A comparison between organic and inorganic matrices is presented below.

4.4.2.1 Organic and polymeric matrices

Many optically transparent polymers (PMMA, MMA, PVC, polyvinyl alcohol, Tensol) have been synthesized for wave guidance, among other applications. Conveniently, the high solubility of organic fluorophores [123] in these polymers has made it possible to develop film and plate concentrators with good spectral characteristics [124]. Poly (methyl methacrylate) or PMMA, also known as Plexiglas or organic glass, is the polymer most commonly studied [92;125] and used in the fabrication of operating

fluorescent collectors [124-127]. It has more suitable optical properties than any other organic polymer. It is chemically stable, lightweight ($1.19\ g\ cm^{-3}$), and clearer than glass ($\alpha_{glass} \approx 1 \times 10^{-3}\ cm^{-1}$ over the visible spectrum). Studies have shown negligible degradation of its optical properties after 17 years of sunlight exposure in the desert [88].

PMMA is relatively cheap and easy to synthesize; there have even been attempts to co-polymerize it with organic dyes in order to make fully homogeneous slabs. Caution is needed when manufacturing PMMA collectors since their optical properties depend strongly on the manufacturing methods (e.g. die-casting, injection moulding and extrusion). Studies on the matrix fabrication process have shown that casting the medium by pouring it into a glass container and letting it dry in order to make a solid film (the process followed by most research groups) is not optimal. Characteristic solvent peaks in the FTIR (Fourier transform infrared spectroscopy) spectra of the dry plate indicate that the solvent does not evaporate completely, creating inhomogeneous plates with consequent scattering losses [37].

4.4.2.2 Inorganic matrices

Glassy ceramics (Spinel, B-quartz, Petalite-like) and glasses (silicate, phosphate, lithium lanthanum phosphate, lithium aluminium borate, lithium lime silicate, sodium lime silicate, aluminium phosphate, fluorophosphates, tellurite, phosphotungstate) are the most common inorganic matrices [11;77;109;128]. They offer transparent materials with refractive indices reaching $n = 2$ (silicon carbide $n = 2.7$, titanium dioxide $n = 2.5$, glass arsenic trisulphide $n = 2$), which reduces photon transport losses (Section 4.5). However, inorganic plates are often more expensive than organic materials, and are less popular because of fabrication constraints (e.g. the need for a furnace). In recent years nearly all the fabricated collectors reported in the literature were made from organic materials, or were thin-film organic materials deposited on a glass substrate.

4.5 Loss mechanisms in fluorescent solar collectors

Despite controversy in the 1980s over which loss mechanisms were responsible for limiting FSC efficiency, it is now apparent that the major cause of poor efficiency is incomplete absorption of sunlight coupled with re-absorption losses (Chapter 7). Absorption can be increased by raising dye concentrations and by mixing dyes with different absorption bands but, as already noted, in nearly all cases a higher dye concentration leads to reduced quantum yield, and the mixing of laser dyes leads to increased re-absorption losses as a result of the partial overlap of the absorption and fluorescence bands.

For a dye such as Rhodamine 101, which has a quantum efficiency equal to one, re-absorption as such does not represent a loss but a means of red-shifting the luminescence as it is re-absorbed (Chapters 7 and 8). However, re-absorption still has a critical impact on the FSC's operation because of escape cone loss.

4.5.1 Escape cone loss

The application of Snell's law at the air/collector interface shows that, as a result of internal reflection, light can escape from the surface only within a so-called escape cone. The probability of photons emitted after a re-absorption event is linked to the quantum yield; as we use dyes with quantum yields close to one, most absorbed photons are therefore re-emitted. But since re-emission occurs in all directions, photons may return in the direction from which they came, exit the medium within the escape cone or be re-absorbed.

For a glass collector there is a 25 % probability of fluorescence loss from the front face of the collector for each absorption/emission event [7]. After four re-absorptions followed by isotropic re-emission events, a photon has 50 % probability of escaping from the collector. This represents such a severe loss that in early models the photon was considered lost as soon as it was re-absorbed (Chapter 5).

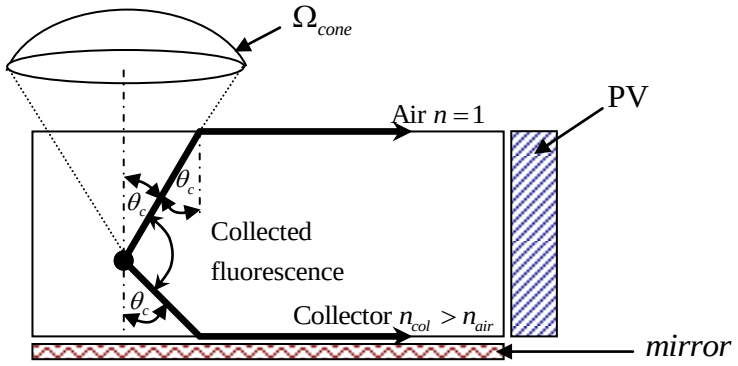

Fig. 140: Cross-section of a typical fluorescent collector showing the escape cone or critical cone:

$$n_{col}\sin\theta_c = n_{air}\sin(90°), \tag{69}$$

$$\theta_c = \sin^{-1}\frac{1}{n_{col}}. \tag{70}$$

The fraction P of untrapped photons is the ratio of the solid angle of the escape cone (Ω_{cone}) to that of a whole sphere ($4\pi\ sr$).

$$\Omega_{cone} = 2\pi(1-\cos(\theta_c)), \tag{71}$$

$$P = \frac{2\pi(1-\cos(\theta_c))}{4\pi} = \frac{1}{2}(1-\cos(\theta_c)). \tag{72}$$

Because light escapes from both faces of the slab, P in Eqn. (72) should be multiplied by two. Thus the fraction of photons escaping the collector is simply:

$$P = 1 - \cos(\theta_c). \tag{73}$$

Substituting Eqn. (70) into Eqn. (73), the fraction of trapped photons is:

$$P = 1 - \cos(\theta_c) = 1 - \cos\left(\sin^{-1}\frac{1}{n_{col}}\right) = 1 - \sqrt{1 + \frac{1}{n_{col}{}^2}}. \tag{74}$$

This assumes that the reflection coefficient within the escape cone is zero. The validity of Eqn. (74) has been verified using TracePro® ray-tracing software [129], taking into account Fresnel reflections inside the escape cone for every angle of light incidence; the results are shown in Fig. 141.

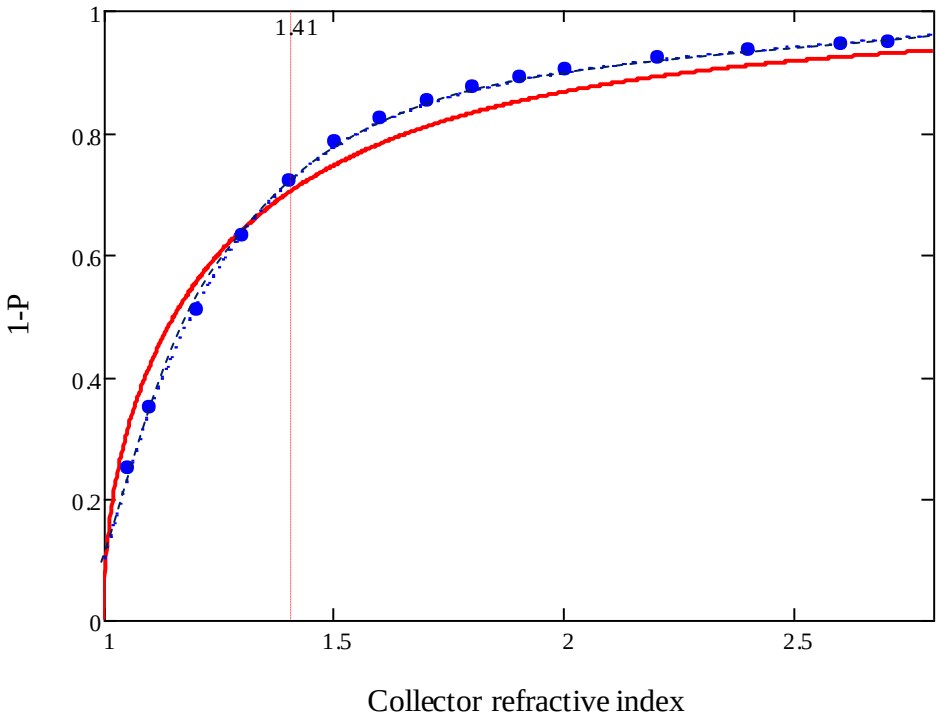

Fig. 141: Photon trapping probability (1-P) as a function of the collector refractive index n_{col} given by Eqn. (74) (red line) compared to ray-tracing simulations (blue dots). (Figure published in [129]).

Fig. 141 shows that the analytical relation (74) describes the photon trapping probability well for the most common materials (e.g. glass, PMMA) in the refractive range $n_{col} = 1.35$ to $n_{col} = 1.5$. Discrepancies occur at higher and lower refractive indices, however. For high n_{col} the ray-tracing simulations show a slightly better TIR trapping probability since reflections inside the escape cone are taken into account. The actual trapping probability is lower than predicted values when the refractive index of the film is

lower than $n_{col} = 1.41$ because for low refractive indices the aperture of the escape cone exceeds $\theta_c > 45°$ and overlaps with the emission cone, decreasing the number of trapped photons.

An empirical expression based on exponential functions can be fit to the ray-tracing results, leading to an effective photon trapping probability:

$$P_{eff}(n_{col}) = A\exp(n_{col}B) + C\exp(n_{col}D), \\ A = 0.81,\ B = 0.059,\ C = -35.23,\ D = -3.836. \tag{75}$$

This function is shown in Fig. 141 by the dotted blue line.

It is important to stress that a small quantity of light within the escape cone will be re-absorbed and might be collected by the solar cell, and that this is not taken in account in Eqns. (74) and (75). A simple way to reduce the escape cone is, of course, to use materials with high refractive index [98].

4.5.2 Re-absorption

As noted in the previous section, the coupling of escape cone loss and re-absorption drastically limits the operation of FSCs. The first analytical model that included re-absorption was developed by Weber [7] and then improved by the Zewail group [74;88]. These models show that re-absorption dictates the photon collection efficiency, which is the probability of photons escaping at the edge of the collector (Chapter 5). Batchelder [84;86] has developed four consistent experimental techniques for assessing re-absorption probabilities in operational devices, methods which are still in use today. These are steady-state spectral convolution, path-length dependent spectral shift, time-resolved emission and polarization anisotropy.

(i) The steady-state spectral convolution technique is carried out using standard spectroscopic measurements, and rests on the application of the Beer-Lambert law to obtain the overall self-absorption probability over the light path length.

(ii) The path-length dependent spectral shift technique uses the red shift of luminescence to estimate the re-absorption probability. As the luminescence passes through the collector, re-absorption increases, leading to a greater shift of the fluorescence. Experimentally, a rod of FSC material is excited with a spot of laser light focused on one side, while fluorescence spectra are recorded at the end of the rod as a function of the laser's distance from the end.

(iii) In the time-resolved emission technique, the time decay of luminescence is correlated with the magnitude of self-absorption. If the collector is pumped with a pulsed light source lasting less than a nanosecond, the fluorescence of the sample decays exponentially with time; the more re-absorption is occurring in the sample, the longer the decay.

(iv) Polarization anisotropy uses the tendency of a dye molecule to act as a dipole antenna. When illuminated with polarized light, dyes tend to emit light which is polarized in the same

direction as the illuminating light. Batchelder demonstrated that fluorescence in the direction of the polarized source is three times as intense as in any other direction. If this luminescence is subsequently self-absorbed, the resulting luminescence will be less polarized.

Nowadays, re-absorption probabilities are usually modelled numerically. Ray tracing [121;129-130], walk models [131] or Monte Carlo simulations [11;91] are often used to determine self-absorption probabilities. The drawback of such modelling is that computations can take several hours, even days. Early analytical models are reviewed in depth in Chapter 5. Based on the model developed by the Zewail group [88] and a detailed-balance argument, a new approach is suggested for assessing re-absorption probabilities analytically and experimentally.

4.5.3 Matrix losses

The matrix in which the dye is diffused, mixed and polymerized is generally not perfectly homogeneous and not completely transparent at low frequencies, where the dye emits the most useful brightness. A small percentage of light is scattered and absorbed within the matrix [132] or reflected at the air/matrix interface. For PMMA collectors approximately 4 % (for normal incidence) of solar radiation is lost by surface reflection.

In addition, it has been observed that matrices made of rigid films usually introduce a larger self-absorption region than liquid ones [133]. Treatments have been proposed for reducing this rigid effect [94]. In principle, the matrix is doped with molecules of high polarity before being formed into a rigid plate. Taleb obtained good results [134] by mixing a dye including 10 % of dopant into polyvinyl alcohol in the preparation of the collector. In this study, the dopant was thionin ($C_{12}H_{10}ClN_3S$) and the dyes tested were Rhodamine 6G, Rhodamine B, Ruthenium bi-byridyl and crystal violet. The experiments indicated that the red shift of the fluorescence is larger when dopant is added to the matrix.

Using similar techniques, Sah [133] showed that a 27 *nm* increase in the Stokes shift is possible using a PMMA matrix doped with 8 % camphor and DMANS fluorophore. Increasing the dipole moment of a matrix to enhance the Stokes shift also has negative effects. The quantum yield of a dye is particularly dependent on the environment and usually decreases with particularly polar solvents. Research has therefore focused in using dopants to increase the refractive index of PMMA while preserving a high dye quantum yield. The results shown in [132] demonstrate that the refractive index of a matrix can be controlled to obtain high optical efficiency.

Optical flatness is also a crucial factor in FSC operation. Both the front and back surfaces of the collector should be perfectly flat to ensure total internal reflection of fluorescence [129]. Matrix losses have been

modelled [125;135], and it has been demonstrated that losses due to the quality of currently available media limit the scaling-up of FSCs to just slightly more than one square meter [136]. Fortunately, matrix scattering and matrix absorption are also of interest in the fields of waveguide and fibre optic communication, so a cross-research investigation seems likely.

4.5.4 Dye losses and photostability

The complicated photochemistry of dye degradation is not fully understood at present. Degradation mechanisms are different for each dye-matrix combination, making the photostability of dyes extremely difficult to model. However, there are some guidelines to be followed in order to maintain the properties of the chemicals discussed here:

- Shield the dye from UV and short wavelength light.
- Keep dye concentrations as low as possible to avoid fluorescence quenching.
- Avoid additives.
- Use clean materials.
- Ensure complete matrix polymerization.
- Avoid the presence of oxygen.
- Avoid sharp variations in temperature.

4.6 Improved FSC designs

Studies on re-absorption losses (Chapter 5) and consideration of efficiencies achieved so far (Table 5) indicate that simple doped plates will not make efficient devices. It is generally agreed that the key to making a good FSC device is to minimize losses during photon transport while ensuring broad absorption of the incident light. Various designs have been proposed for improving traditional collectors.

4.6.1 Photon confinement and light guiding structures

Photon transport losses represent a major limit to collector collection efficiency. To deal with this problem, various confinement systems for enhancing the transport of luminescence have been proposed in the literature.

4.6.1.1 Photonic structures

Photonic band-stop filters (e.g. hot mirrors, rugate filters, cholesteric mirrors, opal filters, distributed Bragg reflectors), proposed for application to fluorescent collectors by B.S. Richards [12], transmit high-energy sunlight (blue ray, Fig. 142) but reflect longer wavelength fluoresced light (red ray, Fig. 142). In theory, covering a collector with a photonic band-stop filter can resolve the escape cone issue.

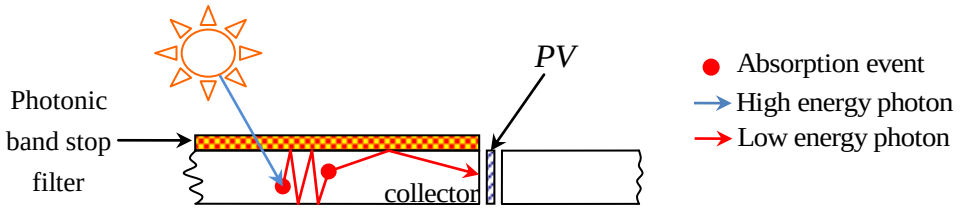

Fig. 142: Schematic diagram of a FSC covered with a photonic band pass filter, confining the fluorescence.

It has been shown that the efficiency limit for such a design exceeds 25 % for FSC plates coupled with c-Si cells [8;105]. B.S. Richards [12], J.C. Goldschmidt [137] and M. Peters [138] have experimentally investigated the effects of photonic filters on FSCs. Although minor increases in efficiency have been reported [12;103] because available photonic mirrors are optimized for specific angles of incidence, such a feature would be of limited value with random fluorescence emission. Advanced photonic band-stop (Opal) filters, with better angular optical characteristics, are currently being tested at the Fraunhofer Institute in Germany [139].

4.6.1.2 Thin-film FSCs

Thin-film collectors, also known as waveguide collectors, consist of a thin doped layer (10 to 100 μm) coated onto a 1 to 5 mm thick transparent substrate. It has been argued [11;76;140] that varying the refractive indices of the substrate and of the thin doped layer permits the decoupling of light absorption and emission processes to some extent (Fig. 143), so that each can be optimized independently of the other.

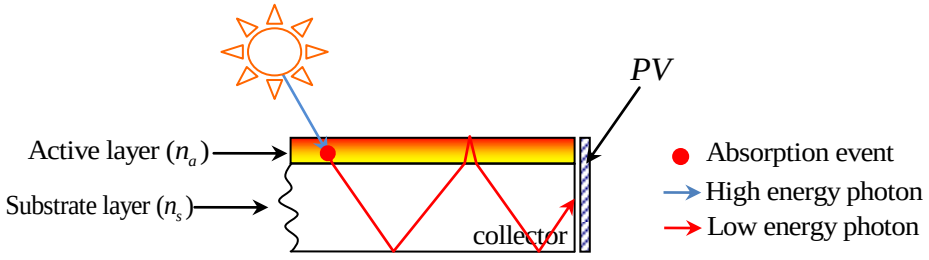

Fig. 143: Schematic of a thin-film FSC in which (for purposes of illustration) the refractive index of the active layer is higher than that of the substrate. The objective is to increase the length of the light path in the clear substrate, free from re-absorption losses, while minimizing it in the absorbing layer.

Thin-film FSCs were introduced in 1978; Table 9 summarizes the performance achieved thus far. Maximum reported efficiencies do not exceed those for FSC plates by more than a few percents. The discussion of thin-film FSCs is extended in Chapters 5 and 7, where the optimal thin-film configuration is examined using ray-tracing models and experimental results.

Table 9: Thin-film FSC performance reported in the literature

Year	Edge solar cell	Gain	Number of dyes	Efficiency (%)	Reference
1978	c-Si	48	1	2.3	[128]
1980	c-Si	33	2	3.2	[141]
1980	GaAs	33	2	4.5	[141]
1983	c-Si	11	1	3.2	[86]
1983	c-Si	11	2	2.5	[86]

4.6.1.3 Liquid fluorescent collectors

Liquid collectors are practical for spectroscopic measurements for several reasons: bubbles and dust settle out naturally; mirrors immersed in the organic solvents are well coupled to the concentrated light; solvents with specific attributes (e.g. polar or highly refractive) can be used to confirm specific conjectures; and dye concentrations and solvents can be changed *in situ* using a pumping system.

A liquid FSC based around a thin glass cuvette containing the fluorescent solution, in which the cuvette walls serve as the clear substrate (Fig. 144), can mimic various inhomogeneous devices (structures characterized by multiple refractive indices). In addition, the ease of replacing the fluorescent solution is convenient for varying the matrix refractive index.

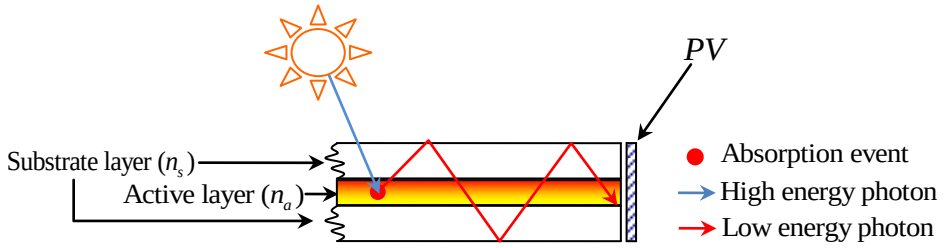

Fig. 144: Schematic of a liquid collector in which (for purposes of illustration) the refractive index of the active layer is equal to that of the substrate.

In 1978 Wood and coworkers at Mobil Tyco Solar Energy Corporation reported on investigations of liquid collector performance, with the aim of developing a FSC in the form of a fluid-filled box in which the fluid can be replaced periodically, depending of the lifetime of the dyes, by simple draining and refilling [142]. The study did not support commercial application because dyes are less stable and bleach more rapidly in a liquid matrix than in a solid one. Experiments showed that within five days of daylight exposure Coumarin 481, Coumarin 540, Rhodamine 6G and Rhodamine 640 completely faded, with absorption dropping to zero. Since then, liquid collectors have only been used for research purposes because of their versatility.

A. Filloux [143] used a tank with mobile reflective walls to study the influence of geometry on collector efficiency. Independently during the same period, A. Goetzberger proposed triangle-shaped collectors to increase photon collection efficiency [75]. Filloux's results [143] did not confirm Goetzberger's theory,

but in fact showed that collection efficiency was independent of shape. The effect of collector shape on FSC efficiency is discussed in greater detail in Chapters 5 and 7.

4.6.2 Energy transfer based collectors

Escape cone and re-absorption losses can be bypassed using non-radiative Förster's energy transfer from an absorbing dye (donor) to an emitting dye (acceptor) within the same clear substrate. The donor concentration is chosen to optimize light absorption while the acceptor concentration is lowered to a minimum value to reduce re-absorption losses [144]. Energy transfer can occur in cascade if the appropriate set of dyes is selected, as shown in Fig. 145.

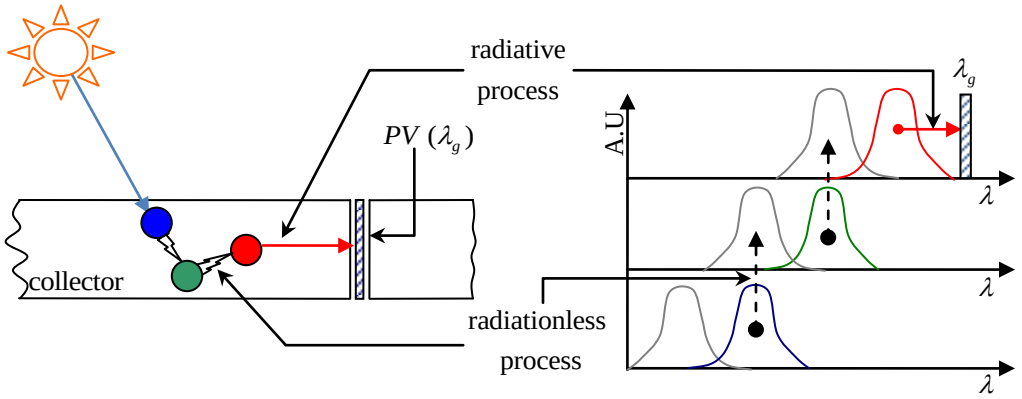

Fig. 145: Illustration of Förster's energy transfer between dyes. Left: a fluorescent solar collector doped with a set of absorbing dyes transferring energy to one another. Right: spectral representation of energy transfer between dyes. The blue dye absorbs high-energy sunlight (grey Gaussian curve), then transmits the absorbed energy to the green dye, which transmits the received energy to the red dye. The last dye re-emits the transferred energy to the solar cell.

R. Reisfeld, A. Goetzberger and W.H. Weber were the first to suggest, in the 1980s, the use of energy transfer to bypass re-absorption losses, but the literature shows few papers on energy transfer based collectors until very recently. It is only since 2007 that research has developed in this field, with the work of G. Calzaferri, who has created an artificial photonic antenna in zeolite L materials, harvesting and transferring solar energy efficiently [95].

4.6.3 Bottom mounted configuration

As suggested and patented in 1980 by Boling [145], a luminescent layer can be placed on top of a solar cell to improve its spectral response, with the dye absorbing high-energy photons and re-emitting at a wavelength at which the solar cell response is optimized. Light concentration is still possible in such an arrangement, since the PV cell need not cover the entire underside of the collector (Fig. 146).

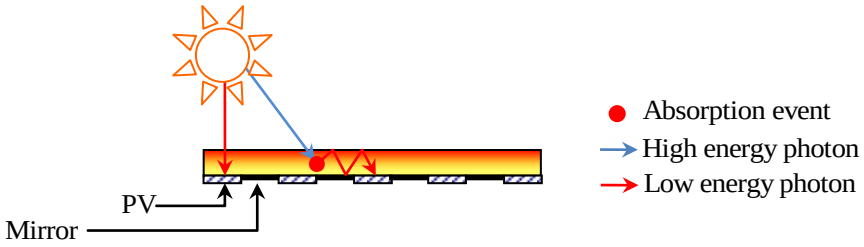

Fig. 146: Cross-section of a bottom mounted arrangement in which the luminescent layer is coated onto the PV cell, and light concentration occurs with the help of mirrors.

The advantage of this configuration is that the PV cells also receive direct illumination, and are less subject to shadowing losses [146]. The electric output of nine interconnected $10\ cm \times 2\ cm$ c-Si cells was measured when a strip of black tape covering at least one cell shadowed the central part of the collector. While the output of the nine bare cells decreased to almost zero when they were partially covered, in the bottom mounted configuration the cells maintained about 50 % of their electrical output. A group led by U. Rau is currently investigating the potential of such a design; in [105] this group modelled the optimal coverage fraction (the ratio of the area of the solar cells to the area of the covering mirror) using ray-tracing techniques. Assuming a perfect photonic band-stop, the optimal coverage fraction was estimated at around 10^{-2}. On the experimental side, only a few papers report the efficiency of such a design: using c-Si cells coupled to the fluorescent layer, T. Oska [147] reported efficiencies of up to 2 % with an optical gain of 3.36.

4.6.4 Stacked FSCs

Fluorescent solar collection plates permit a simple separation of the solar spectrum. Collectors can be arranged in stacks and each plate can be combined with a spectrally adapted solar cell. With such a configuration, higher efficiency is expected than with a single plate (Fig. 147). Stacked collectors were introduced by A. Goetzberger [75] in the 1980s.

Each plate absorbs a part of the solar spectrum and re-emits onto a small solar cell. The stacking of collectors enhances the number of photons absorbed by the device, although the cost per unit area is likely to be higher than for a non-stacked system. Theoretical conversion efficiencies have been estimated by A. Goetzberger; for a stack of four layers, efficiencies exceeding 30 % are achievable. However, efficiencies in practice are well below this limit (Table 10).

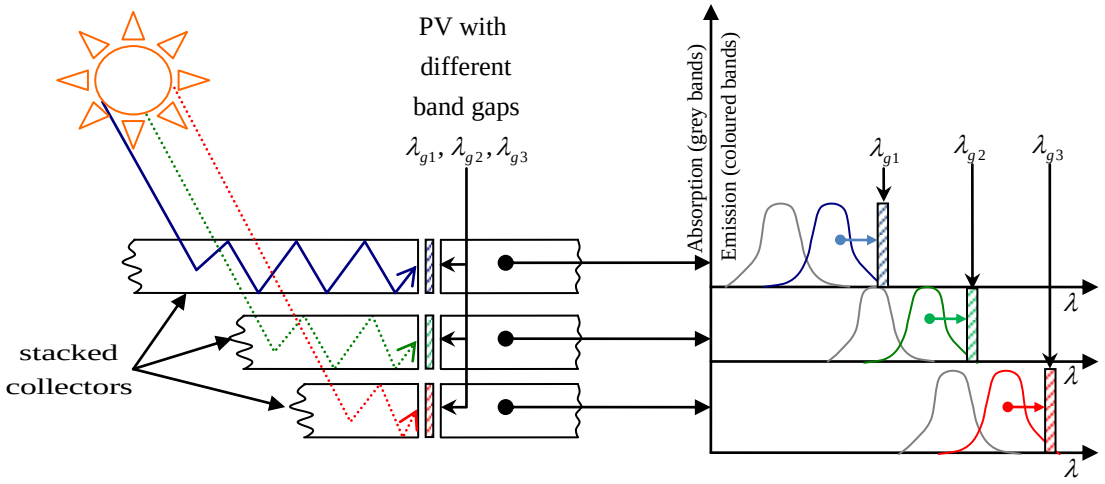

Fig. 147: Left: cross-section of a fluorescent collector stack. Right: absorption and emission spectra of the stacked layers.

Table 10: Collector-stack performance reported in the literature

Year	No of layers	Gain per layer	PV cell	Efficiency (%)	Reference
1981	2	133	c-Si	0.36	[75]
1981	3	133	c-Si	1.17	[75]
1982	3	28	c-Si	3.2	[101]
1982	3	101	c-Si	0.92	[92]
1984	2	33	c-Si/GaAs	4	[148]
2008	2	0.7	InGaP	6.7	[137]

Again, the highest efficiencies reported are for III-V edge cells with a very low gain (the collector with a gain of 0.7 is actually a "de-concentrator", the area of the edge solar cell being bigger than that of the front face of the collector).

4.7 Discussion

The literature review in this chapter has shown that FSCs have great potential as the next generation of cheap and efficient PV systems, with the promise of reduced losses that could mainstream solar energy. The challenge lies in the reduction of losses, especially re-absorption, a limiting factor. Re-absorption can be reduced through the use of photonic filters – theoretically capable of constraining photons within the collector – or by using a mixture of dyes covering the solar spectrum and transferring absorbed energy in a cascade. Better photon management can be achieved by decoupling the absorption and emission of fluorescence. Photostability issues may be resolved with the use of inorganic materials, e.g. quantum dots.

These new ideas explain why research into FSCs is expanding, although efficiencies obtained so far are relatively low. We conclude this review with a map (Fig. 148) showing all the scientific groups involved in the field, with their research interests and the major publications reviewed in this chapter.

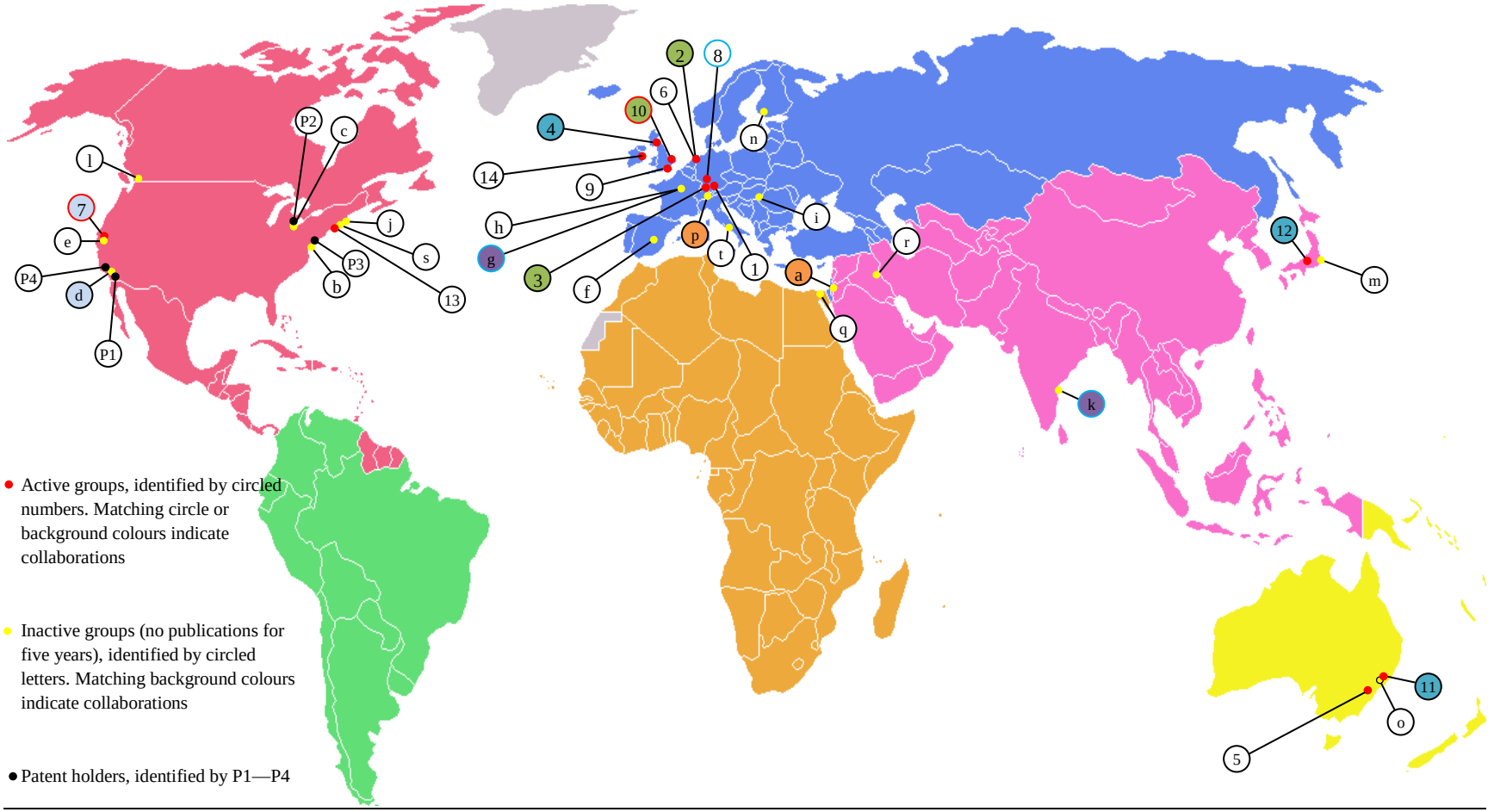

Fig. 148 : Research groups involved in FSC research

Active groups:

1: Stuttgart University, group led by U. Rau; interests: ray tracing, fundamental efficiency limitations, bottom mounted FSC configuration [105;149-150]
2: Energy research Centre of the Netherlands, group led by J.A.M. van Roosmalen; interests: ray tracing, outdoor testing [127;130]
3: Fraunhofer Institute for Solar Energy Systems, group led by A. Goetzberger then by G. Willeke; interests: outdoor testing, third-generation FSCs, liquid collectors, shape optimization, solvent effects [75;78;89;94;100;110;133;148;151]
4: Heriot-Watt University, group led by B.S. Richards; interests: ray tracing, quantum yield measurements, dye chemistry (absorption antennas), photonics [115]
5: Centre for Sustainable Energy Systems, Australian National University, main author K.R. McIntosh; interests: ray tracing [152-153]
6: Utrecht University, main author W.G.J.H.M. van Sark; interests: quantum dots, thin-film FSCs [97]

7: University of California, Berkeley, main author B. Jones; interests: nanorods, quantum dots [72]
8: BASF AG, main author G. Seybold; interests: photo bleaching, quantum yield measurements, synthesis of new dyes [71] [112]
9: University of Southampton, group led by T. Markvart; interests: thermodynamics, fundamental efficiency limitation, ray tracing, energy transfer, thin-film FSCs [8;57;73;106;129]
10: Imperial College London, group led by K. Barnham; interests: thermodynamics, quantum dots/rods, ray tracing [96]
11: Centre of Excellence for Advanced Silicon Photovoltaics and Photonics, Sydney, main author R.P. Corkish; interests: photonics [12]
12: Nagaoka University of Technology, main author: N. Yamada; interests: ray tracing [152]
13: Massachusetts Institute of Technology, group led by M.A. Baldo; interests: energy transfer, thin-film FSCs [98]
14: Dublin Institute of technology, main author: S.J. Mccormack, B. Norton; interests: ray tracing, quantum dots [127]

Inactive groups (no publications for five years):

a: Hebrew University of Jerusalem, main author R. Reisfeld; interests: dye photostability, rare-earth materials, sol gel doping techniques, Monte-Carlo modelling, thin-film FSCs [11;77]
b: Exxon Research and Engineering Company, New Jersey, main author M.L. Lesiecki; interests: photon transport, re-absorption issues, matrices [91-92;123;125]
c: Ford Motor Company Research Laboratory, main author W.H. Weber; interests: photon transport, re-absorption issues, rare-earth materials [7;83]
d: California Institute of Technology, group led by A.H. Zewail; interests: photon transport, re-absorption issues, energy transfer [74;84-86;88]
e: Stanford University, main author R.W. Olson; interests: re-absorption issues [131]
f: University of Madrid, main author G. Lifante; interests: re-absorption issues, outdoor testing, liquid collectors [79;99;154]
g: Conservatoire National des Arts et des Métiers, group led by B. Valeur; interests: liquid collectors, effect of geometry [143]
h: Laboratoire de Photochimie Solaire, CNRS, group led by F. Garnier; interests: photon transport, re-absorption issues [93;155]
i: Jozsef Attila University, Hungary, main author R. Soti; interests: photon transport, re-absorption issues [136]
j: Mobil Tyco Solar Energy Corp, main author J.R. Wood, interest: liquid collectors [142]
k: Indian Institute of Technology Madras, main author R. Kondepudi [156]
l: Simon Fraser University, British Columbia, main author A.H. Rawicz; interests: thin-film FSCs [76;140]
m: Electrotechnical Laboratory, AIST, Japan, main author: K. Sakuta; interests: bottom mounted FSC configurations [146]
n: University of Turku, Finland, main author T. Oksa; interests: bottom mounted FSC configurations [147]
o: University of Technology, Sydney, main author: P.D. Swift; interests: FSC used for lighting, collector stacks[135;157-158]
p: University of Geneva, main author C.K. Jorgensen; interests: inorganic and organic dyes [77]
q: Zagazig University, Egypt, main author A.F. Mansour; interests: outdoor testing, dye bleaching, matrices [108;124;126;132;159-162]
r: University of Baghdad, Iraq, main author A.M. Taleb; interests: self-absorption, solvent effects [134;163]
s: GTE Laboratories, Massachusetts, main author A. Lempicki [109]
t: Assoreni Laboratories, Rome, main author F. Galluzzi; interests: performance evaluation [164]

Patent holders:

P1: Atlantic Richfield Company, Los Angeles, inventors: H.R. Blieden, J.W. Yerkes; patent name: luminescent solar collector [165]
P2: Owens-Illinois Inc; inventor: N.L. Boling; patent name: luminescent solar collector structure [145]
P3: Biomed Solutions LLC, New York; inventor: S.G. MacDonald; patent name: photocell with fluorescent conversion layer [166]
P4: Oxnard CA, inventor: R.M. Murtha; patent name: side-collecting light guide [167]

Chapter 5

Techniques and models for analysis of FSC performance

This chapter reviews techniques and theoretical models for the quantitative analysis of fluorescent solar collector (FSC) performance. In the first section the key analytical models of Weber and Lambe (*W&L*) [7] and Batchelder-Zewail (*B-Z*) [74;84;86;88] are comprehensively reviewed. The major parameters considered in these models include: (i) the ability of a fluorescent collector to absorb light (absorption efficiency Q_a), (ii) the fluorescence quantum yield φ, (iii) the ability to transport light to the edge where a solar cell is located (collection efficiency Q_c), (iv) the re-absorption probability (R), and (v) the optical efficiency of the fluorescent collector (η_{col}).

Considering the balance between photon absorption and emission in the collector [73], it is shown that the models of Weber [7] and Batchelder [88] can be re-derived. This approach, developed by previous co-workers in the group [73] and based on a detailed-balance argument, allows a deeper insight into FSC operation through the determination of spectral re-absorption probability.

In the second section, the validity of the Weber and Lambe model is verified using ray-tracing simulations carried out with TracePro®. These simulations are extended to the modelling of re-absorption probability for collectors of various shapes (e.g. triangle, half disk) as well as for inhomogeneous structures such as thin-film and liquid collectors (Chapter 4).

It is shown from the ray-tracing simulations that, contrary to expectations:

- Novel structures such as thin-film collectors offer no improvement over the corresponding homogeneous collectors, and any variations in the refractive index of film on a glass substrate lead to an efficiency drop.
- The collector shape has little, if any, influence on the efficiency of the device.

5.1 Literature review

Early analytical models provide useful tools for understanding and quantifying the practical limitations of FSCs. First developed by Weber and Lambe in 1976 and improved by the Batchelder-Zewail group in the 1980s, these models have demonstrated their versatility and their applicability to a variety of situations (Refs. [73] and [129]). They also have the advantages of being fairly easy to implement, quickly solved

and less complex than recent semi-numerical, semi-thermodynamic models [118;127;168]. In the *W&L* and *B-Z* models the collector optical efficiency η_{col} is the product of the absorption efficiency Q_a and the collection efficiency Q_c:

$$\eta_{col} = Q_a \times Q_c, \tag{76}$$

where Q_a is proportional to the total number of photons absorbed by the collector, and Q_c is the fraction of absorbed photons reaching the edge solar cell.

The *W&L* and *B-Z* algorithms are fundamentally similar in that both estimate the photon flux escaping from the edge of the collector using this product. However, the models treat re-absorption in different ways, with consequences for the resulting overall efficiency. It is worthwhile comparing them.

5.1.1 Photon flux in a collector

The easiest way to understand the *W&L* and *B-Z* models is by means of a collector photon flow diagram [74], in which one can trace the excitation flows in the device (Fig. 149).

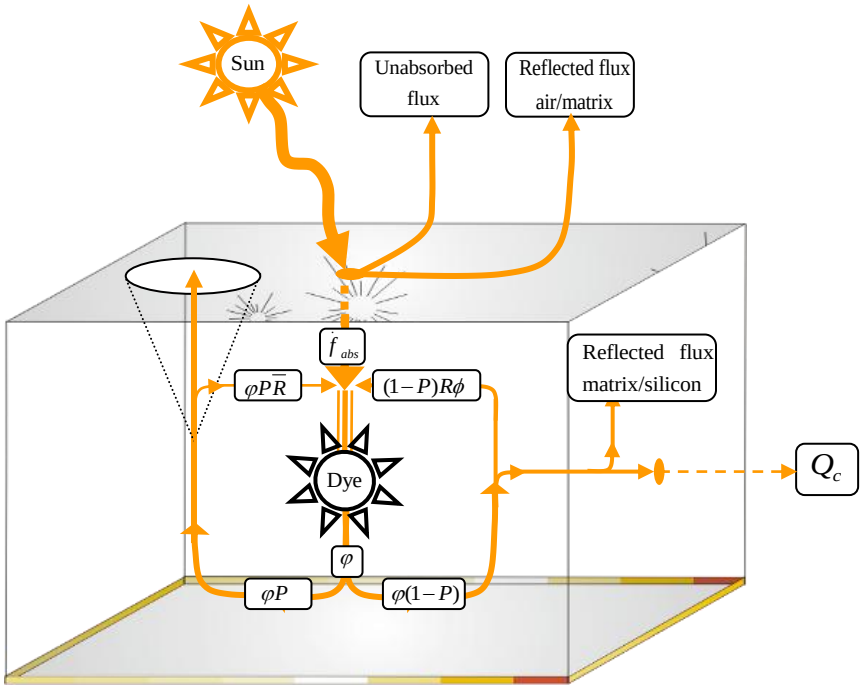

Fig. 149: Photon flow diagram for a single-dye FSC. Incoming sunlight is partially reflected and partially absorbed by the dye/matrix ensemble. Emissions which are not within the critical escape cone will be trapped by internal reflection. Some photons travelling towards the PV cell will be recycled via self-absorption. The collected light is that fraction Q_c which escapes the collector. (Figure adapted from [74])

In Fig. 149 the quantity $\dot{f}_{abs}$ represents the actual light flux absorbed within the collector per unit time. Assuming that the collector is uniformly illuminated and in a steady state, the probability of radiative de-excitation depends on the quantum yield φ of the dye. This fluoresced flux has a probability $P\varphi$ of being

emitted within the critical escape cone, where P is the likelihood of luminescence being emitted within the escape cone, as discussed in Chapter 4 (Section 4.5.1). The luminescence emitted within the critical cone has a probability $\bar{R}$ of being re-absorbed before leaving the collector, so the probability of photons being re-injected into the system is $P\varphi\bar{R}$.

The fluorescent flux $\varphi(1-P)$ emitted outside the escape cone is trapped inside the collector. A part $(1-P)R\varphi$ of this trapped light is re-absorbed, where R is the re-absorption probability outside the escape cone. The remaining photons reach the edge of the collector where they are partly reflected at the interface between the matrix and the silicon solar cell. The collection efficiency Q_c is the fraction of absorbed photons collected at the edge of the collector.

5.1.2 Absorption efficiency

Absorption efficiency is similar in both models, defined as the ratio of absorbed photon flux to incident photon flux. Light absorption inside the collector as a function of wavelength follows from the Beer-Lambert law. The photon flux absorbed across a thickness l of the collector is:

$$\int_0^{\lambda_g} \dot{f}_{sun}\,(\lambda, T_{sun}\,, \Omega_{sun}\,)\left(1-\exp^{-\alpha(\lambda)2l}\right) d(\lambda), \tag{77}$$

where $\dot{f}_{sun}\,(\lambda, T_{sun}\,, \Omega_{sun}\,)$ is the incident solar flux per unit area and bandwidth as defined in Chapter 1, and λ_g is the cut-off wavelength of the semiconductor placed at the edge of the collector.

The resulting absorption efficiency Q_a is then:

$$Q_a = \frac{\int_0^{\lambda_g} \dot{f}_{sun}\,(\lambda,T_{sun}\,,\Omega_{sun}\,)\left(1-\exp^{-\alpha(\lambda)2l}\right)\, d(\lambda)}{\int_0^{\lambda_g}\, \dot{f}_{sun}\,(\lambda,T_{sun}\,,\Omega_{sun}\,)\, d(\lambda)}. \tag{78}$$

Special attention should be paid to the spectral integration limits, which depend on the type of experiment being performed. Under monochromatic conditions the limits will be narrow, leading to an absorption efficiency close to one, whereas for outdoor testing the spectrum of the incident photon flux will be broader. It is instructive to evaluate the absorption efficiency of a "standard" dye. Common organic dyes show, on average, an absorption band $80\,nm$ wide at full width half maximum (FWHM) – e.g. Rhodamine 6G ($87\,nm$ FWHM) or Coumarin 540 A ($76\,nm$ FWHM). Assuming that a standard fluorophore absorbs all the incoming daylight in its absorption band, the absorption efficiency of a single dye is approximately ≈ 15 %.

The definition of Q_a is straightforward, and can be refined by including losses such as reflectivity at the air/matrix interface ($\mathbb{R}_{front}$) and reflectivity at the back mirror ($\mathbb{R}_{back}$) (Fig. 150).

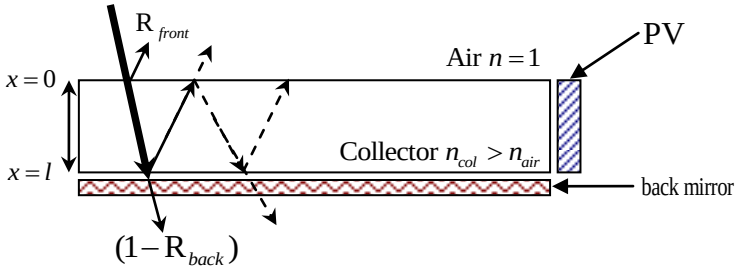

Fig. 150: Absorption photon path length in the collector. The thicknesses of the arrows indicates the number of photons remaining after each reflection. Although the process is infinite, only the first few reflections are shown.

Assuming the device in Fig. 150 is uniformly illuminated perpendicularly to the collector's front surface, the number of photons absorbed in the first passage across the collector thickness is given by Eqn. (77) multiplied by $(1 - \mathbb{R}_{front})$. Taking account of the reflectivity of the back mirror, the probability of photon absorption in the second pass is given by:

$$\int_0^l (1 - \mathbb{R}_{front})\left(\exp^{-\alpha l}\right)\mathbb{R}_{back}(\exp^{-\alpha x})\alpha d(x). \tag{79}$$

Since the illumination is assumed to be perpendicular to the collector's front surface, only forward and backward passes are considered here. Summing the probabilities of photon absorption, the absorption efficiency is given by:

$$Q_a = \frac{\int_0^{\lambda_g}(1-\mathbb{R}_{front})\left((1-\exp^{-\alpha(\lambda)l})+\mathbb{R}_{back}(\exp^{-\alpha(\lambda)l})(1-\exp^{-\alpha(\lambda)l})\right)\times \dot{f}_{sun}(\lambda,T_{sun},\Omega_{sun})\, d(\lambda)}{\int_0^{\lambda_g} \dot{f}_{sun}(\lambda,T_{sun},\Omega_{sun})\, d(\lambda)}. \tag{80}$$

The reflectivity of the collector front surface can be determined using the Fresnel equations and the reflectivity of the back mirror can be characterized using an ellipsometer (Chapters 6 and 7).

5.1.3 Collection efficiency

To simplify the derivation of the collection efficiency we initially ignore photon recycling or self-absorption. In the photon flow diagram for the collector (Fig. 149), without re-absorption the photon recycling feedback loop disappears and the collection efficiency Q_c is approximately equal to the quantum yield of the dye minus the escape probability P for a photon within the critical cone: $Q_c = (1 - P)\varphi$. Removing self-absorbed photons from $(1 - P)\varphi$ and ignoring reflection losses at the collector/silicon interface, the fraction of luminescence reaching the edge of the collector is:

$$Q_c^1 = \varphi(1 - P) - (1 - P)R\varphi = \varphi(1 - R)(1 - P). \tag{81}$$

In essence, Eqn. (81) gives the collection efficiency for the first generation of photons, i.e. the fraction of photons reaching the solar cell after a single absorption/emission event (this is indicated by the

superscript 1 in Q_c^1) – in other words, as soon as a photon is re-absorbed it is considered lost. This is the approximation of the Weber and Lambe model [7].

In reality, of course, first-generation photons can be re-absorbed and re-emitted, becoming second-generation photons, with the possibility of being collected. Q_c can therefore be obtained either by summing a geometric series of re-absorption events [74;86] or simply by considering the balance between photon absorption and emission in the collector [73] (Section 5.1.5). The total collection efficiency Q_c is the sum of the collection efficiencies of each photon generation:

$$Q_c = \sum_{i=1}^{i=\infty} Q_c^i \, . \tag{82}$$

From the photon flow diagram for the collector it can be shown that the probability of first-generation photons being re-absorbed is $P\varphi\bar{R} + (1-P)R\varphi$. The product $Q_c^1[P\varphi\bar{R} + (1-P)R\varphi]$ is the second-generation collection probability, Q_c^2. This progression is reiterative, with the overall Q_c expressed as a sum of the collection efficiencies for each generation of photons:

$$\begin{aligned} &Q_c = Q_c^1 + Q_c^2 + Q_c^3 + Q_c^4 + \ldots Q_c^\infty \\ &Q_c = \varphi(1-R)(1-P) && \rightarrow W\&L \text{ model} \\ &+[\varphi(1-R)(1-P)] \cdot \varphi[\bar{R}P + R(1-P)] \\ &+[\varphi(1-R)(1-P)] \cdot \varphi^2[\bar{R}P + R(1-P)]^2 \\ &+\ldots\ldots+[\varphi(1-R)(1-P)] \cdot \varphi^\infty[\bar{R}P + R(1-P)]^\infty && \rightarrow B-Z \text{ model.} \end{aligned} \tag{83}$$

This is a geometric series, which can be summed up as:

$$Q_c = \varphi \frac{(1-R)(1-P)}{1-\varphi[\bar{R}P+R(1-P)]}. \tag{84}$$

The value of $\bar{R}$ has been studied experimentally and analytically in [86], and it has been shown that for collectors doped with a single dye $\bar{R}$ can be neglected, allowing Q_c to be simplified to:

$$Q_c = \varphi \frac{(1-R)(1-P)}{1-\varphi R(1-P)}. \tag{85}$$

Eqn. (85) stresses the importance of three factors with a major influence on collection efficiency: (i) dye quantum yield, (ii) escape cone probability and (iii) re-absorption probability. Fig. 151 illustrates the difference between collection efficiencies computed using the *W&L* and the *B-Z* models.

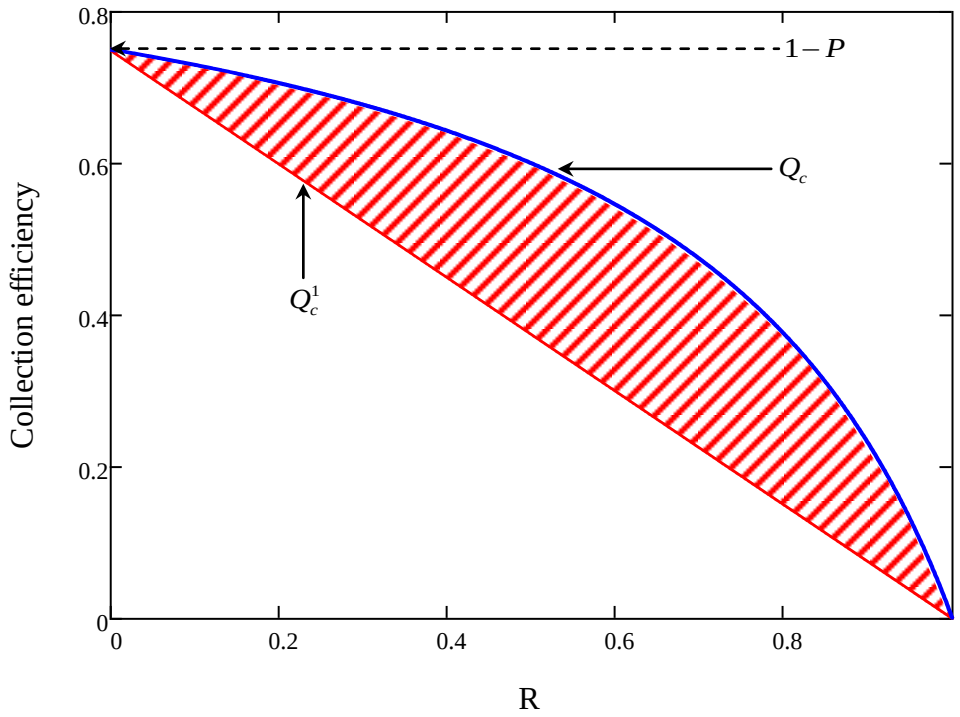

Fig. 151: Collection efficiency as a function of re-absorption probability. The *W&L* approximation is shown by the red line (Eqn. (81)), and the full *B-Z* model including photon recycling by the blue line (Eqn. (84)). The collector is assumed to have a refractive index of 1.5 and to be doped with a fluorescent dye with a quantum yield of unity. In reality, the experimental collection efficiency will be somewhere between the two curves (hatched area) since the collection of all photon generations is very unlikely. In the discussions that follow, we favour the use of re-absorption probability for comparing collector efficiencies.

The quantum yield of modern dyes has reached unity (e.g. Rhodamine 101 [114]) and the reduction of the escape cone probability (Chapter 4) has been experimentally demonstrated by using high refractive index materials [98]. The only remaining parameter that has not been experimentally enhanced is the re-absorption probability, and this is the main focus of the following sections.

5.1.4 Re-absorption probability

Weber and Lambe have proposed a simple model for estimating re-absorption probability, based on the geometry of an infinite ribbon collector of width L [7]. This model assumes a uniform distribution of excited molecules throughout the collector, perfectly flat specular reflecting surfaces, no scattering of light inside the collector, and no absorption of light except by the dye (see Fig. 152). It can de shown (see Appendix A) that the re-absorption probability of such a collector can be written as:

$$R(L,\alpha,P) = \frac{\int_0^L \int_0^{\pi} \int_{\theta_c}^{\pi-\theta_c} \left(e^{\frac{-\alpha(L-y)}{\sin(\theta)\sin(\vartheta)}} + e^{\frac{-\alpha(L+y)}{\sin(\theta)\sin(\vartheta)}} \right) \sin(\theta) d(\theta) d(\emptyset) d(y)}{4\pi L P}, \tag{86}$$

where $\emptyset$ and θ are the usual spherical coordinates defining the direction of emission. The attenuation of light in Eqn. (86) is computed using the classical Lambert's law, with a term $(L-y)$ or $(L+y)$ for the

light emitted towards the silicon cell or in the direction of the mirror, respectively. The denominator in the exponential term corresponds to the projection of the rays onto the *y*-axis. The integration excludes rays emitted at an angle $\theta_c < \theta < \pi - \theta_c$, i.e. within the escape cone.

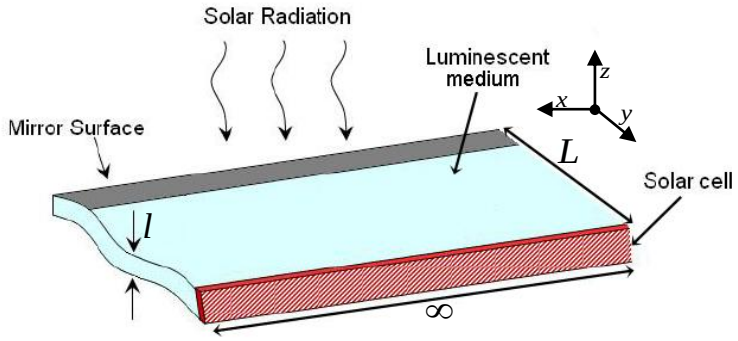

Fig. 152: Collector geometry used in the *W&L* model [7]. (Figure taken from [6])

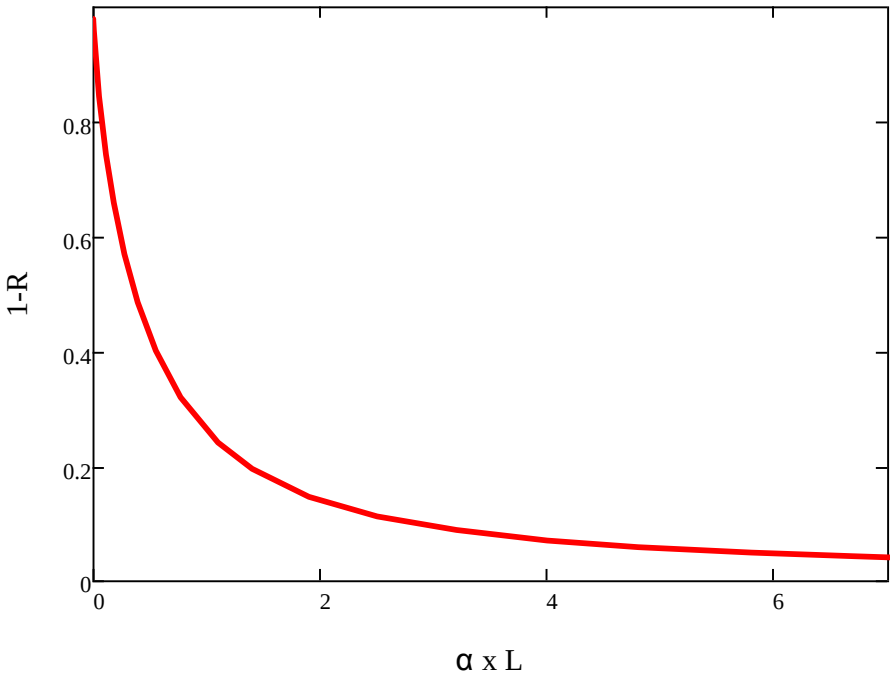

Fig. 153: Re-absorption profile as a function of the product αL for an infinite ribbon collector of width L.

Fig. 153 shows the re-absorption probability R of an infinite glass ($n_{col} = 1.5$) ribbon collector, computed using Eqn. (86). Clearly the collection efficiency, which is linked to re-absorption probability, strongly depends on the product αL.

5.1.4.1 Fundamental limitation imposed by re-absorption

The fundamental limitation imposed by re-absorption can be illustrated by plotting collection and absorption efficiencies as a function of αL. As noted in Chapter 1, the absorbance and fluorescence bands are thermodynamically linked [29], and it is impossible to create a window completely free of re-

absorption using material that absorbs sunlight efficiently [8;57]. To illustrate this constriction imposed by re-absorption, consider a glass collector with geometry similar to that of Fig. 152, with $L = 100\, l$, doped with a dye having a main broad step function of absorbance over the solar spectrum and a second band with a weak but significant absorbance coefficient (α_{em}) over the emission region. The absorbance coefficients of the dye at emission and absorption wavelengths are linked by $\alpha_{abs} = 100\, \alpha_{em}$, as shown in Fig. 154. This ratio has been arbitrarily chosen for the purpose of illustrating the fundamental limitation imposed by re-absorption; more realistic situations are derived in [8] and [105].

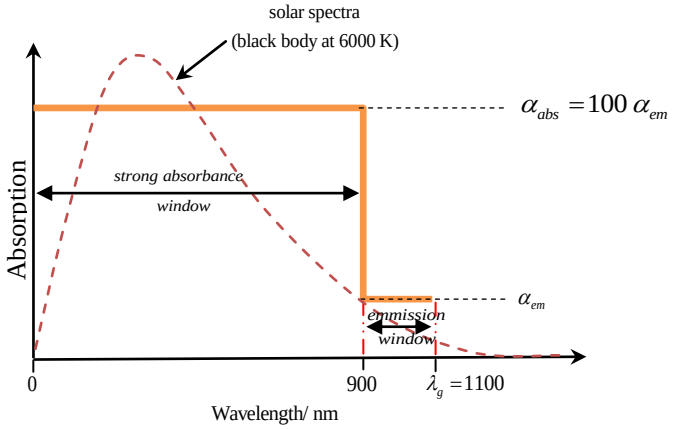

Fig. 154: Spectral dependence of dye absorption bands showing a broad step function of the main absorbance band over the solar spectrum at α_{abs} and a narrow emission region with a weak but non-negligible absorbance coefficient at α_{em}. All absorbed light is assumed to be emitted within the emission region.

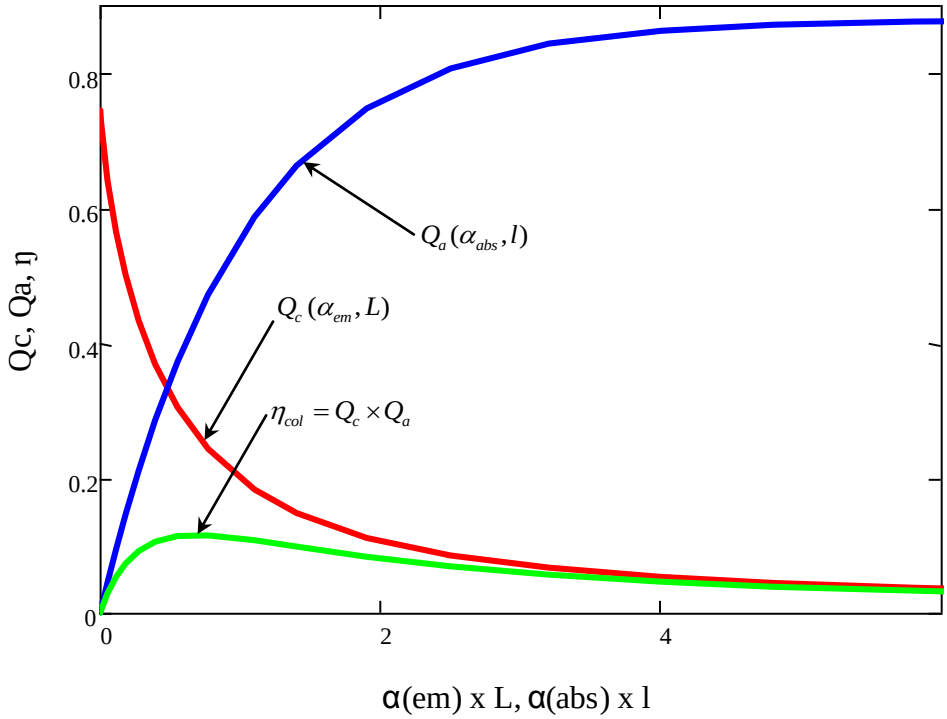

Fig. 155: Typical functional dependence of collector efficiency (η_{col}) on absorption and collection efficiencies. The quantum efficiency of the dye is taken as one, and the refractive index as 1.5. (Graph adapted from [57])

The typical functional dependences of Q_a, Q_c and η_{col} on the dimensionless product of the absorption coefficient and the corresponding length are shown in Fig. 155. Q_a is obtained from Eqn. (78) and Q_c from Eqns. (81) and (86).

Although the parameters in Fig. 155 have been subjectively chosen, the figure illustrates perfectly the limitation imposed by re-absorption. If one tries to increase the optical density of the collector to enhance absorption of incident radiation, the collection efficiency decreases. Clearly, for an efficient collector the ratio $\alpha_{abs} / \alpha_{em}$ must be maximized.

5.1.5 The two-photon-fluxes model

In this section the detailed balance between photon absorption and emission in the collector is considered [73]. This approach, which leads to the same results as the *B-Z* model, allows the determination of: (i) the concentration of excited molecules, and (ii) the spectral re-absorption probability. In this model the collector efficiency η_{col} and the absorption efficiency Q_a keep their original definitions, given by Eqns. (76) and (78), respectively.

5.1.5.1 Photon balance in a collector

We now consider the photon balance in a collector by identifying two distinct photon fluxes: a "direct flux" $\dot{f}_{abs}$ resulting from direct absorption of solar illumination, and an "induced flux" $\dot{f}_{ind}$ resulting from self-absorption consequent on re-emission events. According to this view, there are two mechanisms – direct and induced – by which molecules in their ground state can be excited. The photon balance can be illustrated using a very simple diagram with two quantum states (Fig. 156).

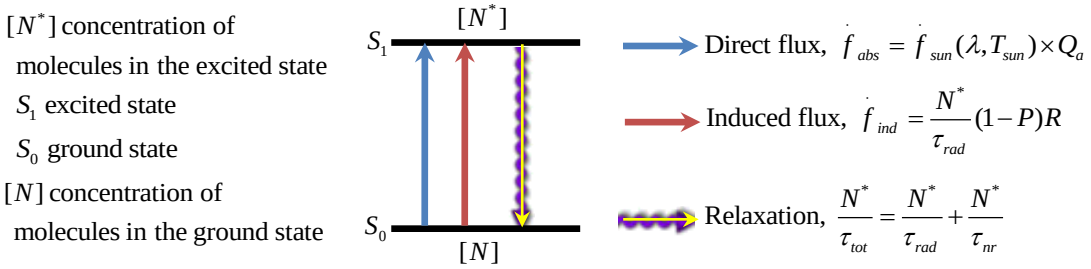

Fig. 156: Graphical view of the photon balance in a fluorescent solar collector using two quantum states.

The photon balance within the collector can be written as:

$$\dot{f}_{abs} + \dot{f}_{ind} = \frac{N^*}{\tau_{tot}}, \tag{87}$$

where N^* is the number of excited molecules and τ_{tot} is the total lifetime of the dye. Equation (87) maintains its full generality here, including the contribution from non-radiative de-excitation of the

fluorophore. The total relaxation rate N^*/τ_{tot} is related to the actual relaxation processes in the collector by:

$$\frac{N^*}{\tau_{tot}} = \frac{N^*}{\tau_{rad}} + \frac{N^*}{\tau_{nr}}, \tag{88}$$

where τ_{tot}, τ_{rad} and τ_{nr} are respectively the total lifetime, radiative lifetime and non-radiative lifetime of an excited molecule. The radiative lifetime is linked to the quantum yield φ of the dye by:

$$\frac{1}{\tau_{rad}} = \varphi \frac{1}{\tau_{tot}}. \tag{89}$$

With the help of the photon flux diagram (Fig. 149) and Eqns. (87) and (89), we may now describe the photon fluxes in a collector in terms of the relaxation rate of the dye.

The rate of relaxations occurring in the collector (N^*/τ_{tot}) is the sum of non-radiative (N^*/τ_{nr}) and radiative (N^*/τ_{rad}) contributions. From the photon flux diagram it is clear that the radiative flux includes photons escaping from the collector (within the escape cone) as well as those trapped inside by total internal reflection (TIR):

$$\frac{N^*}{\tau_{tot}} = \frac{N^*}{\tau_{rad}} + \frac{N^*}{\tau_{nr}} = \overbrace{\frac{N^*}{\tau_{rad}}(1-P)}^{photons\ trapped\ by\ TIR} + \underbrace{\frac{N^*}{\tau_{rad}}P}_{\substack{lost\ photons \\ (escape\ cone)}} + \frac{N^*}{\tau_{nr}}. \tag{90}$$

The induced flux is the rate of photon emission outside the escape cone times the re-absorption probability:

$$\dot{f}_{ind} = \frac{N^*}{\tau_{rad}}(1-P)R. \tag{91}$$

Using the photon balance relation (Eqn. (87)), the absorbed flux $\dot{f}_{abs}$ – the number of photons absorbed per unit time by the collector from the incident solar beam – can be expressed as:

$$\begin{aligned} \dot{f}_{abs} &= \frac{N^*}{\tau_{tot}} - \dot{f}_{ind} \\ &= \frac{N^*}{\tau_{tot}} - \frac{N^*}{\tau_{rad}}(1-P)R \\ &= \underbrace{\frac{N^*}{\tau_{tot}}(1-\varphi(1-P)R)}_{\text{two-photon-fluxes model}} = \overbrace{\dot{f}_{sun}(\lambda, T_{sun}, \Omega_{sun}) \times Q_a}^{W\&L\ \text{model}} \end{aligned} \tag{92}$$

The useful edge photon flux, seen by the solar cell ($\dot{f}_e$), corresponds to the flux of photons emitted outside the escape cone minus the flux re-absorbed.

$$\begin{aligned} \dot{f}_e &= \frac{N^*}{\tau_{rad}}(1-P) - \frac{N^*}{\tau_{rad}}(1-P)R \\ &= \frac{N^*}{\tau_{rad}}(1-P)(1-R). \end{aligned} \tag{93}$$

The collection efficiency Q_c is the fraction of absorbed photons which reach the edge of the collector or, using the definition of Weber and Lambe:

$$Q_c = \frac{\dot{f}_e}{\dot{f}_{abs}} = \frac{(N^*/\tau_{rad})(1-P)(1-R)}{(N^*/\tau_{tot})(1-\varphi(1-P)R)} = \frac{\varphi(1-P)(1-R)}{(1-\varphi(1-P)R)}. \tag{94}$$

Eqn. (94) leads to the re-derivation of the Batchelder-Zewail model. Using the definition of absorption efficiency, the optical efficiency of the collector is given by the compact expression:

$$\eta_{col} = \frac{\dot{f}_e}{\dot{f}_{sun}} = \frac{\dot{f}_e}{\dot{f}_{abs}} \frac{\dot{f}_{abs}}{\dot{f}_{sun}} = Q_c \times Q_a. \tag{95}$$

This derivation based on the photon balance expressed by Eqn. (87) demonstrate the validity of the Weber and Lambe model, and offers a broad view of the concepts relevant to the operation of fluorescent collectors. However, for convenience the photon balance is often rearranged to permit the quantification the photon flux $\dot{f}_{front}$ escaping through the front face of the collector (Chapter 7). The photon balance becomes:

$$\dot{f}_{abs} = \dot{f}_e + \dot{f}_{front} + \dot{f}_{th}, \tag{96}$$

where $\dot{f}_{th}$ is the photon flux lost as heat due to non-ideal quantum yield of the dye.

Using the detailed-balance Eqns. (87) and (90), it can be shown that:

$$\begin{aligned} \frac{N^*}{\tau_{tot}} &= \dot{f}_{abs} + \dot{f}_{ind} \\ &= \dot{f}_{sun} Q_a + \frac{N^*}{\tau_{tot}} \varphi(1-P)R \\ &= \frac{\dot{f}_{sun} Q_a}{1-\varphi(1-P)R}, \end{aligned} \tag{97}$$

and

$$\begin{aligned} \frac{N^*}{\tau_{rad}}(1-P)(1-R) &= \frac{\varphi(1-P)(1-R)}{(1-\varphi(1-P)R)} \dot{f}_{sun} Q_a \\ \frac{N^*}{\tau_{rad}} &= \frac{\varphi \dot{f}_{sun} Q_a}{(1-\varphi(1-P)R)}. \end{aligned} \tag{98}$$

Using Eqns. (97), (98) and (90) the photon balance given in Eqn. (96) can be re-written as:

$$\dot{f}_{sun}\,Q_a = \underbrace{\frac{\varphi\,\dot{f}_{sun}\,Q_a(1-P)(1-R)}{(1-\varphi(1-P)R)}}_{\dot{f}_e} + \underbrace{\frac{P\varphi\dot{f}_{sun}\,Q_a}{1-\varphi(1-P)R}}_{\dot{f}_{front}} - \underbrace{\frac{\dot{f}_{sun}\,Q_a(-1+\varphi)}{1-\varphi(-1+P)R}}_{\dot{f}_{th}}. \tag{99}$$

This relation can be corroborated by considering the collection efficiency Q_c, defined in Eqn. (95) as $\dot{f}_e/\dot{f}_{abs}$. Using Eqn. (99) it can be shown that:

$$Q_c = \frac{\dot{f}_e}{\dot{f}_{abs}} = \frac{\dot{f}_e}{\dot{f}_e+\dot{f}_{front}+\dot{f}_{th}} = \frac{\varphi(1-P)(1-R)}{(1-\varphi(1-P)R)}. \tag{100}$$

Clearly the photon balance expressed in Eqn. (87) is equivalent to the photon balance expressed in Eqn. (96).

To be of practical use, however, photon collection efficiency, and hence re-absorption probability, must be specified as a function of wavelength. The reasoning will be based on the photon balance in the collector, mathematically expressed in Eqn. (87).

5.1.5.2 Spectra re-absorption probability $r(\lambda)$

Consider the number of photons emitted within the collector in the wavelength band $d\lambda$. This corresponds to the rate of radiative relaxations, weighted by the profile of the fluorescence band:

$$\frac{N^*}{\tau_{rad}}\tilde{f}_1(\lambda)d\lambda\,, \tag{101}$$

where $\tilde{f}_1(\lambda)$ is the normalized profile, or photon distribution, of the fluorescence spectrum free from re-absorption – in other words, the fluorescence spectrum of the first photon generation (indicated by the subscript 1). The normalization rule is:

$$\int \tilde{f}_1(\lambda)d\lambda = 1. \tag{102}$$

Because of re-absorption, only a fraction of the fluoresced photons will reach the edge of the collector. Using Eqn. (93) and introducing the re-absorption probability $r(\lambda)$ as a function of wavelength, the rate of photon emission at the edge of the collector can be written as:

$$\dot{f}_e(\lambda) = \frac{N^*}{\tau_{total}}\tilde{f}_1(\lambda)\varphi(1-P)\big(1-r(\lambda)\big). \tag{103}$$

Replacing N^*/τ_{total} with Eqn. (97):

$$\dot{f}_e(\lambda) = \dot{f}_{sun}\,Q_a\,\frac{\varphi(1-P)(1-r(\lambda))}{1-\varphi(1-P)R}\tilde{f}_1(\lambda). \tag{104}$$

Equation (104) shows that the spectral probability of re-absorption for each photon emitted outside the escape cone can be found from the ratio of two quantities, $\tilde{f}_e(\lambda)$ and $\tilde{f}_1(\lambda)$:

$$\frac{\tilde{f}_e(\lambda)}{\tilde{f}_1(\lambda)} = 1 - r(\lambda), \tag{105}$$

where $\tilde{f}_e(\lambda)$ is the edge fluorescence spectrum normalized to the flux of absorbed photons:

$$\tilde{f}_e(\lambda) = \frac{\dot{f}_e(\lambda)}{\dot{f}_{sun}\, Q_a} \times \mathbb{C} = \frac{\dot{f}_e(\lambda)}{\dot{f}_{abs}} \times \mathbb{C}\,, \tag{106}$$

where the constant $\mathbb{C}$ is equal to:

$$\mathbb{C} = \frac{1-\varphi R(1-P)}{\varphi(1-P)}. \tag{107}$$

It is worth noting that for the case of negligible re-absorption, i.e. when there is no overlap of the absorbance and fluorescence bands ($R \approx 0$), the normalized edge fluorescence spectrum is given by the very simple relation:

$$\tilde{f}_e(\lambda) = \frac{\dot{f}_e(\lambda)}{\varphi(1-P)\dot{f}_{abs}}. \tag{108}$$

Equation (108) provides a direct link between experiment and theory. Calculating the ratio of the fluorescence spectrum observed at the edge to the first-generation spectrum is a quick and easy way to characterize the re-absorption probability. The first-generation spectrum $\tilde{f}_1(\lambda)$ can be obtained from spectroscopic databases or from simple spectroscopic experiments (Chapter 6), the flux absorbed in the collector can be deduced from the dye absorbance spectrum, and P is easily computed from Eqn. (75).

The key feature of this characterization technique is its simplicity of application. One might assume that absolute measurements of incoming flux are required to scale down the edge fluorescence spectrum Eqn. (108). However, this is not the case because in the long-wavelength region, where re-absorption can be neglected, the shape of the loss-free and edge fluorescence spectra are expected to be similar [169]. The scaling constant (Eqn. (107)) can then be easily determined by scaling down one edge fluorescence spectrum until it coincides with the loss-free re-absorption fluorescence spectrum in the long-wavelength region, as is shown in Chapter 7.

5.1.5.3 Spectral photon collection probability χ(λ)

Using the results derived in the previous section, Eqn. (103) can be presented in the form:

$$\dot{f}_e(\lambda) = \dot{f}_{abs}(\lambda)\tilde{f}_1(\lambda)\chi(\lambda), \tag{109}$$

where $\chi(\lambda)$ is the spectral photon collection probability, defined as:

$$\chi(\lambda) = \frac{(1-P)(1-r(\lambda))}{1-\varphi(1-P)R}\,. \tag{110}$$

The collection probability derived here is, of course, very similar to that in the *B-Z* model [74] but differs in its spectral dependence. To avoid confusion, $\chi(\lambda)$ is used to represent the spectral collection probability derived here, while Q_c represents the overall collection efficiency as defined by Batchelder and Zewail. The two are linked by the relationship:

$$Q_c = \int_0^\infty \chi(\lambda)\tilde{f}_1(\lambda)\, d\lambda, \tag{111}$$

and the spectral re-absorption $r(\lambda)$ is linked to the re-absorption probability *R* by:

$$R = \int_0^\infty r(\lambda)\tilde{f}_1(\lambda) d\lambda. \tag{112}$$

As in the *B-Z* model, this treatment is based on a number of simplifying assumptions, including a uniform distribution of excited molecules throughout the collector, perfectly flat specular reflecting external surfaces, no scattering of light within the collector, and no absorption of light except by the dye. It is also assumed that, at the edge of the collector, light is emitted within a full hemisphere on account of the high refractive index of the edge solar cell.

For the models reviewed in this section, the efficiency depends strongly on the re-absorption probability. Using Eqn. (105) the key variable $r(\lambda)$ can be plotted as a function of wavelength, or of the product of the absorption coefficient (using the absorption spectrum of the dye) and the length *L* of the collector. This allows the "experimental" re-absorption probability to be compared with the analytical model of *W&L* (Eqn. (86)). The results are presented in Chapter 7.

However, before embarking on a comparison between experimental data and analytical calculations it is essential to examine the validity and limitations of the Weber and Lambe model. In the following section, re-absorption probability is investigated using ray-tracing simulation techniques carried out with TracePro®.

5.2 Study of re-absorption ray by ray-tracing techniques

The infinite ribbon geometry used in the *W&L* model was reproduced in the ray-tracing software by using two perfect reflectors placed in the *xy* plane (Fig. 157). By unfolding the geometry of collectors bounded by mirrors by the method of images, and by straightening the zig-zag optical paths formed by multiple reflections of trapped light, one can show that the geometry of a device coated with mirrors is the same as an infinite ribbon since the path lengths of the trapped photons are equivalent and symmetry is conserved.

The collector studied was $50\,mm \times 50\,mm$ in area, and in the modelling its thickness was varied to change the gain. The refractive index of the collector was set at $n_{col} = 1.5$, the surfaces were assumed to be perfectly flat, and each mirror was assumed to have perfect reflectivity.

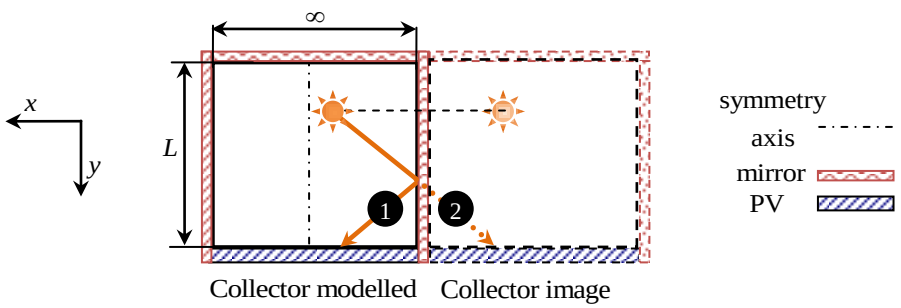

Fig. 157: Left: collector implanted in TracePro® (view from the top) using mirrors to mimic an infinite ribbon. Right: symmetrical collector image where the path length of the rays ❶ and ❷ are shown to be identical.

Following the assumptions of *W&L* the re-absorption probability was modelled using three different approaches. The first approach, using the concept of infinite geometry, consisted in placing point sources, emitting over $4\pi\ sr$, uniformly along the symmetric *y-axis* (Fig. 157). The second approach consisted in filling up the volume of the collector with 1×10^6 sources, placed either uniformly or using a Monte Carlo algorithm. The third technique used the fluorescence built into the TracePro® algorithm.

The collector was uniformly illuminated with 1×10^6 rays normal to the surface, and the wavelength of the incident rays corresponded to the maximum absorption of the fluorophore. The position of the absorption/emission event was randomly selected along the path of the excitation ray, somewhere between the points of entry to and exit from the fluorescing object; and the direction of the fluoresced ray was arbitrarily chosen over $4\pi\ sr$. For all three techniques, the re-absorption probability was then deducted by counting the numbers of photons reaching the edge solar cell.

Similar re-absorption probabilities were obtained with all three approaches, and they also were in agreement with the *W&L* model to within 1 %. Varying the collector gain revealed the limitations of the analytical model for small gain. Discrepancies between the analytical model and ray-tracing simulations were negligible for gains equal to or greater than 20. Comparisons between the analytical Eqn. (86) and the ray-tracing simulations are shown in Fig. 158.

Other assumptions linked to the *W&L* model imply perfect optical interfaces. For the same collector configuration (gain 20), the re-absorption probability was re-computed for an arrangement of standard-quality rather than perfect mirrors. The specular coefficient of the modelled mirrors was set at 0.95, with 5 % absorbance; light scattering was modelled using the bidirectional scattering distribution function (BRDF) [170] and the Harvey-Shack "shift invariant" approximation [171] for scattering which is mainly due to residual surface roughness after polishing. The BRDF a, b and g coefficients were set at 0.0001, 0.15 and 2, respectively, leading to a 0.13 % Gaussian scatter distribution. Fig. 159 illustrates the effect of imperfect optics on TIR photon transport.

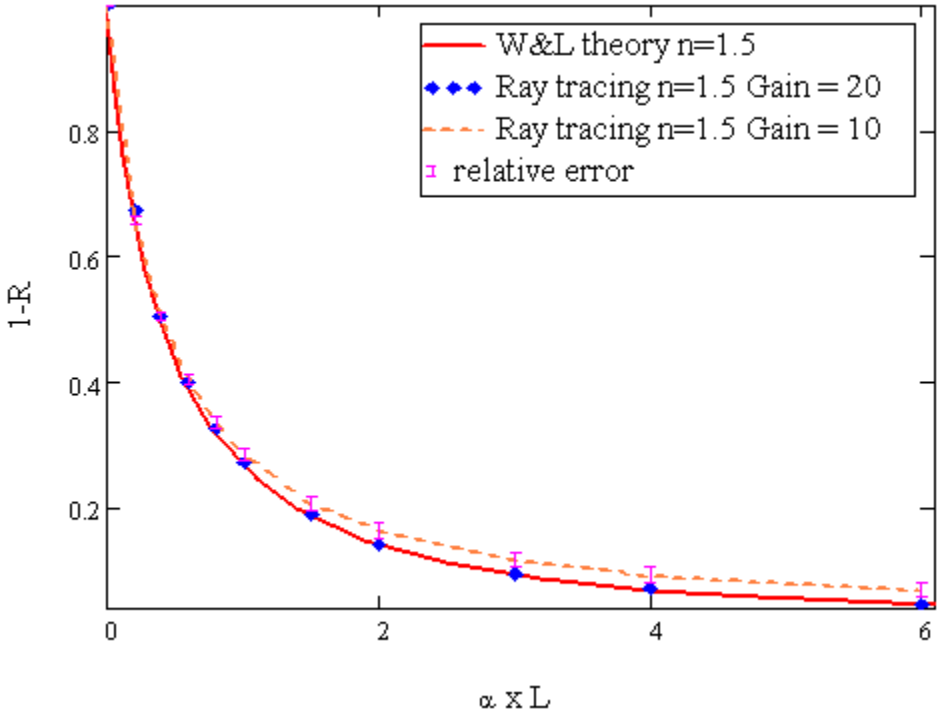

Fig. 158: Re-absorption probability computed analytically using Eqn. (86) for a collector with a refractive index $n_{col} = 1.5$ (red line) compared with ray-tracing simulations for different gains. (Graph published in [73])

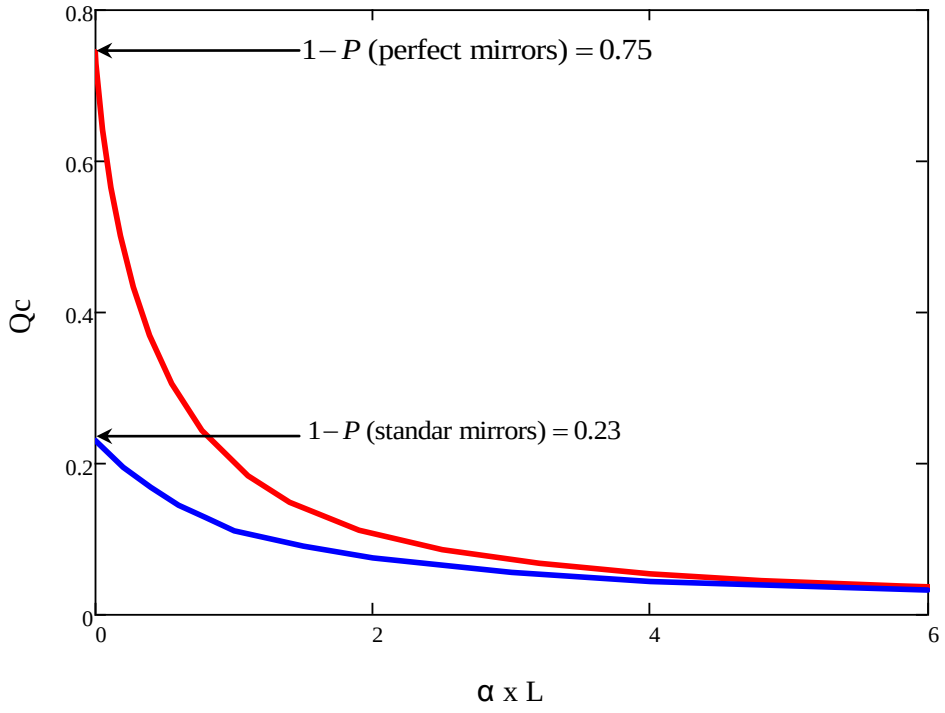

Fig. 159: Effect of light scattering on re-absorption probability and photon collection efficiency. The refractive index of the collector is set at 1.5. (Graph published in [129])

The ray-tracing results show that both the re-absorption probability and the probability of photon loss within the escape cone are affected by light scattering. Fig. 159 indicates that for a collector with rough surfaces (blue line), photon collection efficiency in a collector with rough surfaces (blue line) decreases dramatically – by a factor of about three – compared to a collector with perfect interfaces (red line). This scattering effect was negligible in all the collectors studied experimentally (Chapter 6) because their surfaces were highly polished, to the standard of [172].

5.2.1 Influence of collector geometry

With the validity of the Weber and Lambe established, the ray-tracing technique was used to model re-absorption probability for various collector shapes, using the techniques described in the previous section. The collector shapes studied were rectangle, half-disk, triangle and quarter-disk. The collection surface area of $2500\ mm^2$ and a concentration factor of 50 were kept constant in all designs. Details of collector geometry are shown in Table 11.

Table 11: Collector shapes studied using ray-tracing simulations; $\mathbb{R}$ indicates a perfect reflector, **G** is gain and PV refers to the photovoltaic cell

Shape	Properties	Shape	Properties
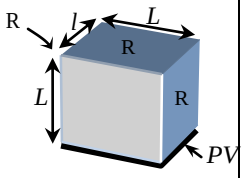	rectangular collector $L = 50\ mm$ $l = 1\ mm$ **G** = 50	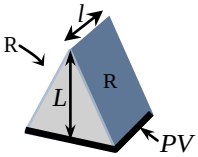	triangular collector $L = 100\ mm$ $l = 1\ mm$ **G** = 50
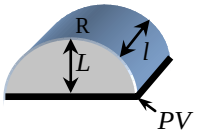	½ disk collector $L = 39.9\ mm$ $l = 0.627\ mm$ **G** ≈ 50	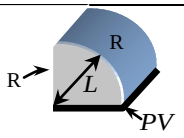	¼ disk collector $L = 56.42\ mm$ $l = 0.886\ mm$ **G** ≈ 50

The validity of using perfect mirrors to mimic infinite structures is confirmed by the agreement between the re-absorption probability of the rectangular collector in Fig. 158 and the *W&L* model. Thus any symmetrical shape which can be "unfolded" using perfect reflectors will result in the same re-absorption probability.

Using arguments similar to those for the rectangular collector, it can be shown that a triangular collector of length L is strictly equivalent to a rectangular collector of length $L/2$. Indeed, the method of images used in Fig. 157 shows that a mirror can be placed in the symmetry plane of the collector without changing the outcome of the ray-tracing simulation. It is therefore clear that any triangular collector is equivalent to half of a rectangular collector (Fig. 160).

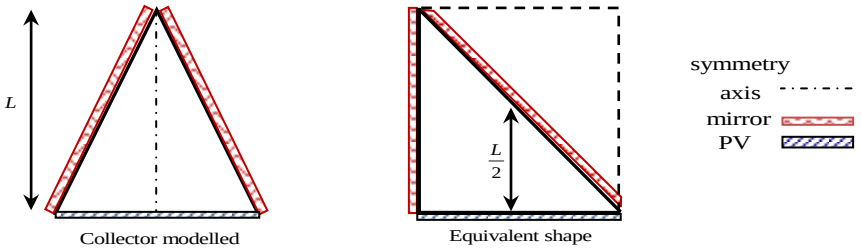

Fig. 160: Left: triangular collector modelled using TracePro®. Right: equivalent shape showing that any triangular collector of length L is strictly equivalent to a rectangular collector of length $L/2$.

Fig. 161 presents re-absorption probabilities for various collector shapes. The probability of photons escaping within the critical cone is the same for all the collectors considered; hence, the re-absorption probability in this graph is directly related to the collection efficiency.

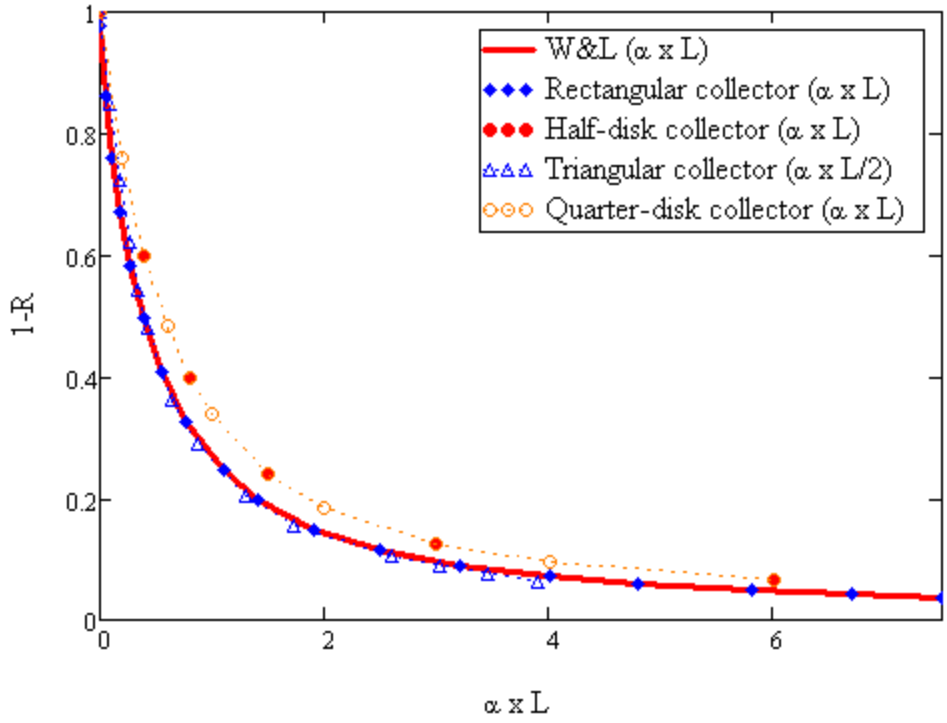

Fig. 161: Re-absorption probability for various collector geometrical shapes as a function of the product αL.

Fig. 161 clearly shows that the shape of the collector has little influence on the re-absorption probability. As expected, the triangular and rectangular shapes have identical re-absorption profiles, while the disk collector appears to slightly reduce re-absorption losses. However, if an effective length L proportional to the average photon path length in the collector is used as a parameter, rather than the physical distance between the solar cell and the opposite mirror (Fig. 162), all the re-absorption profiles are similar (Fig. 163), indicating that collector shape has no influence on the re-absorption profile, and therefore on

collector efficiency. These results confirm experiments by Roncali [93] in which no efficiency improvement was recorded with various collector geometries.

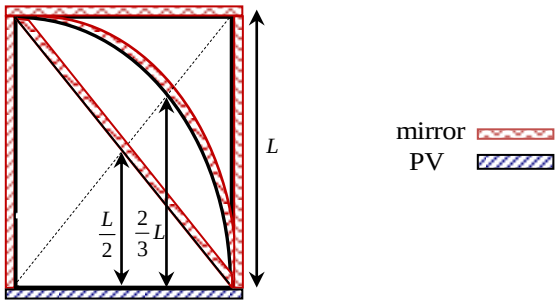

Fig. 162: Superposition of triangle, disk and rectangular collector geometries, indicating their effective lengths L, proportional to the average photon path lengths.

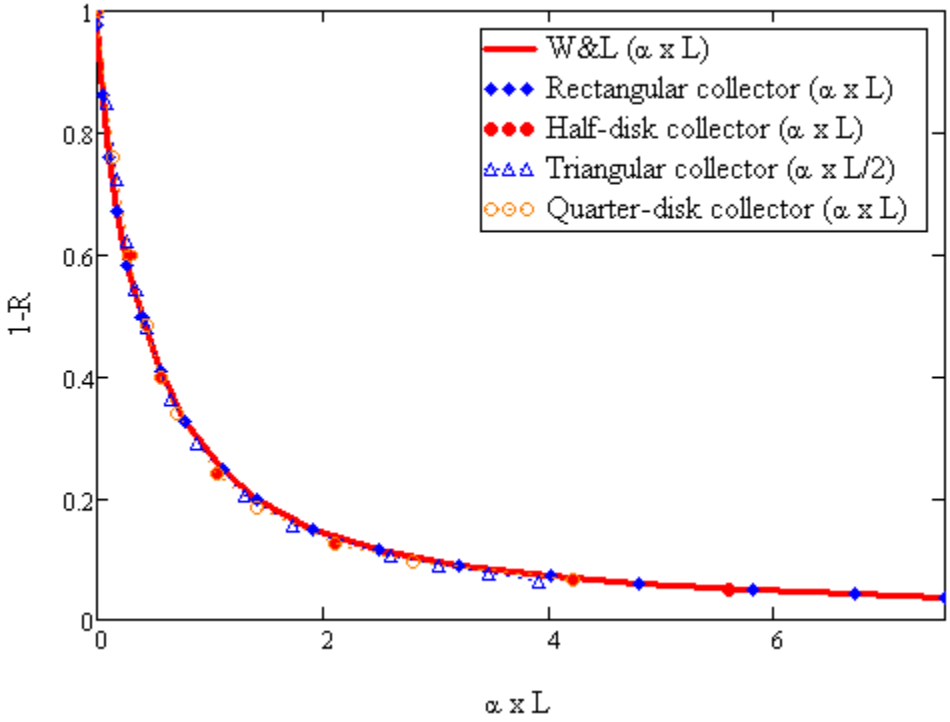

Fig. 163: Re-absorption probabilities for various collector shapes as a function of the product αL, where L is the effective length shown in Fig. 162.

5.2.2 Influence of collector homogeneity

Re-absorption probabilities for thin-film and liquid collectors were also investigated and compared with the *W&L* model. These devices are inhomogeneous in the sense of having more than one refractive index. Details of the collectors modelled are presented in Table 12. Gain and surface collection area were again kept constant at 50 and 2500 mm^2, respectively.

Table 12: Inhomogeneous collectors studied by ray-tracing simulations. ℝ indicates a perfect reflector, **G** is gain and PV refers to the photovoltaic cell

Shape	Properties	Shape	Properties
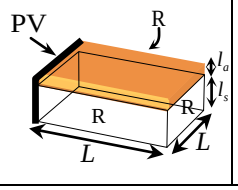	thin film $L = 50\ mm$ $l_s = 1, l_a = 0.001\ mm$ $\mathbf{G} \approx 50$	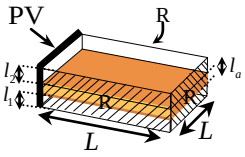	liquid collector $L = 50\ mm$ $l_a = 0.25\ mm$ $l_s = l_1 + l_2 = 0.25\ mm$ $\mathbf{G} = 50$

In order to compare the re-absorption profiles of homogeneous plate collectors with those of non-homogeneous structures, we first considered the simple case in which the refractive index of the doped layer (the active layer) is identical to that of the substrate: $n_a = n_s$. For practical purposes, an effective absorption coefficient (α_{eff}) linking the structures shown in Table 12 to flat-plate collectors can be used to evaluate the relative absorption of inhomogeneous devices:

$$\alpha_{eff} = \alpha \frac{l_a}{l_s + l_a}, \tag{113}$$

where α is the absorption coefficient of the absorbing layer.

Eqn. (113) can be justified by a simple geometrical consideration of the optical path of the rays emitted by the dye that reach the edge of the collector, as they are generally reflected many times from the front and rear surfaces along their path [6]. The comparison between ray-tracing simulations and the *W&L* model is shown in Fig. 164.

The results show that such inhomogeneous collectors are equivalent to homogeneous collectors when $n_a = n_s$. Experimental re-absorption profiles of liquid collectors, obtained using the analytical methodology developed in Section 5.1.5, and validating these numerical simulations, are presented in Chapter 7.

With inhomogeneous structures, the refractive index of the substrate can of course be modified to direct the light into preferential layers of the device. Several liquid collectors and films, with identical absorbances but different refractive indices, were prepared and characterized in order to assess their wave-guiding potential. All the experiments showed a drop in efficiency as soon as the refractive index of the fluorescent layer was different from that of the substrate, indicating a failure of the thin-film "waveguide" collector concept. It is, however, important to stress that changing the solvent to modify the refractive index of the fluorescent layer also affects the surroundings of the fluorophore and hence the fluorescence properties of the dye (e.g. its quantum yield). Therefore, a direct comparison of efficiencies

for a range of solvents is not possible. This drop in efficiency was examined using ray-tracing simulations, as discussed in the next section.

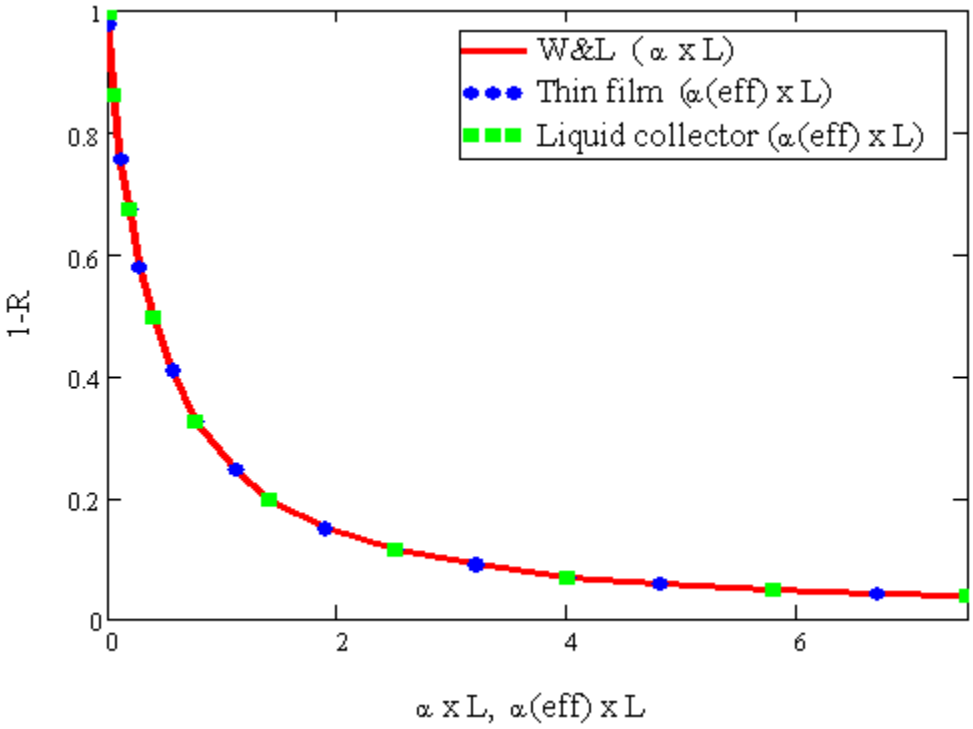

Fig. 164: Re-absorption probabilities for thin-film and liquid collectors, compared with the *W&L* model. (Graph published in [129])

5.2.2.1 Influence of the layers' refractive index

To understand the drop in efficiency observed in the experiments, the two variables *P* (the probability of emission within the escape cone) and *R* (the re-absorption probability) were numerically determined for various film refractive indices using TracePro®. To limit the number of case studies, the refractive index of the substrate was fixed at that of glass, $n_s = 1.5$, since this is the most common substrate referred to in the literature.

A thin-film collector $10\ mm \times 10\ mm$ with a film thickness of $200\ \mu m$ and a clear substrate of thickness $2\ mm$ was modelled. Two configurations where considered: (i) film on top of the substrate and (ii) substrate on top of the film. The collector materials were assumed to be perfectly clear, and the refractive index of the film was varied from $n_a = 1.1$ to $n_a = 2.7$.

The probability of emission outside the escape cone was calculated by examining the flux escaping from the edge of the collector. The results were dependent only on the refractive index of the fluorescent layer, and unaffected by the collector configuration. The probability of emission outside the escape cone thus

follows the same set of laws as for homogeneous devices (Eqn. (75)), which means that, in this respect, thin-film devices are again equivalent to flat-plate collectors.

A careful examination of light propagation as a function of the refractive index of the film showed that light tends to propagate within the film if its refractive index is different from that of the substrate.

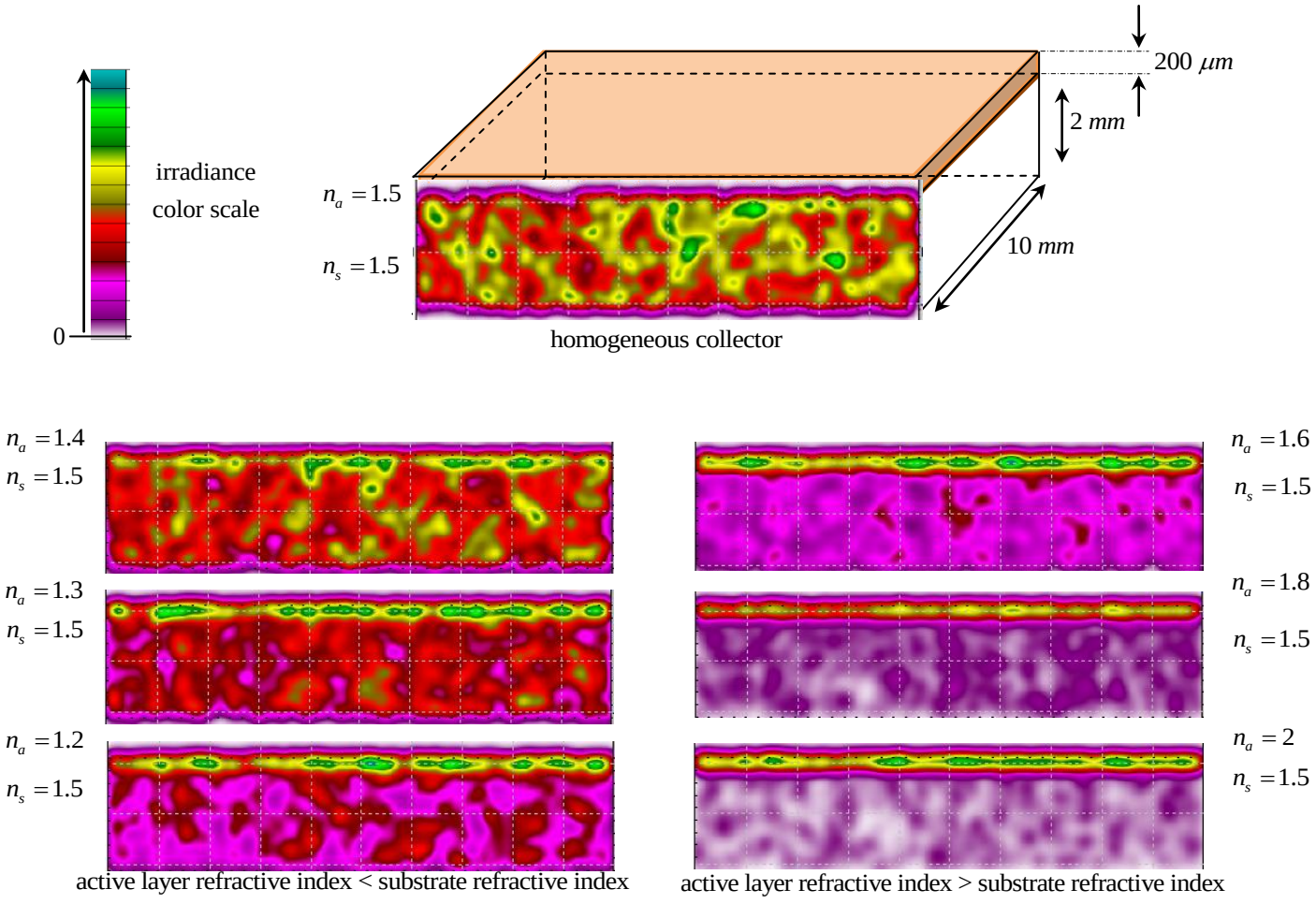

Fig. 165: Irradiance received by the edge solar cell as a function of the active layer refractive index.

Fig. 165 shows the light intensity incident on the edge solar cell for various values of the refractive index of the thin film. The photon flux emitted by the dyes trapped in the film was the same in each simulation, allowing comparison of the results. Although fluorophore emission levels were chosen subjectively in order for the ray-tracing simulations to run, the colour scale indicates the magnitude of the photon flux hitting the solar cell. In the simulations, the inclusion of re-absorption allowed a comparison between inhomogeneous devices and flat-plate collectors. The best re-absorption profile was obtained for $n_a = n_s$, with any other combination of refractive indices leading to an increase in the re-absorption probability, which explains the drop in efficiency observed in the experiments (Fig. 65).

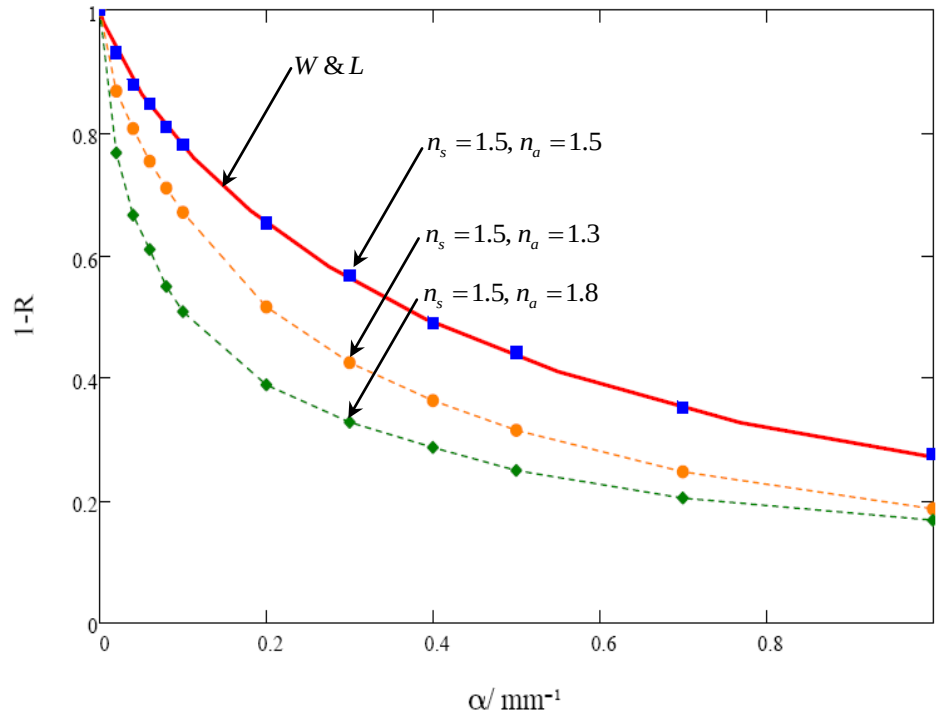

Fig. 166: Probability of re-absorption for various refractive indices (n_a) of a thin film coated onto a glass substrate with $n_s = 1.5$, as a function of the absorption coefficient of the thin film.

5.3 Discussion

The analytical models reviewed in this chapter demonstrate quantitatively the fundamental limitations imposed by re-absorption loss. Clearly the photon collection efficiency depends mainly on re-absorption probability. A recent model, the two-photon-fluxes model, derived by previous coworkers [73] and based on the work of Weber and Lambe and of Batchelder and Zewail, was thoroughly reviewed. The derivation of this model led to a new and simple experimental technique for characterization of the spectral re-absorption probability in a collector.

The validity of the *W&L* model was verified by means of ray-tracing simulations. Simulations of flat-plate, liquid and thin-film collectors demonstrated the validity and versatility of the Weber and Lambe model for re-absorption at high gain ratios. The ray-tracing simulations showed that collector geometry has no influence on collector operation.

In addition, it was shown that thin-film structures perform no better than standard collectors. The optimal configuration is reached when the refractive index of the film is the same as that of the substrate. In this case a thin-film device can be treated like a homogeneous device, with a resulting efficiency identical to a plain collector. High efficiency is then obtained for high refractive indices of the film and the substrate [98].

Chapter 6

Experimental procedures

This chapter presents the methodology for measurements performed on liquid collectors, specifically an original type of fluorescent collector in which absorption and fluorescence take place in the liquid phase. Although liquid-based collectors have no obvious practical or commercial application (Section 4.6) they represent a useful fundamental system which can mimic inhomogeneous (e.g. thin-film) structures, in order to validate models presented in the previous chapter.

Four types of measurements are required to fully characterize a liquid collector: (i) incoming photon flux intensity, (ii) absorbance, (iii) edge spectroscopy and (iv) first-generation spectroscopy.

This chapter is divided into three main sections. The first describes the structure and properties of materials used in the fabrication of liquid collectors. The second section is methodology-oriented, presenting an overview of the procedures for measurements (i) to (iv). The final section describes the process of calibrating the detection system (i.e. spectrometer and solar cell) and provides technical details of the equipment used.

6.1 Liquid collector design

A liquid fluorescent collector consists of four distinct elements: cuvette, luminescent agent, solvent and solar cell. The aim here was to select materials for a prototype liquid collector that resembled a genuine device as closely as possible.

The liquid collector used in this work is comparable to a "stretched" spectroscopic cuvette, a quartz tank of optical dimensions $50\ mm \times 50\ mm$ with a $0.5\ mm$ gap for filling the cuvette. A c-Si cell was coupled to one edge of the cuvette, creating a working device (Fig. 168).

The practical advantages of liquid collectors are numerous: the dye dissolved in a solvent forms a naturally homogeneous matrix, and issues of doping gradient and substrate optical coupling are avoided. In addition, in a cuvette-like collector, the liquid matrix can be changed in a few seconds, ready for a new series of experiments.

6.1.1 Cuvette dimensions and optical properties

Although the collector was designed at Southampton University, fabrication was made by Hellma GmbH in Germany. Suprasil® quartz with $n_s = 1.456$ @ 656.3 nm [173] was used for the tank. Each quartz wall was 1 mm thick, giving a light concentration gain **G** of 20 (Fig. 168).

All structural components of the cuvette were polished to extreme flatness, cleaned and joined using a direct fusing process to ensure that the boundaries or joints between components disappeared, resulting in a continuous structure. The temperature of the fusing process was below the softening point of quartz, so all components remained absolutely flat during the fabrication process (Fig. 167), maintaining the number of permitted defects in accordance with DIN standard 58170/54 [172] .

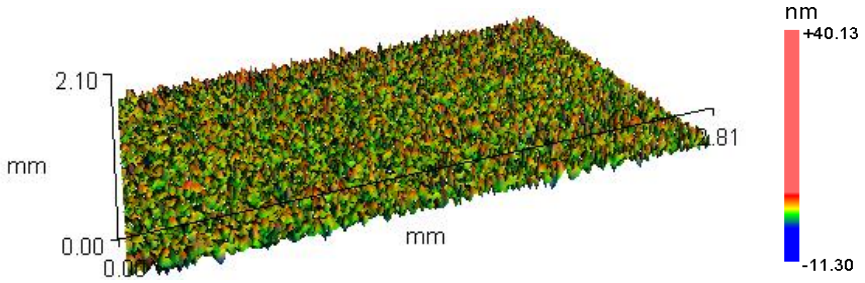

Fig. 167: Cuvette surface as rendered by an atomic force microscope. The roughness of quartz was measured by Lambda Photometrics over an area of 4 mm^2. Using the standard procedure developed in [174], Lambda Photometrics estimated a collector roughness of less than 1 *nm*, ensuring no scattering losses (Chapter 5).

6.1.2 Fluorescent material

It was impossible to study all available dyes because of their sheer numbers. Rare-earth dyes were omitted because of their high prices, while inorganic dyes were discarded because of unacceptable low quantum efficiencies. Laser dyes appeared to be the fluorophore category of choice. Eight of these were selected, four of them well known standard dyes: Rhodamine 6G (R6G), Rhodamine B (RB), Coumarin 540A (C540-A) and 4-dicyanomethylene-2-methyl-6-p-dimethylaminostyryl-4 H-pyran (DCM-dye). Although these standard dyes have already been thoroughly investigated [27], further studies on them allowed comparisons to be made with results from other coworkers, and helped to validate some novel measurement techniques (e.g. front fluorescence, Section 6.2.3). The four remaining dyes tested were the latest series of Lumogen dyes from BASF: Fyellow 083 (F083), Frot 305 (F305), Forange 240 (F240) and Fviolet 570 (F570).

The standard dyes were purchased from Acros with an original purity of around 99.5 %, and were used as received without further purification. The Lumogen dyes, kindly donated by BASF, were also used as received, without further purification. Properties of the dyes (quantum yield, extinction coefficient etc) are summarized in tables presented in Chapters 4 and 8.

6.1.3 Solvent

The main requirements for the solvent were:

- refractive index close to that of the cuvette, i.e. $n_s = 1.456 \,@\, 656.3\, nm$, in order to minimize inhomogeneity in the collector (Chapter 5)
- polar properties which permit the dye being studied to dissolve completely in it
- high boiling point, to mimimize evaporation during experiments
- negligible absorption coefficient over the visible and near infrared spectrum
- availability at high purity (i.e. spectroscopic quality).

In addition, the solvent should ideally be non-toxic and inexpensive. Table 13 presents the solvents considered.

Table 13: Solvent properties

Solvent	Molecular formula	Refractive index	Dipole moment (debye)	Boiling point (˚C)
Toluene	C_7H_8 ($C_6H_5CH_3$)	1.49† 1.494 @ 632.8 nm [175]	0.36 [176]	110.6 [176]
Butanol	$C_4H_{10}O$	1.39†	1.52 [176]	117.7 [176]
Dimethyl sulfoxide (DMSO)	C_2H_6OS	1.48† 1.48 [143]	3.96 [176]	189.1 [176]
Propan-2-ol	C_3H_8O	1.38†	1.66 [176]	82.3 [176]
Dichloromethane (DCM)	CH_2Cl_2	1.42†	1.14 [177]	39 [176]
Acetone	CH_3COCH_3	1.35† 1.357 @ 632.8 nm [178]	2.91 [176]	56.5 [176]
Methanol	CH_3OH	1.33† 1.325 @ 632.8 nm [179]	2.87 [177]	64.7 [176]
Water	H_2O	1.33† 1.333 @ 632.8 [176]	1.87 [177]	99.9 [176]
Ethanol	CH_3CH_2OH	1.36† 1.359 @ 589nm [179]	1.87 [177]	78.4 [176]

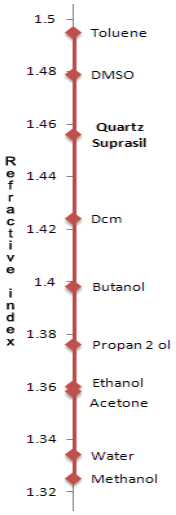

† Measurements made at Southampton University with a refractometer and a white tungsten light source

Butanol, propan-2-ol, acetone, water and methanol were discarded because of their low refractive indices, and toluene because of its weak dipole moment. The two solvents of choice were dichloromethane (DCM) and dimethyl sulfoxide (DMSO); both are highly polar solvents favouring dye dissolution, and both have refractive indices close to that of Suprasil® quartz.

One or the other of these was used in all experiments with Lumogen dyes, depending on favourable interaction with the selected dyes. During light exposure, the temperature of the cuvette was maintained between 20˚C and 26˚C with the help of fans, preventing any evaporation of the solvent.

For the standard dyes, ethanol was used in preference to either DCM or DMSO: despite its low refractive index, ethanol is the main spectroscopic solvent used in most fluorophore databases, allowing comparisons to be drawn.

6.1.3.1 Sample preparation

Each solution was prepared independently, using a known mass of crystalline dye dissolved in a known volume of spectrometric quality solvent, dispensed with ± 0.5 % accuracy and ± 0.1 % reproducibility using a bottle-top dispenser (Dispensette brand). Witness solutions of identical concentration were prepared independently during sample preparation, and used to check the accuracy and reproducibility of the measurements.

6.1.4 Sample holder

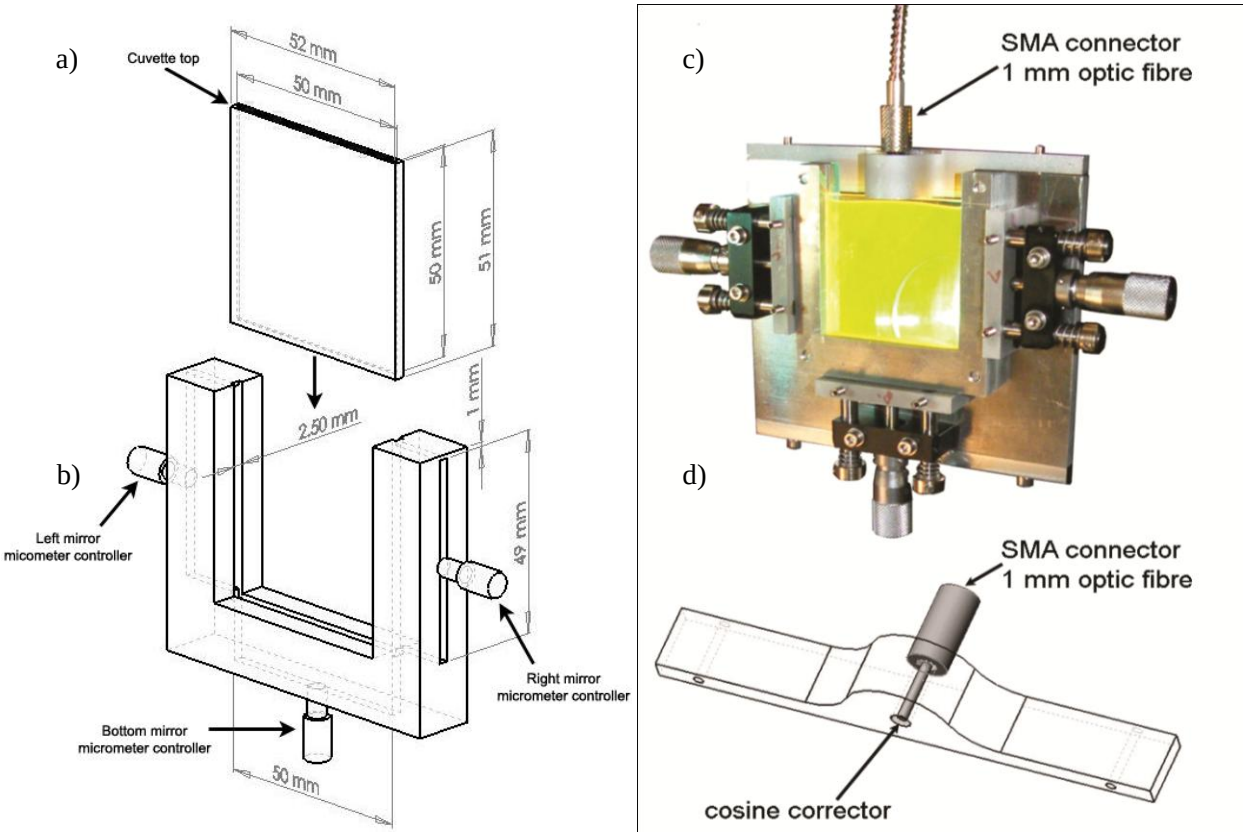

Fig. 168: a) Perspective view of the cuvette, showing how it was slotted into the sample holder. b) Perspective view of the U-shaped sample holder. c) Photograph of the liquid collector under test; the edge fluorescence was studied using various metallic brackets. d) Example of a metallic bracket designed for spectroscopic measurements of edge fluorescent flux. (Graphs published in [9])

The aluminium sample holder was designed to mimimize uncertainty in the position of the liquid device during measurements of fluorescence spectra. The sample holder was manufactured on a computer-controlled mill with a tolerance of less than $\pm 5\ \mu m$ on all dimensions shown in Fig. 168. When slotted

into the U-shaped sample holder, the quartz collector (external dimensions $51\ mm \times 52\ mm \times 2.5\ mm$) rested on two ledges (dimensions $1\ mm \times 2.5\ mm$). To avoid axial movement of the collector, the whole quartz structure fitted into a $1\ mm$ deep, $2.5\ mm$ wide trench, as shown in Fig. 168b.

The sample holder made use of movable mirrors to achieve the same geometrical configuration as in the *W&L* model (Chapter 5), the mirrors ensuring that light escapes only from that edge of the collector where the solar cell is placed. Three extrusions allowed micrometer-controlled mirrors to slide through the sample holder. The extrusions' dimensions, corresponding to the edge mirrors' dimensions, were $49\ mm \times 2.5\ mm$ for the mirrors at the left and right edges and $50\ mm \times 2.5\ mm$ for the mirror at the bottom edge.

Two types of reflectors were used to confine the light. The edge reflectors were made of Vikuiti™ polymer film enhanced specular reflector (98 % reflectance across the visible spectrum [180]). Such reflectors are easy to manipulate and can be cut to match the area of the collector edge. The rear mirror (not shown in Fig. 168), covering the entire rear face of the collector opposite the illumination source, was a quarter-wavelength first-surface mirror from Edmund Optics, with reflectivity > 80 % across the visible spectrum. The $50\ mm \times 50\ mm$ mirror was held against the collector using springs.
The sample holder was designed in such way that various spectroscopic measurements could be taken without moving the collector. Metallic brackets adapted to each type of measurement could be mounted on the sample holder as shown in Fig. 168c – to measure the edge fluorescence spectrum, the bracket shown in Fig. 168d was used, while for measuring the intensity of the edge fluorescence a calibrated c-Si solar cell covering the whole edge of the collector was used.
During experiments the collector was mounted upright, with the edge fluorescence always detected at the open edge – the top of the cuvette. This avoided reflectance at the quartz/matrix interface, and mimicked real devices in which the photovoltaic cell is coupled directly to the matrix.

6.2 Overview of the measurements procedure

As noted in the introduction to this chapter, four types of measurements are required to fully characterize a collector: incoming photon flux intensity (Section 6.2.1), absorbance spectrum (Section 6.2.2), first-generation spectrum and edge fluorescence spectrum (Section 6.2.3). All measurements were made in a light-proof black box; the uniform illumination incident on the collector was delivered by a calibrated source (CL2) placed $26.5\ cm$ away.

The characterization methodology which arises from the two-photon-fluxes model discussed in Chapter 5 is based on accurate measurements of the fluorescence and absorbance spectra. Each emission spectrum

presented in this report has therefore been corrected for instrumental imperfections using a method proposed by Lakowitz [27] which relies on the use of a spectrometer to characterize the spectral photon distribution and a solar cell to measure the intensity of the photon flux.

6.2.1 Incoming photon flux

A Bentham CL2 universal spectral irradiance standard lamp (calibration traceable to the National Physical Laboratory, Teddington, UK) with a wavelength range $250\,nm$ to $3000\,nm$ and a colour temperature of $3270\,K$ (Fig. 169) was used to illuminate the liquid collector. The first parameter to be measured was the number of photons striking the collector per second; three methods were used to characterize this photon flux.

1. Using the inverse square law of radiation, the spectrum of the lamp at $26.5\,cm$ was computed from calibration data.
2. The incident spectrum of the lamp was directly recorded using a calibrated AvaSpec-2048 spectrometer and a $1\,mm$ diameter cosine-corrected optical fibre. Cosine-corrected optical fibres can be used as irradiance probes collecting radiation over 2π steradians, eliminating the optical interface problems associated with the sampling geometry inherent in bare fibres and other sampling devices. The diffusing material used in the cosine corrector is a thin disk of Teflon with a $3900\,\mu m$ diameter, optimized for applications from $200\,nm$ to $1100\,nm$, placed at the end of a stainless steel barrel screwed onto the fibre SMA connector.
3. The intensity of the incident light was measured with a calibrated $1\,cm^2$ DH-Si silicon low-noise photodiode. The integration of photodiode spectral response, $SR_{dh}(\lambda)$, times the energy flux of the CL2 source, $f_s(\lambda)$, gives the current expected over a unit area:

$$J_{sc} = \int SR_{dh}(\lambda) f_s(\lambda)\ d(\lambda)\ . \tag{114}$$

All three techniques agreed to within 1 %. In practice, during data analysis the incident spectrum was modelled by a blackbody radiator at $3270\,K$ with a solid angle of $7.66 \times 10^{-6}\,sr$. Fig. 169 shows the actual recorded data compared to a blackbody function.

When the spectrum of the CL2 lamp was not suitable for excitation of a fluorescent dye, a xenon lamp with a photon distribution approximating the AM 1.5 spectrum in the short wavelength region was used.

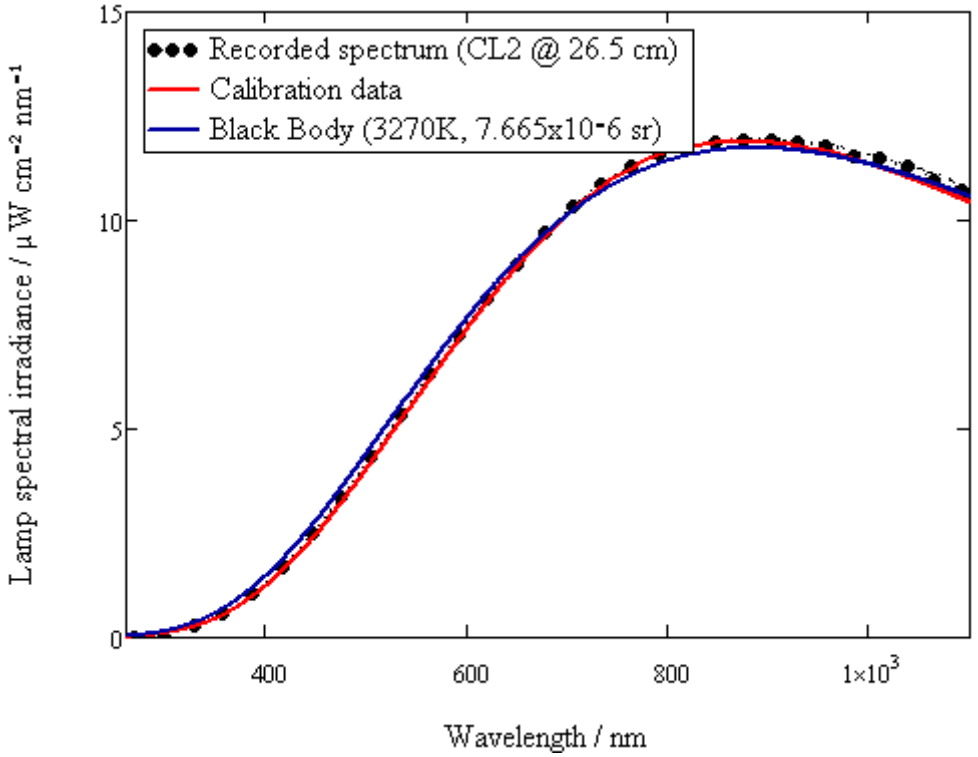

Fig. 169 Spectrum of the CL2 lamp at 26.5 *cm*. Black dots: spectrum measured with Avantes spectrometer. Blue line: blackbody spectrum at 3270 *K*. Red line: calibration data. (Graph published in [58])

6.2.2 Absorbance measurements

The absorbance spectra were measured in a standard fashion. The CL2 lamp delivered a uniform, stable beam of light over the whole surface of the collector, and an optical fibre at the back of the collector measured the spectrum of the transmitted light.

To avoid instrumental error the absorbance spectra of highly concentrated solutions were measured within the liquid collector (short light path 0.5 *mm*) while the absorbance spectra of more dilute solutions were determined using a standard 1 *cm* light path quartz cuvette. In the course of data analysis the absorption spectra were scaled for a light path of 1 *mm*, corresponding to the path of light in the collector with the addition of the back specular reflector.

6.2.3 Fluorescence measurements

In Chapter 5 it was shown, using Eqn. (105), that the ratio of the edge fluorescence spectrum to the re-absorption-free fluorescence spectrum is sufficient to characterize the re-absorption probability.

Measurements of edge fluorescence are fairly straightforward, using an optical fibre connected to a spectrometer at the edge of the collector (Fig. 168c). However, the recording of the first-generation fluorescence spectrum $f_1(\lambda)$ requires some care.

The standard procedure [27] for recording $f_1(\lambda)$ consists of measuring the fluorescence of a weakly doped solution, thus avoiding any re-absorption effects. The fluorescence of weakly doped solutions was studied in a standard $1\,cm$ fluorescence cuvette. The maximum absorption per centimetre was kept below $\alpha = 0.07\,cm^{-1}$, where the effect of re-absorption appears in the fluorescence spectra [27]. The excitation source was a IL1 Bentham lamp filtered by a Tmc300 monochromator, and fluorescence was detected at a 90˚ angle from the illumination. The results of first-generation spectra measured in this way agreed within 1 % with those reported in the literature [27].

This technique worked well because of the homogeneity of the matrix solution, whereas for a non-liquid device (e.g. film coated on substrate) it would fail because of the difference in composition between bulk material and thin film [6]. Subsequently, two generic methods were developed, estimating $f_1(\lambda)$ from the fluorescence escaping from the front of the collector.

Front fluorescence is a good approximation to the first-generation spectrum (see Fig. 173) because the fluorescence escaping within the critical cone at the air/collector interface undergoes few re-absorption events, and is thus negligibly affected by re-absorption phenomena (e.g. red shift). In fact there is a very small chance of photon re-absorption within the thickness of the matrix for perpendicularly re-emitted light. In this thesis, emission spectra collected from the front face of the collector are referred to as front fluorescence spectra. Front fluorescence was measured using either a Y-fibre or a bias illumination. It is important to note that the first-generation spectrum is normalized during data analysis, so only the spectral shape is of interest here.

6.2.3.1 Y -fibre front detection

Y-fibres (Fig. 170) are special optical fibres in which the detection and excitation fibres are located in the same tip, allowing simultaneous illumination and fluorescence detection.

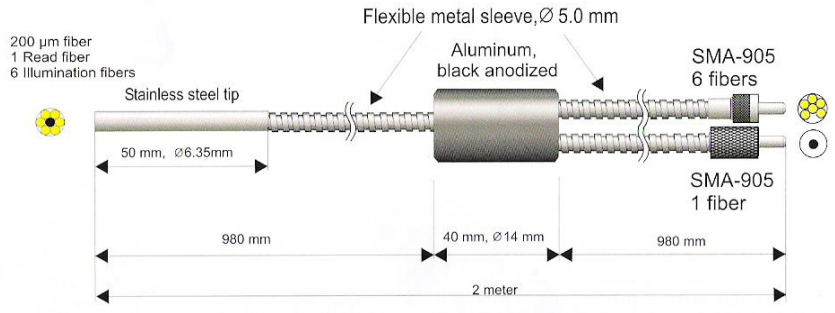

Fig. 170: Schematic of a Y-fibre. The detection fibre (black) is surrounded by six illumination fibres (yellow), allowing simultaneous unidirectional illumination and detection of the collector. During measurements the SMA-905 (illumination bundle) was directly connected to the output of a monochromator (TMc300) while the detection fibre SMA-905 was directly linked up with the AvaSpec-2048 spectrometer.

One advantage of a Y-fibre is that the detection fibre can measure emission spectra within a very narrow solid angle; thus if the tip of the Y-fibre is mounted perpendicular to the collector front face it will detect only the fluorescence emitted within the escape cone (Fig. 171).

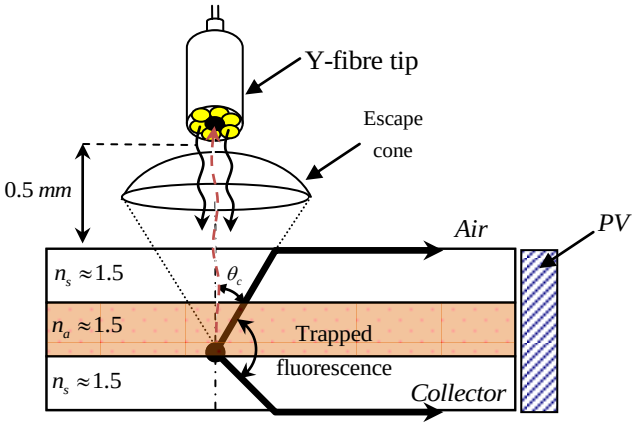

Fig. 171: Y-fibre front fluorescence measurement setup, with excitation rays and detected fluorescence represented by black and red arrows, respectively.

6.2.3.2 Bias illumination

Results obtained with the Y-fibre were compared with a second series of measurements using a different technique, "bias illumination". Using a combination of suitable filters and lenses, a standard optical fibre was used to illuminate a spot on the front surface of the collector. The incident beam was fixed at 30° relative to the normal of the substrate. Fluorescence was then detected using a standard 1 *mm* diameter fibre (Fig. 172).

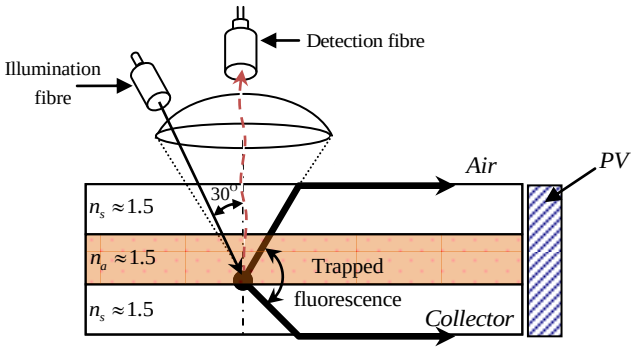

Fig. 172: Setup for bias illumination detection. The excitation ray and detected fluorescence are represented by black and red arrows, respectively.

The results recorded using Y-fibre and bias illumination detection were compared to data from the literature (Fig. 173). The recorded spectra (blue and green dots) are in good agreement with the reference spectrum (red line), thus validating the methods proposed here.

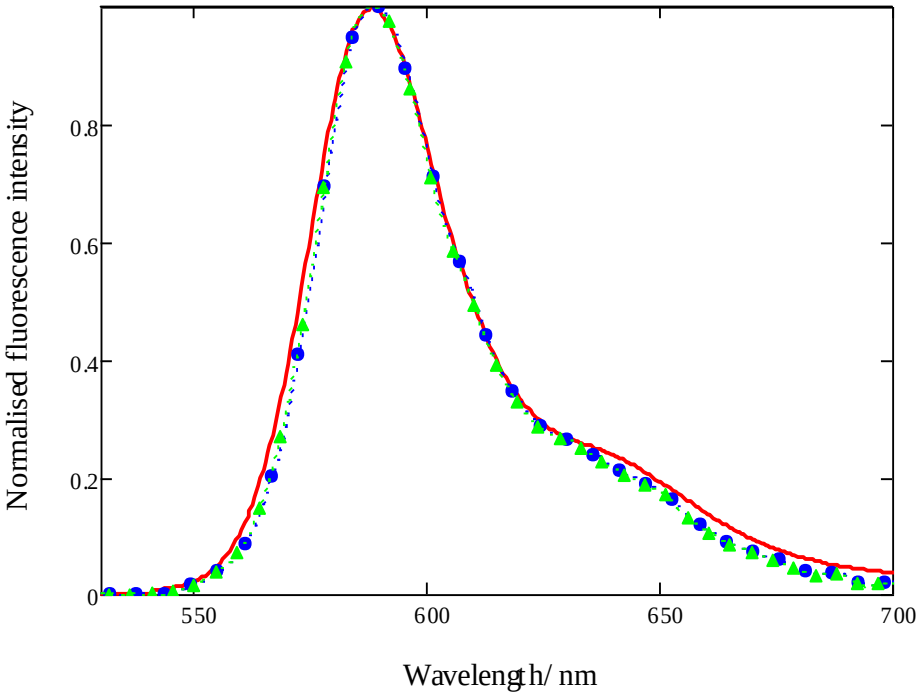

Fig. 173: First-generation spectrum of R101 in ethanol at 300 *K*. Red line: data from [181]. Blue dots: Y-fibre detection. Green triangles: bias illumination detection.

6.2.3.3 Edge fluorescence

The fluorescence emitted at the edge of the collector was detected at 90˚ to the incident radiation. The CL2 lamp, placed 26.5 *cm* away from the collector, illuminated the whole device uniformly. The collector was surrounded by mirrors pressed against the sides and back of the collector to generate the same geometric configuration as in the *W&L* model. Edge fluorescence spectra were measured using the Avantes spectrometer and a 1 mm diameter cosine-corrected optical fibre placed at the middle of the collector edge, as shown in Fig. 168c. Spectra were recorded with an integration time of 300 ms, averaged 50 times with their maximum intensity normalized to unity. Only the corrected fluorescence profile is of interest at this stage.

Once the contours of the fluorescence spectra were recorded, the optical fibre was replaced by a calibrated solar cell covering the whole top side of the cuvette. The cell and collector were optically coupled using an index matching gel (ThorLabs). The short-circuit current (I_{sc}) recorded by the cell was used to scale the intensity of the fluorescence spectra previously obtained. The normalized fluorescence profile was multiplied by an appropriate constant so that the following relation holds:

$$I_{sc}/\mathrm{A}_{edge} = \int SR_{pv}(\lambda)\tilde{f}_e(\lambda)\ d(\lambda), \tag{115}$$

where $SR_{pv}(\lambda)$ is the spectral response of the cell and $\tilde{f}_e(\lambda)$ is the scaled fluorescence spectrum.

The edge cell short-circuit current was measured with a calibrated analogue-to-digital DC amplifier (Bentham 487) module. The spectral response of the solar cell was characterized using the following procedures.

6.3 Calibration procedure

Absolute measurements of fluorescence are crucial for the data analysis (Chapter 7). A two-step methodology using a spectrometer and a c-Si solar cell were used to carry out these measurements accurately. The following sections report the procedure followed to calibrate the spectrometer and the methodology employed to characterize the edge solar cell.

6.3.1 Spectrometer calibration

The Avantes AvaSpec-2048 spectrometer is based on a symmetrical Czerny-Turner design with a 2048 pixel CCD detector array (Fig. 174). It has a fibre optic entrance connector, and collimating and focusing mirrors with a diffraction grating allowing measurements in the $300 - 1100\ nm$ wavelength range, giving an ideal spectral range of $800\ nm$ for the study of UV/visible spectra (Table 14).

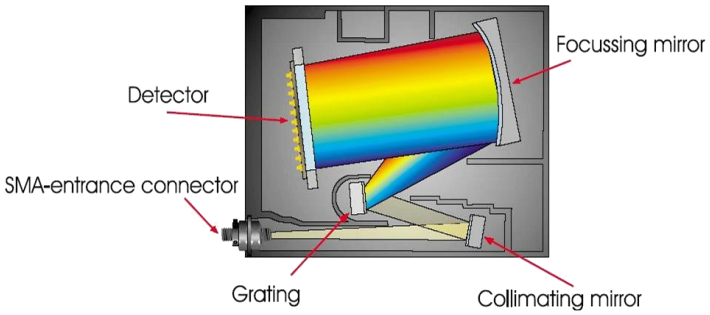

Fig. 174: Symmetrical Czerny-Turner spectrometer design. Light enters the optical bench through a standard SMA905 connector and is collimated by a spherical mirror. A plane grating diffracts the collimated light; a second spherical mirror focuses the resulting diffracted light. An image of the spectrum is projected onto a one-dimensional linear CDD detector (figure taken from the Avantes user's manual).

Table 14: AvaSpec-2048 technical data (source: Avantes user's manual)

Optical bench	Resolution	Sensitivity	Signal/noise	Integration time	Sample speed
Czerny-Turner $75\ mm$ focal length	$0.04\ nm$ to $20\ nm$	$5000\ counts\ \mu W^{-1}\ ms^{-1}$	250:1	$2\ ms$ to $60\ s$	$17\ ms/scan$

In order to record accurate fluorescence spectra, the whole detection system – spectrometer and fibre optics – must be corrected to take account of the wavelength-dependent efficiency, since the optical fibres guiding the fluorescence signal generate losses. The correction method used in the present research is based on the comparison of technical records with known emission spectra [27].

The efficiency of the detection system was calibrated in intensity against the spectrum of the CL2 lamp, in a three-step process:

1. The CL2 lamp spectrum was measured at a known distance, in $counts\ s^{-1}\ m^{-2}\ nm^{-1}$ (default units) over a wavelength range of $250 - 1100\ nm$, using the cosine-corrected optical fibre adopted in the experiments.
2. A transfer function for converting the photon count of the detection system was calculated as the ratio of the recorded spectrum to the calibrated CL2 lamp data.
3. The corrected spectra were obtained by dividing the measured spectra by the transfer function.

The validity of this correction method was confirmed by comparing the emission spectra of several standard fluorescent compounds – Rhodamine 6G (R6G), Rhodamine B (RB) and Coumarin 540A (C540-A) – with the reference data for each. The agreement between the reference and the measured spectra was excellent, within 1.5 % deviation over the range $300 - 900\ nm$.

It is important to stress here that this procedure does not calibrate the spectrometer intensity (since recorded and standard spectra are compared after normalization), but the spectral response of the detection system.

Calibrating a spectrometer's output intensity is difficult and time-consuming – and even after careful calibration the results are only accurate to ± 15 % [27] since optical fibres are typically manipulated, disconnected and reconnected between the calibration and the actual measurements – which explains why many authors prefer to report normalized spectra. Given that the uncertainty in intensity may exceed the accuracy required in the present research, only the shapes of the fluorescence spectra were recorded with the spectrometer. The absolute magnitudes of the recorded spectra were then determined using calibrated solar cells.

6.3.1.1 Noise reduction and pixel smoothing

Two techniques are frequently used to reduce noise in the spectral measurements:

- averaging of replicate scans
- smoothing algorithms.

An average replicate scan is useful for reducing the noise in the main part of the spectrum, while it has been shown that the Boxcar pixel-smoothing algorithm [182] significantly reduces the noise in spectral measurement traces.

The pixels are the specific locations in a CDD sensor where signal intensity is interpreted by the spectrometer. Incoming light is directed to a particular place on the sensor according to its wavelength, with a set of pixels detecting a particular wavelength. The number of pixels defines the spectral accuracy of the spectrometer. In a Boxcar smoothing, for a particular pixel the spectrometer uses a percentage of the intensity of neighbouring pixels for the smoothed value; the further away a neighbouring pixel, the smaller its effect on the smoothed value.

Throughout the measurement procedure, each spectrum was Boxcar-smoothed over five pixels, with an average of 50 replicate scans for each record.

6.3.2 Solar cell calibration

The solar cell coupled to the collector edge was a $50\,mm \times 2.5\,mm$, $120\,mm^2$ active area, c-Si solar cell from Solartec. Prior to all measurements using a given cell, the *IV* characteristics of the cell were studied to characterize its efficiency, while the spectral response was studied to scale the recorded fluorescence spectra in intensity.

6.3.2.1 *IV* characteristics

The *IV* characteristics of the cell were measured using a solar simulator (TS-Space Systems) equipped with a xenon lamp. A HP4142B DC source/monitor and Kelvin connections, which separate the channels for voltage and current measurements, eliminating voltage drops across cable connections, were used to minimize measurement errors. Computer software developed in [6] to control the HP4142B DC was used to apply voltages from $-0.6\,V$ to $0.7\,V$ to the solar cell; the current was then recorded with a lock-in amplifier. The *IV* characteristics were recorded for the cell in the dark and under $1000\,W\,m^{-2}$ white illumination. The standard white illumination was supplied by a $300\,W$ xenon lamp and the light intensity was calibrated at $AM1.5$ with the help of a standard silicon solar cell of $2 \times 2\,cm^2$ area calibrated against a primary reference at NREL (USA). The temperature of the cell was checked and regulated in the range $25\,°$ to $26\,°$ C.

The experimental *IV* curves (Fig. 175) were analysed with IVFIT® software, extracting FF, I_{sc}, V_{oc}, R_s, $R_{//}$, I_0, I_{02} and η_{PV} (Chapters 2 and 3). IVFIT uses an orthogonal distance regression fitting method which reduces uncertainty in the extracted values. The parameters for the cell used with the fluorescent collector are presented in Table 15.

Table 15: Solar cell parameters extracted from the *IV* curves

$J_{sc}(mA\,cm^{-2})$	$V_{oc}(V)$	$R_s(\Omega)$	$R_{//}(\Omega)$	$I_{01}(A)$	$I_{02}(A)$	$FF(\%)$	$\eta_{PV}(\%)$
27.2	0.515	2.07	198.33	$7.35\text{x}10^{-13}$	$1.28\text{x}10^{-7}$	67.7	9.32

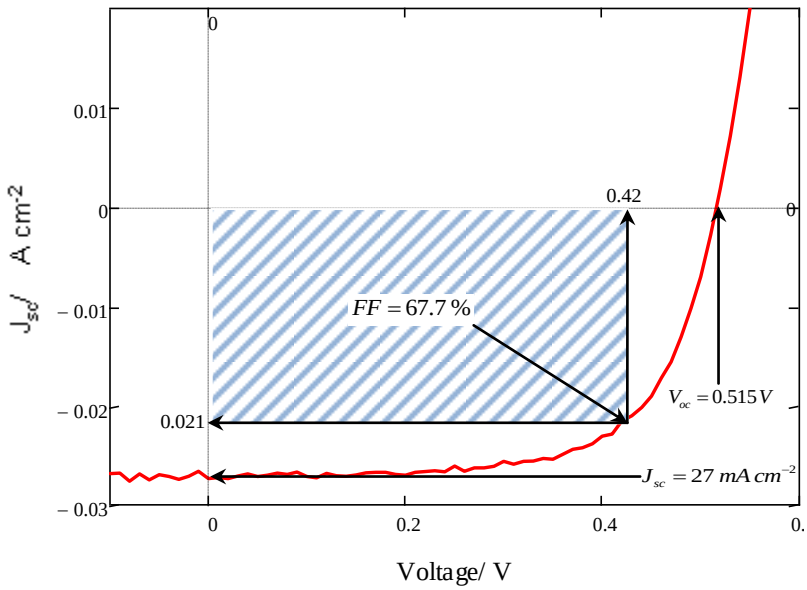

Fig. 175: *IV* characteristics of the edge c-Si solar cell under *AM* 1.5.

6.3.2.2 Spectral response and cell quantum efficiency

The spectral response of the edge solar cell, in amperes generated per watt of incident light, was measured against a calibrated 1 cm^2 DH-Si silicon low-noise photodiode. The spectral response is linked to the external quantum efficiency *EQE* (Chapter 3) by the relation:

$$SR(\lambda) = \frac{q\lambda}{hc} EQE(\lambda) = \frac{q\lambda}{hc} IQE(\lambda)\big(1 - \mathbb{R}(\lambda)\big), \tag{116}$$

where

$$SR(\lambda) = \frac{J_{sc}}{\frac{hc}{\lambda} \times \dot{f}_s(\lambda)}, \tag{117}$$

$\dot{f}_s(\lambda)$ is the incident photon flux per unit area and IQE is the internal quantum efficiency of the cell.

The measurement technique proposed here is based on the use of an IL1 quartz-halogen lamp controlled by a stabilized and calibrated Bentham 605 power supply coupled to a TMc300. The TMc300 is a monochromator using a precision microprocessor-controlled micro-stepping drive to a grating; mechanical resolution of the grating drive is 0.00072° per motor step.

The Bentham IL1 is an ultra-stable irradiance lamp with a wavelength range of 350 nm to 2500 nm and an irradiance peak of 1.3 $mW\ cm^{-2}\ nm^{-1}$ at 800 nm. When the IL1 lamp is connected to the 605 power supply the stability of the lamp is better than 0.1 % over an eight-hour running period.

The measurement synopsis is as follows: The light emitted by the IL1 lamp is filtered by the TMc300 in 5 nm steps. The light escaping from the monochromator is guided to the solar cell by a 1 mm UV/visible

optical fibre. The response of the cell is measured in amperes at each rotation of the monochromator. The spectral response of the cell (in $A\ W^{-1}\ nm^{-1}$) is then determined from this procedure. However, prior to any measurement with an actual solar cell, the whole illumination system composed of the IL1 lamp, TMc300 monochromator and optical fibre must be calibrated against a reference (1 cm^2 calibrated DH-Si silicon low-noise photodiode).

The DH-Si silicon low-noise photodiode has a sensitivity range of $200\,nm$ to $1100\,nm$, with a peak sensitivity at $960\,nm$. In the experiments the photodiode current was measured using a Bentham 487 module, an accurate integrating analogue-to-digital converter DC amplifier. The typical dark current of the photodiode was $200\,nA$.

To calibrate the illumination system, the optical fibre linked to the TMc300 was placed perpendicular to the active face of the DH-Si photodiode. The distance between the fibre end and the photodiode was $2\,mm$, ensuring that the entire illumination spot was absorbed by the photodiode. The spectral response of the illumination system was then recorded from $200\,nm$ to $1100\,nm$, in $5\,nm$ steps.

Knowing the current generated at every rotation of the grating, and the spectral response of the photodiode, it was possible to determine the incident photon flux escaping the optical fibre as a function of wavelength. Once the illumination system is characterized it suffices to simply replace the photodiode with an unknown solar cell.

The Bentham PVE300 Photovoltaic Characterization System, now available commercially, automates this entire procedure. The advantages of this technique reside in the use of the monochromator, allowing step variations of $5\,nm$ or less, a major benefit when compared to traditional solar simulators equipped with $50\,nm$ step filter wells.

The validity of this technique rests on the uniformity of the cell tested. Indeed, the illumination spot delivered by the optical fibre does not illuminate the whole sample but only a part of it. The cell spectral response is assumed to be independent of the position of the illumination fibre. Considering the way cells are made, layer by layer, this assumption should be valid for most of the devices.

Several tests where made by recording the spectral response of the cell by moving the position of the illumination fibre, variations of $\pm$ 2.5 % on the different measurements were observed. To validate the spectral response measurements shown in Fig. 176, obtained with the method presented here, the results were compared with a classical measurement method [6] by testing the cell in a solar simulator (TS-Space Systems) equipped with a xenon lamp and a filter selection wheel ($400 - 1000\,nm$, $50\,nm$ steps) calibrated against an NREL reference solar cell. The comparison is shown in Fig. 177.

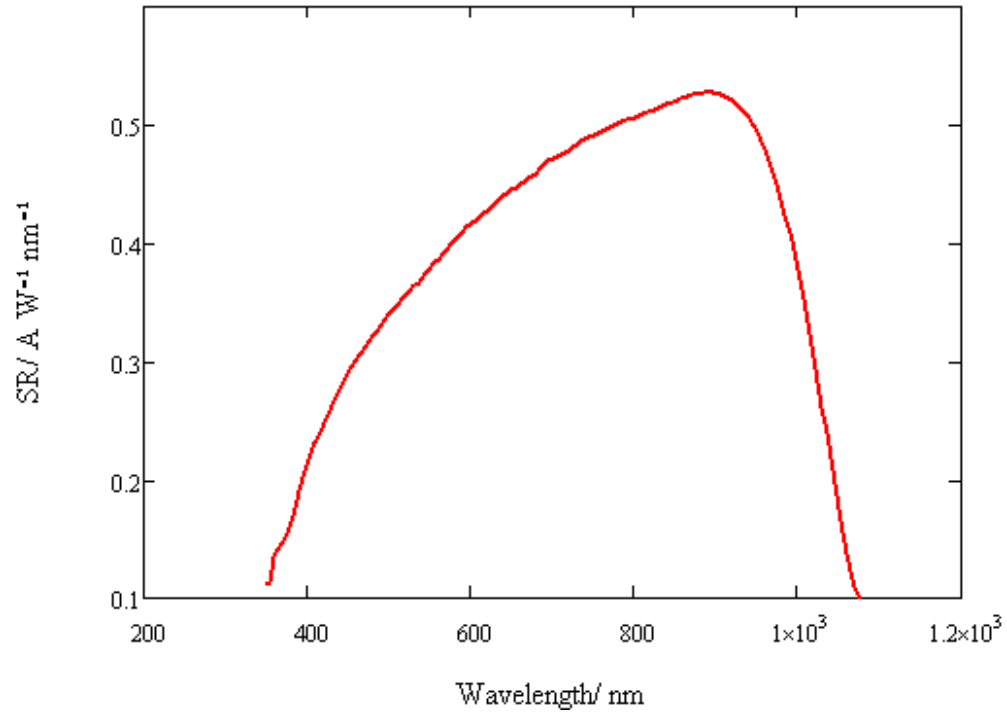

Fig. 176: Spectral response of the edge solar cell, measured with the spectrometer.

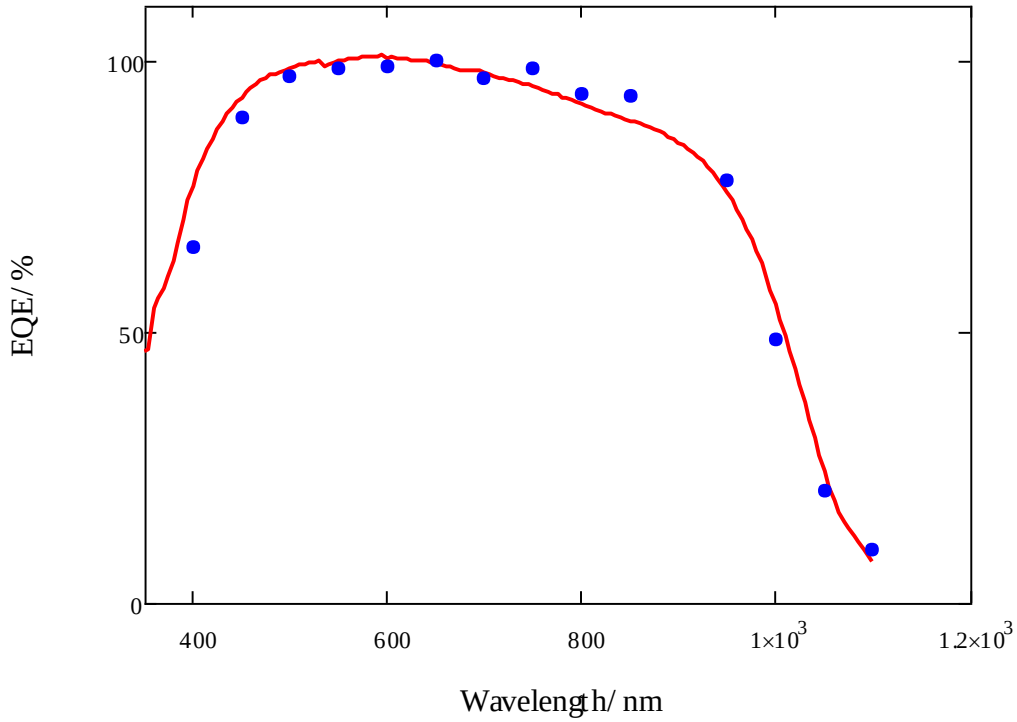

Fig. 177: Normalized external quantum efficiency of the edge solar cell. Red line: measurements obtained with the technique presented here. Blue dots: standard measurement technique using a solar simulator (TS-Space Systems) equipped with a xenon lamp.

6.4 Discussion

In this chapter the experimental procedure, collector design, characterization and calibration methods have been presented. Four spectra – incident light, absorbance, and first and edge fluorescence – necessary for the characterization of a collector in operation where measured. Absolute measurements of fluorescence were made using a calibrated spectrometer (to record the shape of each spectrum) and a solar cell (to characterize the intensity of the photon flux).

Two techniques for estimating the first-generation spectrum using the photon flux escaping from the front of the collector were presented and validated. However, it is important to stress here that, because of technical limitations, this technique does not allow accurate measurement of the front fluorescence photon flux – indeed it is impossible to record accurately the intensity of the front fluorescence with a solar cell, since the shadow of the cell would block the incoming light.

Therefore we have only investigated the shape and relative magnitude of the front-generation spectrum. As noted in Chapter 5, this spectrum – the optimal fluorescence that can be collected at the edge of the collector – will serve as a reference for scaling the edge spectrum in the following chapter.

Chapter 7

FSC performance characterization

This chapter will demonstrate how fluorescence spectroscopic analysis can be used to evaluate the performance of a fluorescent solar collector.

The first section deals with the performance characterization of collectors doped with a single dye. FSC performance is evaluated either by direct measurement of incoming and escaping photon fluxes or by application of the two-photon-fluxes model to spectroscopic data sets. The validity of this model is demonstrated by comparing experimental data with predicted values – absorption efficiency, collection efficiency and re-absorption probability of collectors doped with R6G, R101, F305 or RB dye are reported. Using re-absorption data obtained from the application of the two-photon-fluxes model it is shown that inhomogeneous collectors such as liquid or thin-film collectors perform identically to flat-plate collectors, as predicted by ray-tracing simulations (Section 5.2).

The second part of the chapter examines collectors doped with multiple dyes. With a mixture of F305 and DCM-dye dissolved in DMSO, the optical efficiency of the fabricated liquid collector reaches $\eta_{col} \approx 7\ \%$ (under *AM* 1) – one of the highest efficiencies reported in the literature. Nevertheless, practical limitations mean that the system is still far from its theoretical performance. Using data from the collector performance characterization, a map can be made of the losses occurring during photon transport. It is shown that the shortage of suitable laser dyes limits the operation of FSCs coupled with c-Si cells. The optimal semiconductor band gap is investigated.

Before starting the data analysis a qualitative discussion is in order. Typical edge fluorescence spectra of collectors doped with a single dye are shown in Fig. 178. The spectra for each concentration were obtained under identical illumination conditions. Each spectrum corresponds to the same incident photon flux delivered by the CL2 lamp (Chapter 6). As already pointed out, edge fluorescence spectra display two facets of photon transport in the collector:

(i) a high-energy spectral region where re-absorption brings photons into thermal equilibrium

(ii) a low energy spectral region where light, trapped by total internal reflection, travels freely in the collector.

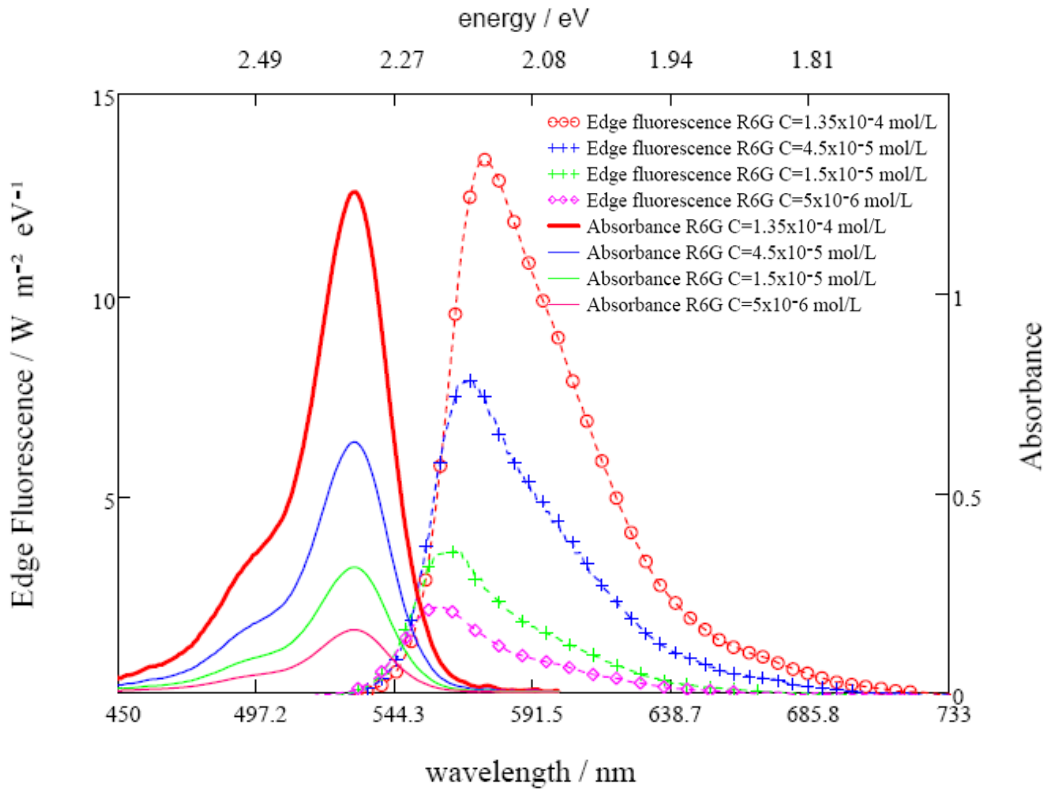

Fig. 178: Typical edge fluorescence spectra (Rhodamine 6G in ethanol) and associated absorption spectra; the legend indicates dye concentration in the solvent.

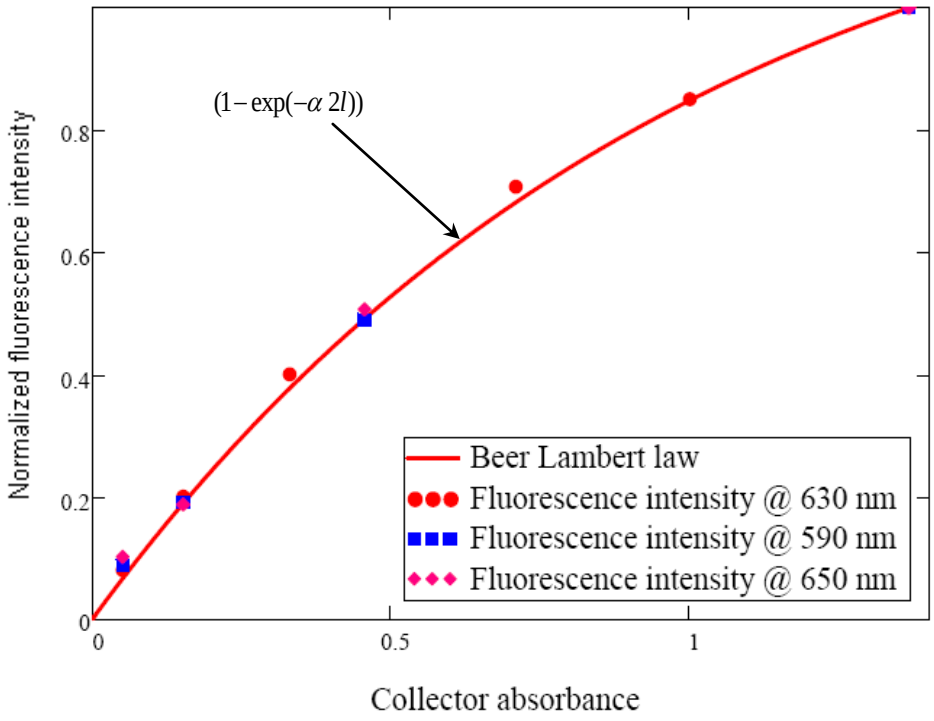

Fig. 179: Normalized intensity of edge fluorescence compared to the relative number of photons absorbed by the collector.

Fig. 178 is a typical recorded data set, illustrating perfectly the two facets of photon transport in a collector:

- At the high-energy end of the fluorescence spectra the data overlap in a single line which resembles a quasi blackbody function.
- In the long-wavelength region, where re-absorption is negligible, fluorescence intensity is proportional to dye concentration.

The thermodynamic behaviour of fluorescence is treated in Chapter 8. For now, we focus on the long-wavelength region. To demonstrate the connection between fluorescence intensity and photon absorption, in Fig. 179 the fluorescence intensities at three long wavelengths ($590\,nm$, $630\,nm$ and $650\,nm$) are plotted against collector absorption and compared to the Beer-Lambert law. Clearly in this spectral region fluorescence intensity is proportional to the number of photons absorbed. Deviation from this ideal behaviour can occur if the fluorescence is quenched (Chapter 1).

From this one might expect the shape of all normalized edge fluorescence spectra to be the same, and to resemble the first-generation fluorescence spectrum. This is indeed the case, and is the key argument for the simple application of the two-photon-fluxes characterization method.

7.1 Characterization of liquid collectors doped with a single dye

In Chapter 5 the optical efficiency of a fluorescent collector (η_{col}) was defined as the product of the collection efficiency (Q_c) and the absorption efficiency (Q_a). If the collector is coupled to a solar cell with an efficiency (η_{PV}), the overall performance of the FSC is given by the product $\eta_{FSC} = \eta_{col}\eta_{PV} = Q_a Q_c \eta_{PV}$.

In this section, two techniques for characterizing the performance of the fabricated liquid collectors are compared:

- an experimental technique consisting of measuring the number of photons coming into and escaping from the collector, the ratio of these two quantities directly giving (η_{col})
- a semi-analytical, semi-experimental technique based on the two-photon-fluxes model, characterizing collector efficiency through the re-absorption probability.

7.1.1 Experimental characterization

The experimental characterization technique uses a solar cell as a detector, to determine the incident and escaping photon fluxes. In practice, the same calibrated solar cell is placed in front of the source to assess the number of incoming photons and then at the rim of the collector covering the whole top edge of the cuvette (Chapter 6). The photon flux was measured by means of the short-circuit current of the solar cell. Taking into account the spectral response of the solar cell, the ratio of the two directly measured fluxes gives the optical efficiency of the collector (η_{col}).

Using the relation $Q_c^{\exp} = \eta_{col}/Q_a$, the experimental collection efficiency was determined, to allow direct comparison with the two-photon-fluxes model. The absorption efficiency was computed from the known absorbance spectra of the dyes doping the collectors (Eqn. (80)).

The collectors studied in this section were single-dye devices, designed to operate under monochromatic light. Hence the absorption efficiency was defined in the region where the dye absorbs the light, with wavelength integration limits defined as the points where absorbance has dropped to 10 % of its peak value.

Since $Q_c^{\exp}$ is measured with an actual collector and solar cell it includes photon transport losses. A comparison of experimental data with the results of a two-photon-fluxes analysis is shown in Fig. 183.

7.1.2 Two-photon-fluxes characterization

The two-photon-fluxes method defines collection efficiency as the mean of the spectral re-absorption probability. Using the definition derived in Chapter 5, collection efficiency in this model is given by:

$$Q_c = \int \frac{\varphi(1-P)\left(1-r(\lambda)\right)}{1-\varphi \mathrm{R}(1-P)} \tilde{f}_1(\lambda)\, d\lambda, \tag{118}$$

where $\tilde{f}_1(\lambda)$ the normalized first-generation fluorescence.

All the parameters of Eqn. (118), apart from the re-absorption probability, have been previously defined. The probability of emission within the escape cone (P) is obtained using Eqn. (74), and the first-generation spectrum is approximated by the front fluorescence spectrum (Chapter 6). The dye quantum yield (φ) is obtained from the literature.

As demonstrated in Chapter 5, the spectral re-absorption probability in the wavelength region where re-absorption is negligible is given by:

$$r(\lambda) = 1 - \frac{\tilde{f}_e(\lambda)}{\tilde{f}_1(\lambda)}, \tag{119}$$

where $\tilde{f}_e(\lambda)$ is the normalized edge fluorescence spectrum ($\tilde{f}_e(\lambda) = \dot{f}_{\mathrm{e}}(\lambda)/\varphi(1-P)\dot{f}_{abs}(\lambda)$).

Normalization of the edge fluorescence spectra is simplified by making use of the facts that fluorescence intensity is proportional to the number of photons absorbed and that $1/\varphi(1-P)$ is a constant independent of the dye concentration. In the following development, the edge spectra are directly scaled down to first-generation spectra [73].

The following steps were used in the data analysis:

- Normalize the front fluorescence spectrum, $\int \tilde{f}_1(\lambda)d\lambda = 1$
- Define the upper boundary of the "common reference region", where re-absorption is negligible and does not affect the edge fluorescence spectrum. This boundary was defined using the absorbance spectra of the dye, for an absorption $\alpha < 0.007\ cm^{-1}$ [27]
- Within the common reference region, fit the edge fluorescence spectra to $\tilde{f}_1(\lambda)$ using a least-squares algorithm
- Compute the re-absorption probability $r(\lambda)$ through the ratio of the two scaled spectra.

Typical results for a single-dye collector are shown in Fig. 181.

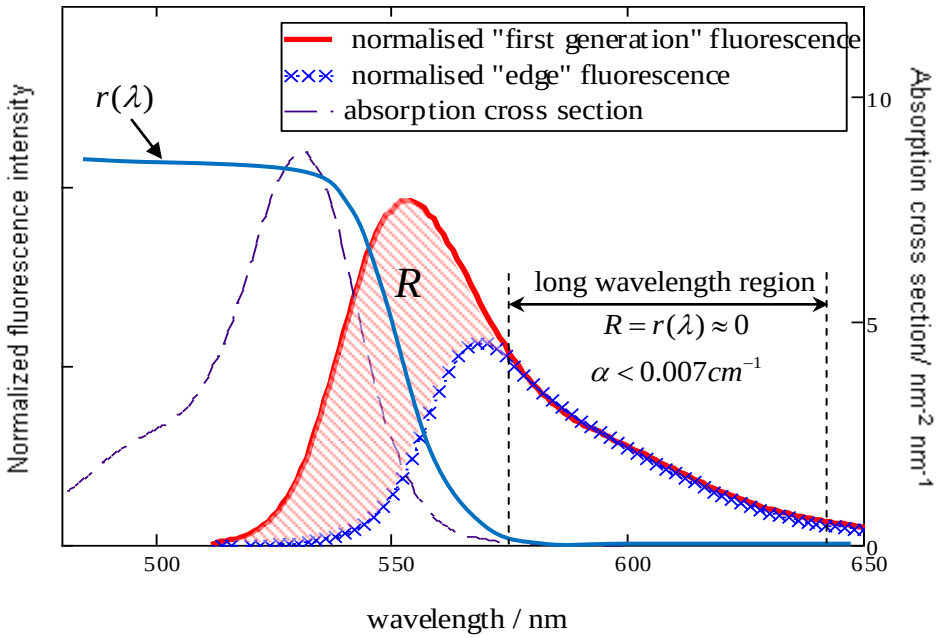

Fig. 180: Normalized edge fluorescence spectrum and first-generation spectrum for Rhodamine 6G. The ratio of these two spectra gives the spectral re-absorption probability $r(\lambda)$. The hatched area is equal to the probability R of re-absorption.

The analysis illustrated in Fig. 180 represents a convenient graphical method for determining the total re-absorption probability. After normalization of the edge fluorescence it becomes apparent that:

$$R = \int \tilde{f}_1(\lambda)d\lambda - \tilde{f}_e(\lambda)d\lambda = 1 - \tilde{f}_e(\lambda)d\lambda. \tag{120}$$

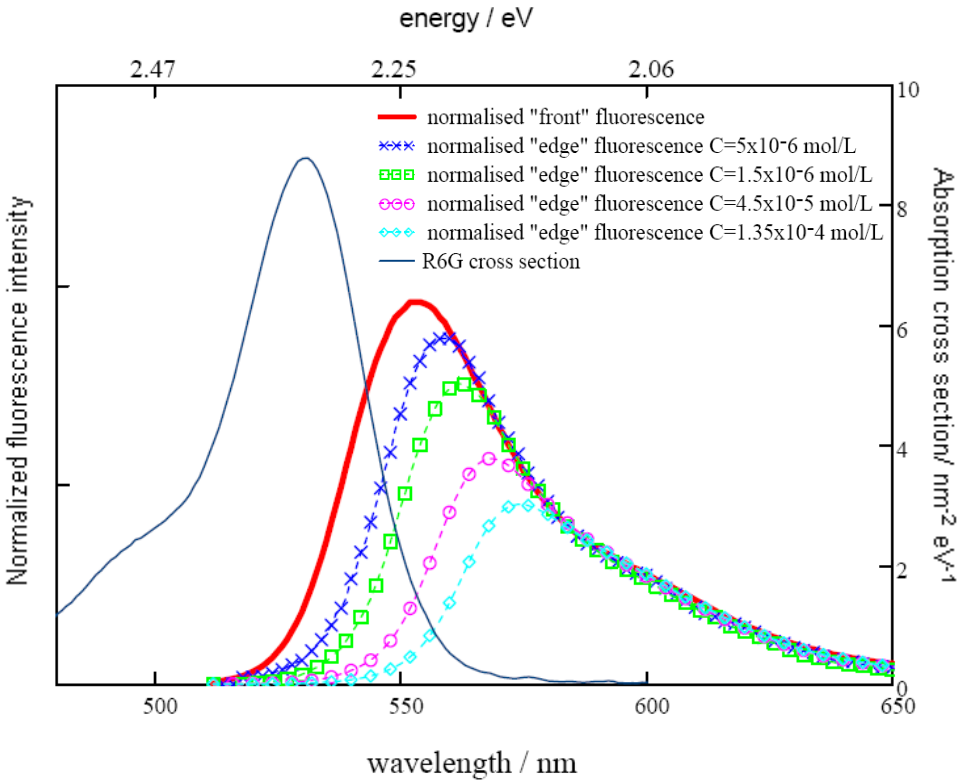

Fig. 181: Typical data set: edge fluorescence spectra of Rhodamine 6G in ethanol at various concentrations, normalized to the front fluorescence spectrum. The legend shows the dye concentrations in the solvent. (Graph published in [183])

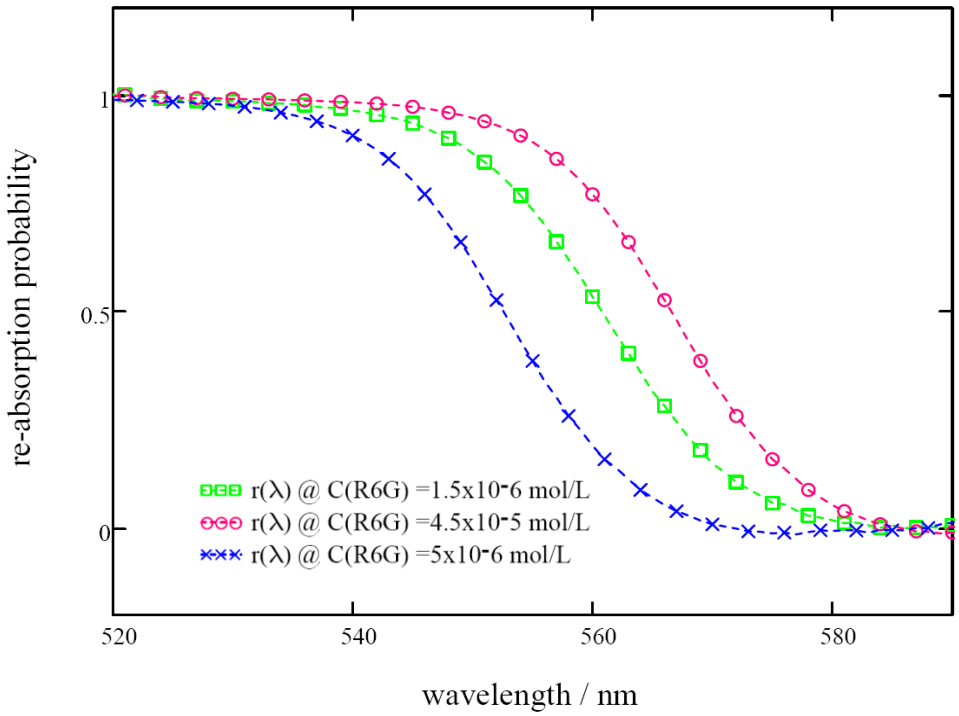

Fig. 182: Spectral re-absorption probability $r(\lambda)$ calculated using Eqn. (119) and the data in Fig. 181.

A typical data set showing various normalized edge fluorescence spectra (R6G in ethanol) is shown in Fig. 181. The dye cross-section, rather than the various absorbance spectra, is reported for each concentration. This figure clearly demonstrates that edge fluorescence spectra fit well with first-generation spectra in the long-wavelength region. Once the spectra are normalized, the spectral re-absorption (Fig. 182) is obtained from Eqn. (119).

7.1.3 Comparison of results

Fig. 183a to 82d present absorption efficiencies, collection efficiencies and optical efficiencies, with each figure showing the results for a different fluorophore.

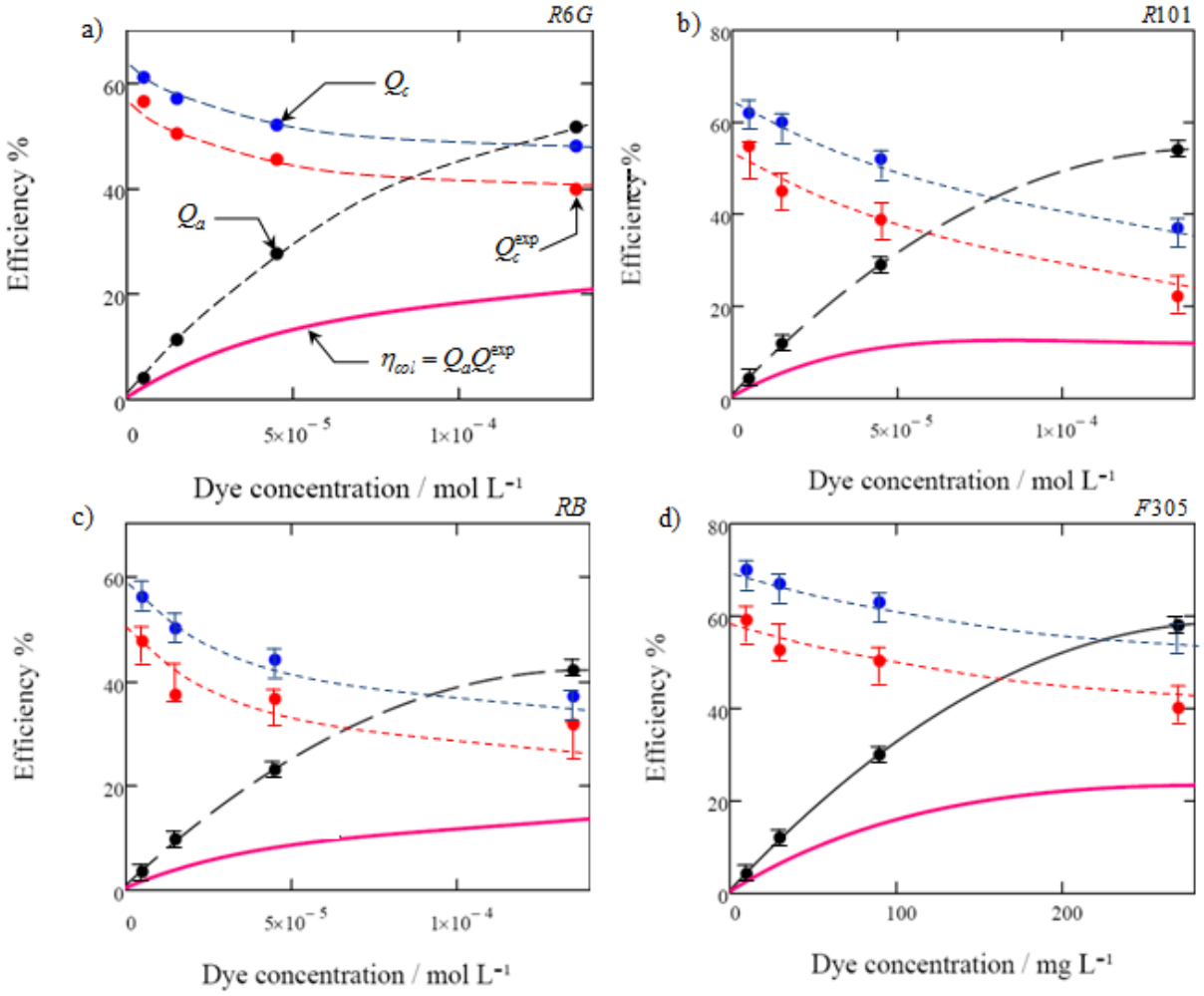

Fig. 183: Efficiencies of FSCs as a function of dye concentration: a) R6G in ethanol; b) R101 in ethanol; c) RB in ethanol; d) Frot 305 in DCM. Error bars show the uncertainties in the recorded values, these errors bars represent the maximum variation recorded during the experimental measurements. No errors bars are shown on Fig. 82a in order to avoid an overloaded figure.

The blue dots represent the collection efficiency computed using Eqn. (118). The red dots show the "experimental" collection efficiency ($Q_c^{\exp}$). The black dots correspond to the absorption efficiency. The dashed lines show polynomial regressions of the measured data to guide the eye, and the solid pink lines show the efficiency of the collector computed from the product of the "experimental" collection efficiency and the absorption efficiency.

These graphs clearly demonstrate the conflicting behaviours of absorption and collection efficiencies: as photon absorption increases the collection efficiency decreases. The collectors fabricated here reached ≈ 20 % efficiency under the monochromatic limitation imposed on the absorption efficiency.

The two-photon-fluxes analysis fits the variation in experimental collection efficiency well. However, all the measured data are below the predicted values. Sources of discrepancy include:

- reflectivity losses $\mathbb{R}_{cell}$ at the matrix/silicon interface
- reflectivity $\mathbb{R}_{edge}$ of the mirrors surrounding the collector
- matrix absorption losses
- imperfect coupling between the edge solar cell and the collector
- variations in dye quantum yield due to high-concentration effects
- collector roughness.

The reflectivity of the mirrors surrounding the collector was investigated using an ellipsometer. In situ, the reflectivity of the 3M reflective Vikuiti™ polymer film dropped from its original ≈ 95 % to ≈ 75 % across the visible spectrum, a result of the fact that the film was glued to a substrate before manipulation, creating or increasing surface roughness. Using Fresnel's law the reflectivity coefficient at the air/collector and matrix/c-Si cell interfaces were calculated – $\mathbb{R}_{front} = 0.004$ for normal illumination and $\mathbb{R}_{cell} = 0.18$ for isotropic illumination.

These losses explain the discrepancies between actual and predicted efficiencies. To keep the analytical relations simple in the following development, all photon transport losses are included in a single term, denoted $\mathfrak{N}$. This term was determined from the ratio of $Q_c^{\exp}$ to Q_c; for the results shown in Fig. 183, $\mathfrak{N} \approx 0.7 \mp 0.05$. A breakdown of the photon transport losses is carried out in Section 7.2.2.

Despite this discrepancy, the re-absorption data obtained from the two-photon-fluxes analysis can be used to verify the ray-tracing results of Chapter 5.

The ray-tracing simulations (Section 5.2.2) showed that thin-film and liquid collectors operate optimally when the refractive index of the film is the same as that of the substrate. In such a configuration, which is

the configuration chosen for the experiments, the re-absorption profile of inhomogeneous collectors is similar to the re-absorption profile given by the *W&L* model (Eqn. (86)) for homogeneous flat-plate collectors. Using the spectral re-absorption data (Fig. 182) and the absorption spectra of the dye (which is also wavelength-dependent), re-absorption probability was plotted as a function of the dye absorption coefficient, allowing comparisons between experimental data, the *W&L* model and the ray-tracing simulations (Fig. 184).

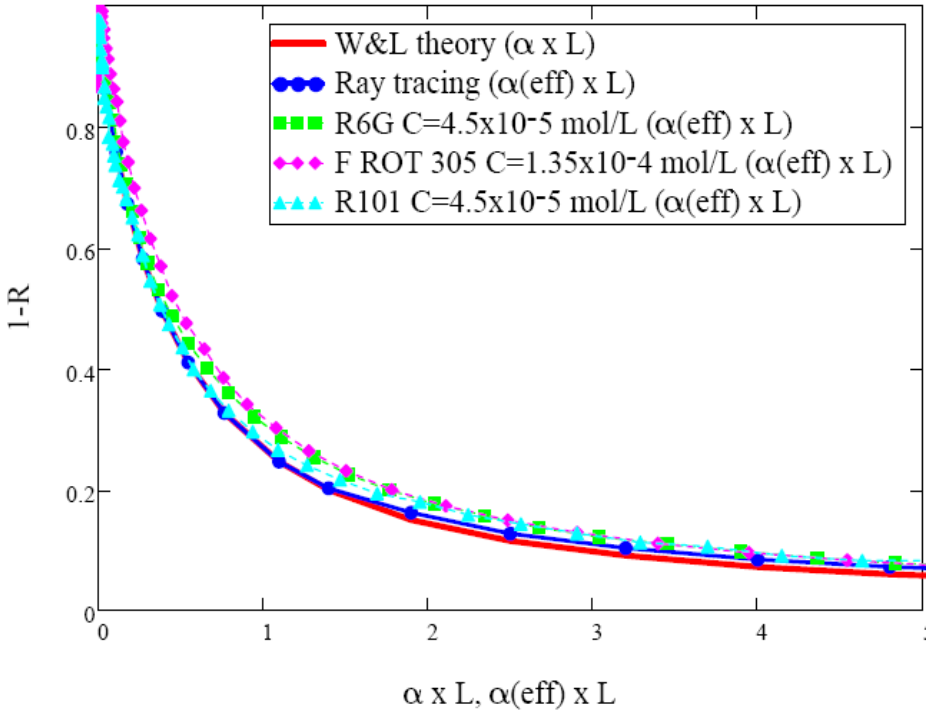

Fig. 184: Experimental re-absorption probability profiles for a liquid collector, compared with ray-tracing simulations and the *W&L* model. Experimental data are plotted as a function of $\alpha_{eff}(\lambda)\, L$ to take account of the clear substrate (Section 5.2). The legend gives dye concentrations in the solvent. (Graph published in [129])

Fig. 184 compares experimental re-absorption probability profiles for a liquid collector, using various dyes (R6G, F305, R101). Clearly the experimental data fit the analytical and ray-tracing results well. Errors in the re-absorption probabilities were estimated at ± 8 %. This represents the average deviation of the $1 - R$ probability from those derived from the *W&L* model.

Using the same methodology, re-absorption profiles for a thin-film collector (PMMA, $n_{PMMA} = 1.5$, film of thickness ≈ 10 μm coated onto glass, 2.6 cm by 2.6 cm) were experimentally determined for various concentrations of R6G. The results are shown in Fig. 185.

Fig. 184 and Fig. 185 clearly demonstrate the agreement between the simulations and the experiments. As predicted by ray-tracing simulations, the re-absorption probability is the same for both thin-film and liquid collectors.

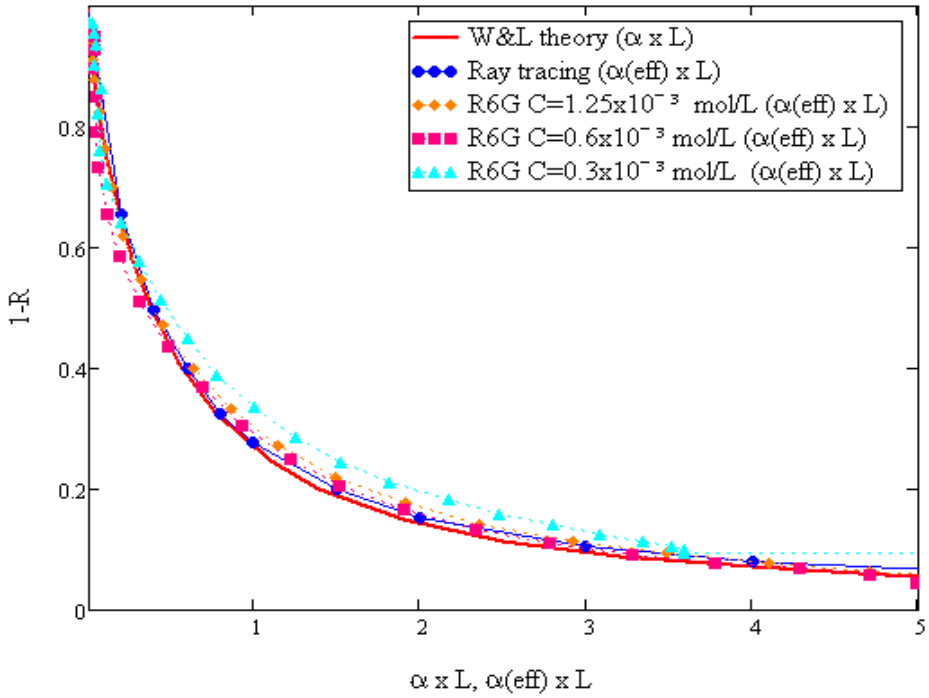

Fig. 185: Re-absorption probability profiles for a thin-film collector, compared with ray-tracing simulations and the *W&L* model, showing various concentrations of R6G in the film. The legend gives dye concentrations in the solvent. (Data obtained with the help of Dr. P. Kittidachachan [6])

Given the good fit between theory and experiment, these results demonstrate that thin-film collectors perform identically to standard collectors provided the refractive index of the substrate matches that of the active layer.

7.1.4 Performance limitations of collectors doped with a single dye

The collectors examined in the previous section are limited by weak absorption efficiencies; indeed, in order to demonstrate the validity of the two-photon-fluxes analysis the dye concentrations were intentionally kept low to avoid fluorescence quenching issues (Chapter 1).

The study then assessed the performance limitations of highly doped liquid collectors under broad-spectrum illumination. The illumination source was changed to a xenon lamp (Fig. 186) which approximates the solar photon distribution and allows adequate illumination in the 400 nm region.

The dye chosen for this study was BASF Lumogen Frot 305 in DCM, since it has:

- two absorption bands allowing efficient absorption from 400 to 620 nm (Fig. 186)

- high quantum yield, conserved up to $\approx 600\ mg\ L^{-1}$ [115;184]
- solubility exceeding several grams per litre in PMMA or DCM [71]

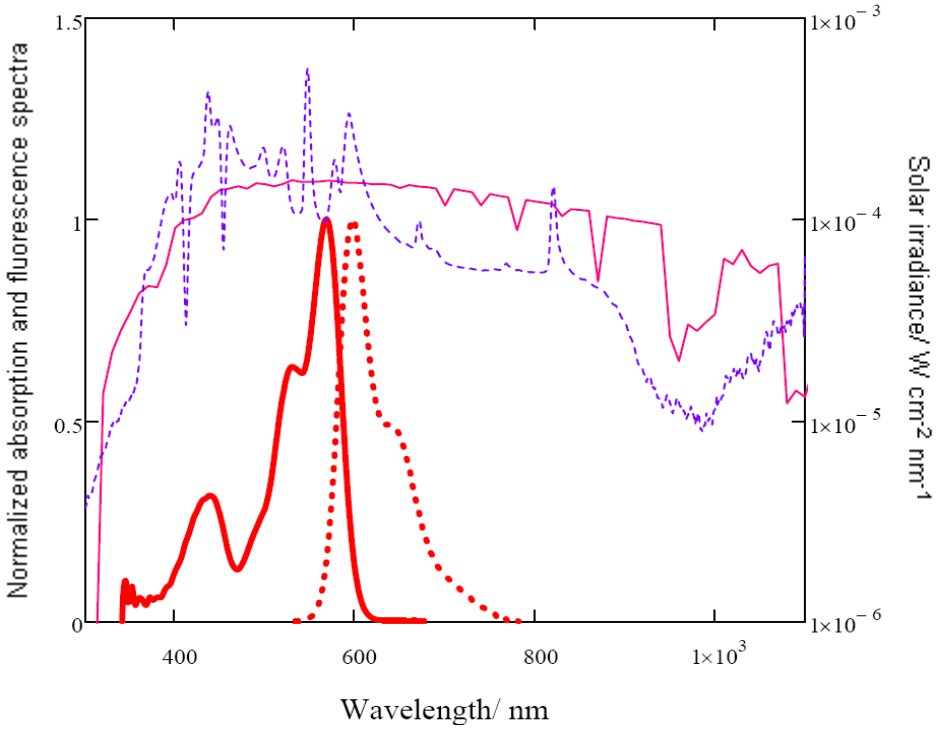

Fig. 186: Normalized absorption (solid red line) and fluorescence (dotted red line) spectra of Lumogen Frot 305 dye in DCM. Pink line: AM 1.5 photon distribution. Dashed violet line: xenon lamp spectrum (scaled by a factor of 15).

7.1.4.1 Electrical characterization

The performance of the collector doped with the Lumogen Frot 305 dye was assessed by measuring the average short-circuit current of the edge solar cell when the front area of the FSC was uniformly illuminated.

As already introduced in Chapter 5, a FSC's intensity output is directly proportional to the number of photon reaching the edge solar cell. In practice the electrical output is a combination of current generated from fluorescence and a background current arising from the scattering of incoming light within the matrix. The background current, measured using a blank solution, was subtracted from the results. Using the relations already developed in Chapter 5 and assuming the collector in steady state the cell's short-circuit current was then simply proportional to the product of :

- the rate of absorbed photons at the excitation wavelength (ex), $A_{front}\ Q_a \int_0^{\lambda_g} \dot{f}_s(\lambda_{ex})\, d\lambda_{ex} = K_{abs}$
- the collection efficiency at the edge of the device Q_c
- the cell quantum efficiency weighted by the fluorescence spectral distribution $\widetilde{f_e}(\lambda_{em}) IQE_{pv}(\lambda_{em})$

The full relation taking in account the refection losses at the collector/silicon interface can be expressed as:

$$I_{sc}(\lambda_{em}) = K_{abs} \times \overbrace{Q_c(1-\mathbb{R}_{cell})}^{\text{Number of photons collected at the edge}} \times \underbrace{\widetilde{f_e}(\lambda_{em})}_{\text{Photon spectral distribution}} \times \overbrace{qIQE_{pv}(\lambda_{em})}^{\text{Charge generated per photon}} \quad (121)$$

where $\widetilde{f_e}(\lambda_{em})$ is the normalized edge fluorescence spectrum. The subscripts em and ex refer to fluorescence emission and source excitation, respectively.

Equation (121) is based on several assumptions. It assumes a perfect matrix and perfect reflectivity of the surrounding mirrors. In addition, photon recycling upon reflection from the solar cell is neglected. To be of practical use the fluorescence emission is usually considered at a single wavelength, the relation (121) can be simplified, on the basis of the following arguments:

- The fluorescence bands of laser dyes are relatively sharp.
- The response of the solar cell is wavelength-independent in the region of emission of the Frot 305 fluorophore.

With these approximations and including photon transport losses contained in the term $\mathfrak{N}$, Eqn. (121) becomes:

$$I_{sc} \approx K_{abs} \times Q_c \times \mathfrak{N} \times qEQE_{pv}(\lambda_{em}^{\max}), \quad (122)$$

where $\lambda_{em}^{\max}$ is the wavelength at the maximum of the fluorescence spectrum.

The I_{sc} data obtained from the measurements – recorded after $50\ s$ of constant illumination, averaged over 25 values taken at $1\ s$ intervals – are plotted against dye concentration and compared to values calculated using Eqn. (122) in Fig. 86.

The short circuit current was determined as a function of dye concentration using the collection efficiency calculated as a function of the dye concentration:

$$Q_c(C_{dye}) \approx \frac{\varphi(1-P)(1-R(C_{dye}))}{1-\varphi \mathrm{R}(C_{dye})(1-P)}, \quad (123)$$

where the only parameter depending on the dye concentration is the re-absorption probability.

The re-absorption probability was experimentally characterised as a function of dye concentration using the methodology described in Section 7.1.2 – the experimental data were then fitted by a mathematical function which was used in Eqn. (123). The comparison between the data and the empirical function are shown in Fig. 87.

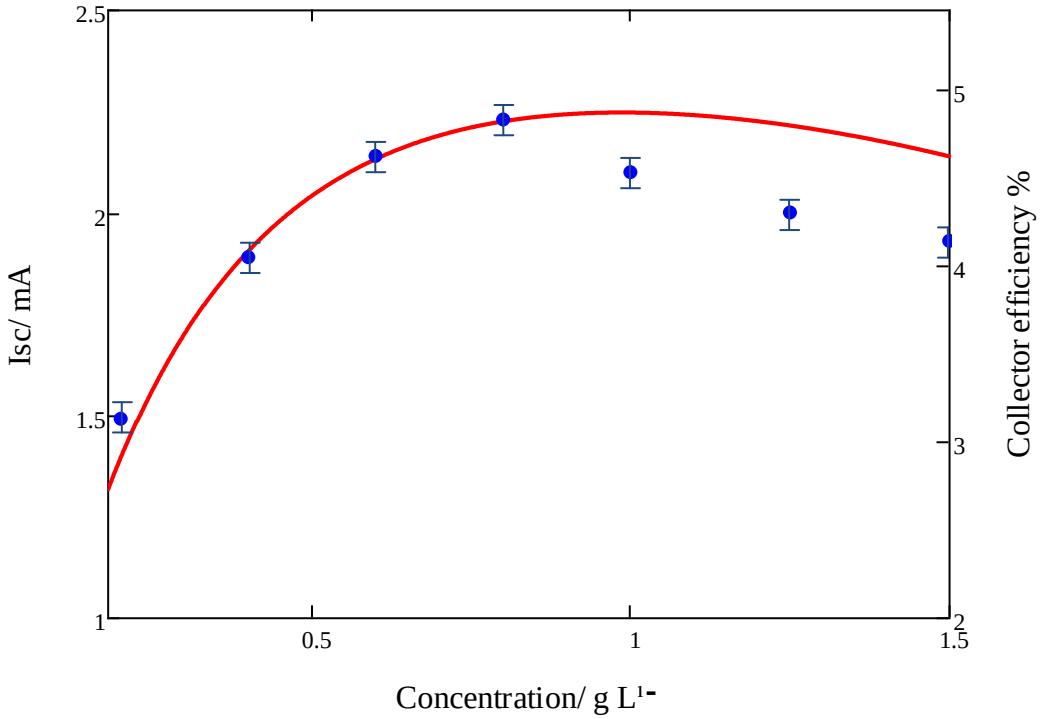

Fig. 187: Short-circuit current of the edge solar cell as a function of dye concentration. Blue dots: experimental short current measurements, red line results of Eqn. (122) with $\lambda_{em}^{\max} = 655\,nm$, $EQE_{pv}(\lambda_{em}^{\max}) = 0.81$. As the short circuit current is proportional to the collection of the efficiency through Eqn. (122) both short circuit current and collection efficiency can be compared on the same graph.

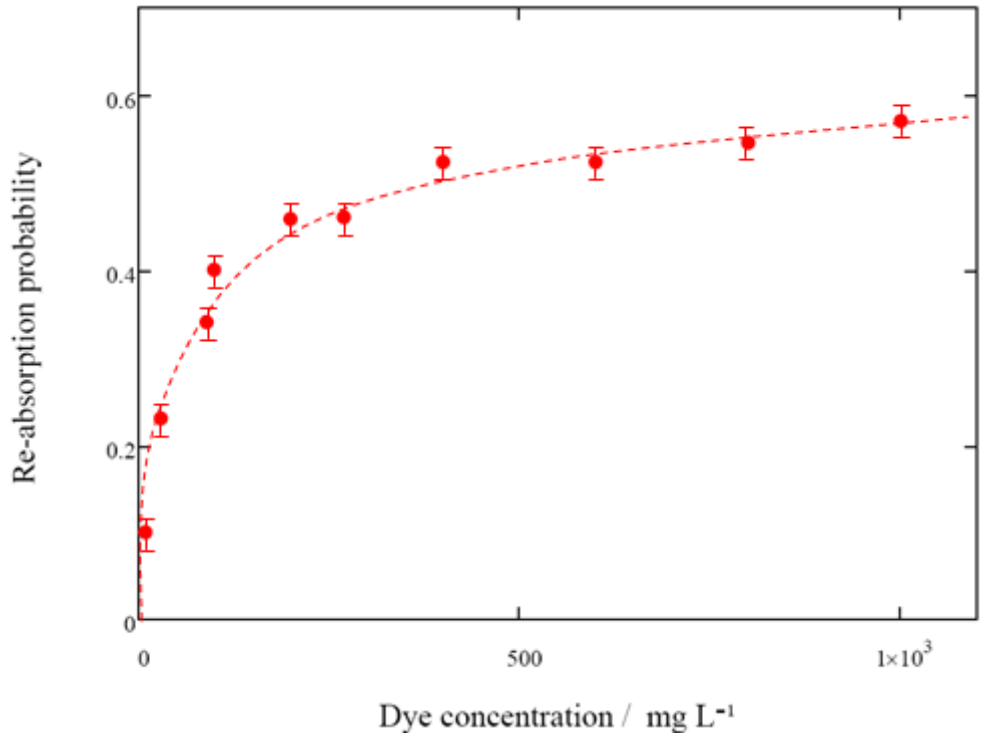

Fig. 188: Re-absorption probability as a function of F 305 dye concentration. The red dashed line represents an exponential fit, $R(C_{dye}) \approx 0.45\exp(0.23C_{dye}) - 0.40\exp(-15.75C_{dye})$ used in Eqn. (122).

Equation (122) fits the experimental measurements well. The trend of the results is quite similar to that from the data analysis shown in Fig. 183. This is not surprising, since the measured current is directly related to the efficiency of the FSC and to the photon flux available at the edge. This figure illustrates the trade-off between strong absorption and an increasing re-absorption probability. The discrepancy between the theory and experiments is the result of a quantum yield drop at high concentration [184].

The best collector efficiency was $\eta_{col} = 4.9$ % under illumination provided by the xenon lamp (F305 concentration $= 800\ mg\ L^{-1}$). Absorption efficiency reached ≈ 80 % in the $400 - 600\ nm$ region.

Coupling the fluorescent collector with a theoretical 25 % efficient c-Si solar cell would lead to an overall device efficiency of $\eta_{FSC} = 1.2$ % – comparable to efficiencies reported by other research groups (Table 5).

7.2 Collectors doped with multiple dyes

The practical feasibility of a multiple-dye collector is now of interest: with available chemicals, can a set of fluorophores absorb most of the incoming sunlight and re-emit it efficiently without suffering from further re-absorption losses?

It is possible to combine available dyes in such a way as to absorb most of the incoming sunlight, but the low quantum yield of the dyes in the near infrared (Fig. 38) limits the operation of multiple dyes FSCs. Fig. 189 perfectly illustrates this major material issue; there is a crucial lack of suitable fluorophores which emit efficiently in the $650 - 1100$ nm wavelength region.

In addition, the Stokes shift is short for dyes which absorb and emit efficiently in the $300 - 650$ nm wavelength region, so strong re-absorption effects are expected for collectors doped with a combination of Lumogen dyes. Efficient photon transport will therefore depend on energy transfer between dyes.

The key to efficient energy transfer between dyes is the specific orientation of donor and acceptor molecules [144]. Since this strategy cannot be adopted with liquid solutions, most absorbed energy is re-emitted rather than being transferred to an acceptor. Primary tests using collectors doped with several Lumogen dyes were inconclusive; recorded efficiencies were below those obtained for single-dye systems.

Nevertheless, a promising two-dye collector solution was found in DCM-dye mixed with the Frot 305 dye in DMSO (Fig. 190).

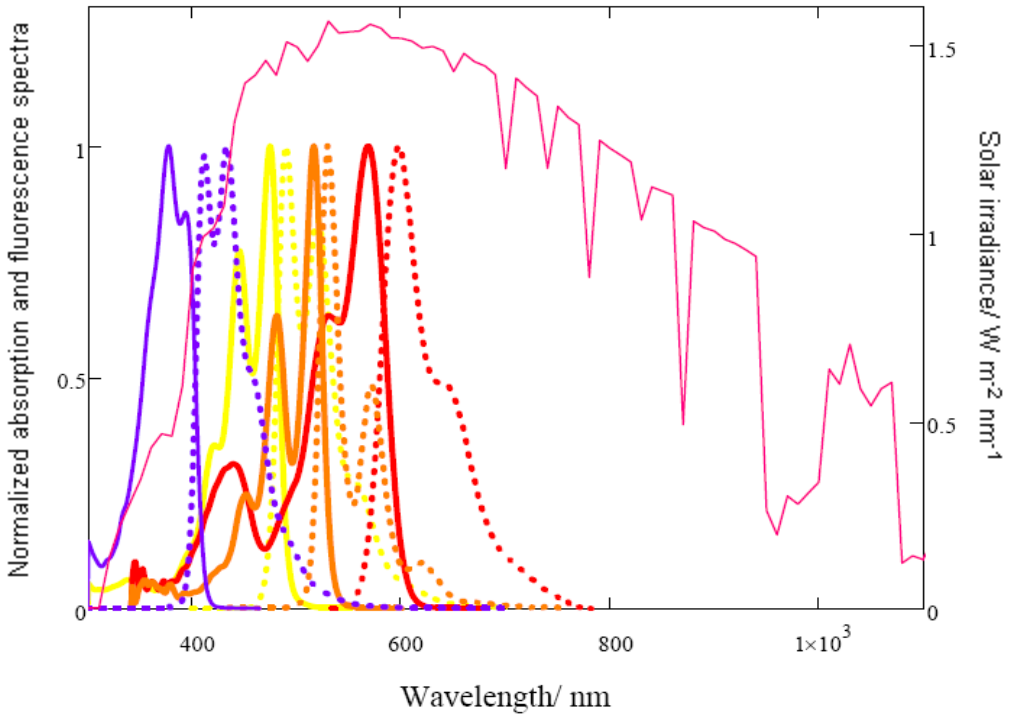

Fig. 189: Absorption (thick solid lines) and fluorescence (dotted lines**)** spectra of a selection of BASF Lumogen fluorophores plotted with the AM 1.5 spectrum (pink). The fluorophores are: Fviolet 570 (violet), $\varphi = 0.93$ [184]; Fyellow 083 (yellow), $\varphi = 0.93$ [184]; Forange 240 (orange), $\varphi = 1$ [184] and Frot 305 (red), $\varphi = 0.98$ [115]. Spectra and quantum yields were measured in DCM.

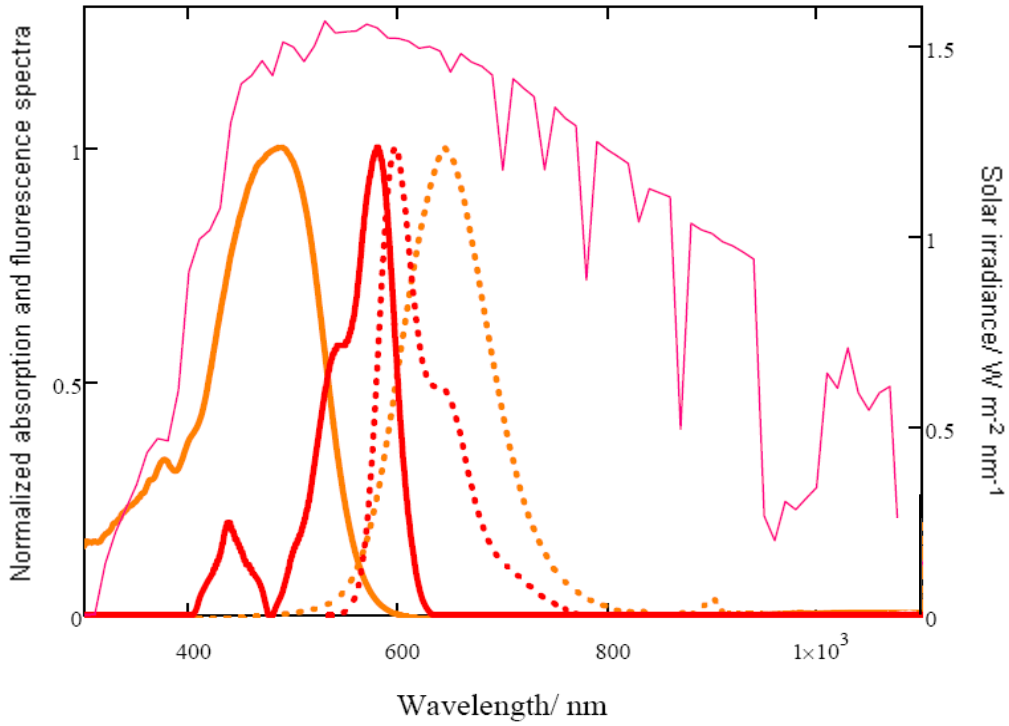

Fig. 190: Absorption (thick solid lines) and fluorescence (dotted lines) spectra of DCM-dye (orange), $\varphi = 0.8$ [185]; and Frot 305 (red), $\varphi \approx 0.9$ in DMSO, plotted with the AM 1.5 spectrum (pink).

This nearly ideal situation is unique to liquid collectors fabricated here because:

- DCM-dye shows virtually no re-absorption losses (Stokes shift of 171 nm) and a quantum yield of 0.8 in DMSO (these properties are less optimal in any other solvent or solid matrix).
- Quantum yield and absorption properties of Frot 305 dye in DMSO (Fig. 190) differ only slightly from its optimal optical characteristics in DCM (Fig. 189).

7.2.1 Performance characterization

Collector performance was again characterized by measuring the average short-circuit current of the edge solar cell. The results are presented in Fig. 191.

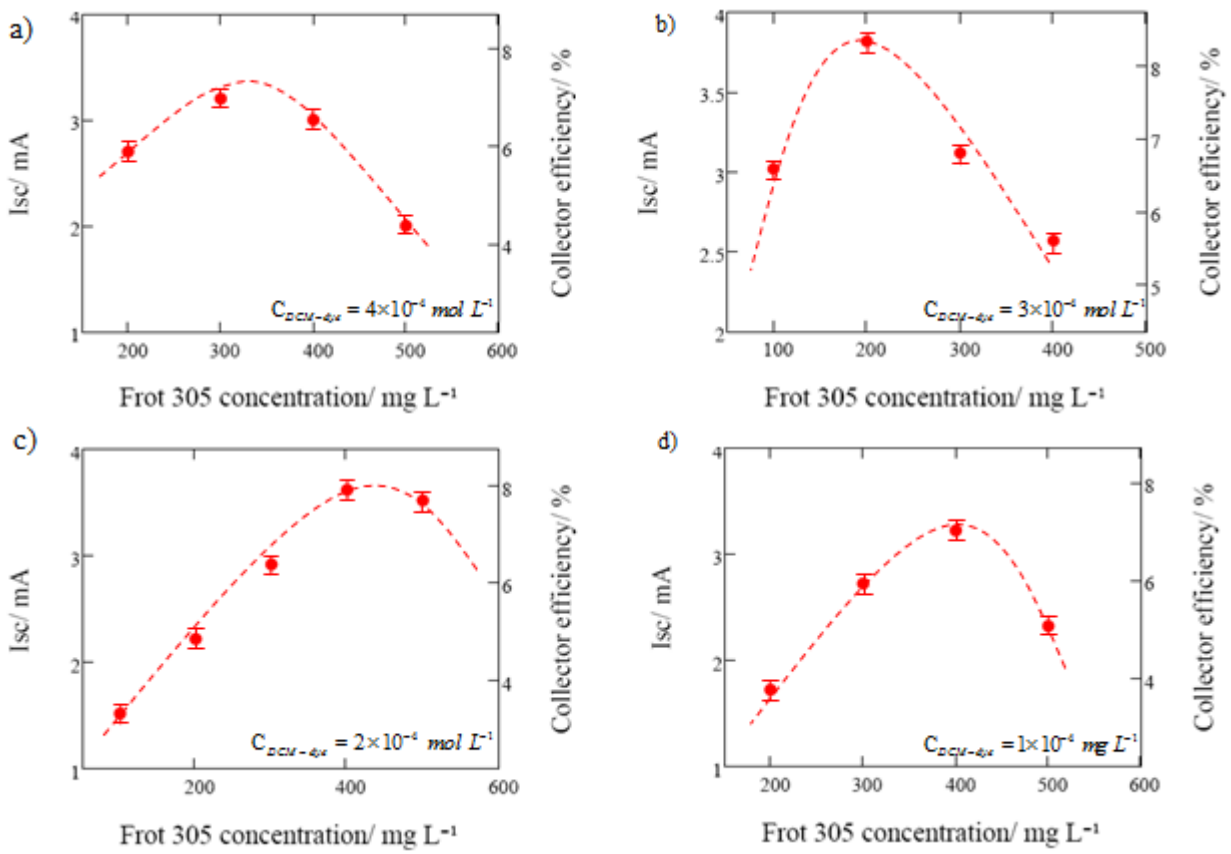

Fig. 191: Short-circuit current of the edge solar cell as a function of Frot 305 dye concentration for a fixed concentration of DCM-dye; dashed lines are added to guide the reader's eye. a) DCM-dye concentration $C_{DCM-dye} = 4 \times 10^{-4}\, mol\, L^{-1}$. b) $C_{DCM-dye} = 3 \times 10^{-4}\, mol\, L^{-1}$. c) $C_{DCM-dye} = 2 \times 10^{-4}\, mol\, L^{-1}$. d) $C_{DCM-dye} = 1 \times 10^{-4}\, mol\, L^{-1}$.

The strategy was to limit re-absorption by strongly doping the matrix with the DCM-dye and progressively increase the concentration of F305. The optimal concentration of DCM-dye was determined to be $C = 3 \times 10^{-4}\, mol\, L^{-1}$; at such a concentration the dye's quantum yield $\varphi = 0.8$ [185] and the probability of photon absorption is optimized ($Q_a > 80\,\%$ in the $350 - 500\, nm$ region) (Fig. 190). For

higher concentrations the quantum yield of the DCM-dye started to drop, to a level where it dominated the efficiency of the collector.

The best collector efficiency was $\eta_{col} \approx 8.5$ % under xenon lamp illumination, and $\eta_{col} \approx 7$ % under *AM* 1 spectrum – a 58 % relative increase compared with the best single-dye system for the same absorption efficiency. The optimal dye mixture was DCM-dye at $C = 3 \times 10^{-4}\ mol\,L^{-1}$ mixed with Frot 305 at $C = 200\ mg\ L^{-1}$

Coupling the fluorescent collector with a theoretical 25 % efficient c-Si solar cell would lead to an overall device efficiency of $\eta_{FSC} = 1.7$ % – one of the highest efficiencies reported so far (Table 5).

7.2.1.1 External quantum efficiency

It is pertinent to quantify the beneficial effect of the collector. Using the characterization method developed in Section 6.3.2.2 the response of the edge solar cell with and without the collector was characterized; the results are shown in Fig. 192. The orange line is the EQE of the bare solar cell directly facing the light. The blue dotted line is the spectral response of the solar cell coupled to the edge of the collector. Clearly the response of the edge solar cell increases in the region where the collector absorbs light (Fig. 193).

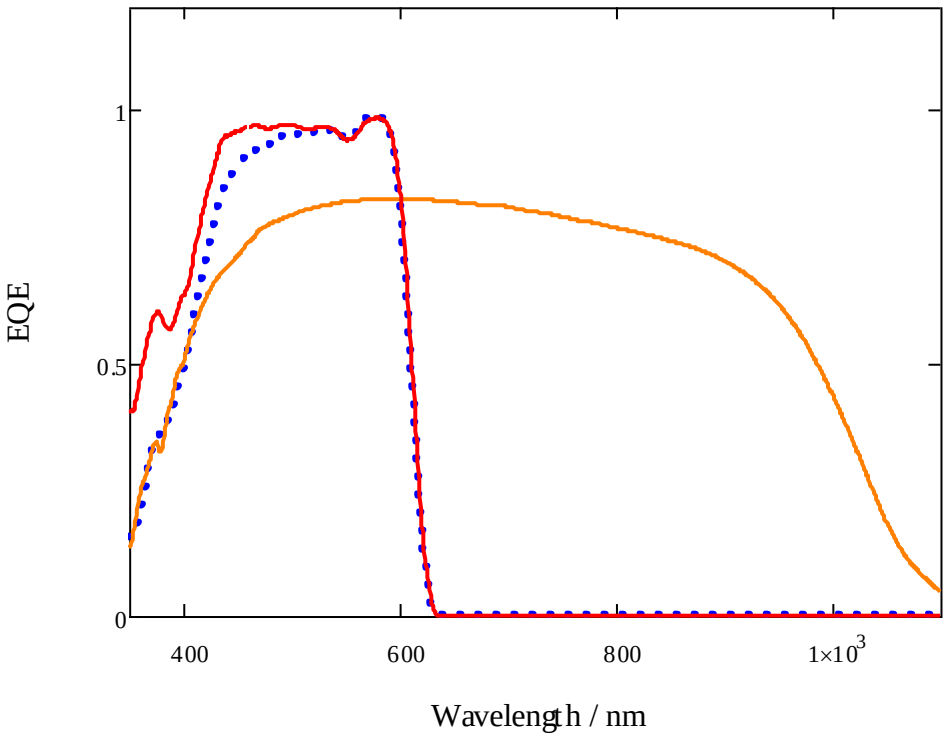

Fig. 192: External quantum efficiency of the bare c-Si cell (orange) compared to the collector's spectral response (blue dots). The red line corresponds to Eqn. (124) with $\lambda_{em}^{max} = 655$ nm, $EQE_{pv}(\lambda_{em}^{max}) = 0.81$.

Using the relations developed for single-dye collectors (Eqns. (121), (122)) the expected EQE can be modelled. Assuming fluorescence emission at a single wavelength:

$$\mathrm{EQE}(\lambda_{ex}) \approx \frac{A_{front}}{A_{edge}}(1-\exp(-(\alpha_{DCM}(\lambda_{ex})+\alpha_{F305}(\lambda_{ex}))\cdot 2l)Q_c \times \mathfrak{N} \times EQE_{pv}(\lambda_{em}^{\max}). \quad (124)$$

The EQE computed using Eqn. (124) is shown in Fig. 192 (red line). Above 500 nm the analytical model fits the experimental data well. Discrepancies under 500 nm are due partly to noise in the absorbance spectra recorded with the Avantes spectrometer (below 420 nm) and partly to the reflectivity of the back mirror, which was not taken into account.

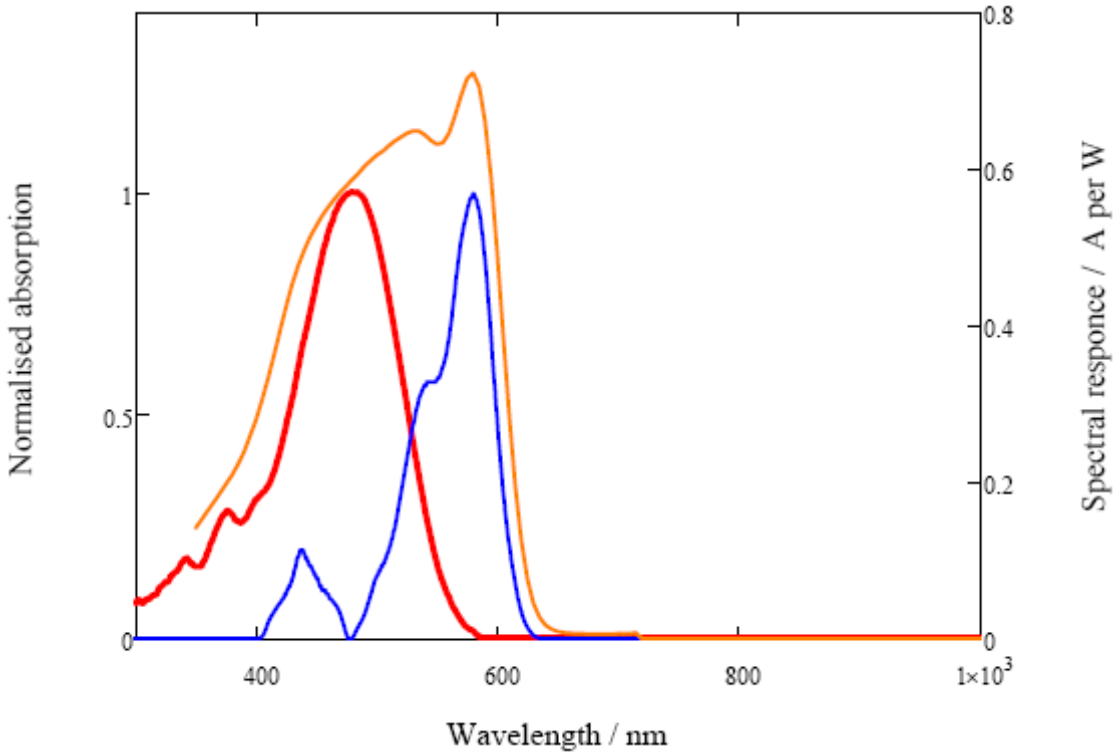

Fig. 193: Spectral response (orange line) of the collector coupled to the c-Si cell compared to the normalized absorption of Frot (blue line) and DCM-dye (red line) in DMSO.

The optical efficiency of the best collector fabricated ($\eta_{col} \approx 8.5$ % under the xenon lamp illumination) is still far from the theoretical limit. It has been shown [73] that a TIR-based collector can reach 58 % optical efficiency (for a gain of 20). Using data from the characterization of fluorescent collectors, a quantification of the losses occurring during photon transport is carried out in the next section.

7.2.2 Breakdown of losses

Three major types of losses affect the operation of collectors in practice: non-radiative losses, re-emission lost from the front face, and optical losses.

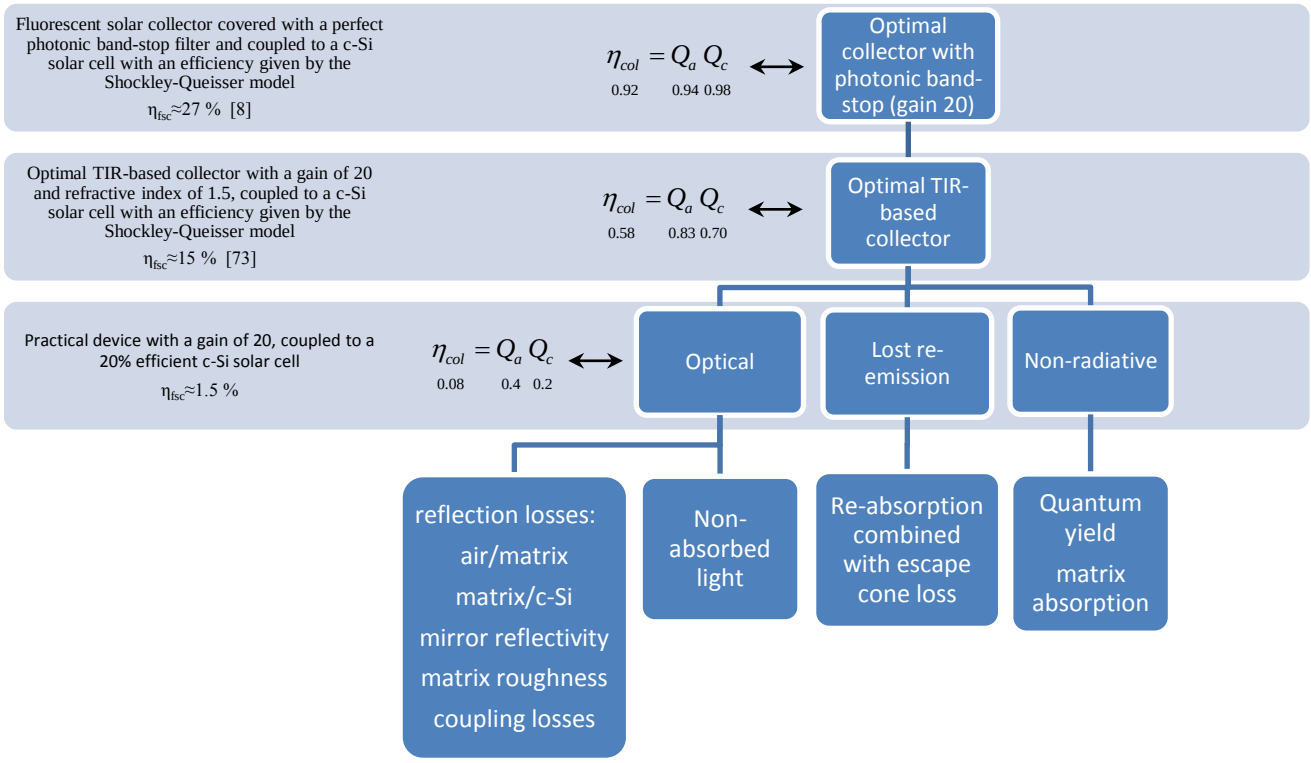

Fig. 194: Scope of the losses occurring in a TIR-based fluorescent solar collector.

Using the photon balance in a collector (Section 5.1.5) and the definition of Q_a which takes account of the reflectivity of the front and back mirrors (Eqn. 80), it is possible quantify the losses occurring during photon transport.

Considering the absorption properties of the best collector fabricated (Fig. 193), illuminated with an *AM* 1 spectrum, only 39 % of incoming photons are absorbed. Of these, only 13 % are theoretically collected. The rest of the absorbed light is lost thought the front face of the collector or as heat (Fig. 195).

This calculation was carried out using (Eqn. (99)) with:

- $P = 0.26$
- $R = 0.75$, from the addition of the re-absorption for each dye ($R = 0.48$ for the single dye F305 at 200 $mg\ L^{-1}$ (Fig. 187) and $R = 0.27$ for DCM-dye at $C = 3 \times 10^{-4}\ mol\ L^{-1}$)
- $\varphi = 0.8$ [163;184-185].

Fig. 195 illustrates these losses schematically.

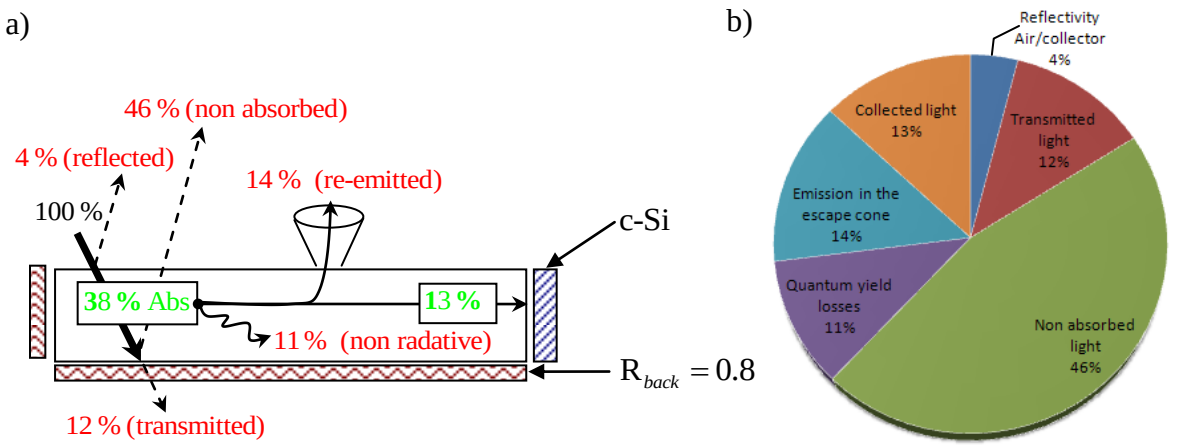

Fig. 195: Map of the losses occurring in a TIR based fluorescent solar collector. The schematic diagram (a) and pie chart (b) are built on the results obtained for the most efficient FSC fabricated. The percentage of absorbed light is defined using the absorption spectrum of the fluorophores doping the collector. The emission form escape cone loss is obtained through the two-photon-fluxes model. The reflectivity loss of the back mirror was investigated using an ellipsometer. The reflectivity at the air/collector interface was defined by Fresnel's expressions.

Two points are worth discussing: (i) the optical efficiency reported in Fig. 195 reaches ≈ 13 %, while the experiments showed $\eta_{col} \approx 7$ %; (ii) non-absorbed light is the main loss.

(i) The figures in Fig. 195 assume that reflectivity of the surrounding mirrors, reflectivity at the matrix/PV cell interface are perfect and that matrix absorption and collector surface roughness are negligible. Using the collector's square geometry it is possible to estimate reflection losses. Assuming isotropic re-emission of the fluorescence, three-quarters of re-emitted light will be reflected at least once by the surrounding mirrors and one-quarter will be emitted directly towards the c-Si solar cell. The collection efficiency decreases by:

$$\frac{3}{4} Q_c \mathbb{R}_{edge} + \frac{1}{4} Q_c (1 - \mathbb{R}_{cell}). \tag{125}$$

This approximation does not take into account multiple reflections, and neglects the recycling of photons reflected by the solar cell. Including these losses in the results shown in Fig. 195 causes the collection efficiency to drop from ≈ 13 % to ≈ 10 %. The remaining losses are associated with matrix absorption and collector roughness; unfortunately it was not possible to characterize these experimentally.

(ii) Changing the edge solar cell band gap is the easiest and most efficient way to minimize losses due to photon non-absorption (Fig. 196). The loss of current from using semiconductors with larger band gaps is compensated by a higher open-circuit voltage (Chapter 8).

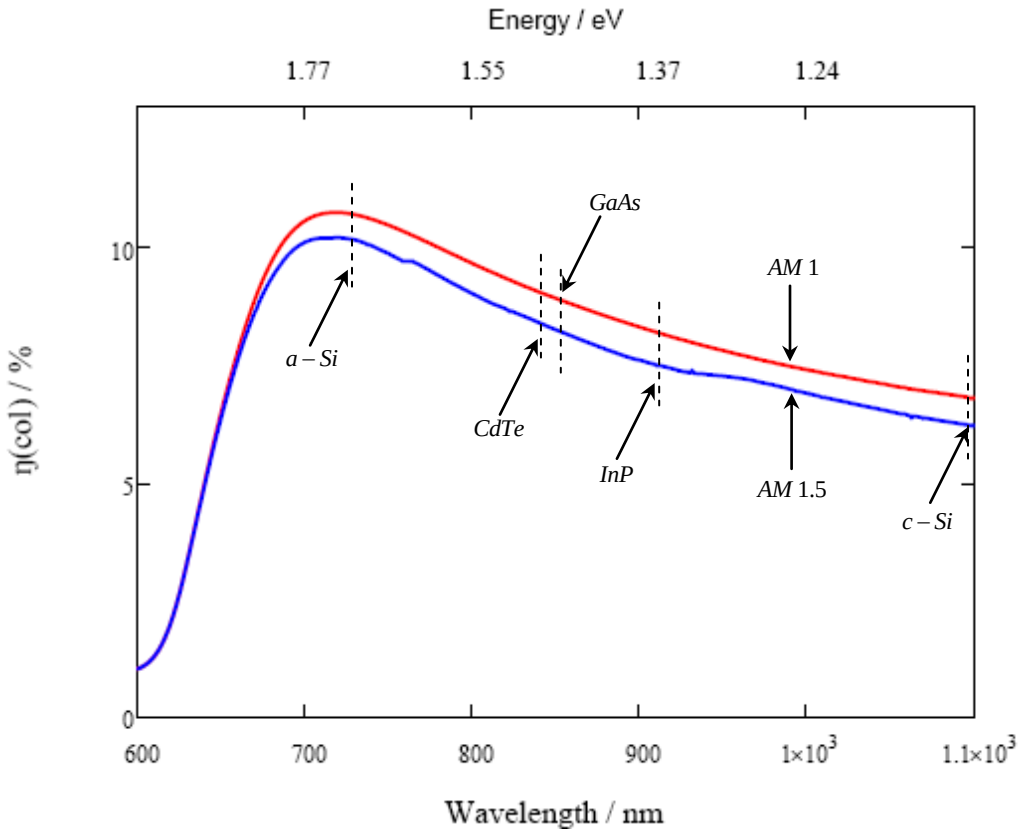

Fig. 196: Optical efficiency of the best fluorescent solar collector under *AM* 1 and *AM* 1.5 as a function of the semiconductor band gap.

Amorphous silicon presents the best band gap match. However, the optimal available material is gallium arsenide, since the practical efficiency of such a cell reaches $\eta_{GaAs} \approx 25\ \%$ compared with $\eta_{a-Si} \approx 10\ \%$ for a-Si cells (Chapter 2).

7.3 Conclusion

This chapter has discussed attempts to develop and characterize the performance of liquid fluorescent solar collectors.

Experimental results for collectors doped with a single dye allowed the validation of the two-photon-fluxes characterization technique. The characterization of experimental re-absorption profiles permitted a comparison of inhomogeneous and homogeneous collectors. As predicted by ray-tracing simulations, the experimental results demonstrated that thin-film and liquid collectors perform identically to standard collectors when the refractive index of the substrate matches that of the active layer.

A photon management scheme was developed for a system composed of two dyes, and compared with a single-dye collector with the same absorption efficiency. Relative efficiency increases of up to $\approx 60\ \%$ were observed in the two-dye system, which minimized re-absorption.

A breakdown of losses showed that lack of absorption, emission lost through the collector's front face and imperfect re-emission severely limit the operation of FSCs. The best collector reached an optical efficiency $\eta_{col} \approx 7\ \%$ under $AM\ 1$. Several attempts, using photonic structures (purchased from Reynard Corp), were made to optimise the best collector. Cut-on wavelengths photonic filters at $515\ nm,\ 530\ nm,\ 555 nm\ and\ 570\ nm$, were placed on top of the collector. A decrease in overall performance was observed (up to $\approx 25\ \%$) as a result of reflectivity losses and the poor optical properties of the photonic filter at angles different from normal incidence, as discussed in Refs. [137-139].

The optimization of the solar cell band gap was discussed; it was shown that gallium arsenide is the optimal semiconductor, although the economic aspects of using GaAs cells were not discussed.

Chapter 8

Photon chemical potential

The analytical models and ray-tracing simulations developed in the previous chapters for characterizing FSC performance only consider the number of particles (photons) incident on a surface (solar cells). In this chapter the energetic aspects of the fluoresced photons are examined, using the concept of chemical potential.

Thermodynamic limitations on the efficiency of a fluorescent solar collector have been discussed in a recent series of publications [8;57;73;105;150]. The key argument in [8;57;73] is the assumption of thermal equilibrium for the emitted photons, implying an equal chemical potential μ for the trapped photon flux. In this chapter, the chemical potential μ_{flux} of the edge fluorescent flux incident on the solar cell is characterized and compared with the chemical potential μ_{dye} of the excited state of the dye.

Three distinct approaches to the determination of the chemical potentials involved in FSC operation are presented:

- Determination of the chemical potential μ_{flux} of the edge fluorescent flux relies on the hypothesis that this flux reaches thermal equilibrium upon multiple re-absorption and re-emission events. Consequently the photon distribution is described by a specific temperature and a non zero chemical potential [186-187] (Section 8.1.1).
- An effective chemical potential μ_{dye} of the photoexcited dye is defined as in standard thermodynamics texts [188] (Section 8.1.2).
- A theoretical estimate μ_{theo} for the photon chemical potential is made using a model derived in [8]. This expression resembles the Carnot engine type relation [19], used with success for the open-circuit voltage of solar cells (Chapter 2) and adapted for fluorescent collectors [8] (Section 8.1.3).

We verify that these chemical potentials are in fact identical and that, for all practical purposes, μ_{dye} equals the chemical potential of an ideal photon gas, thus validating the assumption of thermal equilibrium upon multiple re-absorption and re-emission events.

8.1 Photon chemical potential: theory

This section presents theoretical details for each of the three approaches to determining the chemical potentials in a FSC. The experimental results are shown in Section 8.2.

8.1.1 Chemical potential μ_{flux} of the edge fluorescent flux

Let us assume that the collector is doped with a dye with a quantum yield φ of unity. This is true to a good approximation for most of the dyes studied in the present research. Such a dye would re-emit all the absorbed photons within the collector. As noted in Section 1.3, this perfect emission-absorption cycle would bring the re-emitted light into thermal equilibrium with the absorbing/fluorescent species. The photon occupation numbers can then be described by a Bose-Einstein distribution (Eqn. (1)) with, in general, a non-zero chemical potential.

The assumption of thermal equilibrium provides a natural framework for measuring the actual chemical potential of a fluorescent flux escaping from the edge of the collector. At thermal equilibrium, one would expect the spectrum of the edge fluorescence to resemble a quasi-blackbody spectrum at a temperature T, with a non-zero chemical potential enforced through the conservation of photons. The term quasi-blackbody used here refers to a blackbody emitter with non zero chemical potential.

One would further expect the temperature T in the photon distribution function to be equal to the dye-solvent temperature. As was shown in Chapter 1, a more rigorous determination of temperature based on the Kennard–Stepanov relation [29] is often needed.

In the wavelength region where re-absorption affects photon transport, the edge fluorescence spectrum can be approximated by:

$$\mathcal{F}_e\left(T^*, \mu_{flux}, \nu\right) \approx \frac{2\pi h\nu^3}{(c)^2} \exp\left(\frac{-h\nu}{kT^*}\right) \exp\left(\frac{\mu_{flux}}{kT^*}\right). \tag{126}$$

Stimulated emission is neglected in this function.

Fig. 197 illustrates the application of Eqn. (126) to an experimental edge fluorescence spectrum (R6G, broken red line). It is clear that the quasi-blackbody function agrees remarkably well with experiment in the spectral region where the absorption and fluorescence bands of the dye overlap. From this fit μ_{flux} can be determined.

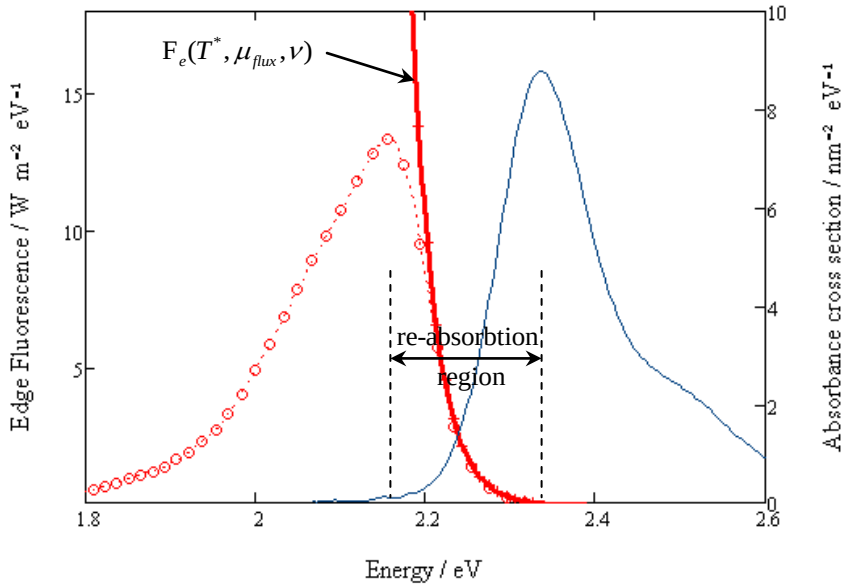

Fig. 197: Experimental edge fluorescence spectrum of R6G (broken red line) compared to a blackbody function (solid red line). In the spectral region where re-absorption affects photon transport, the edge fluorescence spectrum resembles a quasi-blackbody function.

8.1.2 Effective chemical potential μ_{dye} of the photoexcited dye

Consider in the first instance a simple chemical reaction $N \leftrightarrow N^*$, where the chemical potential of the species N and N^*can be written as [188]:

$$\begin{aligned} \mu_N &= \mu_{N_{(0)}} + kT\ln[N] \\ \mu_{N^*} &= \mu_{N^*_{(0)}} + kT\ln[N^*], \end{aligned} \tag{127}$$

where $[N^*]$ and $[N]$ represent molecular concentrations.

In each expression in Eqn. (127) the first term, with subscript "(0)", is the standard chemical potential or intrinsic molecular free energy of the molecules, as defined by the IUPAC. In general they contain the pressure and volume conditions of the chemical reaction. The second, logarithmic, term is related to the entropy of the reaction. At equilibrium, due to the concentration of the species N and N^* adjusts so that the chemical potentials μ_{N^*} and μ_N become equal [189]:

$$\frac{[N]}{[N^*]} = \exp - \left(\frac{\mu_{N_{(0)}} - \mu_{N^*_{(0)}}}{kT}\right). \tag{128}$$

In the case of a photochemical reaction where the species are not in equilibrium; it is usual to consider the reaction in steady state, where in this state the free energy change is given by the difference of the chemical potential given by Eqn. (127) [190]:

$$\mu_N - \mu_{N^*} = \mu_{N_{(0)}} - \mu_{N^*_{(0)}} + kT\ln\frac{[N]}{[N^*]}. \tag{129}$$

The quantity $\mu_N - \mu_{N^*}$, denoted μ_{Dye} in this thesis, corresponds to the free energy per particle in this reaction. For a photochemical reaction in which a molecule N in the ground state absorbs a photon of energy $h\nu$ and becomes excited (N^*) it has been argued that the intrinsic quantity $\mu_{N_{(0)}} - \mu_{N^*_{(0)}}$ is the energy of the electronic transition $S_0 \rightarrow S_1$, denoted by $h\nu_0$ in the following development [9]. Under steady illumination, the chemical potential of the excited dye can be written as:

$$\mu_{dye} = h\nu_0 + kT^* \ln\left(\frac{[N^*]}{[N]}\right). \tag{130}$$

Equation (130) can be interpreted as the difference between the chemical potentials of the ground and excited states of the dye molecule – in other words, the "splitting" of the two chemical potentials, as commonly used in quantum solar energy conversion. Resting on the approximation of negligible volume variation, this equation can easily be used to characterize the effective chemical potential of the dye in a fluorescent solar collector.

In a simple model where the vibrational potential curves are approximated by parabolas with equal frequency, the energy separation represented by $h\nu_0$ corresponds to the midpoint between the wavelengths of maximum absorption and maximum fluorescence [27]. Neglecting re-absorption within the escape cone of the fluorescent collector, the concentration $[N^*]$ of excited dye molecules can be approximated by Eqn. (97).

Replacing Eqn. (97) in Eqn. (130), the dye chemical potential is computed using:

$$\mu_{dye} = h\nu_0 + kT^* \ln\left(\frac{\frac{\dot{f}_{sun}\ Q_a\ \tau_{tot}}{1-\varphi(1-P)R}}{[N]}\right), \tag{131}$$

where the concentration of molecules in the ground state, denoted by $[N]$, is approximated by the dye concentration.

8.1.3 Theoretical chemical potential μ_{theo}

It is instructive to compare the experimental values of μ_{flux} and μ_{dye} with theory. To this end we shall use the upper limit of the chemical potential, which can be obtained by equating incident flux to total emitted flux. For a collector, doped with a unit quantum yield dye, illuminated by a thermal source at T_s the photon balance, as shown in Chapter 5, is given by:

$$\dot{f}_s(T_s, \nu, \mu = 0) = \dot{f}_e(T^*, \nu, \mu_{theo}) + \dot{f}_{front}(T^*, \nu, \mu_{theo}), \tag{132}$$

where $\dot{f}_{front}$ is the fluorescence photon flux emitted through the front face (Section 5.1.5)

For a collector which absorbs all the incoming light with frequency up to ν_{abs} (absorption cut-off frequency), covered by a perfect photonic band-stop mirror which reflects all light with frequency $< \nu_{abs}$, the fluorescent photon fluxes $\dot{f}_{front}$ and $\dot{f}_e$ have been described [57] [8] using Planck's law:

$$\dot{f}_e(T^*, \mu_{theo}, \nu) \approx \underbrace{n^2 \pi A_{edge}}_{edge\ \ etendue} \int_{\nu_g}^{\infty} \frac{2\nu^2}{c^2} \exp\left(\frac{-h\nu}{kT^*}\right) \exp\left(\frac{\mu_{theo}}{kT^*}\right)\ d\nu, \tag{133}$$

and

$$\dot{f}_{front}(T^*, \mu_{theo}, \nu) \approx \overbrace{\pi A_{front}}^{\substack{front \\ etendue}} \int_{\nu_{abs}}^{\infty} \frac{2\nu^2}{c^2} \exp\left(\frac{-h\nu}{kT^*}\right) \exp\left(\frac{\mu_{theo}}{kT^*}\right)\ d\nu. \tag{134}$$

Substituting Eqns. (133) and (134) into Eqn. (132), the theoretical chemical potential can then be extracted:

$$\mu_{theo} = h\nu_{abs}\left(1 - \frac{T^*}{T_s}\right) + kT_c \ln\left(\frac{T_s}{T^*}\right) + kT_c \ln\left(\frac{\Omega_s}{\pi}\right) + kT_c \ln\left(\frac{1+\wp(\nu_{abs}, T^*)}{1+\wp(\nu_g, T^*)}\right) + kT^* \ln(1 - Q_c), \tag{135}$$

where the function $\wp(\nu, T)$ is a small correction term defined by Eqn. (48)

Equation (135) assumes that the chemical potential of the incident light is zero and, as before, it neglects stimulated emission.

The Carnot engine type relation (Eqn. (135)) resembles Würfel's expression [52], reviewed in Chapter 2, in which the first three terms determine the open-circuit voltage of a solar cell. The addition of the last term, derived by Markvart in [8], gives a more accurate formula for the operation of fluorescent solar collectors, taking into account the difference between the absorption and emission wavelengths and the reduction of the photon chemical potential on account of the collection efficiency. The chemical potential calculated using this relation is the upper limit of the chemical potential, since the photon fluxes arise from thermodynamic arguments which do not consider any practical losses.

In the experiments the solid angle and the temperature of the source were determined by comparing the illumination spectrum with a blackbody radiator, as shown in Chapter 6. The collection efficiency was measured directly as the ratio of the number of photons emitted at the edge to the number of photons absorbed.

8.2 Photon chemical potential: results

Before comparing the results of the three characterization methods set out in Section 8.1, the effective temperatures of the dyes were calculated using the Kennard-Stepanov law (Chapter 1). Fig. 198 presents the application of this law to the R6G absorbance and fluorescence spectra.

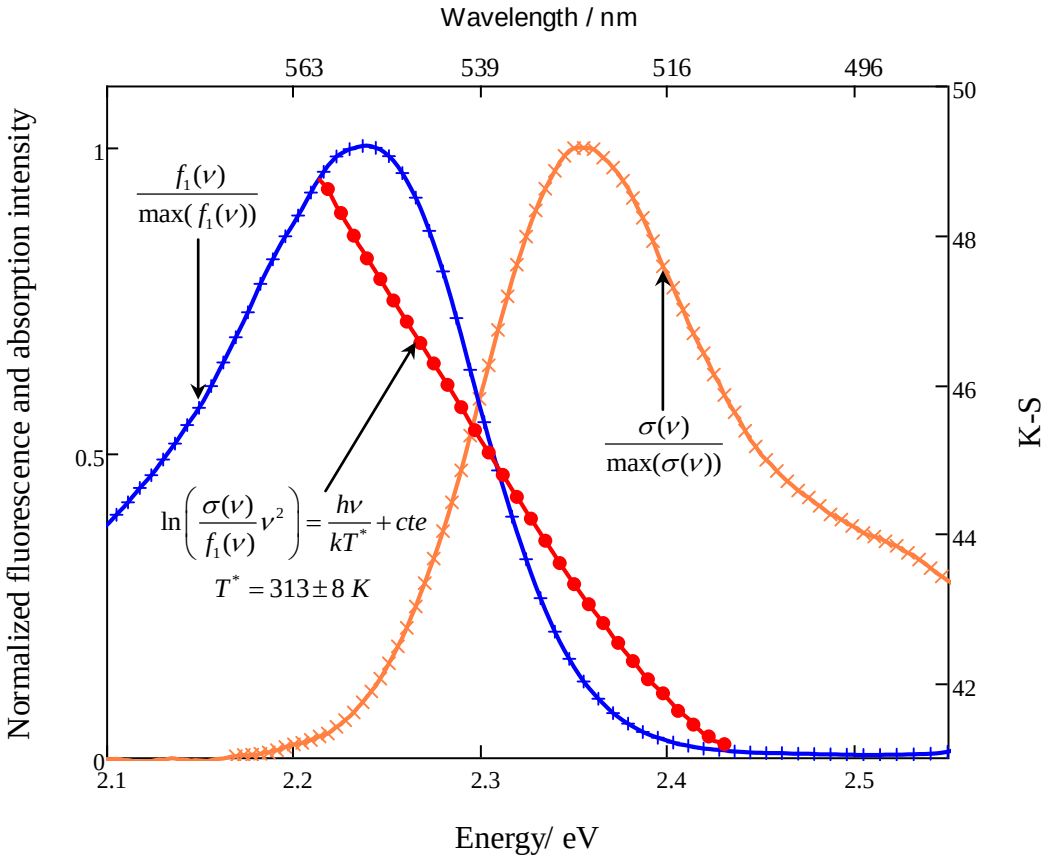

Fig. 198: Kennard-Stepanov relation applied to the spectra of Rhodamine 6G. (Graph published in [183])

The temperature of the ethanol bath was 297 K and the effective temperature of the fluorescence was $T^* = 313 \pm 8\ K$. The Kennard-Stepanov law worked well for dyes with a small Stokes shift (e.g. Frot 305 (43 nm), R6G (44 nm) and R101 (41 nm)). For dyes with a large Stokes shift (e.g. DCM-dye (162 nm) and C-540A (111 nm)) T^* was impossible to determine because the re-absorption region (Fig. 190) almost disappeared. A summary of effective temperatures for the various dyes is given in Table 16.

As Fig. 96 shows, the thermodynamic behaviour of the fluorescence is demonstrated by how well the data fit a quasi-blackbody function (Eqn. (126)). Experimental values of the chemical potential μ_{flux} obtained from this fitting procedure were surprisingly close to the thermodynamic limit μ_{theo} (Table 16).

Fig. 199 to 100 show edge fluorescence spectra for R6G, Frot 305 and R101. The thermodynamic behaviour of fluorescence is highlighted in the logarithmic plots (Fig. 199b to 100b). As expected from Eqn. (126), the edge fluorescence becomes linear in the re-absorption region, with a slope given by the inverse temperature. These edge fluorescence spectra resemble the spectrum of thermal radiation using the Kennard-Stepanov temperature of the absorbing/emitting species. The uncertainty in the chemical potentials (broken and solid lines in the figures) was estimated to be $0.01\ eV$.

Attempts to estimate the chemical potential of dyes with large Stokes shifts were made using DCM-dye in DMSO. The recorded edge fluorescent contours were Gaussian shaped, drastically different from those for dyes with small Stokes shifts, and it was impossible to determine chemical potentials.

Table 16: Summary of results, showing chemical potentials estimated for R101, R6G, and Frot 305 dyes. The uncertainty in these chemical potentials was estimated to be $0.01\ eV$; other uncertainties are indicated in the table. The missing data for Frot 305 is due to the lack of information on the dye's molar mass.

Dye	Solvent	$h\nu_0$ (eV)	τ_{tot} (ns)	φ	T^* T_{col} (K)	μ_{flux} (eV)	μ_{Dye} (eV)	μ_{theo} (eV)
R101	Ethanol $n = 1.36$ [a]	2.15	4.46 ± 0.03 [b] 4.92 *S&B*	1 [b]	297 ± 8 297	1.63	1.64	1.68
R6G	Ethanol $n = 1.36$ [a]	2.29	3.99 ± 0.03 [c] 3.88 *S&B*	0.95 [c]	313 ± 8 297	1.69	1.71	1.81
Frot 305	DCM $n = 1.42$ [a]	2.08	5.74 ± 0.02 –	0.98 [d]	306 ± 8 295	1.57	–	1.64

[a] Reference [176] [b] Reference [114]
[c] Reference [191] [d] Reference [115]

The lifetimes reported in Table 16 for R101 and R6G were taken from [114], and checked against the Strickler-Berg relation (Section 1.2.1.3). For the recently synthesized Frot 305 dye, the lifetime was measured using a fluorescence lifetime spectrometer (FluoTime 200®). The quantum yield of Frot 305 was obtained from [115] and verified using the method of Williams [32].

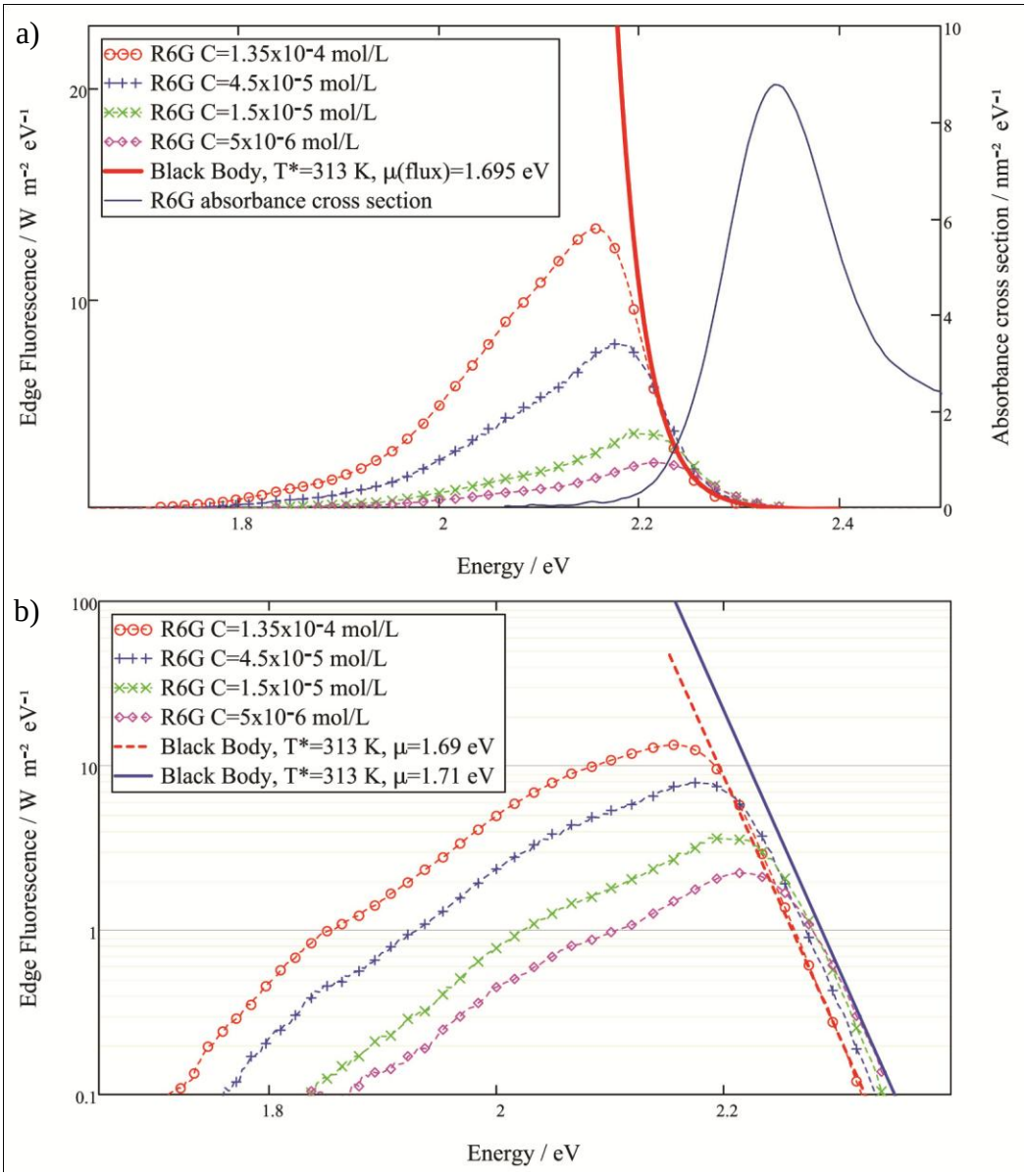

Fig. 199: (a) Typical edge fluorescence spectra of Rhodamine 6G compared with a blackbody function at $T^* = 313 \mp 8\ K$ and $\mu_{flux} = 1.695 \pm 0.01\ eV$. (b) Log plot of Fig. 199a showing the uncertainty band on the chemical potential calculated. Numbers in the legend give the dye concentration in the solvent. (Graph published in [9])

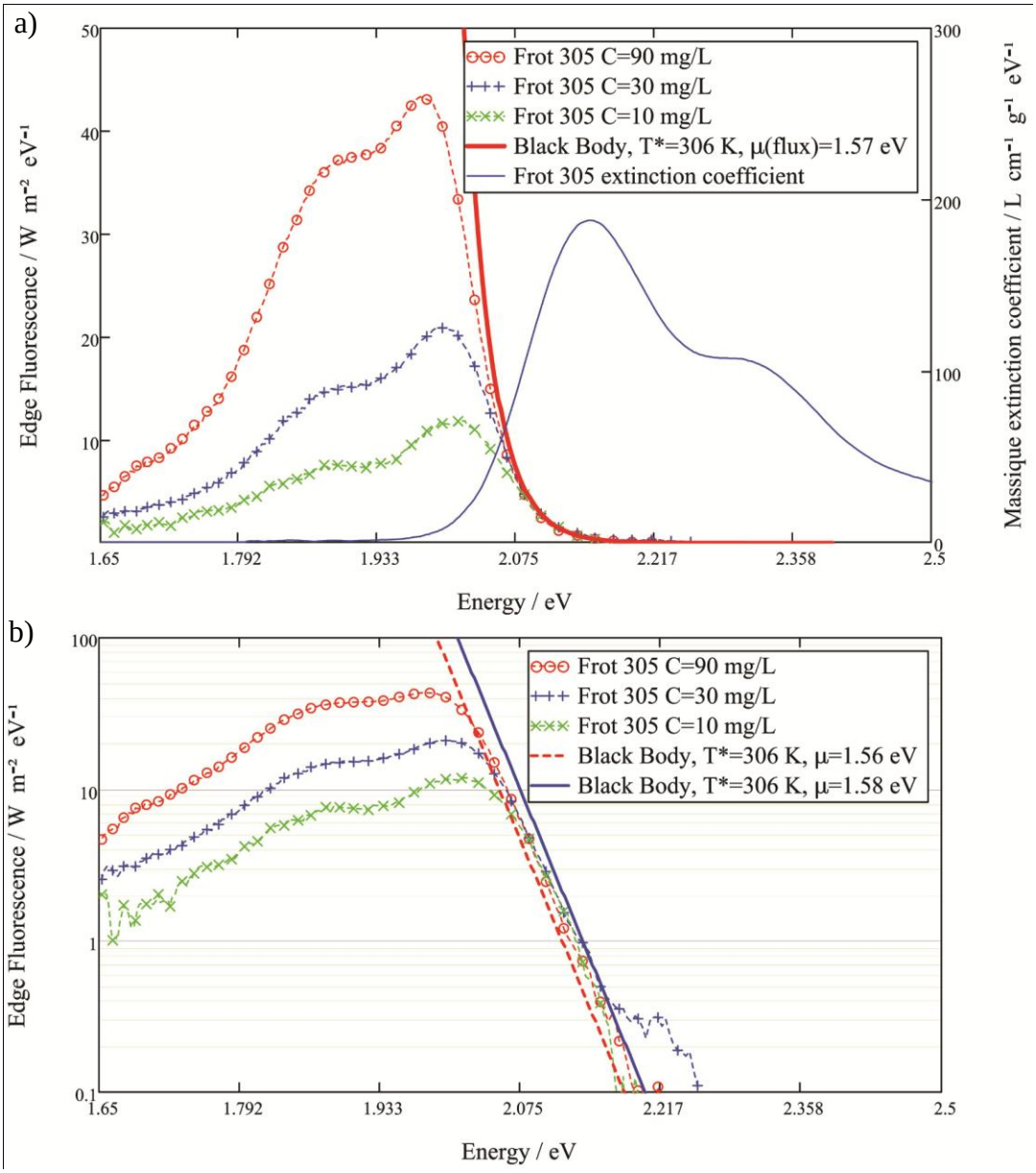

Fig. 200: (a) Typical edge fluorescence spectra for Frot 305 compared with blackbody function at $T^* = 306 \pm 8\ K$ and $\mu_{flux} = 1.57 \pm 0.01\ eV$. (b) Log plot of the same data. Legend gives dye concentrations in the solvent. (Graph published in [9])

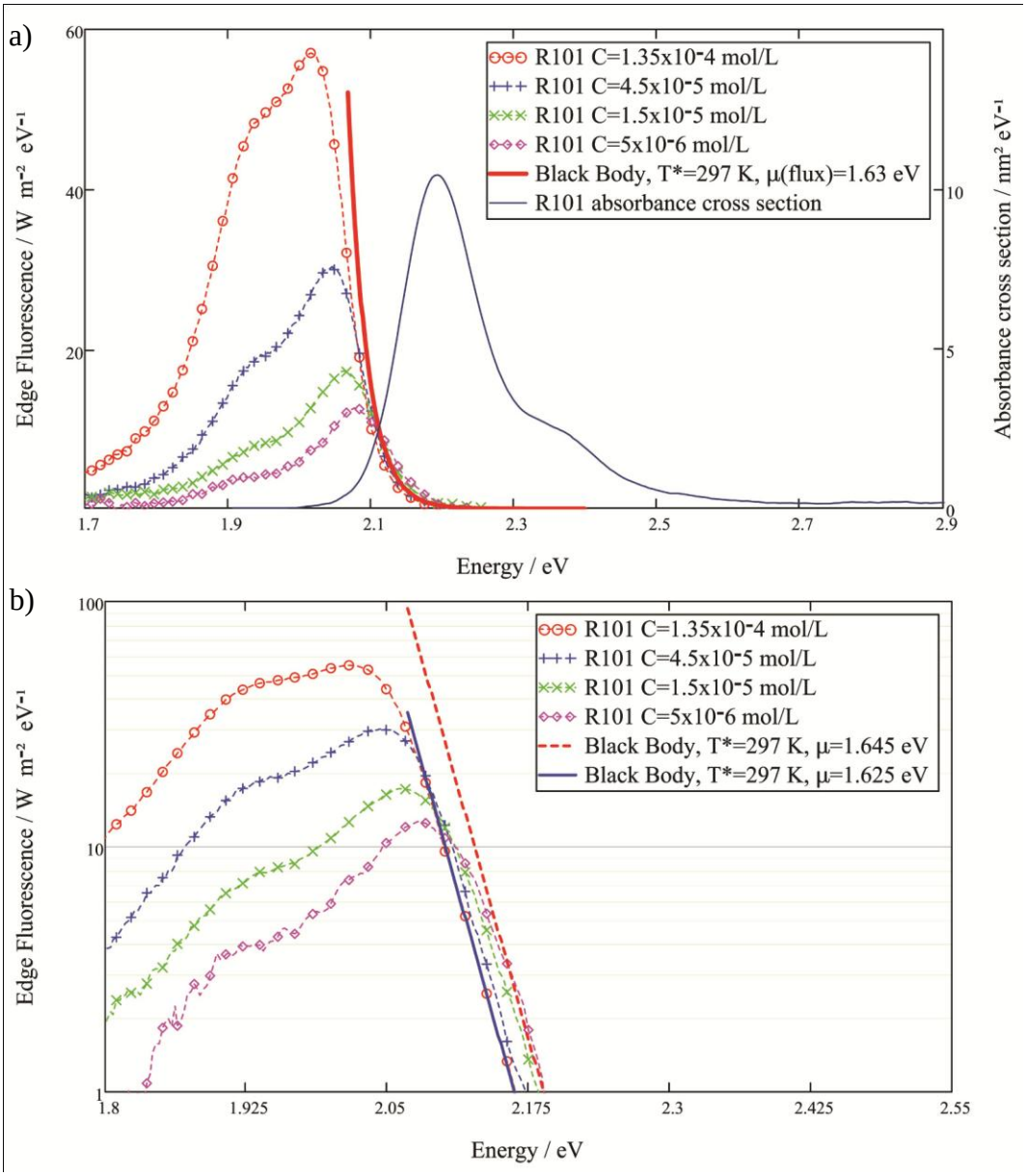

Fig. 201: (a) Typical edge fluorescence spectra for Rhodamine 101 compared with blackbody function at $T^* = 297 \mp 8\ K$ and $\mu_{flux} = 1.635 \pm 0.01\ eV$. (b) Log plot of the same data. Legend gives dye concentrations in the solvent. (Graph published in [9])

8.3 Discussion

Three different techniques were used to assess the chemical potential of the photons in a FSC:

(i) experimental characterization of the edge fluorescent flux chemical potential μ_{flux} based on the hypothesis of thermodynamic equilibrium
(ii) evaluation of the photoexcited dye chemical potential μ_{dye} using standard thermodynamic theory and relationships arising from the two-photon-fluxes model
(iii) theoretical determination of μ_{theo}, an upper limit for the chemical potential, from a detailed-balance argument between the incoming light and the re-emitted flux.

Central to this analysis, the chemical potential of the edge fluorescence flux, estimated using thermodynamic theory for an ideal photon gas, was remarkably close to the dye chemical potential and to theoretical limits (Table 16). This demonstrated that fluorescent collectors operate like blackbody convertors in a restricted frequency range, transforming a hot incident photon flux at temperature T_s and with zero chemical potential into a cold fluorescent flux at temperature T^* and with a chemical potential close to the thermodynamic limit.

The measured chemical potential is related to the open-circuit voltage V_{oc} of the edge solar cell since, once the photon flux has cooled down, there are no thermodynamic losses to prevent the photo-conversion. Hence:

$$qV_{oc} = \mu_{flux} \approx \mu_{Dye} \,, \tag{136}$$

where q is the elementary charge.

Equation (136) simply sets the splitting of the two chemical potentials characterizing the photoexcited dye molecule equal to the open-circuit voltage. This argument is similar to those commonly used for solar cells in which the splitting of the quasi-Fermi levels defines the upper limit of the open-circuit voltage (Chapter 2). The key difference here is that for FSCs the practical chemical potential μ_{flux} is closer to the thermodynamic limit than is the chemical potential observed for solar cells.

The similarity of the three photon chemical potentials validated the model developed in [8], demonstrating that optimal photon management can lead to remarkably efficient collectors. In this publication it is shown that the overall efficiency of a fluorescent solar collector in an optimal configuration, can reach 27% – about 90 % of the output from a directly illuminated c-Si solar cell.

Conclusion

This thesis presents the results of PhD research carried out over 4½ years with the support of the Supergen consortium Photovoltaic Materials for the 21st Century (PV-21). The principal aim of the work was to increase the fundamental understanding of photon transport in fluorescent collectors, in order to improve the energy collection and reduce the costs of c-Si solar cells.

The components of a fluorescent solar collector (FSC) – the fluorescent collector and the solar cell – were studied separately. This is reflected in the structure of this thesis: c-Si solar cells are examined in the first part (Chapters 2 and 3), fluorescent collectors in the second part (Chapters 4 and 5) and the full FSC in the last part (Chapters 6 to 8). The key results from each part are summarized below.

The first part was concerned with the study and development of c-Si cell performance. Highly efficient $n^+/p/p^+$ structures were designed in order to minimize the practical losses in crystalline silicon. Their fabrication, in Southampton University's clean-room facilities, was in its final stage when a major fire destroyed the facilities. The focus of the research focus subsequently shifted to solar cell theory.

An analytical model of cell operation highlighted the importance of charge carrier diffusion length and front surface passivation: long carrier diffusion length and a passivated surface are essential to a good solar cell.

The upper efficiency limits of standard P-N junctions and tandem cells were derived using a semi-analytical model stressing the thermodynamic origins of the open-circuit voltage. This unusual approach showed excellent agreement with the original model of de Vos [61]. The thermodynamic approach sets V_{oc} equal to the difference in chemical potential between the Fermi levels. This argument was used in the final part of the thesis to show that the chemical potential of the fluoresced photons in a fluorescent collector is closer to the thermodynamic limit than is the chemical potential in a solar cell.

The second part of this thesis reported on investigations into photon transport in the collector. Analytical methods, including the two-photon-fluxes model, and numerical simulations (ray-tracing) show that the challenge for FSCs lies in the reduction of losses, especially re-absorption. This is the main limiting factor, and formed the focus of the rest of the thesis.

The analytical re-absorption model of Weber was reviewed, and its limitations studied using ray-tracing simulations. For collectors with high optical gain, this model was shown to agree very well with the simulations, while deviations were found for collectors with gain factors below 10. The application of ray-tracing simulations to collector geometry and homogeneity indicated that geometry has no influence on the re-absorption profile and that thin-film structures perform no better than standard collectors. The optimal configuration for inhomogeneous structures was with equal film and substrate refractive indices.

Experimental work carried out in the third part was aimed at verifying the validity of the ray-tracing simulations. This was done by studying the fluorescence spectra emitted by a special type of fluorescent collector, where absorption and fluorescence take place in a liquid medium, in effect a liquid fluorescent collector. Re-absorption probabilities were studied for liquid and thin-film devices using the two-photon-fluxes data analysis technique. It was shown that the experimental data agree well with the ray-tracing simulations and the *W&L* model.

Using the concept of photon management, the efficiency of a two-dye collector in minimizing re-absorption was compared to that of a single-dye system with the same absorption probability. The results showed a relative increase of 58 % in efficiency for the multiple-dye system. The feasibility of photon management across the full solar spectrum was discussed. The lack of suitable dyes in the long-wavelength region was shown to limit the operation of FSCs. The optimal semiconductor band gap was investigated, and it was shown that GaAs cells are the best choice for coupling with collectors.

The chemical potential of the fluoresced photons was discussed in the final chapter. It was demonstrated using three different approaches that the chemical potential of the edge fluorescence flux, characterized using the theory of an ideal photon gas, is remarkably close to the dye chemical potential and to theoretical limits. This indicates that, within a restricted frequency range, fluorescent collectors operate like blackbody convertors, and that photon management can achieve remarkable collector efficiencies – up to 90 % of those for directly illuminated c-Si solar cells as shown in Ref. [8].

Suggestions for further work

Practical efficiencies for fluorescent solar collectors are still far from their theoretical limits, and can be significantly improved through the development of:

- photonic mirrors whose optical properties are independent of angle of incidence
- new laser dyes or quantum dots with large Stokes shifts and unit quantum yield

- efficient energy transfer between dyes, using organized structures such as zeolites or Langmuir–Blodgett films
- tandem devices based on designs such as that shown in Fig. 101

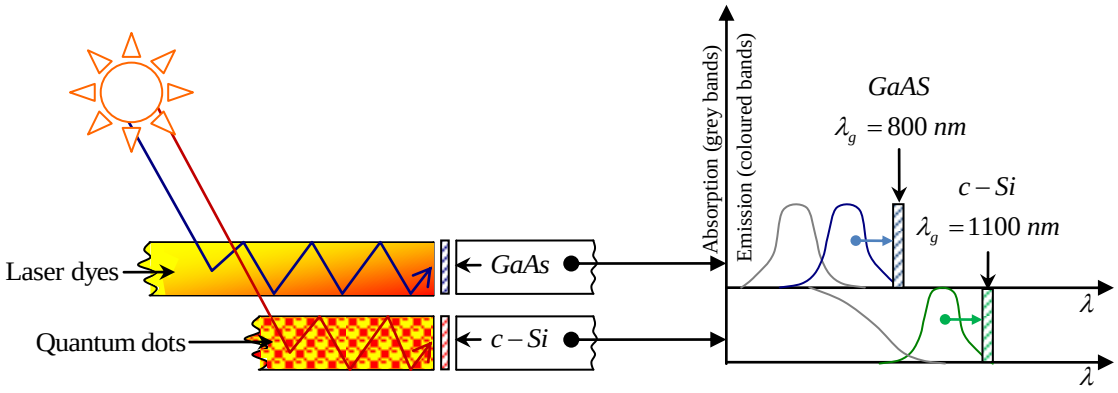

Fig. 202: Tandem FSC design using quantum dots and laser dyes.

The tandem collector illustrated in Fig. 101 uses a laser dye mixture to efficiently absorb high-energy photons while a matrix doped with quantum dots absorbs low-energy photons. Such a tandem system would resolve the absorption issue because quantum dots can be tuned to absorb and emit efficiently in the long-wavelength region.

The practical efficiency of such a system could surpass the ≈ 10 % efficiency milestone. However, its viability needs to be studied further, to take account of:

- price increases resulting from the use of quantum dots and GaAs cells
- re-absorption issues associated with quantum dots.

Appendix A

The Weber and Lambe analytical re-absorption model

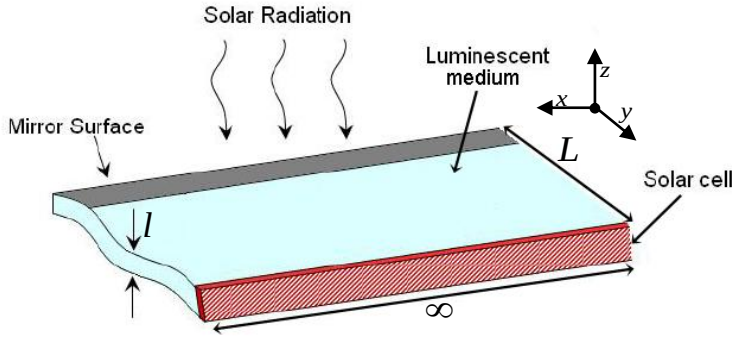

Using the coordinate system for collector geometry employed in the *W&L* model [7] (figure redrawn above) the path length of a random ray emitted within the collector can be estimated using its projection onto the *y*-axis.

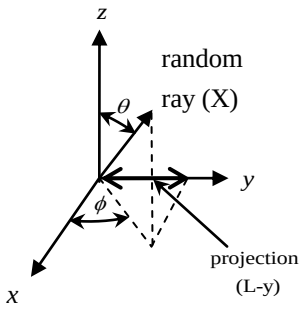

$$(L \pm y) = X \sin(\theta)\sin(\phi) \tag{137}$$

$$X = \frac{(L-y)}{\sin(\theta)\sin(\phi)} \text{ , or} \tag{138}$$

$$X = \frac{(L+y)}{\sin(\theta)\sin(\phi)} \text{ .} \tag{139}$$

Equation (138) refers to the path length of a light ray emitted towards the cell while Eqn. (139) refers to the path length of a random ray towards the mirror.

Using the Beer-Lambert law to estimate absorption over the path length ($L \pm y$) leads to:

$$e^{\frac{-\alpha(\lambda)(L-y)}{\sin(\theta)\sin(\phi)}} \text{ or } e^{\frac{-\alpha(\lambda)(L+y)}{\sin(\theta)\sin(\phi)}}. \qquad (140)$$

In the model of Weber and Lambe the probability of photon arrival is integrated over all possible photon paths (over L, θ_c and ϕ), excluding rays emitted into the angle $\theta_c < \theta < \pi - \theta_c$, corresponding to light escaping within the critical cone:

$$\int_0^L \int_0^{\pi} \int_{\vartheta_c}^{\pi-\theta_c} \left(e^{\frac{-\alpha(\lambda)(L-y)}{\sin(\theta)\sin(\phi)}} + e^{\frac{-\alpha(\lambda)(L+y)}{\sin(\theta)\sin(\phi)}} \right) d(\theta) d(\phi) d(y) \qquad . \qquad (141)$$

The collection efficiency for the first photon generation the ratio of the solid angle described by the trapped photon to the solid angle of a complete sphere:

$$\frac{\int_0^L \int_0^{\pi} \int_{\vartheta_c}^{\pi-\theta_c} \left(e^{\frac{-\alpha(\lambda)(L-y)}{\sin(\theta)\sin(\phi)}} + e^{\frac{-\alpha(\lambda)(L+y)}{\sin(\theta)\sin(\phi)}} \right) \sin(\theta) d(\theta) d(\phi) d(y)}{4\pi} \qquad . \qquad (142)$$

Finally, the collection efficiency is here expressed per unit length, and adjusted for the quantum yield of the dye:

$$Q_c{}^1(L, \alpha) = \varphi \frac{\int_0^L \int_0^{\pi} \int_{\vartheta_c}^{\pi-\theta_c} \left(e^{\frac{-\alpha(\lambda)(L-y)}{\sin(\theta)\sin(\phi)}} + e^{\frac{-\alpha(\lambda)(L+y)}{\sin(\theta)\sin(\phi)}} \right) \sin(\theta) d(\theta) d(\phi) d(y)}{4\pi L} . \qquad (143)$$

References

[1] **P. Würfel.** *Physics of solar cells.* 2005. p. 186. IBSN:3527404287.

[2] *Basic research needs for solar energy utilisation.* **N.S. Lewis et al.** 2005, Report on the basic energy sciences workshop on solar energy utilisation, US departement of energy.

[3] *World consumption of primary energy by energy type and selected country groups.* Energy information administration, U.S. department of energy. 1980-2007.

[4] **A. Goetzberger, J. Knobloch, B. Voss.** *Crystalline silicon solar cells.* 1998. p. 237. IBSN:047197144.

[5] **T. Markvart.** *Solar electricity.* 1994. p. 298. ISBN:0471988529.

[6] **P. Kittidachachan.** *Reducing the cost of crystalline silicon solar cells by using fluorescent collectors.* 2007. Southampton, PhD thesis.

[7] *Luminescent greenhouse collector for solar radiation.* **W.H. Weber, J. Lambe.** 10, 1976, Applied optics, Vol. 15, pp. 2299-2300.

[8] *Detailed balance method for ideal single-stage fluorescent collectors.* **T. Markvart.** 2006, Journal of applied physics, Vol. 99, pp 026101-3

[9] *The chemical potential of light in fluorescent solar collectors.* **T.J.J. Meyer, T. Markvart.** 6, 2009, Journal of applied physics, Vol. 105, pp. 063110-8.

[10] *Detailed balance limit of efficiency of p-n junction solar cells.* **W. Shockley, H.J. Quiesser.** 3, 1961, Journal applied physics, Vol. 32, pp. 510-519.

[11] *Photostable fluorescent glass films for solar concentrators.* **R. Reisfeld, V. Chernyak, M. Eyal.** 1992, Proceedings of the SPIE conference, Vol. 1727, pp. 299-305.

[12] *A low escape-cone-loss luminescent solar concentrator.* **B.S. Richards, A. Shalav, R.P. Corkish.** 2004. Proceedings of the 19th European photovoltaic solar energy conference and exhibition, Paris, France.

[13] *Quantum dot solar concentrators.* **S.J. Gallagher, P.C. Eames, B. Norton.** 2002, Proceedings of the world renewable energy congress, Cologne, Germany, pp. 364-368.

[14] *Quantentheorie des einatomigen idealen gases (Quantum theory of monatomic ideal gases).* **A. Einstein.** 1924, Sitzungsberichte der Preussichen akademie der wissenschaften physikalisch—mathematische klasse, pp. 261-267.

[15] **S. Wenham, M. Green.** *Applied photovoltaics, University of New South Wales.* 2006. p. 313. ISBN:073342175X.

[16] *What is an air mass 1.5 spectrum?* **C. Riordan, R. Hulstron.** 1990, 21st IEEE photovoltaic specialist conference, Kissimmee, Florida, USA, Vol. 2, pp. 1085-1088.

[17] **M.A. Green.** *Solar cells.* 1992. p. 237. IBSN:0858235803.

[18] **A. Luque, S. Hegedus.** *Handbook of photovoltaic science and engineering.* 2003. p. 1168 . ISBN 0471491969, 9780471491965.

[19] *The chemical potential of luminescent radiation.* **P. Würfel, W. Ruppel.** 1981, Journal of luminescence, Vol. 24/25, pp. 925-928.

[20] *Light with nonzero chemical potential.* **F. Herrmann, P. Würfel.** 6, 2005, American journal of physics, pp. 1-5.

[21] *Quenching of photoluminescence of solutions.* **A. Jablonski.** 1954, Acta physica polonica, Vol. 13, pp. 175-186.

[22] **P. Atkins, J. de Paula.** *Physical chemistry 8th edition.* 2006. p. 1064. IBSN:9780198700722.

[23] *On the interaction of radiation with matter and on fluorescent exciting power.* **E.H. Kennard.** 1926, Physical review, Vol. 28, pp. 673-683.

[24] *A universal relation between the absorption and luminescence spectra of complex molecules.* **B.I. Stepanov.** 1956, Lenin Byelorussian State University, pp. 81-83.

[25] *A theory of intensity distribution in band systems.* **E. Condon.** 1926, Physical review, Vol. 28, pp. 1182-1201.

[26] *Elementary processes of photochemical reactions.* **J. Franck.** 1926, Transactions of the Faraday society, Vol. 21, pp. 536-542.

[27] **J.R. Lakowicz.** *Principle of fluorescent spectroscopy 3rd edition.* 2006. ISBN:0387312781.

[28] *General relations between absorption and emission for the modulation spectra of polyatomic molecules.* **B.S. Neporent.** 1958, Soviet physics doklady, Vol. 3, pp. 337-339.

[29] *On the thermodynamics of fluorescence.* **E.H. Kennard.** 1, 1917, Physical review, Vol. 9, pp. 29-39.

[30] **B.I. Stepanov.** *Correlation between the luminescent and absorption spectra of complex molecules.* Institute of physics and mathematics, Academy of sciences of the Belorussian SSR. 1957.

[31] **B.I. Stepanov.** *Correspondence of the absorption and luminescence bands of complex molecules.* Institute of physics and mathematics, Academy of sciences of the Belorussian SSR. 1959.

[32] *Relative fluorescence quantum yields using a computer controlled luminescence spectrometer.* **A.T. R. Williams, S.A. Winfield, J.N. Miller.** 1983, Analyst, Vol. 108, p. 1067.

[33] *An improved experimental determination of external photoluminescence quantum efficiency.* **J.C. de Mello, H.F. Wittmann, R.H. Friend.** 3, 1997, Advanced materials , Vol. 9, pp. 230-232.

[34] *Absolute measurments of photoluminescence quantum yields of solutions using an integrating sphere.* **L. Porres, A. Holland, L.O. Palsson, A. Monkman, C. Kemp, A. Beeby.** 2, 2006, Journal of fluorescence , Vol. 16, pp. 267-273.

[35] *Relationship between absorption intensity and fluorescence lifetime molecules.* **S.J. Strickler, R.A. Berg.** 4, 1962, The journal of chemical physics, Vol. 37, pp. 814-822.

[36] *English translation: On the quantum theory of radiation, by D. ter Haar.* **A. Einstein.** 1917, Physikalishce zeitschrift, Vol. 18, p. 121.

[37] *Rhodamine B and rhodamine 101 as reference substances for fluorescence quantum yield measurements.* **T. Karstens, K. Kobs.** 14, 1980, Journal of physical chemistry , Vol. 84, pp. 1871-1872.

[38] **S.M. Sze.** *Physics of semiconductor devices, 2nd edition.* 1981. p. 868. IBSN:0471056618.

[39] *Influence of radiative recombination on the minority-carrier transport in direct band-gap semiconductors.* **O. von Roos.** 1983, Journal of applied physics, Vol. 54, p. 1390.

[40] *Photon-radiative recombination of electrons and holes in germanium.* **W. van Roosbroeck, W. Shockley.** 1558, Physical review letters, Vol. 94, pp. 1558-1560.

[41] *Spectroscopic investigations of intramolecular relaxations in organic complex molecules*. **B.S. Neporent.** 1-2, 1974, Pure applied chemistry, Vol. 37, pp. 111-146.

[42] *The relationship between the electronic absorption and luminescence spectra of complex molecules.* **Yu. T. Mazurenko, B.S. Neporent,.** 1962, Optical society of America, Vol. 12, pp. 571-575.

[43] *Universal relationship between optical emission and absorption of complex systems: An alternative approach.* **D.A. Sawicki, R.S. Knox.** 6, 1996, Physical review A, Vol. 54, pp. 4837-4841.

[44] *Einstein coefficients, cross sections f values, dipole moments, and all that.* **R.C. Hilborn.** 11, 1982, American journal of physics , Vol. 50, pp. 982-986.

[45] *Excited-state equilibration and the fluorescence absorption ratio.* **R.S. Knox.** 1999, Acta physica polonica A, Vol. 95, pp. 85-103.

[46] *Exctions and their equilibration.* **R.S. Knox.** 6, 1997, Pure and applied chemistry , Vol. 69, pp. 1163-1170.

[47] *Relationship between the absorption and emission spectra and the "red drop" in the action spectra of fluorescence in vivo.* **L. Szalay, E. Rabinowitch, N.R. Murty and Govindjee.** 1967, Biophysical journal, Vol. 7, pp. 137-149.

[48] *The Kennard-Stepanov relation for time-resolved fluorescence.* **R.S. Knox, L.F. Marshall.** 2000, Journal of luminescence , Vol. 85, pp. 209-215.

[49] *Relationship between the absorption and luminescence spectra of concentrated polar solutions of complex organic compounds.* **N.R. Senatorova, L.V. Levshin, B.D Ryzhikov.** 3, 1981, Optics and spectroscopy, Vol. 50. ISSN: 0030-400X CODEN: OPSUA3.

[50] *The relationship between the electronic absorption and luminescence spectra of complex molecules.* **Yu. T. Mazurenko, B.S. Neporent.** 1962, Optical society of America, Vol. 12, pp. 571-575.

[51] **A. de Vos.** *Thermodynamics of solar energy conversion.* 2008. p. 192. IBSN:978352740842.

[52] *Upper limit for the conversion of solar energy.* **W. Ruppel, P. Würfel.** 4, 1980, IEEE transactions on electrons devices, Vol. 27, pp. 877-882.

[53] *The Carnot factor in solar-cell theory.* **P.T. Landsberg, T. Markvart.** 4, 1998, Solid state electronics, Vol. 42, pp. 657-659.

[54] *Absolute limiting efficiencies for photovoltaic energy conversion.* **G.L. Araujo, A. Marti.** 2, 1994, Solar energy materials and solar cells, Vol. 33, pp. 213-240.

[55] *Detailed balance efficiency limits with quasi-Fermi level variations.* **S.P. Bremner, R. Corkish, C.B. Honsberg.** 10, 1999, IEEE transactions on electron devices, Vol. 46, pp. 1932-1939.

[56] *Detailed balance efficiency of a three level system with thermionic transitions.* **S.P. Bremner, C.B. Honsberg.** 2002, Conference record of the IEEE photovoltaic specialists, New Orleans, LA, United States, pp. 1051-1054.

[57] *Detailed balance efficiency of ideal single stage fluorescent solar collectors.* **T. Markvart, L. Danos, P. Kittidachachan, R. Greef.** Proceedings of the 20th european photovoltaic solar energy conference, Barcelona, Spain. pp. 171-174.

[58] *The chemical potential of fluorescent light.* **T.J.J. Meyer, T. Markvart.** 2008, Proceedings of the 23rd European photovoltaic solar energy conference, Valencia, Spain, pp. 399-403. 1CV.1.53.

[59] **T. Markvart, L. Castaner.** *Practical handbook of photovoltaics: fundamentals and applications.* 2003. p. 500. ISBN: 9781856173902.

[60] *Solar cell efficiency tables (version 32).* **M.A. Green, K. Emery, Y. Hishikawa and W. Warta.** 2008, Progress in photovoltaics: research and application, Vol. 16, pp. 435-440.

[61] *Detailed balance limit of the efficiency of tandem solar cells.* **A. de Vos.** 1979, Journal of applied physics, Vol. 13, pp. 839-846.

[62] *Modelling the efficiency of multijunction solar cells.* **T.J.J. Meyer, T. Markvart.** 2005, Proceedings of the 2nd photovoltaic science application and technology conference, Loughborough, UK.

[63] *A review of analytic solutions for a model p-n junction cell under low-injection conditions.* **M.D. Archer, J.R. Bolton, S.T.C. Siklos.** 2, 1996, Solar energy materials and solar cells , Vol. 40, pp. 133-176.

[64] *Limiting loss mechanisms in 23% efficient silicon solar cells.* **A.G. Aberle, P.P. Altermatt, G. Heiser, S.J. Robinson, A. Wang, J. Zhao, U. Krumbein, M.A. Green.** 7, 1995, Journal of applied physics, Vol. 77, pp. 3491-3504.

[65] *24% efficient PERL silicon solar cell: recent improvements in high efficiency silicon cell research.* **J. Zhao.** 1, 1996, Fuel and energy, Vol. 37, pp. 438-439.

[66] *Sliver solar cells: high-efficiency, low-cost PV technology.* **E. Franklin, V. Everett, A. Blakers, K. Weber.** 2007, Advances in optoelectronics, Vol. 2007, pp. 1-9.

[67] *An analysis of a "dead layer" in the emitter of n+pp+ solar cells.* **P. Kittidachachan, T. Markvart, G.J. Ensell, R. Greef, D.M. Bagnall.** 2005, 31st IEEE photovoltaic specialists conference, pp. 1103-1106.

[68] *Minimization of the effect of the collecting grid in a solar cell based silicon* . **A. Chekname, B. Benyoucef, J.P. Charles, R. Zerdoum, M. Trari.** 1-4, 2005, Solar energy materials and solar cells, Vol. 87, pp. 557-565 .

[69] *Mphill transfert report* . **S.A. Boden.** 2008, Southampton university.

[70] **B.G. Streetman, S. Banerjee.** *Solid state electronic devices 5th edition.* 2000. p. 558. IBSN:0130261017.

[71] **BASF Corporation.** *Lumogen F Dyes performance chemicals.* 2007.

[72] *Nanocrystalline luminescent solar converters.* **B. Jones, M. Scarpulla, J. Baker, K. Sivula, K. Alveri.** 2004, Photovoltaic materials, Vol. C226.

[73] *Photon collection efficiency of fluorescent solar collectors.* **P. Kittidachachan, L. Danos, T.J.J. Meyer, N. Alderman, T. Markvart.** 12, 2007, Chimia, Vol. 61, pp. 780-786.

[74] *Luminescent solar concentrators (LSC) I: theory of operation.* **J. S. Batchelder, A. H. Zewail, T. Cole.** 18, 1979, Applied optics, Vol. 18, pp. 3090-3109.

[75] *Fluorescent planar collector - concentrators: a review.* **A. Goetzberger, V. Wittwer.** 1981, Solar cells, Vol. 4, pp. 1-23.

[76] *Thin-film luminescent concentators for integrated devices: a cookbook.* **S.A. Evenson, A.H. Rawicz.** 31, 1995, Applied optics, Vol. 34, pp. 7302-7306.

[77] *Luminescent solar concentrators for energy conversion.* **R. Reisfeld, C.K. Jorgensen.** 1, 1982, Structure and bonding, Vol. 49, pp. 2-34.

[78] *Physical limitations of the concentration of direct and diffuse radiation.* **A. Goetzberger, W. Stahl, V. Wittwer.** 1985, Proceedings of the 6th European photovoltaic solar energy conference, pp. 209-216.

[79] *Temperature effects on the efficiency of luminescent solar concentrator (LSC) for photovoltaic systems.* **F.J. Meseguer, F. Cusso, F. Jaque.** 1981, Journal of luminescence, Vol. 24/25, pp. 865-868.

[80] *Radiance amplification by multi-stage fluorescence system.* **W.A. Shurcliff.** 3, 1951, Journal of the optical society of America, Vol. 41, pp. 209-209.

[81] *The collection of light from scintillation counters.* **R.L. Garwin.** 1960, Review of scientific instrumentation, Vol. 31, pp. 1010-1011.

[82] *Radiance amplification by a fluorescence radiation converter.* **G. Keil.** 9, 1969, Journal of applied physics, Vol. 40, pp. 3544-3545.

[83] *Materials for luminescent greenhouse solar collectors.* **J.A. Levitt, W.H. Weber.** 10, 1977, Journal of applied optics, Vol. 16, pp. 1684-2689.

[84] *Luminescent solar concentrators (LSC).* **J.S. Batchelder, A.H. Zewail, T. Cole.** 1980. Proceedings of the SPIE 24th international technical, San Diego, California, USA. Vol. 248, pp. 105-108.

[85] *Photon trapping and energy transfert in multiple-dye plastic matrices: an efficient solar-energy concentrator.* **B.A. Swartz, T. Cole, A.H. Zewail.** 2, 1977, Optics letters, Vol. 1, pp. 73-77.

[86] *Luminescent solar concentrators (LSC) II : experimental and theoretical analysis of their possible efficiencies.* **J.S. Batchelder, A. H. Zewail, T. Cole.** 21, 1981, Applied optics, Vol. 20, pp. 3733-3754.

[87] *Luminescent solar concentrators (LSC): their physics and chemistry.* **T. Cole, A.H. Zewail.** 1983. Proceedings of the photochemistry and photobiology international conference, Alexandria, Egypt. Vol. I and II, pp. 743-749.

[88] *Luminescent solar concentrators : An overview.* **A.H. Zewail, J.S. Batchelder.** 1983, Polymers in solar energy utilisation, Vol. 220, pp. 331-337.

[89] *Solar energy conversion with fluorescent collectors* . **A. Goetzberger, W. Greubel.** 1977, Journal of applied physics , Vol. 14, pp. 123-139.

[90] **V. Petrova-Koch, R. Hezel, A. Goetzberger.** *High efficient low cost photovoltaics.* 2009. IBSN:978354079358.

[91] *Light transport in planar luminescent solar concentrators: the role of DCM self absorption.* **J. Sansregret, J.M. Drake, W.R.L. Thomas, L. Lesiecki.** 4, 1983, Applied optics, Vol. 22, pp. 573-577.

[92] *Organic dyes in PMMA in a planar luminescent solar collector: a performance evaluation.* **J.M. Drake, M.L. Lesiecki, J. Sansregret, W.R.L. Thomas.** 16, 1982, Applied optics, Vol. 21, pp. 2945-2952.

[93] *Photon transport properties of luminescent solar concentrators: analysis and optimisation.* **J. Roncali, F. Garnier.** 16, 1984, Applied optics, Vol. 23, pp. 2809-2817.

[94] *Influence of the solvent matrix on the overlapping of the absorption and emission bands of solute fluorescent dyes.* **R.E. Sah, G. Baur.** 1980, Journal of applied physics, Vol. 23, pp. 369-372.

[95] *Dye in nanochannels boosts performance of artificial photonic antenna systems.* **G. Calzaferri.** 2009, SPIE Newsroom. DOI: 10.1117/2.1200805.1162.

[96] *Quantum dot concentrator and thermodynamic model for the global redshift.* **K. Barnham, J.L. Marques, J. Hassard.** 9, 2000, Applied physics letters, Vol. 76, pp. 1197-1199.

[97] *Modeling improvement of spectral responce solar cells by deployement of spectral converters containing semiconductor nanocrystals.* **W.G.J.H.M. van Sark, A. Meijerink, R.E.I. Schropp, J.A.M. van Roosmalen, E.H. Lysen.** 8, Semiconductors, Vol. 38, pp. 1000-1006.

[98] *High-efficiency organic solar concentrators for photovoltaics.* **M.J. Currie, J.K. Mapel, T.D. Heidel, S. Goffri, M.A. Baldot.** 226, 2008, Science, Vol. 321, pp. 226-228.

[99] *Outdoor evaluation of luminescent solar concentrator prototypes.* **M. Sidrach de Cardona, M. Carrascosa, F. Meseguer, F. Cusso, F. Jaque.** 13, 1985, Applied optics, Vol. 24, pp. 2028-2032.

[100] *Efficiency and concentration ratio measurments of fluorescent solar concentrators using a xenon measurments systems.* **K. Heilder.** 5, 1981, Applied optics, Vol. 20, pp. 773-777.

[101] *Fluorescent planar concentrator (FPC): Monte-Carlo computer model. Limit efficiency and latest experimental results.* **K. Heidler, A. Goetzberger.** 1982, Proceedings of the fourth E.C. photovoltaic solar energy conference, Stresa, Italy.

[102] *The luminescent solar concentrator: a parameter study towards maximum efficiency.* **L.H. Slooff, A.R. Burgers, E.E. Bende.** 2008, Proceedings of the SPIE photonics Europe, Strasbourg, France.

[103] *Luminescent solar concentrators- a review of recent results.* **W.G.J.H.M. van Sark, K.W.J. Barnham, L.H. Slooff, A.J. Chatten, A. Buchtemann, A. Meyer, S.J. McCormack, R. Koole, D.J.**

Farrell, R. Bose, E.E. Bende, A.R. Burgers, T. Budel, J. Quilitz, M. Kennedy, T. Meyer, C. Donega, A. Meijerink, D. Vanmaekelberh. 26, 2008, Optics express, Vol. 16.

[104] *A luminescent solar concentrator with 7.1% power conversion efficiency.* **L.H. Sloof, E.E. Bende, A.R. Burgers, T. Budel, M. Pravettoni, R.P. Kenny, E.D. Dunlop, A. Buchtemann.** 6, 2008, Physica status solidi (RRL) - rapid research letters, Vol. 2, pp. 257-259.

[105] *Efficiency limits of photovoltaic fluorescent collectors.* **U. Rau, F. Einsele, G.C. Glaeser.** 17, 2005, Applied physics letters, Vol. 87. ISBN: 171101.

[106] *Fluorescent collectors, photovoltaics and the thermodynamics of light, second Czech renewable energy conference, Brno, Czech Republic.* **T. Markvart.** 2006.

[107] *Investigation of near-infrared emitting lanthanide complexes in luminescent solar concentrators.* **B.C. Rowan, B.S. Richards.** 2007, Proceedings of the fourth PVSAT conference, Bath, UK.

[108] *Optical studies of some dyes as luminescent solar concentrators.* **A.F. Mansour.** 5, 1995, Indian journal of physics, Vol. 69B, pp. 465-470.

[109] *Luminescent solar collectors based on fluorescent glasses.* **L.J. Andrews, B.C. McCollum, A. Lempicki.** 1981, Journal of luminescence, Vol. 24/25, pp. 877-880.

[110] *The physics and application of fluorescent concentrators: a review.* **A. Zastrow.** 1990, Proceedings of the SPIE, Vol. 2255, pp. 534-547.

[111] *Luminescent solar-radiation concentrators and prospects of their use in solar technology.* **V.K. Baranov, M.B. Levin.** 2, 1989, Geliotekhnika, Vol. 25, pp. 21-30.

[112] *New perylene and violanthrone dyestuffs for fluorescent collectors.* **G. Seybold, G. Wagenblast.** 1989, Dyes and pigments, Vol. 11, pp. 303-317.

[113] *Luminescent solar concentrators- a review.* **A.M. Hermann.** 4, 1982, Solar energy , Vol. 29, pp. 323-329.

[114] *Solvent dependence of the fluorescence lifetime of xanthene dyes.* **D. Magde, G.E. Rojas, P.G. Seybold.** 1999, Journal of photochemistery and photobiology, Vol. 70, p. 737.

[115] *Advanced material concept for luminescent solar concentrators.* **B.C. Rowan, L.R. Wilson, B.S. Richards.** 5, 2008, IEEE: selected topics in quantum electronics, Vol. 14, pp. 1312-1322.

[116] *I-V Performance and stability study of dyes for luminescent plate concentrators.* **R. Kinderman, L.H. Slooff, A.R. Burgers, N.J. Bakker, A. Buchtemann, R. Danz, J.A.M. van Roosmalen.** 2007, Journal of solar energy engineering, Vol. 129, pp. 277-282.

[117] *Optical properties of colloidal PbSe nanocrystals.* **H. Du, C. Chen, R. Krishnan, T.D. Krauss, J.M. Harbold, F.W. Wise, M.G. Thomas, J. Silcox.** 11, 2002, Nano letters, Vol. 2, pp. 1321-1324.

[118] *The quantum dot concentrator: theory and results.* **A.J. Chatten, K.W.J. Barnham, B.F. Buxton, N.J. Ekins-Daukes, M.A. Malik.** 2003, Proceedings of the third world conference on photovoltaic energy conversion, Osaka, Japan, pp. 2657-2660.

[119] *Improving the optical efficiency and concentration of a single plate quantum dot solar concentrator using near infra-red emitting quantum dots (In the press).* **M. Kennedy, S.J. McCormack, J. Doran, B. Norton.** 2009, Solar energy. DOI:10.1016.

[120] *The effect of size and dopant concentration of the performance of nanorod luminescent solar concentrators.* **R. Bose, D.J. Farrell, A.J. Chatten, M. Pravettoni, A. Büchtemann, J. Quilitz, A. Fiore, L. Manna, J. Nelson, A.P. Alivisatos, K.W.J. Barnham.** 2008, Proceedings of the 23rd European photovoltaic solar energy conference, Valencia, Spain.

[121] *Luminescent solar concentrators: nanorods and raytrace modeling.* **R. Bose, D.J. Farrell, A.J. Chatten, M. Pravettoni, A. Büchtemann, J. Quilitz, A. Fiore, L. Manna, K.W.J. Barnham.** 2008, Proceedings of the 33rd IEEE photovoltaic specialists conference, San Diego, USA.

[122] *High efficiency carrier multiplication on PbSe nanocrystals: implication for solar energy conversion.* **R.D. Schaller, V.I. Klimov.** 18, 2004, Physics review letters, Vol. 92, pp. 186601-186610.

[123] *Use of the thermal lens technique to measure the luminescent quantum yields of dyes in PMMA for luminescent solar concentrators.* **M.L. Lesiecki, J.M. Drake.** 3, 1982, Applied optics, Vol. 21, pp. 557-560.

[124] *Outdoor testing of luminescent solar concentrators in a liquid polymer and bulk plate of PMMA.* **A.F. Mansour.** 1998, Polymer testing, Vol. 17, pp. 153-162.

[125] *Light transport in planar luminescent solar concentrators: the role of matrix losses.* **W.R.L. Thomas, J.M. Drake, M.L. Lesiecki.** 21, 1983, Applied optics, Vol. 22, pp. 3440-3450.

[126] *Optical efficiency and optical properties of luminescent solar concentrators.* **A.F. Mansour.** 1998, Polymer testing, Vol. 17, pp. 333-343.

[127] *The luminescent concentrator illuminated.* **L.H. Slooff, R. Kinderman, A.R. Burgers, A. Butchtemann, R. Danz, T.B. Meyer, A.J. Chatten, D. Farrell, K.W.J. Barnham, and J.A.M. van Roosmalen.** 2006. Proceedings of the SPIE , photonics for solar energy systems, Strasbourg, France. Vol. 6197, p. 61970k.

[128] *Luminescent solar concentrators.* **C.F. Rapp, N.L. Boling.** 1978, Proceedings of the 13th IEEE photovoltaic specialists conference, New York, USA, pp. 690-693.

[129] *Raytracing techniques applied to the modeling of fluorescent solar collectors.* **T.J.J Meyer, J. Hlavaty, L. Smith, E.R. Ferniere, T. Markvart.** 2009, Proceedings of SPIE Vol. 7211, Physics and simulation of optoelectronic devices XVII, San Jose, CA, USA.

[130] *Modelling of luminescent concentrators by ray-tracing.* **A.R. Burgers, L.H. Sloof, R. Kinderman, J.A.M. van Roosmalen.** 2005. Proceedings of the 20th European photovoltaic solar energy conference, Barcelona, Spain.

[131] *Luminescent solar concentrators and the reabsorption problem.* **R.W. Olson, R.F. Loring, M.D. Fayer.** 17, 1981, Applied optics, Vol. 20, pp. 2934-2940.

[132] *Characterisation of polymer films for fluorescent solar concentrator applications.* **A.F. Mansour, M.H. El Gazaly, M. Gaber, R.M. Ahmed.** 2005, International journal of polymeric materials, Vol. 54, pp. 237-246.

[133] *Stokes shift of fluorescent dyes in the doped polymer matrix.* **R.E. Sah.** 1981, Journal of luminescence, Vol. 24/25, pp. 869-872.

[134] *Self absorption treatment for the luminescent solar concentrators.* **A.M. Taleb.** 2002, Renewable energy, Vol. 26, pp. 137-142.

[135] *Maximising the light output of a luminescent solar concentrator.* **A.A. Earp, G.B. Smith, P.D. Swift, J. Franklin.** 2004, Solar energy, Vol. 76, pp. 655-667.

[136] *Photon transport in luminescent solar concentrators.* **R. Soti, E. Farkas, M. Hilbert, Z. Farkas, I. Ketskemety.** 1996, Journal of luminescence, Vol. 68, pp. 105-114.

[137] *Efficiency enhancement of fluorescent concentrators with photonic structures and material combinations.* **J.C. Goldschmidt, M. Peters, F. Dimroth, S.W. Glunz, G. Willeke.** 2008, Proccedings of the 23rd European photovoltaic solar energy conference, Valencia, Spain.

[138] *Lighttraping with angular selective filters.* **M. Peters, J.C. Goldschmidt, P. Loeper, B. Bläsi, G. Willeke.** 2008, Proocedings of the 23rd European solar energy conference, Valencia, Spain.

[139] *Photonic concepts for solar cells (In the press).* **M. Peters, A. Bielawny, B. Blasi, R. Carius, S.W. Glunz, J.C. Godschmidt, H. Hauser, M. Hermie, T. Kirchartz, P. Loper, J. Upping, R. Wehrspohn, G. Willeke.** 2009.

[140] *Thin-film luminescent concentrators for position-sensitive devices.* **I.S. Melnik, A.H. Rawicz.** 34, 1997, Applied optics, Vol. 36, pp. 9025-9033.

[141] *Calculation of luminescent solar concentrator efficiencies.* **P.S. Friedman.** 1980, LSC contract report, Owens-Illinois, USA, SERI Contract XS-9-8216-1.

[142] *Performance tests of organic dyes in a planar solar concentrator with ribbon photovoltaic cells.* **J.R. Wood, J.F. Long.** 1978, Proocedings of the thirteenth IEEE photovoltaic specialists conference.

[143] *Fluorescent solar concentrators using liquid solution.* **A. Filloux, J. Mugnier, J. Bourson, B. Valeur.** 1983, Revue de physique appliquee, Vol. 18, pp. 273-279.

[144] *Characterisation of fluorescent collectors based on solid, liquid and Langmuir-Blodgett films.* **L. Danos, P. Kittidachachan, T.J.J. Meyer, R. Greef, T. Markvart.** 2006, Proocedings of the 21st European photovoltaic solar energy conference, Dresden, Germany, pp. 443-446. 1CV.1.25.

[145] **N.L. Boling.** *Luminescent solar collector structure. 4190465* 1980. United State patent.

[146] *Luminescent concentrator module of a practical size.* **K. Sakuta, S. Sawata, M. Tanimoto.** 1994, Proceedings of the first WCPEC conference, Hawaii, pp. 1115-1118.

[147] *A modified luminescent solar concentrator.* **T. Oksa, M. Hamalainen, P. Saarinen, J. Harkonen.** 1986, Proceedings of the SPIE, optical materials technology for energy efficiency and solar energy conversion V, pp. 114-118.

[148] *Theory of fluorescent planar concentrators and experimental results.* **V. Wittwer, K. Heidler, A. Zastrow, A. Goetzberger.** 1981, Journal of luminescence, Vol. 24/25, pp. 873-876.

[149] *Geometry effects on photon collection in photovoltaic fluorescent collectors.* **L. Pronneke, U. Rau.** 2008. Photonics for solar energy systems II, proccedings of SPIE. Vol. 7002, pp. 0U1-0U10.

[150] *Response to "Comment on: Efficiency limits of photovoltaic fluorescent collectors".* **U. Rau, F. Einsele, G.C. Glaeser.** 2006, Applied physics letters, Vol. 88, p. 176102.

[151] *Fluorescent solar energy collectors: operating conditions with diffuse ligth.* **A. Goetzberger.** 1978, Applied physics, Vol. 16, pp. 399-403.

[152] *Theoretical comparison of cylindrical and square-planar luminescent solar concentrators.* **K.R. Mcintosh, N. Yamada, B.S. Richards.** 2, 2007, Applied physics B, Vol. 88, pp. 285-290.

[153] *Increased mc-Si module efficiency using fluorescent organic dyes: A ray-tracing study.* **K.R. McIntosh, B.S. Richards.** 2006. IEEE 4th world conference on photovoltaic energy conversion.

[154] *Solar concentrators using total internal reflection.* **G. Lifante, F. Cusso, F. Meseguer, F. Jaque.** 24, 1983, Applied optics, Vol. 22, pp. 3966-3970.

[155] *New luminescent back reflectors for the improvement of the spectral response and efficiency of luminescent solar concentrators.* **J. Roncali, F. Garnier.** 1984, Solar cells, Vol. 13, pp. 133-143.

[156] *Collection parameters of luminescent solar concentrators using mixed dye solutions.* **R. Kondepudi, S. Srinivasan.** Indian journal of pure and applied physics, Vol. 29, pp. 438-442.

[157] *Color consideration in fluorescent solar concentrator stacks.* **P.D. Swift, G.B. Smith.** 25, 2003, Applied optics, Vol. 42, pp. 5112-5117.

[158] *Light to light efficiencies in luminescent solar concentrators.* **P.D. Swift, G.B. Smith, J.B. Franklin.** 1999, Proceedings of the SPIE conference on solar optical material XVI, Denver, Colorado, USA, Vol. 3789, pp. 21-28.

[159] *Trans-thioindigo as a possible dye for solar collectors.* **A.N.A. Rahman, A.F. Mansour.** 1985, Journal of physics D: applied physics, Vol. 18, pp. L49-L52.

[160] *Optical and thermal spectroscopic studies of luminescent dye doped poly(methyl methacrylate) as solar concentrator.* **N.A. Bakr, A.F. Mansour, M. Hammam.** 1999, Journal of applied polymer science, Vol. 74, pp. 3316-3323.

[161] *Optical study of perylene dye doed poly(methylmethacrylate) as fluorescent solar collector.* **A.F. Mansour, M.G. El-Shaarawy, S.M. El-Bashir, M.K. El-Mansy, M. Hammam.** 2002, Polymer international, Vol. 51, pp. 393-397.

[162] *Outdoor testing and solar simulation for oxazine 750 laser dye luminescent solar concentrator.* **A.I. Salem, A.F. Mansour, N.M. El-Sayed, A.H. Bassyouni.** 2000, Renewable energy, Vol. 20, pp. 95-107.

[163] *Spectroscopic study of DCM as an active medium for luminescent solar concentrators.* **A.M. Taleb, T. Baha, T. Chiad, Z.S. Sadik.** 2005, Renewable energy, Vol. 30, pp. 393-398.

[164] *Spectrum shifting of sunlight by luminescent sheets: performance evaluation of photovoltaic applications.* **F. Galluzzi, E. Scafe.** 6, 1984, Solar energy, Vol. 33, pp. 501-507.

[165] **H.R. Blieden, J.W. Yerkes.** *Luminescent solar collectors. 4357486* 1978. United State patent.

[166] **S.G. MacDonald.** *Photocell with fluorescent conversion layer. 6538191* 2003. United State patent.

[167] **R.M. Murtha.** *Side collecting lightguide. 6021007* 2000. United State patent.

[168] *Thermodynamic modelling of the luminescent solar concentrator.* **A.J. Chatten, D.J. Farrel, C.M. Jermym, P.A. Thomas, B.F. Buxton, A. Buchtemann, R. Danz, K.W.J. Barnham.** 2005. Proceedings of the 31st IEEE photovoltaic specialists, Orlando, USA. pp. 82-85.

[169] *Characterisation of fluorescent collectors in terms of fluorescence collection efficiency.* **P. Kittidachachan, T.J.J. Meyer, L. Danos, R. Greef, T. Markvart.** 2007, Proceedings of the 22nd European photovoltaic solar energy conference, Milan, Italy, pp. 301-305. 1CV.1.23.

[170] **J.C. Stover.** *Optical scattering: measurement and analysis, Second edition.* 1995. IBSN:0819419346.

[171] **J.E. Harvey.** *Light scattering properties of optical surfaces, Ph.D. dissertation, University of Arizona.* 1976.

[172] *Inscription of dimensions and tolerances for optical systems; blemishes.* **Deutsches institut fur normung E.V. (German national standard).** 1980, p. 2. DIN 58170-54.

[173] *SUPRASIL® 1, 2, 3 and SUPRASIL® standard.* 2007, Heraeus Quarzglas, GmbH.

[174] *Surface texture (surface roughness, waviness, and lay).* 2002, American society of mechanical engineers, American national standard institute.

[175] *Optical and electrical properties of materials.* **H. El-Kashef.** 6, 1994, Review of scientific instrument, Vol. 65, pp. 2056-2061.

[176] *2008 Handbook of chemistry and physics.* s.l. : Taylor and Francis group, ISBN: 0849304849. Vol. 88.

[177] *Solvent dipole moment.* 2007, Macromolecular studies group, Louisiana state university.

[178] *Laser-based optical facility for determination of refractive index of liquids.* **F. Samedov.** 2006, Optics & laser technology, Vol. 38, pp. 28-36.

[179] *Physical and excess properties of binary and ternary mixtures of 1,1-dimethylethoxy-butane, methanol, ethanol and water at 298.15K.* **A. Arce, A. Arce (Jr), A. Soto.** 2005, Thermochimica acta, Vol. 435, pp. 197-201.

[180] *Vikuiti™ enhanced specular reflector (ESR).* **3M.** 2005, Electronic display lighting optical system division.

[181] **A. Noelle, G.K. Hartmann, A. Fahr, D. Lary, S. Le Calvé, J.J. Orlando, A.C. Vandaele, R.P. Wayne, C.Y.R. Wu.** *The 6th edition of the "UV/VIS spectra data base".* 2008. ISBN:978-3-00-026588-4.

[182] **N. Knighton, B. Bugbee.** *Spectrometer curve smoothing using replicate scans and running averages.* Physiology lab, Utah state university. 2004.

[183] *Spectroscopic characterisation of liquid fluorescent solar collectors.* **T.J.J. Meyer, T. Markvart, L. Danos, R. Greef, P. Kittidachachan.** 2007, Proceedings of the 3rd photovoltaic science application and technology, Durham, UK.

[184] *Measurment method for photoluminescent quantum yields of fluorescent organic dyes in polymethyl-methacrylate for luminescent solar concentrators.* **L.R. Wilson, B.S. Richards.** 2, 2009, Applied optics, Vol. 48, pp. 214-220.

[185] *Photophysics and CIS-trans isomerization of DCM.* **J.M. Drake, M.L. Lesiecki, D.M. Camaioni.** 6, 1985, Chemical physics letters, Vol. 113, pp. 530-534.

[186] *Spontaneous and stimulated recombination radiation in semiconductors.* **G. Lasher, F. Stern.** 1964, Physical review, Vol. 133, pp. A553 - A563.

[187] *The chemical potential of radiation.* **P. Würfel.** 1982, Journal of physics C: solid state physics, Vol. 15, pp. 3967-3985.

[188] **C. Kittel, H. Kroemer.** *Thermal physics.* 1980. p. 473. IBSN-13:9780716710889.

[189] *Transfer and storage of chemical and radiation potential.* **G. Porter.** 1982, Journal of the chemical society, Faraday transaction articles, Vol. 2, pp. 473-482.

[190] **J. Joliot, P. Lavergne.** Thermodynamics of the excited state of photosynthesis. *BTOL-Bioenergetics.* 2000, Chap 2.

[191] *Fluorescence quantum yields and their relation to lifetimes of rhodamine 6G and fluorescein in nine solvents: improved standards for quantum yields.* **D. Magde, G.E. Rojas, P.G. Seybold.** 4, 2002, Photochemistry and photobiology, Vol. 75, pp. 327-334.

[192] *Detailed balance in Förster-Dexter excitation transfer and its application to photosynthesis.* **P.D. Laible, R.S. Knox, T.G. Owens.** 1998, Journal of physical chemistry B, Vol. 102, pp. 1641-1648.